Structural Analysis of Zipping during Dorsal Closure in *Drosophila melanogaster* Embryogenesis

Dissertation

zur Erlangung der naturwissenschaftlichen Doktorwürde

Dr. sc. nat.

vorgelegt der

Mathematisch-naturwissenschaftlichen Fakultät der Universität Zürich

von

Mandy Börmel

aus Deutschland

...

Promotionskomitee

Prof. Dr. Damian Brunner (Vorsitz, Leiter)
Prof. Dr. Ohad Medalia
Prof. Dr. Stefan Luschnig
Prof. Dr. Ewa Paluch

Zürich, 2016

Contents

Acknowledgments

First of all, I am truly grateful to my two Ph.D. supervisors Prof. Damian Brunner and Prof. Ohad Medalia. I want to thank you for the special opportunity to work as a ”shared” Ph.D. student in both your labs at two different institutes at the University of Zurich. Thereby, I could benefit from both your research expertise. I know that this close collaboration was key for the development of my Ph.D. projects. I thank both of you for the constant support and the scientific and personal advice.

I would also like to thank my thesis advisory committee members Prof. Stefan Luschnig and Prof. Ewa Paluch. Your input from different scientific perspectives significantly contributed to this thesis.

I would further like to thank all past and present members of both the Brunner and the Medalia lab. You made my time in Zurich a special one and I am grateful for the friendly, helpful and open atmosphere in the labs. It was a pleasure to share time with you. A special thanks goes to my lab neighbor Magdalene Adamczyk, whom I consider to be a friend before a colleague. Thank you for all the discussions and especially for all the motivation boosts. I hope you have a great time-out exploring the world! I also want to thank Werner Boll, who was always on the spot for help with the light microscopes. He also gave me the hint to have a closer look at the fly stocks generated at Janelia Campus that were invaluable for the correlative imaging project on cell-cell recognition. Thank you Marisa Oliveira, Mirjam Bächler, and Michèle Grüner for critical comments on parts of this thesis. Further, thank you Jan Harapin for introducing and supporting me with the cryo-FIB/SEM technique. Also, many more people made my time special in the two labs: Maria Heimlicher, Laurynas Pasakarnis, Adam Kijowski, Steve Huisman, Erich Frei, Nadia Dube, and David Dreher from the Brunner lab and Simona Sorrentino, Anna Dubrovsky, Bruno Martins, Yagmur Turgay, Monika Zwerger and Matthias Eibauer from the Medalia lab.

I want to express my special gratitude to the staff scientists at the Center for Microscopy and Image Analysis (ZMB, University of Zurich). Andres Käch, Bruno Guhl, Gery

Barmettler, and Therese Bruggmann introduced me to the big, wide world of sample preparation and electron microscopy. Since I spent quite a lot of my time in the imaging facility, I could enjoy the working atmosphere there and I am thankful for the mental support from all team members. I also want to thank Moritz Kirschmann for advise on the software plugin TrakEM2 I employed for analysis of the correlative data. I could train my persistence, fine hand work and use of great machines for imaging of the cellular ultrastructure.

I also thank Prof. Achilleas Frangakis for the opportunity to perform room-temperature electron tomography in Frankfurt. I am very grateful to Mikhail Eltsov for discussions on the optimal sample preparation of fly embryos for electron microscopy.

And last, but of course not least, I want to thank all the people who supported me during my studies and made it possible to complete this thesis. These include all my friends, who shared good and bad times with me and always made me smile at the end. Thank you Sanna and Bogo for reloading batteries during innumerable hikes and runs in the beautiful Swiss mountains. A very special thanks goes to my parents for supporting me on my way over all the years. I know you always stand by me and I can not thank you enough. Finally, thank you Bogo for making me a very happy person. You are my world. I love you.

Summary

During embryogenesis tissues bend, fold, and fuse to create the complex shapes of numerous organs and structures in the body. Epithelial fusion events are a common developmental theme often occurring to seal a gap after epithelia were drawn together. Dorsal closure in mid-embryogenesis of *Drosophila melanogaster* serves as a paradigm for such epithelial fusion events. During dorsal closure, two lateral epidermal sheets are drawn towards the dorsal midline to fuse in a process called zipping.

Cells of opposing sheets fuse according to their anterior-posterior compartmental identity. Thereby, matching cells form large lamellar overlaps that subsequently shorten and transform into normal cell-cell contacts. In the first part of this thesis, I investigated the lamellar overlap organization during zipping. I established correlative light and electron microscopy to study the compartmental identity of cells in correlation with the question whether there is a left/right pattern with respect to which lamellae is on top of the other. Such a pattern would reveal an intriguing new possibility for a cell type-specific mechanism of cell-cell recognition. I investigated eight different zipping sites and describe the cell-cell interactions in a qualitative and quantitative manner. The majority of studied zipping sites showed a common organization of lamellar overlaps within the anterior and posterior compartment. Anterior cells from the left side protruded underneath opposing anterior cells, whereas posterior cells from the left side protruded over posterior cells from the right side. My data provides evidence that besides the anterior-posterior compartmental identity, which is known to be instructive in cell-cell recognition, left-right asymmetry is of importance.

In the second part of this thesis, I studied the microtubule organization and microtubule end morphology in the distal part of the cells forming the leading edge of the closing epidermis. Recent data suggested the importance of microtubules and cortex-tethered dynein as force-generators during mid zipping. It remained elusive how a force produced at the proximal part of a leading edge cell could be transmitted to the distal part to result in the constriction of the interacting cells. I employed electron tomography of

serial plastic sections and showed that the microtubule organization, dynamics, and anchoring appeared different in the distal part of a leading edge cell during mid zipping. The unexpected microtubule organization shows that more data is needed to sufficiently explore possible force transmission mechanisms.

In the last part of this thesis, I describe the establishment of cryo-electron tomography (cryo-ET) for embryogenesis of *Drosophila melanogaster*. Cryo-ET allows studying ultrastructures with near-to-life preservation at unprecedented resolution. I tested two different sample preparation methods to yield a small sample volume for cryo-ET analysis, namely cryo-sectioning and cryo-focused ion beam milling (cryo-FIB). While I achieved ultrastructural understanding of fly embryos by cryo-ET of re-vitrified frozen sections, cryo-FIB/SEM proved to be the more challenging technique. Despite several attempts, technical problems prevented the recording of cryo-electron tomograms. I conclude that cryo-sectioning and subsequent cryo-ET is the most promising technique for obtaining ultrastructural insights into fly biology.

Zusammenfassung

Morphogenetische Ereignisse sind durch Beugung, Faltung und Zusammenschliessen von Geweben charakterisiert. Dadurch entstehen die komplexen Formen zahlreicher Organe und Strukturen im Körper. Das Verschliessen von Epithelien ist ein häufiges Motiv während der Embryonalentwicklung. Nachdem die Epithelien zusammengezogen wurden, verschliessen deren Ränder ein Loch. Die dorsale Schliessung, die während der Mitte der Embryonalentwicklung von *Drosophila melanogaster* stattfindet, stellt ein Modell für einen solchen Verschluss von Epithelien dar. Während der dorsalen Schliessung werden zwei laterale Epidermisschichten zur dorsalen Mittelline gezogen, um in einem Prozess zu fusionieren, der als Zipping bezeichnet wird.

Zellen von gegenüberliegenden Epithelschichten fusionieren entsprechend ihrer anterioren-posterioren Kompartimentidentität. Zusammengehörende Zellen bilden grosse, lamellare Überlappe, welche anschliessend verkürzt und in normale Zell-Zellkontakte umgewandelt werden. Im ersten Teil dieser Doktorarbeit untersuchte ich diese lamellare Membranüberlappungsstruktur während des Zippings. Dafür etablierte ich korrelative Licht- und Elektronenmikroskopie. Damit studierte ich zugleich die Kompartimentidentität der Zellen sowie die Frage, ob ein links/rechts-Muster existiert im Zusammenhang mit der oben/unten Anordnung der lamellaren Überlappe. Eine solche Anordnung würde eine faszinierende, neue Möglichkeit für einen Zelltyp-spezifischen Mechanismus der Zell-Zell-Erkennung aufzeigen. Ich untersuchte acht verschiedene Zipping-Stellen und schildere die Zell-Zell-Interaktionen sowohl qualitativ als auch quantitativ. Die Mehrheit der untersuchten Zipping-Stellen wies eine gemeinsame Organisation der lamellaren Membranüberlappe innerhalb des anterioren und des posterioren Kompartiments auf. Anteriore Zellen der linken Seite tauchten unter gegenüberliegende anteriore Zellen ab, wohingegen sich posteriore Zellen der linken Seite über posteriore Zellen der rechten Seite erstreckten. Meine Daten erbringen einen Hinweis darauf, dass zusätzlich zur anterioren-posterioren Kompartimentsidentität, welche ausschlaggebend für den Zell-Zell-Erkennungsprozess ist, eine Links-Rechts-Asymmetrie wichtig zu sein scheint.

Im zweiten Teil dieser Arbeit untersuchte ich die Organisation von Mikrotubuli und deren Endmorphologie innerhalb des distalen Teils von Epithelzellen der vordersten Reihe. Neueste Daten legten die Bedeutsamkeit von Mikrotubuli und kortikal verankertem Dynein als Kräftegeneratoren während der Mitte des Zippings nahe. Es blieb unklar, wie eine solche Kraft, die im proximalen Teil der Epithelzellen der vordersten Reihe produziert wird, in den distalen Teil der Zelle übertragen werden kann, um eine Konstriktion der interagierenden Zellen auszulösen. Ich wendete Elektronentomographie von seriellen Plastikschnitten an und zeigte, dass die Organisation, die Dynamik und die Verankerung der Mikrotubuli anders im distalen Teil der Epithelzellen der vordersten Reihe während der Mitte des Zippings vorliegt. Die unerwartete Mikrotubuli-Organisation zeigt auf, dass mehr Daten notwendig sind, um mögliche Kräfteübertragungsmechanismen ausreichend zu erforschen.

Im letzten Teil dieser Doktorarbeit beschrieb ich die Etablierung von Kryo-Elektronenmikroskopie (cryo-ET) zum Studium der Embryonalentwicklung von *Drosophila melanogaster*. Cryo-ET erlaubt die Untersuchung der Ultrastruktur mit naturgetreuer Strukturerhaltung und beispiellos hoher Auflösung. Ich testete zwei verschiedene Probenvorbereitungen, um ein kleines Probenvolumen für die Cryo-ET Analyse zu erhalten, nämlich Kryo-Schneiden und die Abtragung biologischen Materials mittels Kryo-fokussiertem Ionenstrahl (cryo-FIB). Wohingegen ich ein Verständnis für die Ultrastruktur von Fliegenembryonen mittels Cryo-ET von re-vitrifizierten, gefrorenen Schnitten erlangen konnte, erwies sich cryo-FIB/SEM (cryo-FIB kombiniert mit Rasterelektronenmikroskopie) und anschliessender Kryo-Elektronentomographie als die kompliziertere Methode. Trotz zahlreicher Versuche machten technische Probleme das Aufnehmen von Kryo-Elektronen- tomogrammen unmöglich. Ich schlussfolgere, dass Kryo-Schneiden und anschliessende Kryo-Elektronentomographie die vielversprechendere Methode darstellt, um Einsichten in die Ultrastruktur der Fliege zu erlangen.

List of Figures

List of Tables

1 Introduction

1.1 *Drosophila melanogaster* is a versatile model organism

The common fruit fly *Drosophila melanogaster* is a powerful model organism for biological research. During the last 100 years its importance for the understanding of cell biological and developmental processes was shown in a multitude of occasions. Studies in *Drosophila* were awarded with four Nobel prizes: the genetic inheritance (Morgan [1910]), the damage of chromosomes by radiation (Muller [1927]), the genetic control of early embryonic development (Nüsslein-Volhard and Wieschaus [1980]), and the mechanisms of the innate immune system (Lemaitre et al. [1996]) were elucidated in the fruit fly. Today, *Drosophila* remains a popular, wide-used model organism for the study of a diversity of biological questions - from genetics to development to physiology to pathology to behavior, to only name a few.

In the Brunner lab, we use *Drosophila* to study epithelial fusions. Epithelial fusion events are a commonly employed motif during development (Martin and Wood [2002]): e.g. during ventral enclosure in *Caenorhabditis elegans*, during neural-tube closure in vertebrates, during palate fusion in mammalian embryos, and during wound closure (Kiehart and Galbraith [2000]). In *Drosophila*, a process during mid embryogenesis closes a dorsal epidermal gap. Dorsal closure (DC) is a paradigm for epithelial fusion events; knowledge gained on this model morphogenetic event regarding signaling molecules and cytoskeletal rearrangements might be widely applied to the aforementioned fusion events (Martin and Wood [2002], Harden [2002]).

In the next section, I give a rough overview on *Drosophila* embryogenesis and highlight in more detail two developmental processes that were interesting for this study; namely the segmentation of the embryo along the anterior-posterior body axis and dorsal closure.

1.2 *Drosophila melanogaster* embryogenesis

Drosophila melanogaster undergoes a quick life cycle of nine to ten days at 25° C, rendering it an attractive model organism. After embryogenesis, *Drosophila* undergoes three larval and a pupa stage before reaching adulthood. These metamorphic developmental stages are accompanied by dramatic changes of the body plan.

Drosophila completes embryogenesis within 24 hours at 25° C. A detailed summary on the embryogenetic events can be found in Campos-Ortega and Hartenstein [1985]. After fertilization of the egg, the nuclei undergo 13 mitotic divisions (Turner and Mahowald [1976]). The nuclei approach the surface of the egg in a step-wise manner. Thereby, nuclei of somatic cell buds, of polar buds and the yolk are specified. The pole cells will give rise to the germ cells at later stages. During the syncytial stage, all nuclei reside in a common cytoplasm without barriers except the cell membrane of the whole egg. The syncytial blastoderm stage is followed by cellularization. Invaginations of the egg membrane surround individual nuclei, thereby specifying the somatic cells. During gastrulation, germ layers are formed, endoderm, mesoderm, and ectoderm. Gastrulation comprises ventral furrow invagination, cephalic furrow formation, and germ band elongation. These major morphogenetic movements result in the formation of mid- and hindgut structures, a pocket containing the pole cells, as well as wrapping of the embryo by mesodermal and ectodermal cells. During germ band elongation, the ectodermal cells become patterned into parasegments and later into segments. This event is tightly genetically controlled and sets up the anterior-posterior body axis. More details are provided in section 1.3. Later, the germ band retracts posteriorly, unfolding the amnioserosa (AS) tissue. This extraembryonic tissue fills the dorsal opening (see also figure 2 A, B). During dorsal closure, the epithelial gap is closed by the convergence of the two lateral epidermal sheets towards the dorsal midline. Dorsal closure is specified in more detail in section 1.4. The extensive morphologic cellular rearrangements are completed by the involution of the head and embryogenesis is continued with the larval developmental stages.

1.3 A tight genetic control patterns the *Drosophila melanogaster* embryo along its anterior-posterior body axis

Studies on the patterning of the early *Drosophila melanogaster* embryo have given great insight into the development not only of insects, but humans alike. During development, segments within the fly embryo are specified, representing repeated units along the length of the embryo, that are further autonomously defined. Thereby, a regulated patterning of later emanating structures such as the larval tracheal, nervous and muscular system is ensured (Krzemien et al. [2012]). Vertebrate development is also characterized by segment development, for instance during the specification of the spinal cord vertebrae along the anterior-posterior axis from neck to caudal.
Great insights on how the fly embryo is patterned have been derived from a systematic screen searching for mutations that affect early embryonic patterning, winning the Nobel prize in 1995 (Nüsslein-Volhard and Wieschaus [1980]). By screening for alterations of the stereotyped denticle pattern within the cuticle, the screen identified the precise regulation of a gene cascade in space and time, patterning the embryo along its anterior to posterior body axis.
Within the next paragraphs, I will introduce this hierarchy in more detail, as reviewed in "Principles of Development, Wolpert et al., 5th edition".

A common theme in development are transcription factors that regulate in serial steps the expression of the next genes in a hierarchical manner. This sequential expression sets up positional information along the body axis. Determination of the anterior-posterior axis of a fly embryo (see figure 1 A) starts via maternal genes, comprising the mRNA and proteins deposited by the mother in the forming egg. For instance, the morphogen Bicoid forms an anterior-posterior gradient specifying the a-p axis.
The maternal genes activate the expression of zygotic genes that are expressed from the nuclei of the developing embryo. The first set of zygotic genes, the so called gap-genes, define broad regions. During the syncytial stage, all nuclei of the embryo share a common cytoplasm. Gradients of morphogens such as Hunchback and Knirps are thus

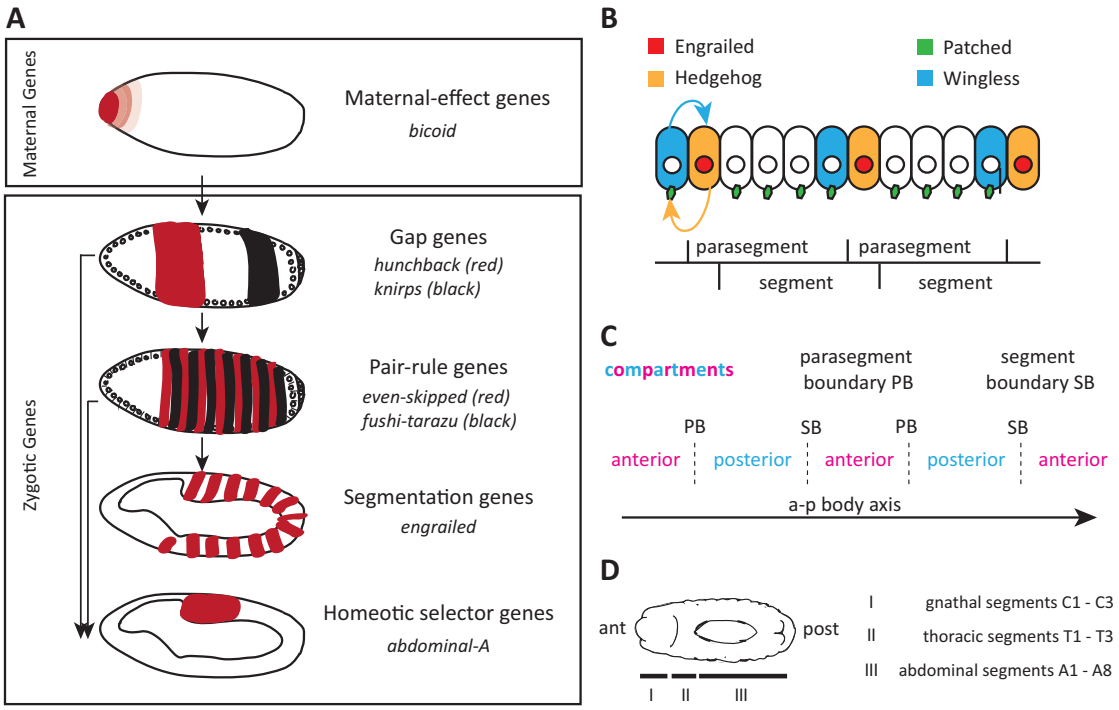

Figure 1: **Development of the *Drosophila melanogaster* anterior-posterior body axis.** **(A)** Segmentation cascade patterning the embryo along its anterior-posterior axis through the tight spatiotemporal control of maternal genes, gap gens, pair-rule genes, segmentation genes and homeotic selector genes. **(B)** Patterning of the embryo in parasegments and further segments. The concerted intercellular communication of Engrailed, Wingless, Hedgehog and Patched ensure the establishment of segment boundaries. **(C)** Specification of cells of each segment into either anterior or posterior compartmental identity by the segmentation genes *engrailed* and *wingless*. Cells of differing compartments never intermingle. Both a parasegment and segment boundary are formed. **(D)** The repetitive segments are further specified into gnathic, thoracic or abdominal identities by the action of homeotic selector genes.

established via diffusion without hindrance by cell membranes. The gap genes represent transcription factors themselves that interact, thereby sharpening the boundaries between broader domains. Hunchback, for instance, represses *knirps* expression.

Next, the parasegments, seven smaller periodic domains are defined by pair-rule genes. Each of the seven transverse stripes is autonomously initiated by the concerted action of local combinations of gap-gene transcription factors. *Even-skipped* specifies the odd-numbered parasegments, whereas *fushi tarazu* defines the even-numbered parasegments within the syncytial embryo (figure 1 A), shortly before cellularization starts (Martinez-

Arias and Lawrence [1985]).

This stage serves as a basis for the next segmentation round by segmentation genes, leading to patterning of the parasegments on either side of the parasegment boundary into segments (reviewed by Sanson [2001]). The segments are out of register relative to the parasegments, where each segment is made up of the posterior part of one parasegment and the anterior part of the next one (figure 1 B). The activated segmentation genes comprise not only transcription factors, but also signaling molecules enabling intercellular communication within the cellularized, gastrulating embryo. In response to the pair-rule genes, the transcription factor Engrailed is expressed within the anterior border of each parasegment, as is the secreted signal protein Hedgehog (figure 1 B). Hedgehog signaling via the Patched receptor in the adjacent cell on the other side of the parasegment boundary initiates the expression of Wingless. Both Wingless and Hedgehog stabilize the boundary by a positive feedback loop by promoting their mutual expression. The transcription factor Engrailed is expressed within 14 stripes along the anterior-posterior axis throughout the life time of the fly to establish and to maintain the posterior identity of cells (Kornberg [1981], Morata and Lawrence [1975]). By the concerted action of the segmentation genes each of the 14 segments (see figure 1 D) along the anterior-posterior axis comprises two compartments, two different cell-lineages. The anterior and posterior cells never intermingle and actively sort into the respective compartment (1 C). Thereby, two boundaries are established: the parasegment boundary between the anterior-posterior interface that represents a lineage-restriction boundary; and a segmental boundary between the posterior-anterior interface, where segmental folds will form (Larsen et al. [2003]). Further, the compartment boundary becomes visible on the ventral epidermis of the abdomen, where anterior cells produce denticles within their cuticle and posterior compartmental cells remain naked. Two hypotheses for the maintenance of the compartment boundaries have been proposed. The cell-lineage restriction within the compartments needs to resist cell proliferation and tissue deformation events during development. Possible mechanisms are either differential cell adhesion, as proposed by Steinberg (reviewed in Steinberg [2007]) or differential mechan-

ical tension (reviewed in Monier et al. [2010], and Dahmann et al. [2011]). Whereas the differential cell adhesion hyopthesis proposes a difference (qualitative and / or quantitative) of adhesion molecules, the differential mechanical tension stresses the differential surface contraction. A locally generated mechanical tension via actin-myosin enrichment could allow for active sorting of cells when in contact with wrong neighbors.

The hierarchical sequence of patterning is followed by the action of homeotic selector genes that further specify the identity of the segments into gnathal, thoracic and abdominal identity (1 D). The selector gene Abdominal-A, for instance, is expressed in parasegments 7 to 13, causing those to adapt the abdominal fate.

1.4 Dorsal closure

A hole on the dorsal side of the embryo is exposed during germ-band retraction (figure 2 A and B). The closure of this hole occurs during mid embryogenesis and is termed dorsal closure. This morphogenetic process controls the proper sealing of the epithelial gap. The hole is not void, but comprised of amnioserosa cells (figure 2 B). Amnioserosa cells are extraembryonic and do not contribute to the adult tissue, as they undergo apoptosis during closure of the dorsal hole (Jacinto et al. [2002b], Toyama et al. [2008]). Dorsal closure starts when the amnioserosa cells decrease their apical surface, thereby bringing the two lateral epidermal sheets closer to the dorsal midline (Kiehart and Galbraith [2000], Jacinto et al. [2002b]). In the epidermal cells, morphogenetic changes occur as well. Epidermal cells elongate along their dorso-ventral axis and a special set of cells is specified as leading edge cells (Jacinto et al. [2002b]). Those cells form the interface with the amnioserosa cells and the dorsal hole. Within the leading edge cells, a thick supracellular actomyosin cable is formed (Kiehart and Galbraith [2000], Jacinto et al. [2002a], figure 3). The force of this cable contributes to the dorsal closure process. To seal the dorsal gap, the two lateral epidermal sheets converge in a coordinated fashion and meet at the anterior and posterior canthus (figure 2 C), which mark off the ends of the eye-shaped opening. This process is termed zipping.

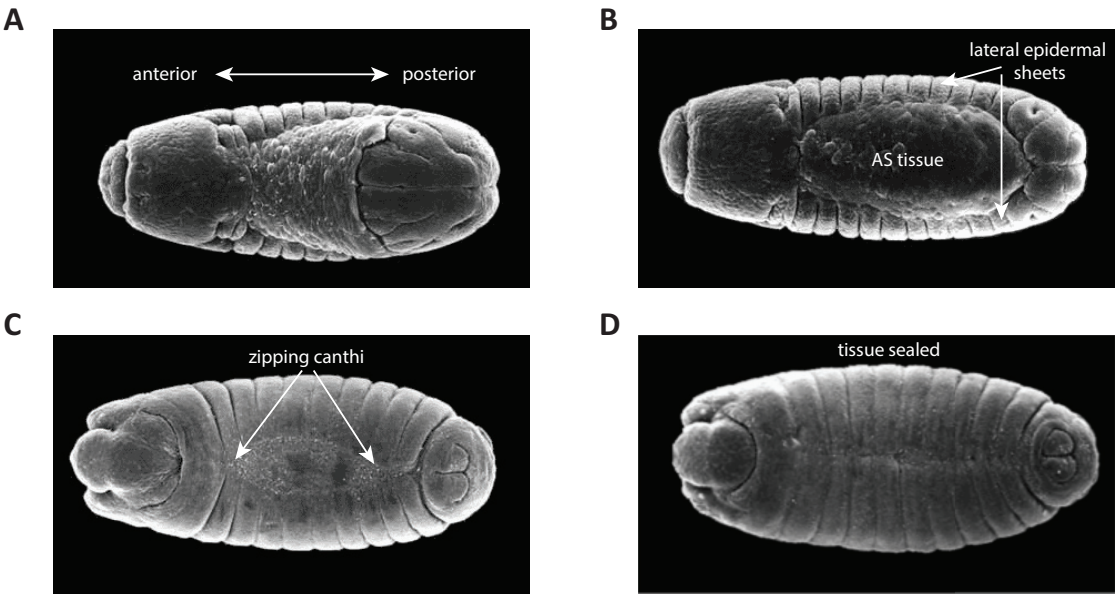

Figure 2: **Dorsal closure during mid embryogenesis of *Drosophila melanogaster*.** **(A)** - **(D)** Scanning electron microscopy images of *Drosophila* embryos during mid embryogenesis (from sdbonline.com). Dorsal view. **(A)** Stage 12 embryo at the end of germband retraction. **(B)** Stage 13 embryo, where the AS tissue is exposed and flanked by two lateral epidermal sheets that begin to move towards the dorsal midline. **(C)** Stage 14 embryo undergoing dorsal closure. The zipping from the two canthi seals the gap successively and completely closes the hole as shown in **(D)**, embryo at stage 15.

Dorsal closure is a paradigm for embryonic epithelial fusions (Martin and Wood [2002]). Knowledge on the involved cytoskeletal elements and signaling pathways might be applied to analogous epithelial fusion events (Harden [2002]), such as ventral enclosure in *C. elegans*, neural-tube closure in vertebrates, palate fusion in mammalian embryos, as well as wound closure (Martin and Wood [2002], Kiehart and Galbraith [2000]). Genetic approaches are more readily facilitated in *Drosophila* compared to genetic modifications and assessment of vertebrates, such as mice. Thus, the study of dorsal closure is an invaluable model system to gain insight into complex morphogenetic cell movements.

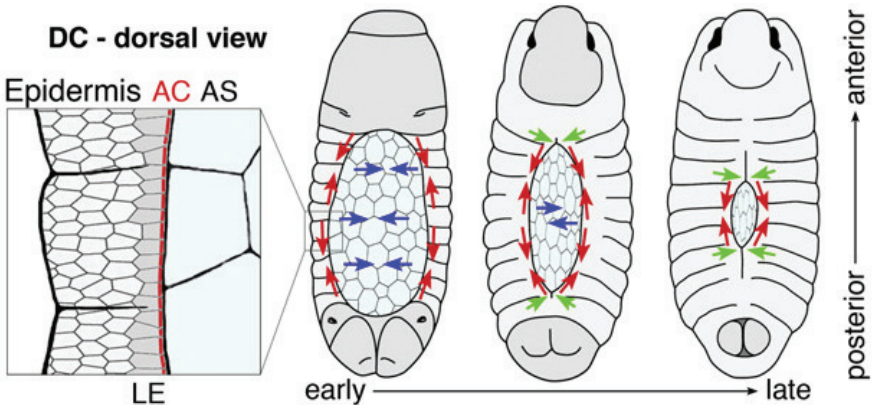

Figure 3: **Forces contributing to dorsal closure.**
(A) Cartoon of an embryo undergoing dorsal closure. The pulsed apical constriction of individual AS cells contributes forces for displacement of the lateral epidermal sheets towards the dorsal midline (blue arrows). The supracellular actomyosin cable within the LE cells contributes further to dorsal closure (red arrows). Finally, the zipping force at the two canthi drags opposing epidermal sheets together, resulting in a completely sealed epidermis (green arrows). From Solon et al. [2009].

1.4.1 Forces contributing to dorsal closure

There are three major forces contributing to dorsal closure: a contractile actomyosin cable within the leading edge (LE) cells, apical constriction of the amnioserosa cells, and the zipping force. To which extent those forces contribute to dorsal closure remains a topic of debate, as multiple contradicting models were proposed. The forces and accompanying models for force contribution during dorsal closure are introduced in more detail below:

Actomyosin cable within the leading edge cells. At the onset of DC, epidermal cells elongate along their dorso-ventral axis (Kaltschmidt et al. [2002]). A special set of cells, the leading edge cells, become specified via Jun amino-terminal kinase (JNK) signaling (Jacinto et al. [2002b]). Within the leading edge cells, activation of the planar cell polarization pathway via non-canonical Wingless signaling results in the redistribution of several cell-surface associated proteins (such as Flamingo, Discs Large and Dishevelled) in the plane of the epithelium (Kaltschmidt et al. [2002]). The planar polarization res-

ults in reorganization of the actin cytoskeleton, as actin-nucleation centers (ANCs) are assembled at the level of adherens junctions (AJs). Thereby, a thick actomyosin cable is formed comprising filamentous actin (F-actin) and non-muscle myosin II (MyoII). The cable runs along the anterior-posterior body axis within each LE cell, facing the dorsal opening. JNK signaling is not necessary for the formation of those ANCs, but is later essential for the maturation of ANCs and proper actin dynamics (Kaltschmidt et al. [2002]). The actomyosin cable is formed as a supracellular cable, spanning the whole dorsal opening. The actomyosin cable within each cell is connected to neighboring cells via adherens junctions (Eltsov et al. [2015]). It was suggested that the actomyosin cable acts as a contractile purse-string (Young et al. [1993], Kiehart and Galbraith [2000], Jacinto et al. [2002a], Franke et al. [2005]), thereby contributing to the convergence of the epidermal sheets towards the dorsal midline. The suggested additive force model predicted that both the actomyosin cable and the apical constriction of amnioserosa cells (described below) would produce force in excess. Both forces would exceed the tension within the lateral epidermis that retards the forward progression of the leading edge cell. Thus, both forces would make comparable contributions to dorsal closure, and one force could compensate the lack of the other (Kiehart and Galbraith [2000], Hutson et al. [2003], Franke et al. [2005]).

Apical constriction of the amnioserosa cells. The apical constriction of the amnioserosa cell surface is another force contributing to dorsal closure. It was suggested that at the onset of DC the amnioserosa cells start to constrict their apical surface in a gradual manner (Kiehart and Galbraith [2000], Franke et al. [2005]). The flanking epidermal sheets would be dragged towards the dorsal midline. The apical constriction is dependent on MyoII activity, as is the contractility of the supracellular actomyosin cable (Franke et al. [2005], Pasakarnis et al. [2016]). Improved time-lapse recordings revealed, that the apical constriction of AS cells even starts before the onset of DC and does not occur gradually, but rather in a pulsed fashion (Solon et al. [2009]). These finding led to a new proposed model, the so called ratchet model. Solon and colleagues

proposed that the pulsed AS apical constriction would result in local dorsal displacement of LE cells that would shorten their part of the actomyosin cable. The dorsal displacement of LE cells would be fixed and the actomyosin cable would act as a clutch or ratchet, preventing the LE cells to retract again to the ventral side when the AS cells relax (Solon et al. [2009]). Thus, both apical AS cell constriction and the actomyosin cable would act in a cooperative manner, ensuring proper dorsal closure progression. However, recent data from the Brunner lab challenges the necessity of the actomyosin cable, thus dismissing the ratchet model (Pasakarnis et al. [2016]). Pasakarnis and colleagues acutely knocked-down MyoII-activity in either the AS tissue or the epidermis, thereby selectively removing force from one of the tissues. They show that the AS tissue is able to drive DC without the actomyosin cable, whereas the cable alone is not sufficient for proper closure (Pasakarnis et al. [2016]). Thus, DC would rather be a single tissue-driven closure event than a system established by the cooperation of several forces.

Zipping force. The final force for dorsal closure comes from the zipping process. When the two lateral epidermal sheet are brought in close proximity, epidermal cells from the opposing sides establish contacts via cellular protrusions (Jacinto et al. [2000]). Zipping proceeds from the anterior and posterior side of the dorsal opening, sealing the epidermal sheets in a zipper-like fashion (figures 2 C and 3). Until recently, actin-mediated protrusion shortening was thought to account for the generation of the zipping force (Jacinto et al. [2000], Millard and Martin [2008]). However, the employment of large-volume electron tomography gave insights into the ultrastructural organization during zipping and dismissed the protrusion-shortening as a generator of force (Eltsov et al. [2015]). Eltsov and colleagues propose microtubules (MTs) as an alternative zipping force generator. This is specified in more detail in section 1.6.

Other force contributors. AS cells decrease their cellular volume during the onset of dorsal closure. Caspases initiate the apoptotic program of AS cells. The resulting cell volume decrease promotes tissue contraction and results in tissue shrinkage, promoting

DC progression (Saias et al. [2015]). Apoptosis was further shown to contribute force later during dorsal closure to the AS tissue (Toyama et al. [2008]). Some AS cells undergo apoptosis and delaminate from the AS tissue. The produced force both facilitates cell extrusion and promotes closure.

1.5 Cell-cell recognition during zipping

A pivotal role for filopodia in guiding the zipping process has been established (Jacinto et al. [2000], Millard and Martin [2008]). Filopodia most likely act as sensors, allowing a cell to realize its positional information in regard to its neighboring cells. By exploring the cellular environment, guidance cues or suitable cells for attachment can be recognized (Millard and Martin [2008]). The importance of filopodia dynamics and morphology is emphasized in mutants with impaired actin cytoskeleton (dominant-negative Cdc42). These embryos either show no zipping at all or severe mismatches (Jacinto et al. [2000], unpublished data Brunner lab). Filopodia were also assumed to re-align cells when initial matching of opposing compartment was not precise at single-cell resolution (Millard and Martin [2008]).

Recent data from the Brunner lab visualized the complex cell-cell interactions at the zipping site by employing large-volume 3D electron tomography (figure 4 C, Eltsov et al. [2015]). Based on the interaction morphology of opposing cells, zipping was subdivided into open, early, mid, and late zipping stages (figure 4 A). Filopodia were observed during the open and early zipping stages, when first contacts were established. These contacts are transformed into simple, single lamellar overlaps. Overlaps occur during early and mid zipping and provide a large interaction surface between opposing LE cells. We hypothesized, that in addition to filopodia large lamellar overlaps could represent ideal sites for recognition and cell-cell communication.

Very interestingly, Millard and Martin described that zipping of opposing cells occurs in a compartment-specific manner (Millard and Martin [2008]). Anterior cells from one side zip with opposing anterior cells, and posterior cells only zip with opposing posterior

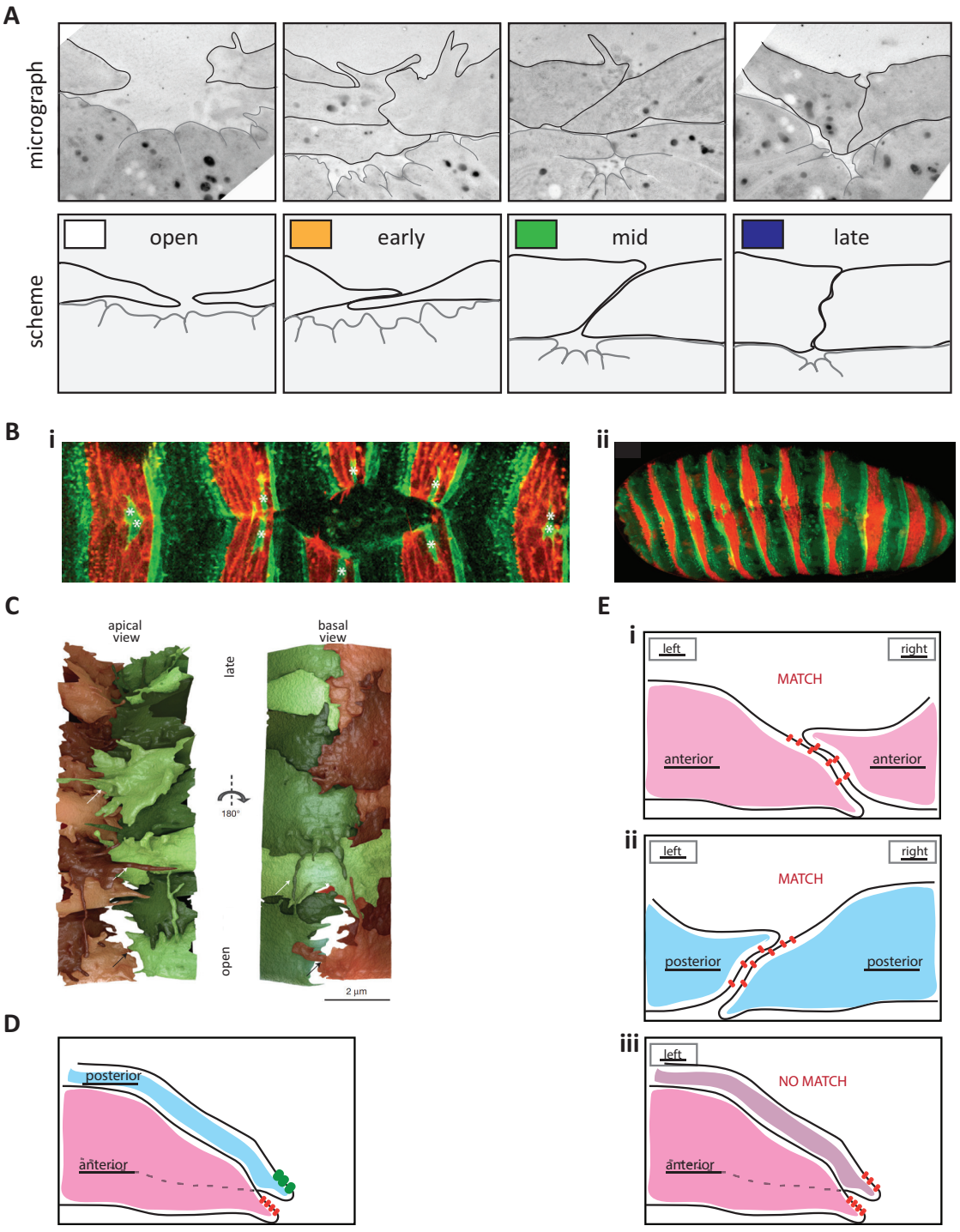

Figure 4: **Cell-cell recognition during zipping.**
(A) The zipping progress can be subdivided into several stages based on the interaction morphology of opposing LE cells. Electron micrographs (sample embryo beta, see part 3) of cross-sections through the embryo and simplified sketches representing the characteristics of open, early, mid, and late zipping. **(B)** The opposing epidermal cells match in a compartment-specific manner. Posterior cells are labeled in red, anterior ones in green.

Dorsal view; stills from time-lapse recordings showing the dorsal hole during closure **(i)** and the whole embryo after DC was finished **(ii)**. Adapted from Millard and Martin [2008]. **(C)** 3d reconstructions of the complex cell-cell interactions at the zipping site. Apical and basal view onto the opposing LE cells. The contact area between cells is mainly accounted for by single, simple lamellar overlaps that become especially visible in the basal view. Adapted from Eltsov et al. [2015]. **(D)** A possible recognition mechanism during zipping, where different recognition molecules (ligand/receptor pairs) are present depending on the anterior or the posterior compartment. **(E)** Another conceivable mechanism involving both the anterior-posterior identity of cells and a left-right asymmetry accounting for differential localization of a recognition molecule. If true, the lamellar overlap organization at the compartment boundary would switch **(i), (ii)**. Interestingly, this mechanism could also account for the fact that cells from the same compartment on the same side never fuse **(i)**, although forming complex, intertwining contacts.

cells (figure 4 B). They also observed that matching could occur between cells of the same compartment but of another segment, leading to X- and Y-shaped mismatching phenotypes (Millard and Martin [2008]).

Several mechanisms for cell-cell recognition during zipping are conceivable: 1) One is, that matching of opposing cells is mechanically constrained by the actomyosin cable within the LE cells. Cells could only establish contacts with their correct counterparts and no recognition mechanism would ensure proper matching. Arguing against this hypothesis is the fact, that initial mismatches occur frequently. Mismatches can be sorted out: Recognition occurs on at least two levels. First, cells meet according to their compartmental identity (Millard and Martin [2008]). These initial contacts can sometimes be imprecise, when a cell within a compartment does not contact the correct opposing cell within the opposing compartment. Sorting occurs after first interactions between opposing cells were formed and after lamellar shortening took place (force generation during zipping, see next section). Cells establish their correct partners within the opposing compartment and establish permanent adhesion structures.

2) Cell-cell recognition could also be achieved if each cell within the epidermis would possess a unique set of recognition cues that could only be recognized by one opposing cell. The lamellar overlap pattern during zipping would appear random.

3) Another conceivable hypothesis on the cell-cell recognition process attributes qualit-

ative different recognition molecules to either the anterior or the posterior compartment (figure 4 D). Cells could distinguish whether they are contacting an anterior or a posterior cell. If LE cells would possess recognition cues depending on their compartmental identity, the lamellar overlap of opposing cells would appear random. Independent on the anterior or posterior identity, cells would sometimes protrude over the opposing cell and sometimes underneath. No pattern of the lamellar overlap organization would become eminent.

4) We could think of yet another hypothesis on how cell-cell recognition is achieved. This hypothesis is based on a very interesting observation. LE cells from one side form not only contacts with opposing cells, but also with cells from the same side (Eltsov et al. [2015]). However, those neighboring cells would never zip and fuse. Somehow, the cells can distinguish neighboring cells that are from the same side from opposing cells. This implies the presence of a left-right asymmetry, as is later present during *Drosophila* embryogenesis (Spéder et al. [2006]). As shown in the cartoon in figure 4 E, correct matching of opposing cells according to their compartmental identity could be achieved when a left-right axis is included. Imagine that dependent on a left-right asymmetry and the compartment, the recognition cues (it could be the same for the two compartments) would be differentially localized along the apico-basal membrane. Thus, correct recognition of anterior-anterior (i) and posterior-posterior cells would be achieved (ii). Since the recognition molecules would be positioned in the same way for cells from the same compartment and the same side, no permanent interactions between neighboring cells could be established (iii). If this last hypothesis was true, one could observe a regulated pattern along the zipping site. The lamellar overlap organization would change at the compartment boundaries. The behavior of an anterior cell would distinguish from a posterior one, and the behavior of a left cell would be likewise distinguishable from a right one.

Testing these suggested hypotheses could be achieved by analyzing the lamellar overlap organization during zipping and simultaneously deciphering the compartmental identity of cells. Correlative light and electron microscopy (CLEM) could be used as a technique

and is further introduced in section 1.7.2.

1.6 Force generation during zipping

Traditional EM suggested that interactions between opposing LE cells were highly complex and cells were highly intertwined (Jacinto et al. [2000]). The authors proposed that actin-mediated protrusion shortening would generate the zipping force.

Many lines of evidence highlight the importance of another cytoskeletal element - that of microtubules - for the zipping process. Microtubules transiently reorganize at the onset of dorsal closure (Kaltschmidt et al. [2002]). Microtubules distribute apically within epidermal cells in anti-parallel bundles along the dorso-ventral axis (Jankovics and Brunner [2006]). The dependence on microtubules for zipping was shown, when microtubules were globally destabilized with the drug colcemid, or enzymatically severed by the protein Spastin (Jankovics and Brunner [2006]). The importance of the dynamics of MTs was further proved when the MT-stabilizing drug taxol was injected into embryos undergoing DC (Adamczyk [2016]). Observed zipping delays and zipping arrests underline the importance of MTs during zipping. Recently, large-volume electron tomography data elucidated the cell-cell interactions at the zipping site with improved resolution, and most of all in a 3D environment (Eltsov et al. [2015]). The overlapping cells from the opposing epidermal sheets formed no complex interactions, but rather a single lamellar overlap that was shortened during mid zipping (figure 4 A). The complex intertwined interactions observed by Jacinto et al. [2000] actually represented interactions between neighboring cells (Eltsov et al. [2015]). Injection of the actin-filament disrupting drug Latranculin B affected immediately both the tension within the AS tissue and the actomyosin cable (Eltsov et al. [2015]). Interestingly, zipping stopped with a delay that was most likely accounted for by observed tissue disintegration. These findings speak against the hypothesis of force-generation by actin-mediated protrusion shortening. On the contrary, Eltsov and colleagues suggest another force-generating mechanism. Both actin and MTs were identified in protrusions of opposing cells during

early zipping, whereas actin bundles were not visible in the lamellar overlaps during mid zipping. Tomographic analysis allowed for the identification and distinction of microtubules and their end polarity: The lamellar overlaps during mid zipping were full of plus end microtubules (Eltsov et al. [2015]). Unexpectedly, the presence of more shrinking than growing microtubules that were situated end-on at putative cell-cell adhesion sites of mid-zipping LE cells was observed (figure 1.6 A). This pointed towards a significance of freely depolymerizing MTs, since within an equilibrium more MTs are in the state of growth, that takes kinetically longer than the catastrophe event (Kirschner and Mitchison [1986]). The authors suggested a force-generation mechanism involving shrinking MTs and the minus-end directed motor protein Dynein. Reminiscent to spindle positioning within *C. elegans* or human cells (Nguyen-Ngoc et al. [2007], Kotak et al. [2012]), membrane-tethered dynein would capture incoming MTs plus ends, and pull on them by walking towards their minus end even while microtubules are depolymerizing (figure 5 B, I). The produced zipping force drags opposing epithelial sheets together. Studies interfering with various protein domains of Dynein could not definitely establish the importance of dynein for the zipping process, as the experimental set-up did not allow for depletion of maternally contributed Dynein mRNA and protein (Adamczyk [2016]).

If microtubules are the generator of the zipping force, the question remains how pulling on and depolymerization of MTs could be transferred into forward movement of the whole LE cell. Knowledge is needed on the MT organization and dynamics within the distal part of the LE cell, where they contact epidermal cells of the second row (figure 1.6 B, II). Are microtubules also anchored at the distal part? Is the antiparallel organization of the MT bundles an indication for MT sliding? Could MT motors such as dynein crosslink and slide MTs, resulting in the shrinkage of the LE cell (Tanenbaum et al. [2013])?

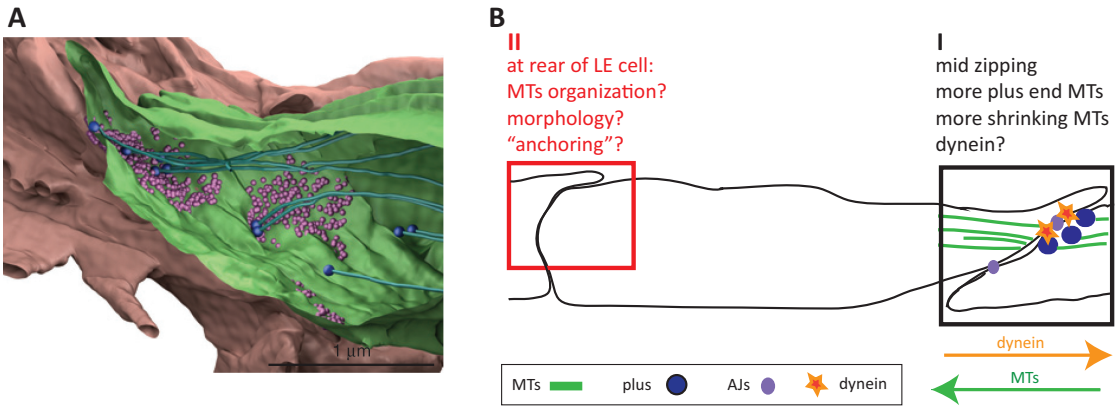

Figure 5: **Force generation and transmission during zipping.**
(A) Isosurface representation of opposing LE cells during mid zipping. Within the green LE cell, shrinking MTs (green lines with blue balls) are in close proximity to the cell cortex and to adhesion sites (purple balls). From Eltsov et al. [2015]. **(B)** Whereas the ultrastructural organization of MTs was elucidated at the proximal part of a LE cell **(I)**, the organization at the distal part remains unclear **(II)**. Structural studies will give insight on how force transmission of the zipping force occurs from the proximal to the distal part of the LE cell.

1.7 Structural analysis by electron microscopy / tomography

1.7.1 A short introduction to electron microscopy and tomography

Imaging is one of the most, if not the most important method that facilitates biological studies. By observing biology on various scales, one achieves great functional and structural insight: Microscopy enables direct imaging of single proteins, macromolecular assemblies, organelles, cells, tissues, and organs. Various microscopy techniques have been developed to study biological phenomena at different resolutions and scales. With medical imaging, such as magnetic resonance imaging and computer tomography scans, whole organs are captured, but the resolution is limited to 1 mm. Biological imaging, such as light microscopy (LM) and especially fluorescence light microscopy (FLM), enables time-lapse recordings of proteins of interest within their physiological surroundings at a resolution of approximately 50 to 200 nm. The resolution in LM is limited by the wavelength of light (Law of Ernst Abbé). The utilization of electrons for imaging by electron microscopy (EM) improves the resolution to less than 1 nm, giving great detailed insight into the cellular ultrastructure and context.

Light microscopy and electron microscopy follow common principles. Instead of a lamp, LED or laser providing photons for light imaging, electrons are emitted from an electron gun for EM. In LM, glass lenses such as the condenser and the objective adjust the number of photons to generate contrast, magnification, and focus. Glass lenses are substituted in EM with electromagnetic lenses that have basically the same function. Both photons and electrons penetrate and interact with the specimen. The resulting image is recorded on cameras. In transmission electron microscopy (TEM), contrast in an image is produced by the diffraction of electrons within the specimen (Vanhecke et al. [2011]). The elastically scattered electrons are recorded on CCD cameras. The best contrast is achieved by staining of the specimen with heavy metals, such that the electrons are more strongly scattered. In scanning electron microscopy (SEM), mainly secondary electrons are used for biological imaging. Those have a lower energy than the primary, penetrating electrons and provide information on the surface topography of a specimen that is recorded with a detector similar to a photomultiplier. Transmission electron microscopy is very similar to wide-field light microscopy, whereas scanning electron microscopy can be compared to confocal laser scanning microscopy.

A variation of electron microscopy is electron tomography (ET, reviewed in Vanhecke et al. [2011]). Thereby, a comprehensive description of the 3D ultrastructure is achieved. ET has proved to be a very powerful tool for structural insights into a whole yeast cell (Höög et al. [2007]), and into a whole zipping site during dorsal closure in *Drosophila* (Eltsov et al. [2015]). The principles of ET are depicted in figure 6. A tilt series of 2D electron micrographs is recorded for different incremental tilt angles (figure 6 A). These recorded projections (figure 6 B) are computationally aligned and processed in order to yield a tomogram (figure 6 C). A tomogram represents electron densities of the investigated sample in 3D. Electron tomography allows for great insight into subcellular organization and is vital for structural analyses.

The majority of any biological specimen consists of water. Therefore, the samples

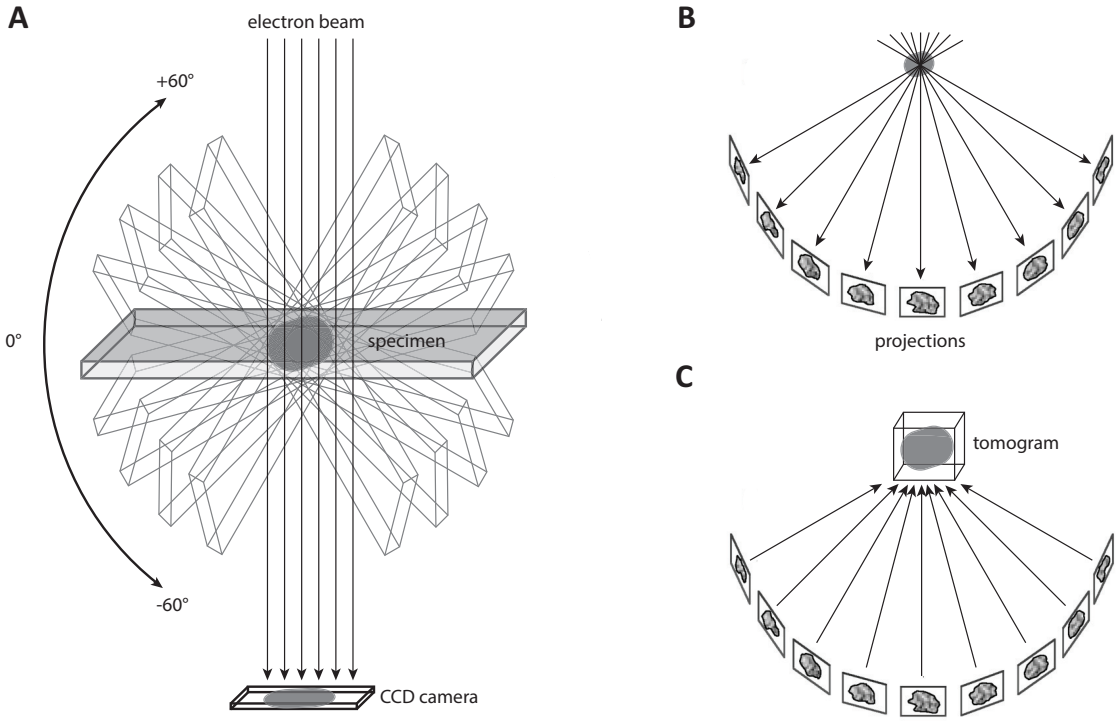

Figure 6: **Electron tomography and the reconstruction of 3D volumes.**
(A) A tilt series of 2D transmission electron micrographs (also termed projections) is recorded at different angles for the specimen of interest (section). Therefore, the specimen holder is tilted incrementally around an axis that is perpendicular to the electron beam and projections are recorded on a CCD camera. **(B)** Schematic representing the recorded projections of a specimen of interest at the various tilt angles. **(C)** Those projections are aligned and computationally processed via weighted backprojection to yield the so called tomogram, representing the 3D volume of the imaged specimen. Adapted from Grünewald et al. [2003].

need to be modified to resist the vacuum and the energetic electron beam in an electron microscope. In a first step for transmission electron microscopy preparation, the sample is fixed either chemically or via cryo fixation. Next, the samples are freeze-substituted, meaning they are dehydrated, often in combination with heavy metal staining. The heavy metals unspecifically bind to sub-cellular structures, e.g. uranyl acetate tends to bind to lipid and proteinaceous structures. Thus, the contrast for imaging is improved. Sample preparation is followed by replacing the water molecules with a resin that is hardened either with heat or UV-polymerization. The hard material is sectioned and

thin samples are introduced into the electron microscope. Thinning has to be performed for many biological samples. The maximum thickness that can be imaged is limited by the acceleration voltage of the electrons. In current microscopes, this is limited to a maximum of 300 kV. Therefore, samples should not exceed a thickness of a few hundred nanometer.

Both LM and EM are meaningful imaging techniques, with advantages and drawbacks. Combining the power of both imaging modalities and bridging scales holds greater informative value. Obviously, the detrimental sample preparation steps of dehydration, freeze-substitution with heavy metal staining, heat and UV-polymerization quench any fluorophore tremendously. The challenge of combining both LM and EM therefore lies in establishing a sample preparation compromise.

1.7.2 Correlative Light and Electron Microscopy

Fluorescence microscopy of labeled proteins enables live imaging of dorsal closure and staging of the process. In addition it allows identifying the compartmental identity of each cell. However, it lacks the z-resolution required to resolve the lamellar overlaps of interest and to unambiguously assign them to particular cells. Electron tomography in contrast, provides the necessary resolution, but it cannot provide the segment identity of cells and staging of the process is extremely difficult. Therefore, such studies can only be done with combined light and electron microscopy. Correlative Light and Electron Microscopy (CLEM; also termed correlated microscopy, de Boer et al. [2015]) is a state-of-the-art technique used to tackle various questions that so far were difficult to approach with a single imaging modality.

Correlative light and electron microscopy (CLEM) combines the virtues of different imaging modalities. CLEM enables the correlation of functional and structural analysis, thereby bridging scales and resolutions. Conventional fluorescence light microscopy

(FLM) allows for the identification of proteins of interest and the study of dynamic processes of a large field of view with an axial resolution of 200 nm. Combining specificity and dynamics of FLM with the increased resolution of electron microscopy, further revealing the cellular context, opens new avenues for the investigation of a plethora of biological questions.

Although the advent of super-resolution microscopy overcomes the diffraction barrier of light and pushes the limits of axial resolution to 20 - 50 nm (Willig et al. [2007], Betzig et al. [2006]), the information on the whole cellular context is still missing and thus super-resolution microscopy is rather an alternative method for conventional fluorescence light microscopy than a competitive approach to correlative microscopy.

Not one CLEM-experiment is similar to another, although they all follow the same theme. Different variants of CLEM have been developed in order to tailor experimental techniques to the specific question at hand (de Boer et al. [2015]). CLEM experiments differ in the specific method employed for light and electron microscopy, in finding back the region of interest, and accordingly in the applied probe for correlation.

De Boer and colleagues give an overview on different CLEM procedures and point out that the specimen, the intended preparation and preservation, and available microscopy set-ups determine the CLEM approach (de Boer et al. [2015]). CLEM enabled even the correlation of rare and fast events such as membrane trafficking by the help of a dedicated rapid transfer system. Thereby, highly dynamic processes within mammalian cells are imaged via FLM and quickly cryo-fixed by high-pressure freezing in less than 5 seconds (Verkade [2008]). Various approaches how to find back the region of interest were developed. Correlation can be achieved via direct correlation of fluorescent fiducials such as quantum dots that have an intrinsic fluorescence and are electron-dense for visualization via EM (Nisman et al. [2004]). Other strategies relied on the identification / creation of distinct landmarks via lasers (Spiegelhalter et al. [2014], Kolotuev et al. [2010]), knifes (Sjollema et al. [2012]), grid patterns (Verkade [2008]), and targeted microtomy (Kolotuev et al. [2012]). Integrated systems have been developed to circumvent possible loss of the sample during the transfer from one to the other microscope and

to ease the correlation. On these integrated systems both LM and EM are performed within one microscope on the very same sample (Agronskaia et al. [2008], Karreman et al. [2009], Peddie et al. [2014]).

Since the sample preparation for light and electron microscopy are mutually exclusive, many labs focus on the development of new probes for facilitation of CLEM. Simply put, two schools can be distinguished: Although both rely on genetically encoded probes for CLEM major differences manifest in the sample preparation.

On the one hand, in-resin fluorescence retention is aimed for. The fluorescence signal is preserved due to compromises made during the sample preparation process, namely reduced heavy metal staining and a sophisticated, long lasting freeze-substitution protocol. The fluorescent signal is preserved through sample steps such as cryo-fixation, dehydration, infiltration in resin, and UV-polymerization. The fluorescence is recorded after sample preparation and correlated with electron microscopic images of the very same region, allowing for a very high accuracy. In-resin fluorescence retention was successfully achieved in zebrafish (Nixon et al. [2009]), *C. elegans* (Watanabe et al. [2011]), yeast and mammalian cell culture (Kukulski et al. [2011]), and *Drosophila* (Fabrowski et al. [2013]). These studies have given insights into diverse biological processes such as microtubule dynamics in fission yeast (Kukulski et al. [2011]) or the sub-cellular localization and correlation of various proteins with super-resolution microscopy and EM (Watanabe et al. [2011]).

The other approach for CLEM relies on the ability of a certain probe to fluoresce and further to produce an electron-dense stain for electron microscopy. Either via photo-oxidation or via peroxidase activity an osmiophilic precipitate of diaminobenzidine (DAB) is generated. Grabenbauer and colleagues studied the sub-cellular localization of various proteins, such as a Golgi-resident protein, by producing oxygen radicals during bleaching of GFP (green fluorescent protein) that photo-oxidized DAB (Grabenbauer et al. [2005]). Another study proved the correct localization of proteins to their respective organelles via the miniSOG construct, that is capable to intrinsically fluoresce and to create singlet oxygen upon blue-light illumination, thereby creating a DAB stain in close

proximity to the miniSOG fusion protein (Shu et al. [2011]). Another probe generating an electron-dense DAB stain via peroxidase activity is APEX2 (Lam et al. [2015]).

I aim to use the power of CLEM to study the cell-cell recognition process during zipping to answer whether the lamellar overlap organization follows a certain pattern that could indicate a certain mechanism regulating matching.

1.7.3 Cryo-electron tomography achieves superior structural insight

Cryo-electron microscopy (cryo-EM) is at the forefront of modern structural biology for the visualization of macromolecular complexes within the cell (Pierson et al. [2011]). Cryo-electron tomography (cryo-ET) bridges the resolution gap between cellular and structural biology and is an indispensable tool for analysis of biological samples in an unperturbed, close-to physiological state (Yahav et al. [2011], Harapin et al. [2013]). Cryo-ET circumvents the adverse effects of conventional sample preparation steps employed for ET of plastic sections at room-temperature. More precisely, dehydration, heavy metal staining, and radiation are avoided, facilitating the study of macromolecular structures in their native environment (Lučič et al. [2013]). The sample is transformed into a vitrified state by cryo-fixation, such as high-pressure freezing or plunge-freezing. Vitrified water at cryogenic temperatures below -140 °C possesses the same volume as does water at room temperature. Contrary to ice crystals, the ultrastructure is preserved within a vitrified sample (McDonald [1999], Vanhecke et al. [2011]).

Both conventional electron tomography at room temperature and cryo-ET must overcome an obstacle during sample preparation. Many biological samples exceed the maximum thickness that can be imaged by current electron microscopes. Cryo-sectioning and cryo-focused ion beam milling are established thinning methods for the creation of thin sections for cryo-microscopy. In cryo-microscopy, image contrast is generated by the different elastic diffraction of electrons in the sample. Since a biological sample consists mainly of elements with a low atomic number and thus electrons, the achieved

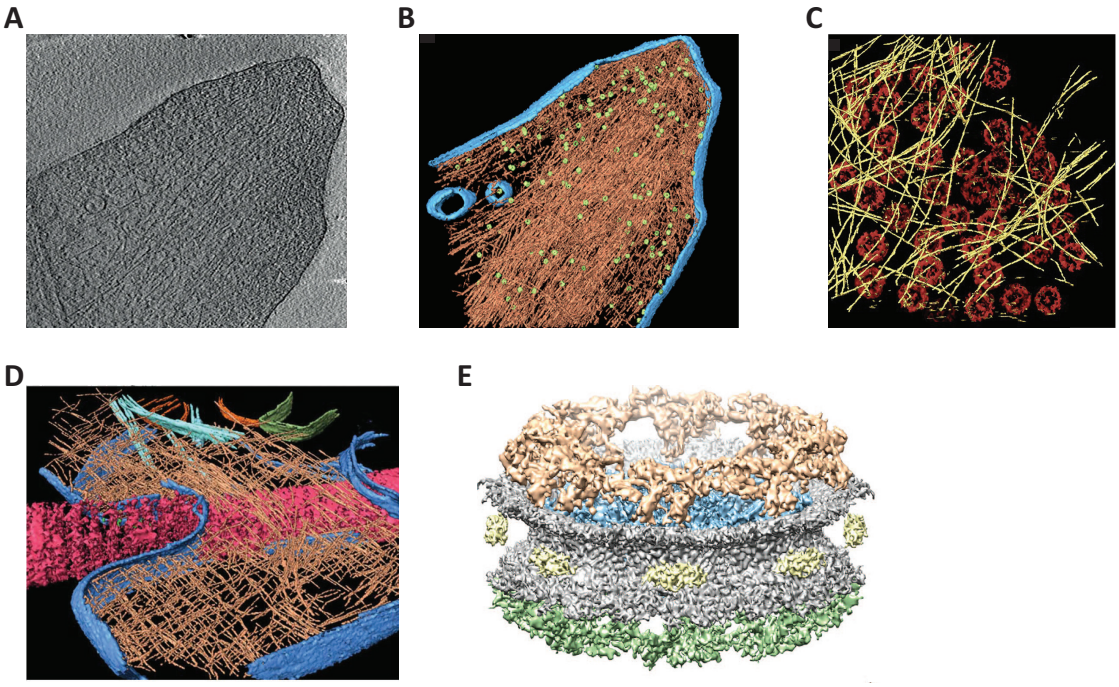

Figure 7: **Structural analysis of supramolecular assemblies by cryo-ET.** **A** Cryo-tomographic slice showing a focal adhesion site within a mammalian cell with aligned actin filaments. **B** Corresponding surface-rendering view of the focal adhesion with actin filaments (brown), membranes (blue), and many adhesion-related particles (green). (A) and (B) from Patla et al. [2010]. **C** A surface-rendered representation of the nuclear lamina formed by *C. elegans* lamin (yellow) that was injected into a *Xenopus laevis* oocyte. Nuclear pore complexes of the underlying *Xenopus* nuclear envelope are depicted in red. From Grossman et al. [2012]. **D** A surface-rendered view of a blood platelet spread on a collagen fiber (pink). The plasma membrane (blue), actin (brown), and microtubules (cyan) were segmented. From Sorrentino et al. [2016]. **E** Surface-rendered grazing view of the nuclear pore comlex of *Xenopus laevis*. 20 Å resolution were achieved by cryo-ET in conjunction with subtomogram averaging. The top of the cytoplasmic ring is shown in light brown, the bottom of the nucleoplasmic ring in green. From Eibauer et al. [2015].

signal-to-noise ratio is very weak compared to conventional electron microscopy that employs additional staining with heavy metals (Pierson et al. [2011]). In addition, the sample is highly sensitive to the electron beam. Therefore, imaging is performed in a low dose mode, where as few electrons as possible facilitate imaging, but reducing also the achieved contrast.

Despite the mentioned technical drawbacks, cryo-ET is a superior method for faithful structural analysis. Numerous publications emphasize its strength in elucidating cellular

networks and macromolecular complexes, such as the actin cytoskeleton in filopodia of *Dictyostelium* at unprecedented resolution (Medalia et al. [2002], Medalia et al. [2007]). Within the Medalia group, various macromolecular assemblies are studied with cryo-electron tomography. A selection is shown in figure 7. For instance, great structural insight into the actin cytoskeleton networks at native integrin-based focal adhesions were gained (figure 7 A, B). The assembly of the nuclear lamina was elucidated in a system, where lamin from *C. elegans* was injected into *Xenopus laevis* oocytes (figure 7). Another project in the lab focuses on the structural analysis of blood platelets (shown in figure 7 D) and more specifically on integrins. Moreover, cryo-ET combined with subtomogram averaging yielded the 3D structure of nuclear pore complexes of intact nuclei of *Xenopus laevis in situ* (figure 7 E).

I aim to establish cryo-electron tomography for the study of fly embryogenesis. Insights into the ultrastructure of flies at unprecedented resolution of samples close to a native state are fundamental for our understanding of biological processes, such as dorsal closure.

1.8 Aims of the thesis

Dorsal closure is a morphogenetic event occurring in *Drosophila melanogaster* that seals an epithelial gap during mid embryogenesis. A process called zipping concludes dorsal closure. Cellular protrusions from opposing epithelial LE cells sample the open space until the gap has closed sufficiently for them to engage with their accurate counterparts. Zipping progresses simultaneously from the anterior and the posterior opening towards the middle and results in the sealing of epidermal sheets and formation of mature adherens junctions (Jacinto et al. [2000]).

1) Cell-cell recognition during zipping

The fly embryo epidermis is neatly segmented into stripes of anterior and posterior com-

partments. During zipping, a precise matching of cells according to their positional identity along the anterior-posterior body axis takes place (Millard and Martin [2008]). Filopodia were implied in guiding the cell-cell recognition process (Jacinto et al. [2000], Millard and Martin [2008]). Recent large-volume electron tomography data of a whole reconstructed zipping site revealed the presence of a significant, single lamellar overlap structure (Eltsov et al. [2015]). One aim of this thesis was to test whether the nature of these overlapping lamellae confers any positional cue. In particular, we wanted to visualize the left/right as well as up/down organization of overlapping lamella in respect to the compartment identities and test for an occurring pattern. To that means, I established correlative light and electron microscopy. The analysis of eight individual zipping sites revealed for the majority a specific pattern of overlapping lamella. Dependent on the compartment identity and a left-right axis, anterior cells from the left side protruded underneath opposing anterior cells, whereas posterior cells from the left side protruded over posterior cells from the right side. These observations indicated additional importance of a left-right asymmetry ensuring proper cell-cell recognition during zipping. The left-right axis is thought to be established later during development to guide hind gut development and rotation of the forming testis by the unconventional myosin MyoID (Spéder et al. [2006]).

2) Microtubule organization and morphology during zipping

Recent data by Eltsov and colleagues suggested a force-generation mechanism during zipping that is mediated by microtubules and dynein. In that model, cortical-tethered dynein would capture plus-ended MTs to pull on them by walking to their minus ends and simultaneously initiate MT depolymerization (Eltsov et al. [2015]). In the second part of this thesis, I aimed at resolving the subcellular ultrastructure of LE cells during mid zipping by means of electron tomography. More specifically, I focused on MT organization and end morphology in the distal part of LE cells. Structural insights would allow to speculate on possible mechanisms for transmission of force from the front, proximal part of a LE cell to the distal part, resulting in the constriction of the interacting

cells. I reconstructed and segmented 18 tomograms from serial plastic sections of the distal part of one LE cell during mid zipping. I showed that MTs displayed both plus and minus ends at the distal apical part of LE cells. I concluded that MTs are most likely anchored differently at the distal part. The MTs are organized in anti-parallel bundles, allowing in principle for sliding of individual MTs in respect to each other by motor proteins. The importance of motor proteins in anchoring MTs to the cortex and in possible sliding needs to be further determined.

3) Establishing cryo-electron tomography for the structural study of fly embryogenesis

In order to study ultrastructure more faithfully, with near-to-life preservation at unprecedented resolution, one takes advantage of cryo-electron tomography. In the last part of this thesis, I describe the attempts undertaken to establish cryo-ET for fly embryos. I employed two different thinning techniques to create thin sections of *Drosophila* embryos for imaging with electron microsopy: cryo-sectioning with diamond knifes (cryo-ET of re-vitrified frozen sections) and cryo-focused ion beam ablation (cryo-FIB/SEM and subsequent cryo-ET, resulting publication included in appendix B). I conclude, that due to technical problems faced with the latter method, cryo-sectioning is the most promising preparation tool for cryo-ET of fly embryos.

2 Materials and Methods

2.1 Fly work

2.1.1 Used fly stocks

All fly stocks were kept, handled and crossed using standard genetic practices.

Used fly stocks were the following:

Table 1: **Utilized fly strains in this study**

Genotype	Description	Source
w; enGal4, UAS-mCherry-Moesin/Cyo	mCherry fused to Moesin to label F-actin, spatiotemporal regulation possible by a Gal4-driver	N. Dube, Brunner lab, $59#2A1 and $59#3A3
w; ; 10xUAS-IVS-myr::GFP-p10/10xUAS-IVS-myr::GFP-p10 in *attP2*	membrane-tethered GFP optimized for enhanced transcription and translation that can be driven by a Gal4 driver	G. Rubin, Janelia Research Campus
w+; UAS-mCherry/UAS-mCherry (7F2); UAS-mCherry/UAS-mCherry(28F14)	cytoplasmic mCherry that can be regulated via the UAS-Gal4 system	generated for this study by myself
w; ; pnrGal4/Tm3, Ser	*pnr* enhancer expressing Gal4 throughout the epidermis	BL #3039
w; ; UAS-mNeonGreen_palm 2-2-1/(TmSb) (SM54 in attP2)	membrane-tethered mNeonGreen, transcription can be regulated via Gal4	S. Luschnig, University of Munster
yw; ; pnr-Gal4w+UASmCherryMoe/Tm6C, Tb, Sb; Va	*pnr* enhancer expressing Gal4 and Moesin-mCherry labeling F-actin throughout the epidermis	E. Frei, Brunner lab
yw; UAS-myr-SNAP40-Sw+/UAS-myr-SNAP40-Sw+	SNAP-tag tethered to membrane, can be regulated via Gal4	original from G. Jefferis, University of Cambridge, outcrossed four times
w+; ; Sqh-Moesin-GFP (SGMCA)/Sqh-Moesin-GFP (SGMCA)	GFP-tagged actin-binding domain of Moesin under the control of ubiquitously expressed promotor / enhancer from the spaghetti squash gene	D. Kiehart, Duke University
w1118	white strain with isogenized chromosomes 2 and 3	Brunner lab
yw: Sp/Cyo(y+); MKRS/TM6B	multi-balancer stock	Brunner lab

2.1.2 Generating transgenic flies by P-element mediated insertion

The *mCherry* sequence was amplified from the plasmid pEntry_mCherry via Phusion-PCR (New England Biolabs) and cloned into pP(UAST) vector. The injection of *w1118* flies was performed according to the standard injection protocol from the lab, using 22.5 μg of purified pP(UAST)::mCherry and 2.5 μg of pTurbo as transposase donor plasmid. Freshly enclosed adults were crossed to *w1118* flies. The offspring was screened for expression of the *mini-white* marker, i.e. yellow to red eye pigmentation. Single flies were crossed to a multi-balancer stock to isolate and determine the chromosome of insertion. Numerous stocks with different insertions on chromosome I, II, or III were obtained and added to the Brunner lab stock collection. Cytoplasmic mCherry can be expressed with the Gal4-UAS system, controlling for tissue- and time-specific expression (Brand and Perrimon [1993], Phelps and Brand [1998]). A driver line with a specific promotor, such as engrailed, that is fused to the transcription factor Gal4 results in expression of Gal4 in posterior epidermal cells from gastrulation onwards. The transcription factor Gal4 binds to upstream-activating sequences that are fused to the gene of interest (here mCherry) - thus this protein is expressed under tight spatiotemporal control.

2.2 Correlative Light and Electron Microscopy

A graphic overview of the experimental steps for Correlative Light and Electron Microscopy established in this study is depicted in figure 8.

2.2.1 Spinning-disc confocal light microscopy

Selecting embryos for subsequent CLEM analysis

w; enGal4, UAS-mCherry-Moesin/Cyo were crossed with *w; ; 10xUAS-IVS-myr::GFP-p10/10xUAS-IVS-myr::GFP-p10 in attP2*. Embryos were collected and aged at 18°C. Dechorionation of embryos was performed with a 50 % hypochlorite solution (7 % javel water) for 3 minutes. The embryos were transferred to imaging dishes (Bioswisstec,

Imaging Dish CG 1.0) and aligned with self-made glue (glue resolved from sticky tape with heptane). To prevent dehydration, the embryos were covered with a dextran solution (30% 40 kDa dextran from Sigma, 0.5 % NP-40 in PBS). A preselection of embryos expressing membrane-tethered GFP in posterior cells and undergoing dorsal closure was done using spinning-disc confocal microscopy (custom-modulated Leica DM IRBE). The microscope was equipped with an iXon3/888 camera controlled by ANDOR IQ software. A 63X objective was used and imaging was performed at 23 - 25 °C. When possible, a time series was recorded to determine the correct progression of dorsal closure. Usually, Z-planes were acquired every μm and maximum-intensity Z-projections were further analyzed.

Controlling for normal dorsal closure progression of the analyzed fly stock

The dorsal closure progression of the analyzed fly stock *w; enGal4, UAS-mCherry-Moesin/Cyo; 10xUAS-IVS-myr::GFP-p10 in attP2/+* was compared to that of *w; enGal4, UAS-mCherry-Moesin/+*. Imaging was performed as described as above, using a 25X oil-immersion objective, recording the whole dorsal closure at an axial resolution of 1μm and a time resolution of 2 minutes. The dorsal closure speed was assessed by measuring the length of the dorsal hole from the anterior to the posterior canthus when the posteriorly labeled protrusions of cells from the thoracic segment T1 started to touch. The ratio of this length with the time needed to completely seal the dorsal gap represented the dorsal closure speed.

2.2.2 Sample preparation

Vitrification by high-pressure freezing

The sample preparation was performed following the described procedures in Eltsov et al. [2015] and Kukulski et al. [2011]. After selecting the embryos for subsequent analysis via CLEM, the embryos were cryo-protected as fast as possible. Thus, the recorded time-lapse movie of the dorsal closure process of a specific embryo represented the actual

stage of the dorsal closure and zipping stage very accurately. Cryoprotection of fly embryos was performed using high-pressure freezing. The high-pressure freezing machine HPM100 (Leica Microsystems) was transported to the vicinity of the spinning disc light microscope. One embryo sample was usually frozen within 2-3 minutes after imaging. One embryo was transferred with a thin paint-brush to the well of an acetone-cleaned, 150 μm deep, 3 mm wide aluminum platelet carrier (Engineering Office M. Wohlwend GmbH) and covered with 1 μl dextran solution (30% 40 kDa dextran from Sigma, 0.5 % NP-40 in PBS). The assembly was completed by placing the flat side of a B-type carrier (Engineering Office M. Wohlwend GmbH) as lid on top. High-pressure freezing of the sandwiched sample was performed without use of ethanol.

Puncturing the vitelline membrane

The lid of the sandwich assembly was removed with a manipulator device featuring a 3 mm wide indentation and by the help of forceps. The procedure was performed in LN_2. The cryo-protected samples were transferred in the lid of a falcon tube filled with LN_2 into the chamber of a cryo-ultramicrotome (Leica, UC6/FC6). The machine was precooled to -150°C to maintain the sample in a vitreous state. The vitelline membrane of the embryos was punctured at the head region with a very fine (sharpened forceps number 5), pre-cooled needle (LN_2-temperature) in order to improve the permeability for the dehydrating and embedding reagents during the subsequent freeze-substitution.

Freeze-substitution and resin-embedding

The freeze-substitution and resin-embedding was performed with an automated system for reagent handling (Leica EM AFS2). The samples were placed into a well of a plastic basket (Leica Microsystems (facing upwards, in order to facilitate optimal permeabilization. The orientation of the aluminum carrier with the embryo surrounded by the dextran solution was monitored with a stereomicroscope attached to the AFS2 system. The samples were freeze-substituted (dehydration, fixation by heavy metals) at -90°C for 48 hours in acetone (molecular sieve) in the presence of 0.1 % uranyl acetate (20 % stock

in absolute methanol, diluted to 0.1 % with acetone) to allow for in-resin fluorescence retention. Following freeze-substitution, the temperature was raised to -45°C throughout 24 hours, continued with further incubation for 16 hours at -45°C. The samples were washed three times with acetone for 10 min each, and infiltrated with Lowicryl HM 20 (Polysciences) with gradually increasing concentrations for 4 hours each, starting with 10 %, followed by 25 %, 50 %, and 75 %. During the last incubation step in 75 % lowicryl, the temperature was raised to -25°C. Resin embedding was completed by three incubations with 100 % lowicryl for 10 hours each, followed by ultraviolet polymerization at -25°C for 48 hours and further 48 hours with gradually increasing temperature to 20°C.

Re-orienting the embryos for subsequent cross-sectioning

The embryos were oriented flatly within the aluminum carrier from the high-pressure freezing process. This orientation only allows longitudinal sectioning, therefore, a re-orientation to facilitate cross-sectioning was performed. With a fine fretsaw and razorblades, the sample-column was cut from the plastic basket and the aluminum carrier was carefully removed without damaging the underlying sample. The blocks were trimmed and re-oriented on a flat surface of an Epon-Araldite column and glued via quick Araldite (Ultra) for 90 min at 45°C in the dark. By omitting Epon as glue, heat polymerization at 60°C and thus deterioration of fluorescent signal was circumvented.

Sectioning

The whole sectioning process was performed in the dark (Watanabe et al. [2011]). The embryos were sectioned perpendicular to the anterior-posterior axis (cross-section) with diamond knifes (MT 6858, DiATOME, size 2 mm, 45° angle, sectioning at 6°) on a Cryo-ultramicrotome (Leica EM FCS). The region of interest, the zipping site, was identified by collecting sections throughout the sample (at least every 10 μm) to assess the position along the anterior-posterior body axis of the embryo. The sections were either stained with toluidine blue and observed with a conventional upright light microscope (Zeiss)

using a 40X air objective. Alternatively, for increased resolution, the sections were imaged with the TEM FEI Tecnai G2 Spirit (FEI, Eindhoven). Semi-thin serial sections (100 - 150) of 300 nm thickness were collected, spanning the whole zipping site. Sections were transferred onto prepared copper slot grids (Agar Scientific, G2500C, 2mm x 1mm slot, 3.05mm). Those slot grids were manually covered with a 100 nm thick-formvar film (Fluka), that was stabilized by 8 nm carbon-coating (Bal-tec MED020). The serial sections were not further post-stained with heavy metals for increased contrast, in order to circumvent the detrimental effects on fluorescence retention. The sections to locate the region of interest, combined with the serial sections, allowed for assessing the identity of the collected zipping site, namely the anterior or the posterior canthus and facilitated the identification of the left and the right side within the sample.

2.2.3 Data acquisition

Spinning-disc confocal light microscopy

Recording the fluorescence signal of in-resin retained GFP within the plastic sections needed to be performed as quickly after section collection as possible, best within a few days. Although the GFP-signal was sufficient in samples that were stored six weeks before sectioning in the dark, the signal intensity was significantly decreased compared to samples sectioned shortly after finishing freeze-substitution and resin-embedding. The slot grids with serial sections were mounted in ddH_2O onto glass dishes (Bioswisstech) and fixed with a piece of silicone, the sections facing the glass. The water improved the fluorescence recovery of GFP (Watanabe et al. [2011]), and the assembly was readily (dis)mounted, easing the whole process. Spinning disc confocal light microscopy was performed using a custom-modulated Leica DM IRBE, equipped with an iXon3/888 camera controlled by the ANDOR IQ software. Using a 63X oil-immersion objective (NA 1.32), several images covering one section were recorded. The 488-laser (100 mW power) was set to 30 % laser power with the AOTF, exposure time of 100 ms with an electron-multiplying gain of 300 yielded a sufficient signal.

2D Transmission electron microscopy

2D transmission electron microscopy was performed using the FEI Tecnai G2 Spirit with an acceleration voltage of 120 kV. The microscope was controlled with the Gatan Digital Micrograph software, recording images with the Gatan Orius (CCD-camera, 4k x 2.6k pixels, 14 bit) detector at several different magnifications, spanning a range from 1400X, with a pixel size 27.9 nm/pixel, to 13000X, with a pixel size of 3.5 nm/pixel.

2.2.4 Data analysis

The reconstruction, segmentation and correlation of the acquired data was achieved with the free plugin TrakEM2 for FIJI (Cardona et al. [2012]), run on a virtual machine supplied by the Center for Microscopy and Image Analysis (ZMB) at the University of Zurich. Within the TrakEM2 plugin, several layers were created, where each represented a 300 nm thin section. One file contained the montage and alignment of subsequent LM images, another one that for the EM images. The correlation of LM and EM images was performed in yet another file. The LM images were manually montaged, aligned and the brightness and contrast normalized manually. For the EM images, an automated montage of 1400x - 13000x images was performed using the TrakEM2-integrated similarity transformation algorithm. The montaged EM images were subsequently manually aligned and the brightness and con-

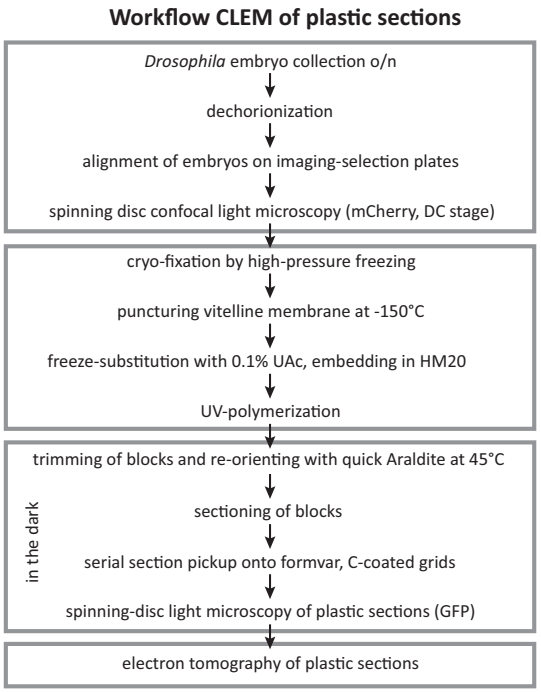

Figure 8: **Experimental steps for correlative light and electron microscopy.**

trast manually normalized. Leading edge cells were manually segmented, creating an arealist per cell with the brush tool. The FIJI implemented 3D viewer was used to display the 3D reconstructions of the segmented zipping site. The correlative analysis was performed by correlating the LM image with the ultrastructural details obtained by the EM image, relying for coarse alignment first on auto fluorescent folds and yolk granules and for finer alignment on the cell outlines of posterior GFP-labeled cells.

2.2.5 Generation of plots and statistics

Data were analyzed, plotted and tested for statistical significance using R software. The types of statistical test used are indicated in the figure legends. Briefly, the assumption of normally distributed data was assessed by the Shapiro-test (Royston [1995]). If the data was normally distributed, a two-sided t-test for unpaired samples (Welsh Two-Sample t-test) was performed, if not, the Mann-Whitney U-test was performed to assess a significant difference for compared datasets. The p-values were as follows: p-value < 0.001 (***). p-value < 0.01 (**).

Lines and boxes within the box-and-whisker plots represent the following: The box extends from the 25th to the 75th percentiles (interquartile range), with a line at the median where 50 % of the data is greater than that value. The whiskers indicate the maximum and minimum values (adding / subtracting 1.5 times the interquartile range to the 75th or 25th percentile, respectively), excluding outliers. The outliers are specified as more / less than 3/2 times of the upper / lower quartile. The notch displays the 95 % confidence interval around the median.

Figures were generated by processing images in FIJI and Adobe Illustrator. They were cropped, rotated, and their contrast and brightness were manually adjusted.

2.3 Electron Tomography of plastic-embedded sections of fly embryos

A graphic overview of the experimental steps for Electron Tomography of plastic-embedded sections employed in this study is depicted in figure 9.

2.3.1 Sample preparation

Vitrification by high-pressure freezing

Embryos were collected o/n at 18° (*w; enGal4, UAS-mCherry-Moesin/Cyo*), dechorionated and aligned for imaging as described in section 2.2.1. The staging of the embryos was performed by fluorescence light microscopy. Since three different high-pressure freezing machines were tested, the availability of a certain fluorescence light microscope differed. First, the Leica HPM100 (Leica Microsystems) available at the Center of Microscopy and Image Analysis (ZMB, University of Zurich) was tested. The used microscope for recording the mCherry-labeled filamentous actin was the LX Leica, equipped with a Hamamatsu EM-CCD (ImageEM) camera, controlled with the Leica AF software. Used objectives were a 20X HC Plan APO DIC oil-immersion (NA 0.7) and a 100X Plan APO PH3 oil-immersion (NA 1.3). The impaired sample preparation, including fragmented microtubules, could be due to the used high-pressure freezer. Therefore, also the Bal-Tec HPM010 at the Scientific Center for Optical and Electron Microscopy of the ETH Zurich was tested for its ability to optimally preserve the ultrastructure. The used light microscope, to select embryos undergoing dorsal closure for vitrification, was an Olympus MM, using a 20X Plan APO air objective (0.75 NA), equipped with a Hamamatsu ORCA-Flash 4.0 V2 camera, controlled by the Metamorph software (Molecular Devices). Also this machine did not achieve sufficient sample preservation, as observed with the single-axis tomography data (figure 27). Therefore, yet another machine was tested, that resulted in optimally preserved microtubule structures. The machine was also a Bal-Tec HPM010, used by the Frangakis group at the Goethe University Frankfurt. Embryos were selected using an inverted Axiovert 40 (Zeiss) with a 20X air objective. Those samples were used for dual-axis tomography acquisition (figure 28).

Freeze-substitution and resin-embedding

Puncturing of the vitelline membrane, freeze-substitution and resin-embedding were performed as described in section 2.2.2, with one aberration: the heavy metal concentration was 0.5 % uranyl acetate for optimal fixation and contrast establishment (Eltsov et al. [2015]).

Re-orienting the embryos for subsequent cross-sectioning

The embryos were reoriented in order to facilitate cross-sectioning. To that means, the blocks were trimmed and re-embedded in Epon-Araldite (Sigma; Epon 812, Durcupan ACM, Dibutylphtalat for stock solution; DDSA and DMP30). Polymerization was performed at 60°C for 28 hours.

Sectioning and post-staining

The sectioning process was performed as described in section 2.2.2. Serial sections covering cells during mid zipping were selected for tomogram acquisition. For enhanced contrast, sections were incubated with 2 % uranyl acetate in 70 % methanol, followed by Reynold's lead citrate. Protein A gold particles of 10 nm were applied to the grids as fiducial markers (Aurion) for the acquisition of single-axis tomograms. Grids subjected to dual-axis tomography were first incubated with 15 nm gold fiducials (CMC University Medical CenterUtrecht) and later with heavy metals for enhanced contrast.

2.3.2 Data acquisition

Single-axis electron tomography

I performed single-axis electron tomography in the lab of A. Frangakis (Goethe University Frankfurt) with an FEI F30, run at 300 kV acceleration voltage. The microscope was equipped with a 4 k x 4 k CCD camera, and was controlled with the FEI software. The serial sections were flattened by exposing them to 2000 - 3000 electron counts per

Å^2. Tilt series were recorded at 12.000x, corresponding to a pixel size of 0.9 nm/pixel at the specimen level. The tilt series was acquired with an increment of 1.5°, from +60 - -60° at a defocus of -4 μm.

Dual-axis electron tomography

I performed dual-axis electron tomography in the lab of A. Frangakis (Goethe University Frankfurt) with an FEI F30, run at 300 kV acceleration voltage. The microscope was equipped with a 4 k x 4 k CCD camera, and was controlled with the FEI software (batch tomography). The grids were placed in the dual axis holder from Fischerione, model 2040. The sections were flattened by exposing them to 2000 - 3000 electron counts per Å^2. Tilt series were recorded at 9.400x, corresponding to a pixel size of 1.2 nm/pixel at the specimen level. The tilt series were acquired with an increment of 1.5°, from +60 - -60°, perpendicular to each other, at a defocus of -0.25 μm.

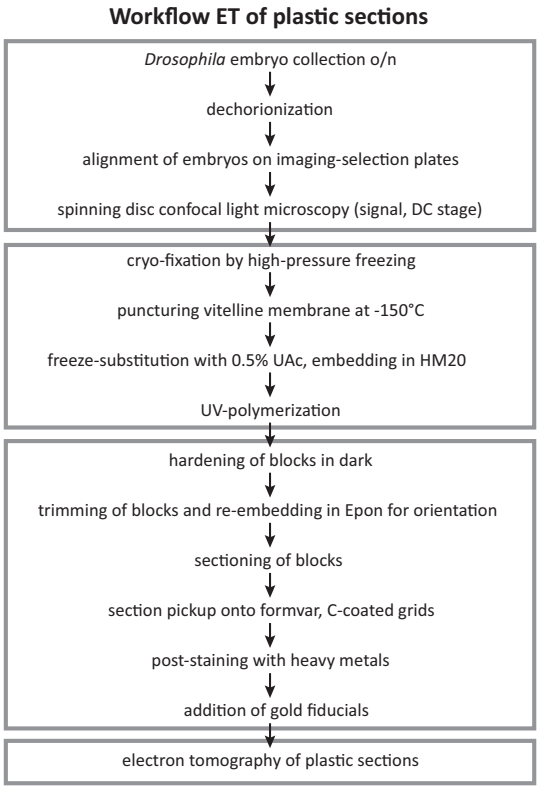

Figure 9: **Experimental steps for ET of plastic sections.**

2.3.3 Data analysis

The tomographic reconstructions were calculated using the eTomo package of IMOD (Mastronarde [1997]). The majority of the reconstructed tomograms of consecutive serial sections were not sufficiently flat and could therefore not be joined.

Automated tracing of microtubules was tested for the single-axis reconstructed tomo-

grams with a free software package for the visualization and data analysis software Amira, that was made available via registration with the Zuse Institute Berlin. Details on the automatic tracing algorithm are specified in section 5.2 and the online available Amira User Guide: section "tracing tube-like structures in electron tomography" (www.fei.com/software/amira-3d-user-guide.pdf).

The manual segmentation of microtubules, microtubule end structures, and plasma membranes within the reconstructed tomograms was carried out with IMOD (Kremer et al. [1996]) (for details see section 5.2) as described previously Höög et al. [2007]).

2.4 Cryo-electron tomography of re-vitrified frozen sections of the fly embryo

2.4.1 Sample preparation

The protocol described by Sabanay et al. [1991] and Bokstad et al. [2012] was adapted to study the ultrastructure within fly embryos. On overview of the experimental steps for cryo-ET of re-vitrified frozen sections (VFSs) is displayed in figure 10, left side.

Drosophila melanogaster embryos (w1118) were collected on agar collection plates. The developmental stage of the embryos was not assessed prior to sample preparation. The embryos were dechorionated as described in (2.2.1). The embryos were transferred with a fine paint-brush to a well of a 6-well plate containing freshly prepared Karnovsky fixative (3% paraformaldehyde, 2% glutaraldehyde, 5mM $CaCl_2$ in 100mM cacodylate buffer, pH 7.4). The chemical fixation was performed at RT first for 20 min on a shaker and further during removal of the vitelline membrane. To that means, several embryos were aligned on a glass slide with the tip of a very fine paint-brush, then transferred with double-sticky Scotch tape to a petridish, where they were covered immediately with the Karnovsky fixative. A fine glass needle, prepared from a glass capillary, was used to puncture the vitelline membrane at the anterior side of the fly embryo. After 10 min of further fixation, the vitelline membrane was removed by stroking it carefully

off the embryo with the glass needle. The devitellinized embryos were washed several times in 100mM cacodylate buffer, pH 7.4, for 20 minutes on a shaker at RT. Next, the embryos were infiltrated by a saturated sucrose solution (2.3 M in 100mM cacodylate buffer, pH 7.4) in a well of a 6-well plate on a shaker at 4°C o/n. Next, the embryos were embedded in 4% low-melting agarose (NuSieve GTG agarose, BioWhittaker Molecular Applications in ddH_2O) within plastic petridishes. The agarose was covered with 2.3M sucrose after cooling below 35°C for further infiltration o/n at 4°C. Cubes containing the embryo embedded in agarose were cut with a razorblade, the cubes further incubated in 2.3M sucrose for 3 hours in an Eppendorf tube on a spinning wheel at room-temperature (RT) for cryo protection. The cubes were then glued with a drop of sucrose onto a cryo-tome pin, such that the orientation of the embryo results in collection of cross-sections. Rapid freezing to –120°C was performed in the cryochamber of a Leica EM FC6 ultra cryo-microtome (Leica Microsystems). The sections were cut at –90°C to thicknesses of 200 nm, using diamond knifes (DiATOME) and the mentioned cryo-ultramicrome with a feed of 0.1–0.3 mm/sec under the action of an anti-static device. Sections were trans-ferred with a droplet of a pick-up solution (2.3M sucrose in 100mM cacodylate buffer, pH 7.4, on ice) to glow-discharged EM grids (Quantifoil, 200 mesh copper grids; plasma cleaner PDC-32G). The grids were rehydrated in a huge drop of ddH_2O at RT for at least 2.5 h. For re-vitrification, the grids were withdrawn from the water. 15 nm colloidal gold fiducial markers were coated with 5M BSA in PBS o/n at RT and were stored to a maximum of a week. 3 μl of fiducials are applied to the EM grid, followed by blotting with filter paper for 2 seconds and immediate plunge-freezing in ethane cooled by LN_2. The re-vitrified, frozen sections were then subjected to cryo-electron tomography.

2.4.2 Data acquisition and analysis

Specimens were analyzed in a 300-kV FEI Titan Krios transmission electron microscope equipped with GIF Quantum energy filters and a Gatan 4k UltraScan CCD camera. Tilt series were acquired covering an angular range of –60° to +60°, with 2.5° tilt increments

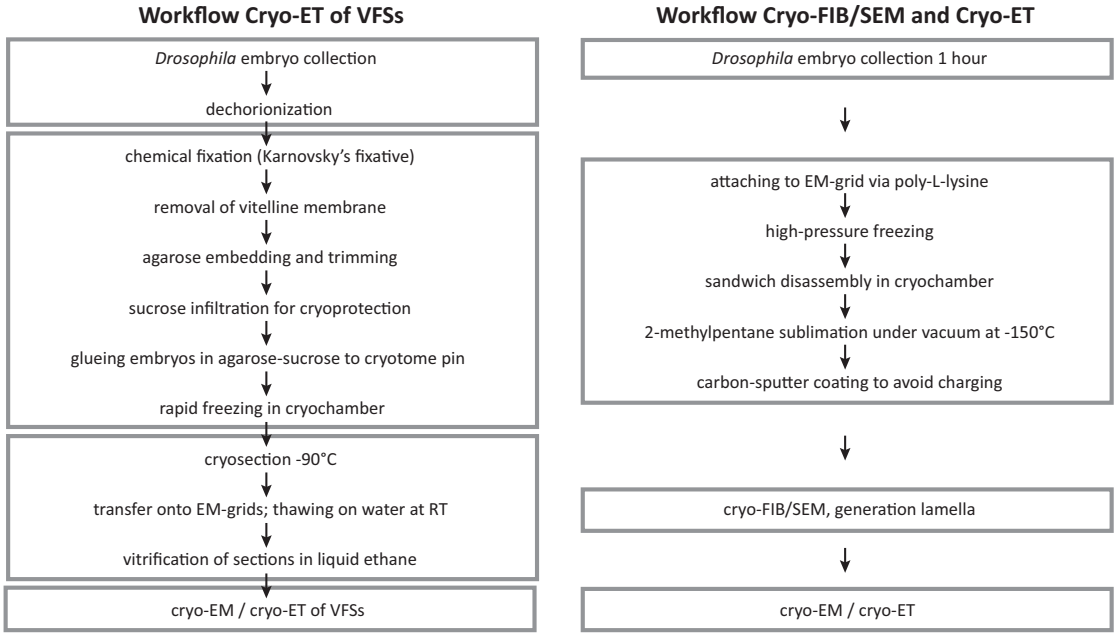

Figure 10: **Experimental steps for cryo-ET of re-VFSs compared to cryo-FIB/SEM with cryo-ET.**

and a defocus of -17 μm, using a magnification of 26.000x. The microscope was run in low dose mode, resulting in a cumulative electron dose below 150 counts per Å^2. Projections were aligned using 15 nm fiducial gold markers, and reconstructed by means of weighted back-projection with the TOM toolbox software package, resulting in a voxel size of 3.8 nm.

2.5 Cryo-focused ion beam milling / scanning electron microscopy

An overview of the experimental steps for cryo-FIB/SEM and subsequent cryo-ET is displayed in figure 10, right side.

Detailed information on the design of the cryo-holder and the shutter, the running of the cryo-FIB/SEM machine are given in Harapin et al. [2015], see Appendix B. Here, I only list aberations from the protocol, due to the processing of fly embryos instead of *C. elegans* embryos and adult worms.

Drosophila melanogaster embryos (w1118) of varying developmental stages were collected

on apple agar plates and dechorionated (when indicated) as described in 2.2.1. Various substrates were tested for the stable attachment of fly embryos onto plasma-cleaned, 200 mesh holey carbon copper EM grids (Quantifoil) prior to cryo fixation: Successful was the utilization of poly-L-lysine. Incubating the glow-discharged grid o/n on droplets of poly-L-lysine within a humidified chamber and subsequent placing of embryos onto the grid was performed. Excessive liquid was removed with a filter paper and the set-up was air-dried for 10 min.

Also tested were the following conditions: A fine layer of silicon grease (Baysilone-paste, Bayer) was applied onto the EM grid and the embryos were placed with a fine paintbrush on top. Alternatively, the floating of the grid on a droplet of 20% BSA in a humidified chamber o/n before placing of embryos and blotting of excessive liquid after 10 min of air-drying was tested. Another approach was to remove the waxy layer of the vitelline membrane to alter the chemical composition of the embryo's surface according to Rand et al. [2010]. The embryos were incubated in a 1:10 solution of 90% R-limone (Fluka), 5% cocamide DEA (Ninol 11 CM, Stepan Chemical), and 5% ethoxylated alcohol (Imbentin U/070, Kolb) for 2 min. After treatment with the embryo permeabilization solvent the embryos were washed 4x in PBS and placed onto an EM grid prepared with poly-L-lysine. Further, application of the heptane-glue mix that is also utilized in alignment of embryos on imaging dishes for spinning disc confocal microscopy (see section 2.2.1) was tested, applied as a fine film between EM grid and fly embryos. Also, incubation of the EM grid o/n on droplets of either the lectin concanavalin A (Calbiochem) or the lectin from *Bandeiraea simplicifolia* (Sigma) within a humidified chamber and subsequent air-drying of embryos on the EM grid prior to high-pressure freezing (HPF) yielded no stable, permanent attachment. Another unsuccessful approach was to dry dechorionated embryos that were attached to a poly-L-lysine coated grid for 3 to 4 min in a silica gel chamber (Roth). Additionally, the use of a yeast paste (baking yeast) was tested in vain.

The assembly, comprising the EM grid with the chorionated embryos attached via poly-L-lysine interaction, was placed into the 150 μm deep indentation of an acetone-cleaned 6

mm aluminum platelet carrier (Wohlwend Engineering), which was premoisturized with a small droplet of 2-methylpentane (Sigma). The cavity of the carrier was further filled with the freezing medium using a Hamilton syringe, covering the embryos completely. The HPF-sandwich was closed with the flat side of a 6 mm B-type carrier, draining excess solution into the surrounding filter paper. Cryo fixation was performed using the Leica HPM100 (Leica Microsystems) without ethanol. Grids with vitrified fly embryos were retrieved from the sandwich by placing the assembly for 10 minutes into a cryo chamber (Leica EM FC6) set to –150°C, causing 2-methylpentane to thaw. After a visual inspection of the vitrified embryos for physical damages such as cracks with the in-built stereomicroscope, the EM grids were stored in LN_2.

Attaching the grid to the modified cryo holder was performed in a dedicated cryo station (Leica Microsystems). Transfer steps were carried out using a VCT100 shuttle. Sublimation of 2-methylpentane was performed under high vacuum conditions within less than 30 min in a BAF060 device (Leica Microsystems), cooled to –150°C. A layer of carbon (15 – 20 nm) was applied by electron beam evaporation while rotating the sample and turning the carbon source to avoid charging problems complicating the SEM imaging. Cryo-FIB milling was performed with the Auriga cross-beam system (Zeiss), which was actively cooled to –156°C, involving a self-refillable LN_2-dewar.

Within subsequent rounds of gallium-ion beam ablation of biological material below and above the region of interest, a thin structure, the lamella, was produced: Coarse-milling was performed using a 16-nA probe, followed by semi-fine milling with a 240-pA probe and further thinning with a 50-pA probe, generating a lamella of 200 – 300 nm thickness within 3 – 4 days of fibbing. The milling depth was set to 7 – 13 μm depth, using 2 – 3 layers. The generated lamella were transferred and stored in LN_2 prior to cryo-electron microscopy. Recording of the lamellae was attempted in the 300 kV FEI Titan Krios transmission electron microscope.

3 Results: Cell-Cell Recognition During Zipping

Dorsal closure occurs in mid embryogenesis and is concluded by the final sealing of the tissue, the zipping process. The initial step of zipping involves cell-cell recognition of opposing leading edge cells resulting in matching of correct cell partners. Millard and colleagues suggested the existence of a positional cue that guides the zipping process, as cells of the anterior compartment only zip with cells from the opposite leading edge that have anterior compartmental identity as well, and similar matching occurs for cells with posterior compartmental identity (Millard and Martin [2008]). How this discrimination is achieved, remains elusive.

The detailed interaction of the leading edge cells at the zipping front was studied by Eltsov and colleagues using electron microscopy (Eltsov et al. [2015]). This study revealed various complex cell-cell interactions. Interestingly, by employing large-volume electron tomography of cells during mid zipping huge interaction surfaces between opposing cells were described. We wanted to study whether the nature of the overlaps generated by the leading edge cells follows a left-right pattern, or whether this interaction is random. Therefore, I aimed for utilizing correlative light and electron microscopy in the fly embryo. First, staging of embryos by fluorescence microscopy is achieved. Second, visualization of both the compartment boundaries by fluorescence microscopy and the details of the membrane interactions by electron microscopy on the very same plastic sections is facilitated.

In this part of the thesis, I first document how I established correlative light and electron microscopy for fly embryogenesis. The success of the method is dependent on a very strong GFP fluorescence signal, that persists past the detrimental sample preparation process. I then present the respective analysis of the lamellar overlap organization of eight different zipping sites. From this I conclude that compartment-specific cell-cell recognition appears to rely on left-right asymmetry. Finally, I discuss how positional information along the anterior-posterior axis is established and how cells could obtain a left-right asymmetry. I speculate on a possible mechanism that mediates proper zipping.

3.1 Establishing correlative light and electron microscopy in *Drosophila melanogaster* embryos

3.1.1 Correlative microscopy of the zipping recognition mechanism by in-resin fluorescence or epitope retention

In general, not one CLEM experiment is like the other, several variations of sample preparation were developed that depend on the investigated model organism and the addressed biological question (see section 1.7.2). Since no unifying method was introduced so far, the need to adjust existing protocols to the own question of interest remains.

Simplified, I could choose between two different ways of performing CLEM: Either a fluorescent signal is retained in-resin after the sample preparation process. Thus, the FLM and EM signal can be recorded on the same plastic section after sample preparation (Nixon et al. [2009]). Alternatively, specialized probes are both capable to fluoresce and to generate an electron-dense material that can be visualized in EM (miniSOG by Shu et al. [2011], APEX2 by Martell et al. [2012]). Thereby, FLM is performed before the sample preparation for EM. In order to avoid chemical fixation and masking of sub-cellular features within the electron micrographs, I decided to establish in-resin fluorescence / epitope retention for correlative microscopy.

Kukulski and colleagues established this method with the genetically encoded fluorophores mCherry and GFP and used it to study microtubule polarity, HIV-entry, and endocytic events in yeast and mammalian cells (Kukulski et al. [2011]). The method relied on a gentle and slow process, alleviating the adverse dehydration, resin embedding, heavy metal staining, and UV-polymerization, and at the same time allowing for optimal preservation of ultrastructure and fluorescence signal for 24 hours. Therefore, I adapted the protocol from Kukulski et al. [2011] following cryo fixation of fly embryos undergoing dorsal closure via high-pressure freezing (see section 2.2.2 in Material and Methods for details).

Studying the cell-cell recognition process during zipping bears challenges: not only is it necessary to retain fluorescence, but the large volume of the specimen of interest holds

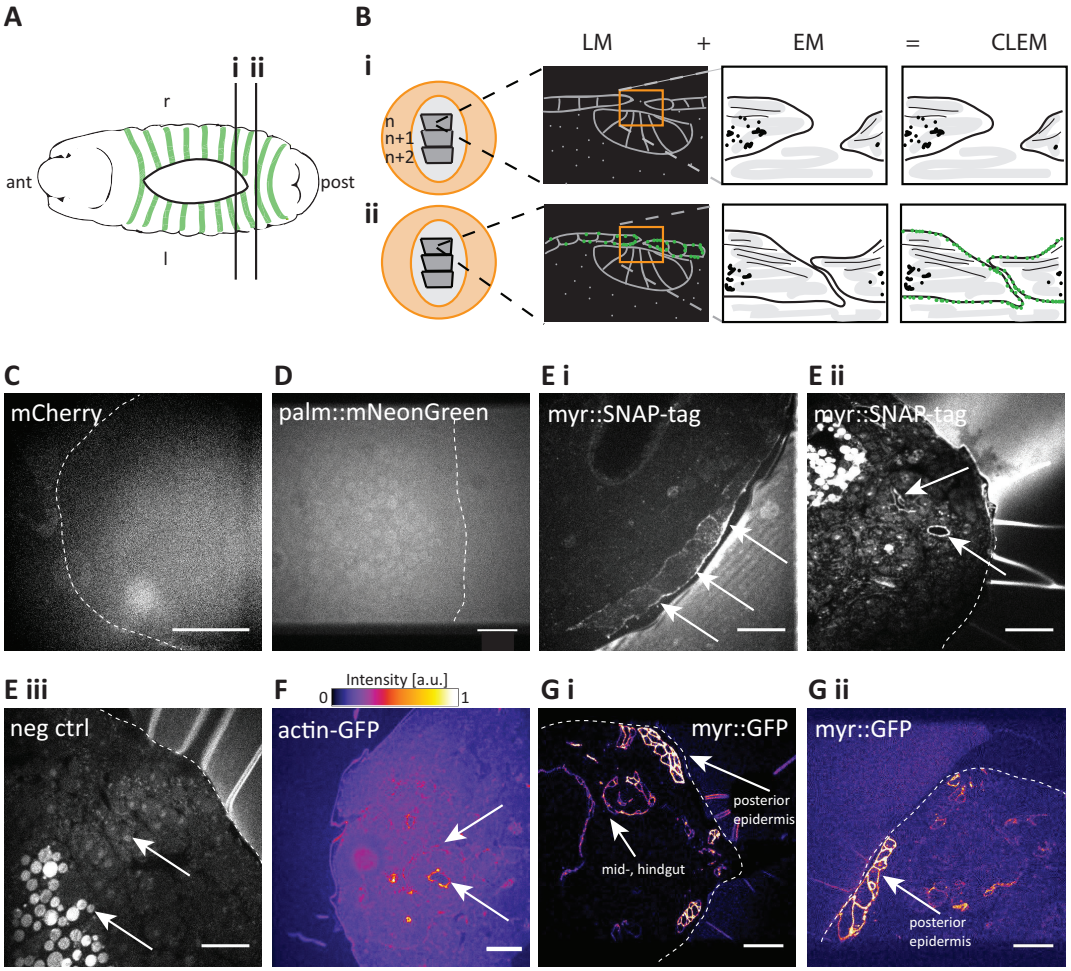

Figure 11: **Establishing correlative light and electron microscopy to study cell-cell recognition and tested fluorophores for the protocol.**
(A) - **(B)** Scheme of the designed CLEM method to study the matching process during zipping: **(A)** Serial cross-sections were collected from the opening of the dorsal hole towards the zipping site spanning approximately 30 μm (100 sections). In the final setup, posterior compartmental cells were labeled via the *engrailed-Gal4-UAS*-system and were thus distinguishable from anterior, unlabeled ones. **(B)** **(i)** Fluorescent light microscopy and further analysis of the very sub-cellular volume with transmission electron microscopy revealed compartmental identity (i anterior, **(ii)** posterior) and further the lamellar overlap structure at the zipping site. **(C)** – **(G)** Fluorescence retention of various fluorophores throughout the sample preparation process including dehydration, UV-polymerization and heavy metal treatment. Sections were tested via spinning disc fluorescence light microscopy for fluorescent signal. Scale bar depicts 20 μm. Section outline indicated when necessary. **(C)** Plastic sections of embryos expressing cytoplasmic mCherry throughout the epidermis using the *pannier-Gal4* driver showed no retention of mCherry. **(D)** Neither was a retention of the membrane-bound fluorophore mNeonGreen achieved, that was expressed via the epidermal driver pannier. **(E)** **(i-iii)** The genetically encoded *SNAP-tag* was tethered to the membrane. The synthetic fluorophore Alexa-647 chemically interacted with the SNAP-tag epitopes that were exposed

on the plastic sections. **(i)** A specific labeling of epidermal cells (*pannier-Gal4* driver for SNAP-tag expression) could be observed in a few sections (arrows). **(ii)** In most of the analyzed sections, no specific labeling could be detected. Some unintended structures (arrows) were labeled with the Alexa-647 fluorophore, although the expression of the SNAP-tag was genetically controlled, pointing towards unspecific affinity of the Alexa fluorophore. **(iii)** The Alexa fluorophore labeled yolk granules and the whole cytoplasm unspecifically of flies with no genetically encoded *SNAP-tag* (arrows). **(F)** Recognizable retention of GFP tagged to cortical actin (sGMCA fly stock) 24 hours after section collection. The intensity of the recorded signal is exemplified by the "fire look-up table", where a strong signal is displayed close to white. **(G) (i-ii)** Two examples displaying the strong retention of membrane-bound GFP in posterior epidermal cells and gut structures (using the *engrailed-Gal4* driver).

another complex level to master. The zipping site comprises a dimension of 30 μm in z, thus, more than one hundred sections need to be collected and analyzed. The conceptual design of CLEM in this study is shown in figure 11 A - B. I identified the region of interest by histological staining and low-magnification assessment of consecutive sections using anatomical markers such as the width of the dorsal opening. Then, I collected serial sections of 300 nm thickness with a diamond knife and transferred them onto formvar grids, supported with a carbon layer. The whole sectioning process was carried out in the dark as recommended for better fluorescence retention (Watanabe and Jorgensen [2012]). For the ease of operation, I collected only one of the two zipping sites within one sample. The first zipping site that was closest to the knife blade was rejected, whereas the second zipping site was identifiable by an experienced experimenter. I started section collection when the width of the dorsal opening gradually decreased, such that opposing leading edge cells were only a few micrometer apart. Within a few days after sectioning, I needed to perform fluorescence microscopy (LM) to record the compartmental identity of the leading edge cells before the fluorescence signal was lost. In the chosen set-up, posterior cells were labeled green prior to dorsal closure (figure 11 ii) by expressing the green fluorescent protein GFP under the control of the *engrailed* promotor using the UAS-Gal4 system (Brand and Perrimon [1993], Phelps and Brand [1998]). Unlabeled cells were treated as having anterior identity (figure 11 i). Further, I simplified the setup by recording 2D electron micrographs of the serial sections (ssTEM - serial section transmission electron microscopy) rather than performing electron tomography on each

section (EM). Unquestionable, tomography provides perfect 3D reconstruction of the investigated volume. Nevertheless, I could identify and follow the zipping cells in 2D to segment the assumed 3D structure with sufficient resolution, thereby saving time.

3.1.2 In-resin fluorescence retention of GFP works best despite the detrimental sample preparation process for EM

Several different fluorophores were tested in order to obtain a strong, persistent signal, allowing for the analysis of hundreds of sections prior to bleaching. To that means, I generated transgenic flies encoding for cytoplasmic mCherry under control of the *UAS-Gal4* system (see Materials and Methods, section2.1.2). The photo stability of mCherry was reported to be greater than that of EGFP when undergoing sample preparation for electron microscopy (Kukulski et al. [2012]). When tested, the fluorescence in these transgenic flies was not retained in the cytoplasm (figure 11 C).

Another strategy was to assess the capability of green fluorescent proteins, such as mNeonGreen (Shaner et al. [2013]) for the CLEM approach. Also, tethering of the fluorophore to a confined volume, like the membrane, to enhance the intensity was tested. Transgenic flies expressing mNeonGreen, tethered to the membrane of epidermal cells via a palmitoylation tag, showed no retention of fluorescence (figure 11 D).

Further, chemical labeling of the genetically encoded *SNAP-tag* post-sample preparation via Alexa fluorophores was attempted (Keppler et al. [2003], Kohl et al. [2014], Perkovic et al. [2014]). Despite the sparse specific labeling of the membrane of epidermal cells (figure 11 E i), the chemical labeling of the SNAP-tag was imprecise in two investigated embryos, and the adjustment of label incubation time and concentration yielded not in improved specificity (figure 11 E ii, iii).

Next, GFP-retention was addressed: GFP bound to the actin cortex throughout the fly embryo (sGMCA flies, Kiehart and Galbraith [2000]) achieved a faint retention of signal up to 24 hours post-section collection. Focussing therefore on the enhancement of the GFP-signal guided us to the employment of transgenic flies engineered for the purpose of

improved fluorescence imaging of neurons at Janelia Farm (Pfeiffer et al. [2010], Pfeiffer et al. [2012]). Pfeiffer and colleagues improved the transcription of GFP by using viral enhancers (Pfeiffer et al. [2012], the generated construct is depicted in figure 12 A). The *UAS*-sequence is repeated 10-times, allowing for increased binding of the transcription factor Gal4. Further, the heat shock promotor *hsp70* was shown to result in two-fold increased protein expression compared to another basal *Drosophila* promotor (Pfeiffer et al. [2010]). Further, an intervening sequence (*IVS*), a part of the *Drosophila myosin heavy chain* intron, was introduced into the construct to facilitate optimal transport of spliced mRNAs to the cytoplasm. By confining the GFP to the membrane via a myristoylation anchor, one achieves an increase in signal. Last, the viral translational enhancer 3'-UTR sequence *p10* from *Autographa californica* achieves a 20-fold increase of GFP expression compared to basal expression.

My established correlative approach relies on the integration of the GFP-transgenic flies by Pfeiffer et al. [2012] into the CLEM set-up involving the protocol developed by Kukulski et al. [2011]. By expressing GFP in the posterior compartment of epidermal cells, a strong labeling was achieved, up to five times stronger than the cortex-bound GFP (compare figure 11 G with figure 11 F). More specifically, the *engrailed-Gal4* driver, that is fused to mCherry-Moesin (an actin-binding protein), was crossed to the flies developed by Pfeiffer and colleagues (*pJFRC29 in attP2*). The offspring featured strong membrane-bound GFP signal in posterior, epidermal cells and further expressed actin labeled by mCherry (figure 12 B). Therefore, live-imaging was performed recording the mCherry signal, conserving the valuable GFP used for correlative microscopy later in the working pipeline.

In order to characterize the behavior of the studied transgenic flies during dorsal closure and to exclude possible adverse effects of the strong GFP-expression, spinning disc light microscopy movies were recorded. The closing time of the dorsal hole of the transgenic flies used in the CLEM study were compared to those of control embryos, namely the outcrossed driver line (with mCherry-labelled Moesin in posterior cells over a wildtype

copy). As shown in figure 12 C and D, both fly types needed a comparable time for closing the gap of 4-5 hours at 25 °C. Figure 12 E shows no significant difference of dorsal closure speed between control and GFP-expressing embryos. We conclude that the flies, despite their strong GFP-expression, could be utilized for the study of dorsal closure and cell-cell recognition during zipping.

3.2 Employing the established CLEM method to study the lamellar overlap at zipping sites

3.2.1 Analysis of acquired light and electron microscopic images and their correlation

After recording the light (spinning disc light microscopy) and electron microscopic images (2D ssTEM), I analyzed the data using the free software plugin "TrakEM2" within the data analysis software FIJI (Cardona et al. [2012]). The data was organized into consecutive layers, each layer representing a 300 nm thick section. Within each layer, images were edited. First, the EM images that were recorded at different magnifications were montaged using a similarity transformation algorithm. Thus, a huge view of the region of interest at low resolution was combined with a high resolution of 3.5 nm / pixel at the lamellar overlap of opposing leading edge cells at the zipping site (figure 13 A). After automatic montage, the sections were manually aligned along the zipping axis, relying on anatomical markers seen at high magnification (figure 13 B), such as mitochondria and cell membranes. The low heavy metal concentration, being five times reduced compared to standard protocols, did not allow for automatic segmentation via pixel classification (data not shown, Ilastik software). Thus, segmentation of the data could only be performed manually of each section (figure 13 C).

Following segmentation, several sections per segmented cell were correlated with their light microscopic image (figure 13 D). Autofluorescent signals of folds within the plastic

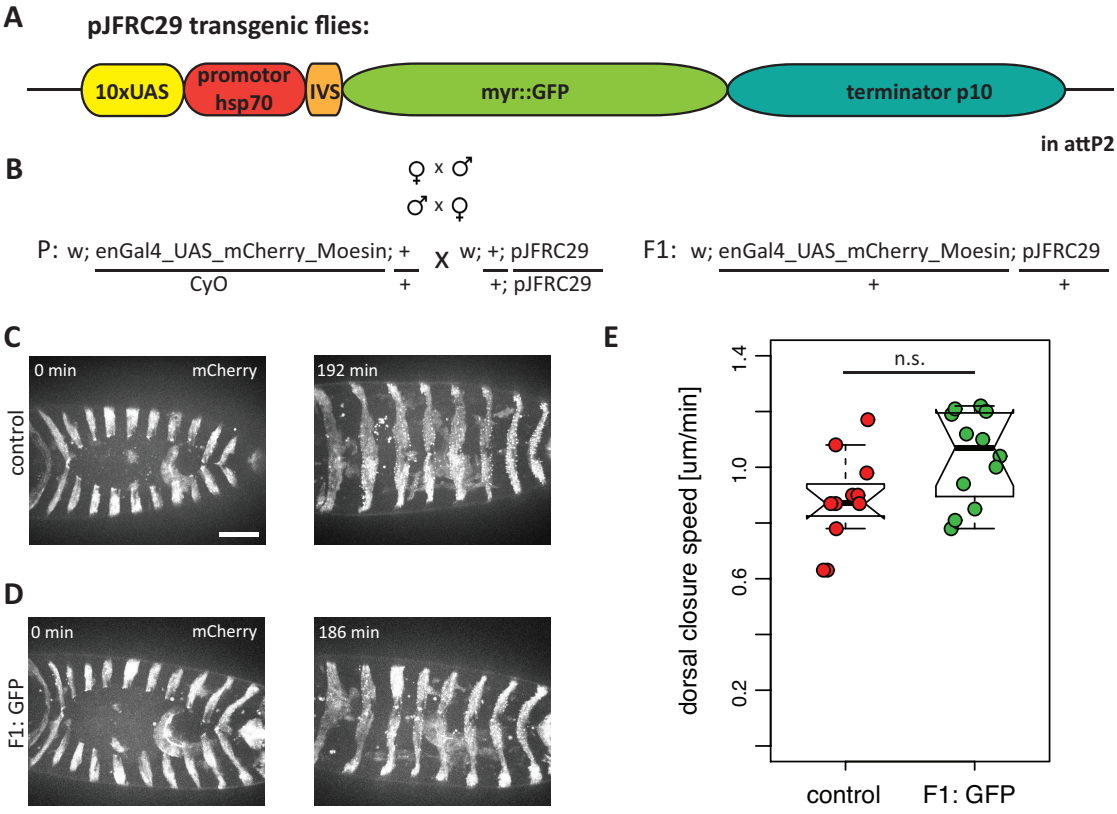

Figure 12: **Utilizing transgenic flies with enhanced GFP-expression for CLEM.** **(A)** Genetic details on the fly stock used further in this study with a ten-fold enhanced GFP-expression due to optimized transcription. **(B)** Crossing scheme to obtain flies with high GFP-expression targeted to the membrane of posterior epidermal cells (F1: *enGal4; pJFRC29*). In addition, those flies expressed mCherry-labeled actin in posterior cells, allowing for selection of embryos with signal and correct developmental stage prior to sample preparation without bleaching of GFP. **(C) – (D)** Selected movie frames of control (C) and GFP (D) embryos during dorsal closure. 0 min designates the first contacts of opposing posteriorly labeled cells of the thoracic T1 segment. Dorsal closure speed was represented by the ratio of total opening width at 0 min divided by the time needed until the gap is completely sealed (last frame shown). Scale bar depicts 50 μm. **(E)** Comparison of dorsal closure speed of control and GFP embryos. The datasets are not normally distributed (Shapiro-test); the Mann-Whitney U-test reveals no significant difference (p=0.05).

section and the vitelline membrane facilitated a coarse alignment of EM and LM images. Fine correlation was achieved by overlaying the posterior cell outlines. Thus, the correlation of LM and EM was simplified and did not rely on additional fiducial markers that would be paramount if a correlation within a few nanometers was intended (Nisman et al. [2004]). Also, note the marvelous retention of fluorescence even 6 weeks after sec-

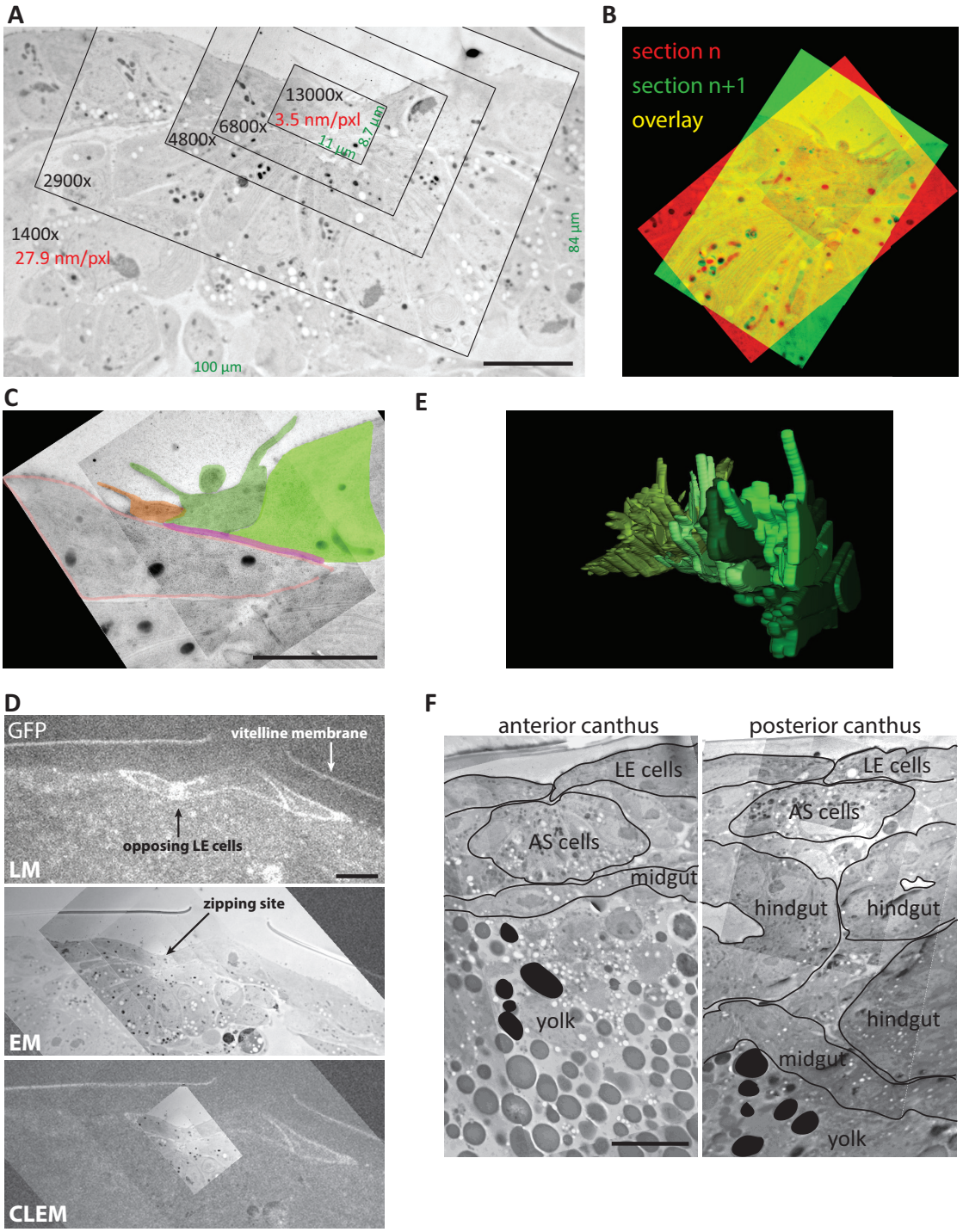

Figure 13: **Data processing employing the TrakEM2 plugin of FIJI.**
(A) Automated montage of several electron micrographs of the same section obtained at different magnifications (black number), with different field of views (green number) and different achieved resolutions (red number). Scale bar depicts 500 nm. **(B)** Manual overlay of consecutive sections based on sub-cellular features. **(C)** Manual segmentation of leading edge cells at the zipping site within the TrakEM2 canvas user interface. Scale bar depicts

500 nm. **(D)** Sample folds, the auto-fluorescent vitelline membrane, autofluorescent yolk granules and most importantly cell outlines were used to correlate the fluorescent signal of posteriorly labeled cells (LM, GFP) with the electron microscopic images revealing the ultrastructure of the interacting cells (EM), resulting in the correlation of cell identity and lamellar overlap organization (CLEM). Importantly, the GFP fluorescence retention 6 weeks after serial section collection still allowed for faithful correlation. Scale bar depicts 1 μm. **(E)** 3D representation of a few right, anterior cells with the FIJI 3D Viewer; the cell front clearly oriented upwards, protruding over the opposing cells (not shown). **(F)** Anatomical landmarks allowed for identification of the anterior or posterior canthus. At the anterior canthus, the midgut engulfing the yolk is directly situated underneath the amnioserosa cells. In contrast, at the posterior canthus, the folding hindgut structures lie between the central midgut-yolk and the dorsal amnioserosa cells. The designated left-right axis resulted from the above orientation. Scale bar depicts 10 μm.

tion collection (figure 13 D). Therefore, several embryos could be processed in parallel, allowing LM of several hundreds of sections prior to signal loss. When the fluorescent signal retained within the plastic section was recorded within a few days after sectioning, the signal was clearly stronger and cell outlines more pronounced (see figure 11 G).

The FIJI implemented 3D Viewer allowed for display of the reconstructed, segmented cells in 3D (figure 13 E).

The collected zipping site needed to be identified as anterior or posterior canthus, impacting the left-right orientation of the embryo. As displayed in figure 13 F, the anterior and posterior zipping site could be distinguished from each other by the absence (anterior canthus) or presence (posterior canthus) of folded hind gut structures ventral of the amnioserosa tissue. During the process of finding the region of interest, consecutive sections of the whole embryo were collected at least every 10 μm, allowing for the identification of the two canthi within the sample and accurate classification of the canthus identity. Out of eight analyzed zipping sites, only one was an anterior one. This bias was not intended during sample processing, the sample was randomly oriented.

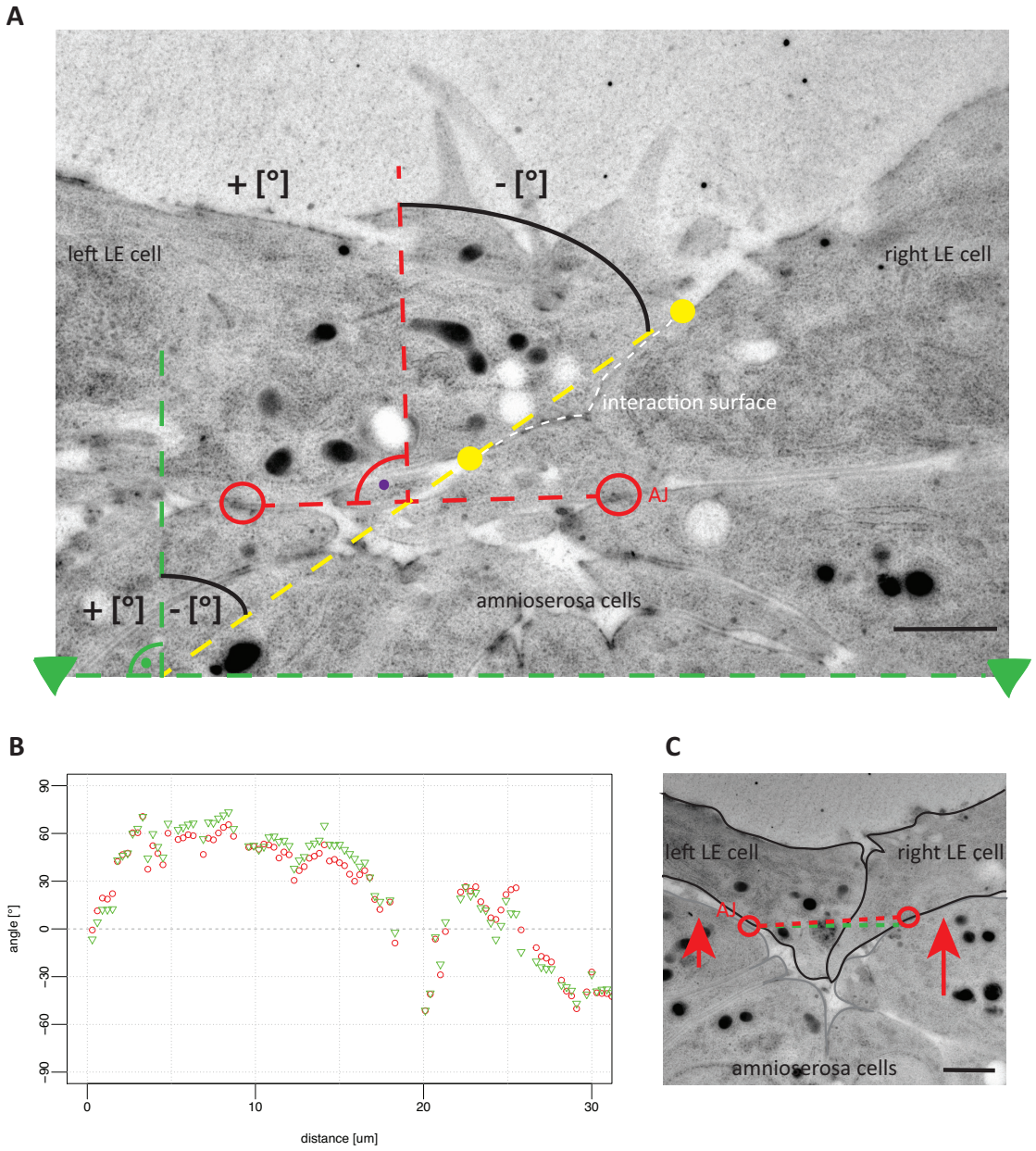

Figure 14: **Illustrating the lamellar overlap organization of opposing LE cells with an angle readout.**

(A) Electron micrograph showing two overlapping leading edge cells, where the left one is protruding over the other. The yellow points and line mark the start and end point of the simplified interaction surface (white dashed line). The angle of this interaction was measured in relation to either 1) the red line, derived from the interaction of leading edge epidermal cells with the underlying amnioserosa cells, as seen by the presence of adherens junctions with electron densities and a typical spacing of approximately 30 nm (red circles). Or 2), the measurement of the angle in relation to the artificial, horizontal green line was tested (green triangles). The value of the angle was defined as positive, if the right-side leading

edge cells protruded over the left ones, and as negative value if the left leading edge cells were on top of opposing right ones. Scale bar depicts 2 μm. **(B)** Angle measurements along the posterior zipping site of one of the collected zipping sites (id: embryo beta) from start (0 μm) to late zipping (30 μm). Note that the influence of the used reference line, either the amnioserosa to leading edge cell interaction via adherens junctions (red circle), or the general artificial, horizontal line (green triangle), showed only minor differences of trend in the angle measurement. **(C)** Electron micrograph presenting the influence of amnioserosa cell behavior on overlaying leading edge cell arrangement. Red arrows show the impact of amnioserosa cells, being stronger on the right side, slightly deforming the above leading edge cells. Thus, the red AJs-reference line deviated from the green artificial, horizontal reference line. Scale bar depicts 2 μm.

3.2.2 The angle of contact between leading edge cells represents a quantitative readout of the lamellar overlap organization at the zipping site

The reconstructed, segmented zipping sites of eight embryos were analyzed. The data is presented in the upcoming paragraphs, and in the appendix. The data was analyzed in two ways: on an observational, descriptive level by generating 3D visualizations of the interacting leading edge cells at the zipping site and on a quantitative level by measuring the contact angle between opposing leading edge cells.

Angle measurements of the overlapping lamellar leading edge cells at the zipping site were performed, as displayed in figure 14 A. The angle value was defined positive when a right LE cell protruded over a left one, and negative when a left LE cells overlaid a right one. The interaction surface of opposing leading edge cells was represented by a simplified line from the first to the last contact point of interacting cells (dashed yellow line). It occurred that more than one cell on one side interacted with more than one cell on the opposing side. Nevertheless, only one representative measurement was performed, taking into account the most dorsal and most ventral interaction points (yellow points). The angle was measured relative to two vertical reference lines, that were derived either from the interaction of LE cells with underlying amnioserosa tissue (red dashed line, adherens junctions, Gorfinkiel and Arias [2007], Eltsov et al. [2015]) or from the artificial horizon of the aligned sections (dashed green line).

It was tested, how consistent measurements proceeded along the zipping side, spanning more than 100 sections representing a ”timeline” from early to late zipping stages. In-

terestingly, the measurements according to the two differing reference lines disagreed only slightly, the overall trend (positive or negative value) was preserved (figure 14 B). Since the reference line derived from the LE cell - AS cell interaction was determined per section, it allowed for adjustments whenever the LE cells and the interaction surface underwent minor shape changes, often as a consequence of AS cells pushing from underneath (figure 14 C). This adjustment was not possible with the artificial, fixed horizon, rendering faithful comparison between different samples more imprecise. Therefore, I chose to perform the angle measurements relative to the LE cell - AS cell plane, determined by the presence of adherens junctions.

3.3 Lamellar overlap organization and correlation to compartmental identity of eight zipping sites

We aim to study the lamellar overlap organization at the zipping site via correlative microscopy. We aim to test whether the lamellar overlap follows a pattern or whether it is random. The hypothesis is that cells of the same compartment (anterior or posterior) align in the same orientation, forming a characteristic overlap pattern that switches at the compartment boundaries. If this pattern existed, I expect to visualize with the established CLEM method cells from one side, of one compartment, to protrude over the other side, and the opposite arrangement for the other compartment. Otherwise, if the overlapping lamella do not follow any positional cue (or not the positional information imposed by the anterior-posterior compartmental identity), I expect to see cells overlapping randomly, independent of the compartmental identity and the left-right axis.

The established CLEM method was by no means a high-throughput process. Drawbacks included a high time-consumption for the manual handling during the sample preparation and a great demand for skillful craftwork when cryo-fixing, substituting, remounting, and sectioning the sample. Further, the used cryo fixation machine and the low uranyl acetate concentration preserved not all samples to the same, sufficient extent.

To illustrate this, I list the processed embryos and the final outcomes: In total, I freeze-substituted 31 embryos. Of those, I processed 20 further to locate the zipping site by means of electron microscopy or light microscopy of histology-stained sections. I collected serial sections spanning a zipping site of 14 embryos. Six sets of serial sections were unusable due to impaired sample preparation or incomplete collection of the zipping site. In some samples the preservation was not continuous. The anterior part would be preserved well, whereas the posterior one was not. Also, a gradual preservation within a section existed. In a section, the dorsal opening and the opposing LE cells represented a rather fragile part of the embryo, being more susceptible to mechanical disruptions during sample preparation, resulting in partial breaks of the sections and folds within the plastic section, deforming the interacting LE cells. For all the mentioned reasons, eight embryos fulfilled the criteria of sample preservation and completeness and were analyzed via CLEM.

Those embryos are termed with greek letters, the first processed embryo being embryo alpha, the last one embryo eta.

3.3.1 A short characterization of observed cell-cell interactions of zipping cells

The versatile, complex interactions of zipping cells was described already by Eltsov and colleagues. By employing electron tomography the observation of fine ultrastructural details at a high resolution was achieved (Eltsov et al. [2015]). In this study, the superior preservation and resolution was traded for additional information on the compartmental identity of the zipping cells. Therefore, comparisons of interacting anterior and posterior cells became feasible.

Table 3 lists for each segmented cell within the eight collected zipping sites interesting details, such as its left or right identity, its compartmental identity, its number of interactions with opposing zipping cells, the percentage of AJs formed within the interaction volume, the width of the interaction surface, its zipping stage, whether it is a mixer cell

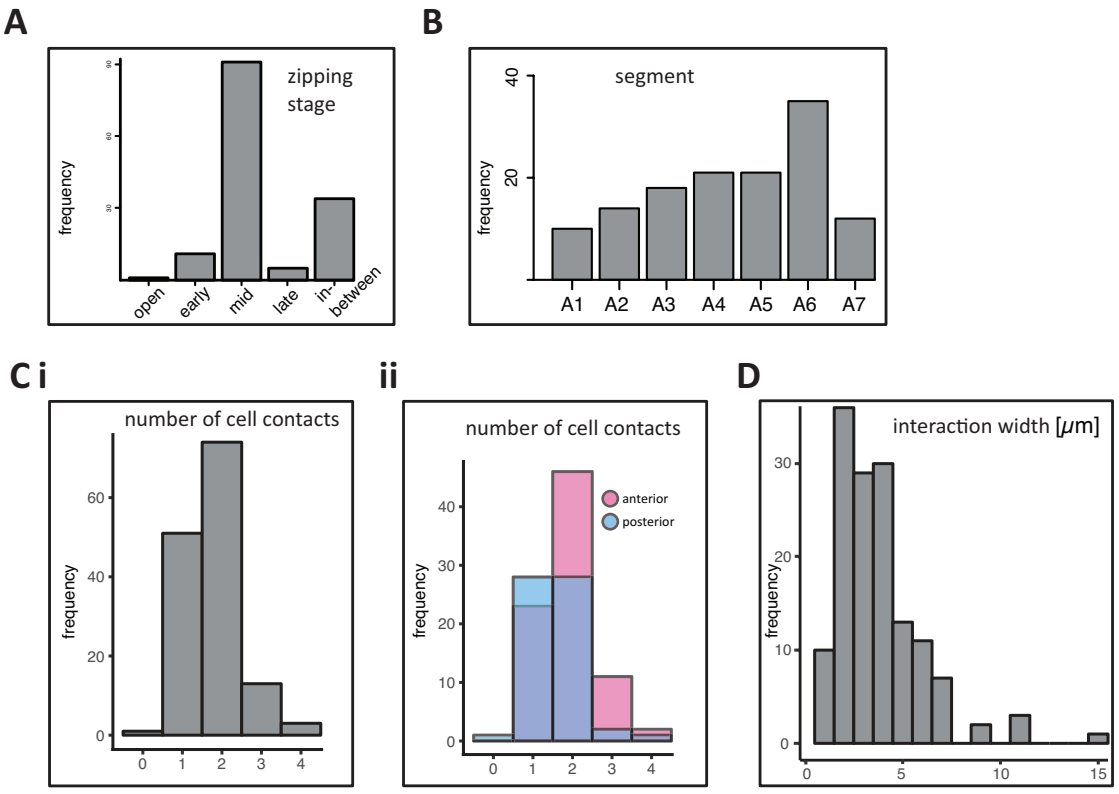

Figure 15: **Characterization of analyzed, segmented interacting LE cells.** **(A)** Frequency of segmented cells classified by their cellular morphology, namely the overlap structure, into open, early, mid and late zipping stages. **(B)** Number of segmented cells per abdominal segment. **(C)** Frequency of the observed number of cell contacts of interacting LE cells for all cells **(i)** and separated by anterior or posterior compartmental identity **(ii)**. **(D)** Frequency of observed interaction width, representing the width of the interaction surface of the segmented cell with opposing ones, but not necessarily the actual width of the segmented cell.

(see section 3.3.6), and whether it has interactions with opposing cells differing in the compartmental identity.

142 cells were segmented within 8 analyzed zipping sites. Within embryo alpha, 11 cells were segmented, whereas the anterior zipping site of embryo delta featured the highest number of cells within the reconstructed zipping volume, namely 24 cells. Embryo delta was the sample representing the latest dorsal closure stage. It appeared that the cells were smaller in width when the dorsal hole was almost completely closed (see also figure 18). In total, 82 anterior and 60 posterior cells were analyzed.

Based on our hypothesis, we would like to decipher the lamellar overlap organization correlated to positional identity information. Since most of the segmented cells represented a mid-zipping stage (73 %) with a pronounced lamellar overlap, the identification of a pattern, if present, could be achieved in principle (see also histogram in figure 15 A). As displayed in figure 15 B, the collected zipping sites span the abdominal segments, with more cells covering the more posterior segments A5 to A7, since seven out of the eight collected zipping sites represented a posterior one (see also figure 22).

On average, a cell interacted with 1.8 opposing cells (figure 15 C i). This clearly represented both the explorative nature of early zipping cells, expanding filopodia and screening for correct interaction partners, but also the slightly shifted overlapping nature of the left versus the right LE cells. As within a zipper, the cells are slightly shifted relative to each other. Further, by interacting with more than one opposing cell, the ability to establish a correct binding is achieved, assessing also the neighboring opposing cells. Only three out of 142 cells interacted with 4 opposing cells. Those featured either a rather wide interaction volume or were situated at a boundary, where they interacted with cells of both the anterior and the posterior compartment on the opposing site, thus establishing the correct recognition. 27 cells out of 142 (19 %) interacted across compartment boundaries, having overlaps with anterior and posterior cells alike.

The width of the interaction surface between one cell with opposing ones differed from a minimum of 1 μm to a maximum of 15 μm. The median was at 3.3 μm and on average it was 3.86 μm, being in agreement with LM data (figure 15 D).

On average, within 48 % of the sections putative adhesion sites were identified based on visual inspection of the 2D EM micrographs (see also section 3.3.5).

A comparison of left and right LE cells within their compartment revealed no major difference in number of interactions, the width of the interaction volume, nor the frequency of anterior-posterior interactions.

The presence of adhesion sites within the interaction surface, and the width of the interaction volume did not differ significantly between anterior and posterior cells (Welch Two Sample t-test). Also, the number of cells interacting both with anterior and posterior

cells appeared similar for anterior (17.1 %) and posterior (21.7 %) cells. Interestingly, anterior cells interacted significantly more with opposing cells (Welch Two Sample t-test, $p < 0.01$ (**), see also histogram in figure 15 C ii). This might be accounted for by the higher number of cells within the anterior versus the posterior compartment, representing more potential interaction partners for an anterior cell.

The next sections are focused on the lamellar overlap between opposing leading edge cells. 3D volumes of reconstructed zipping sites are presented, accompanied by angle measurements representing the lamellar overlap organization between cells of the left or right side and the anterior or posterior compartment.

3.3.2 The majority of investigated zipping sites show a common organization of lamellar overlaps within the anterior and posterior compartment

Of the eight analyzed embryos all except one showed common characteristics. Based on the cell behavior at the lamellar overlaps, as seen quantitatively with the angle readout of opposing LE cells, seven out of eight zipping sites showed a regular pattern.

I will introduce embryo beta as a representative, describing the cell behavior of the majority of the analyzed zipping sites (figure 16).

The arrangement of opposing LE cells of the other six zipping sites is presented in figures 18, and appendix A, figures 37, 38, 39, and 40. A short time lapse was recorded of embryo beta prior to cryo-fixation (figure 16 A), in order to verify normal progressing of dorsal closure and to high-pressure freeze the sample at the time point when zipping occurred at a anterior-posterior compartment boundary. Various 3D representations of the segmented posterior zipping site of embryo beta are displayed from different perspectives in figure 16 B. The bottom view shows the zipping seam. 3D representations of either the left or right LE cells visualize the alternating cell behavior of anterior and posterior compartmental cells. For instance, the left, posterior LE cells (blue) protrude over their right counterparts (yellow). This difference is further shown in figure 16 C,

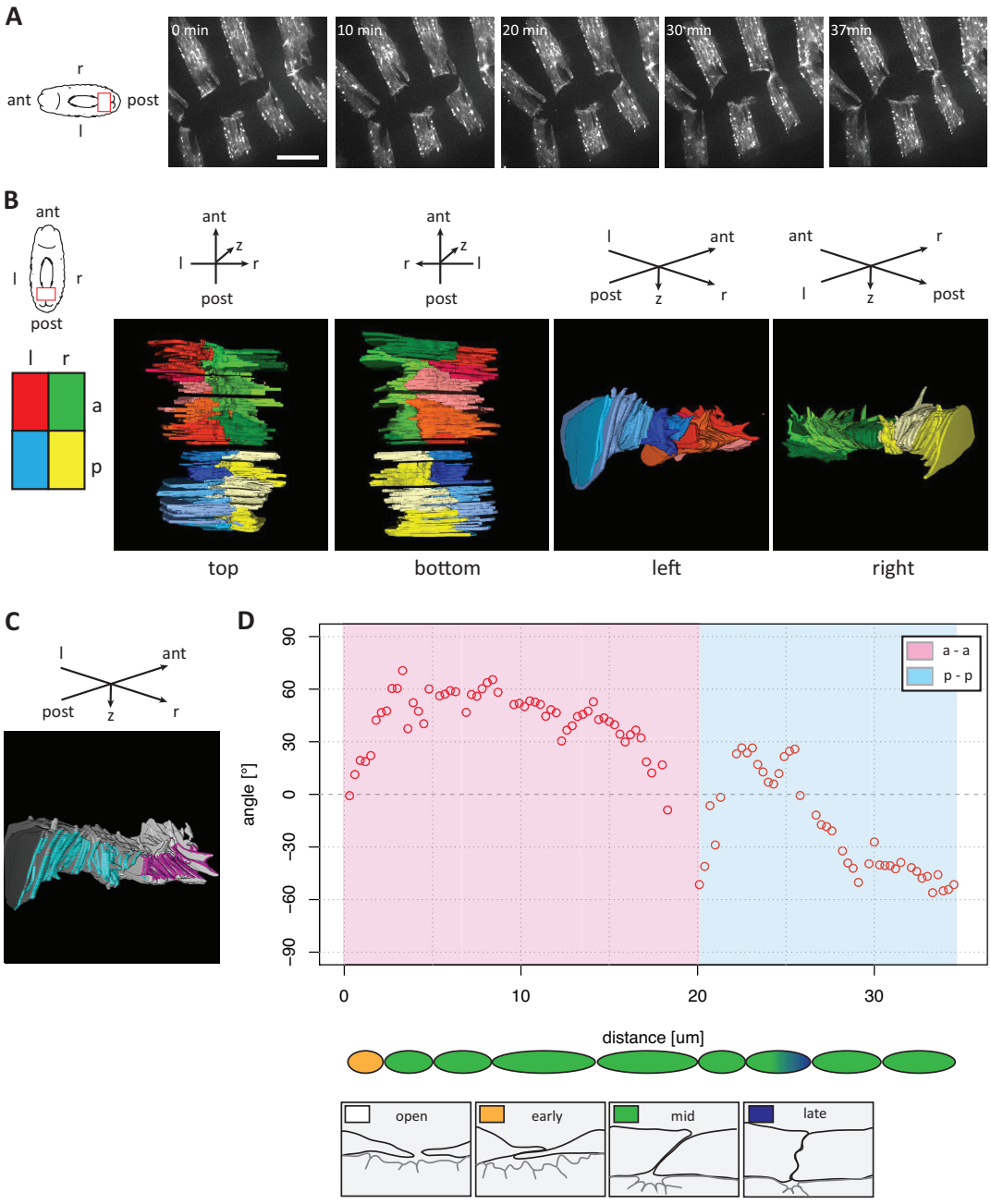

Figure 16: **Analyzing the lamellar organization of embryo beta at the compartment boundary (representative of 7 in 8 zipping sites).**

(A) Selected movie frames of embryo beta prior to high pressure freezing and sample preparation. Scale bar depicts 25 μm. **(B)** Various 3D representations of the reconstructed posterior zipping site. The emblem shows the colour encoding for left (l), right (r), anterior (a) and posterior (p) compartment. **(C)** 3D representation of the reconstructed left leading edge cells (grey), the interaction surface with the opposing right cells (not shown) either in magenta for interactions between anterior compartmental cells or in cyan, representing interactions between posterior compartmental cells. The start of the zipping site is at the

anterior (towards the head of the embryo), late zipping is towards the posterior side of the embryo. **(D)** Angle measurements along the posterior zipping site from start (0 μm) to end of zipping (30 μm). Interactions between anterior or posterior cells are shaded in magenta or cyan, respectively. The zipping stage of interacting leading edge cells is shown in a simplified manner along the zipping axis.

where only left LE cells and the interaction surface with opposing LE cells is displayed. Note the clear switch of the orientation of the interaction surface from posterior (cyan) to anterior (magenta) cells. Angle measurements (see figure 14) of the sections along the zipping site quantify the difference within the anterior or posterior compartment (figure 16 D).

The switch of cell behavior correlated with the compartment boundary. A transition zone at the boundary of anterior and posterior compartment was observed, where the orientation of the interaction surface gradually changed (figure 16 D, appendix A (supplementary panels for embryos gamma, epsilon, eta)). Existing adhesions and tension between neighboring cells may account for this non-acute transition.

3.3.3 One of eight investigated zipping site samples shows an inverted, although organized arrangement of lamellar overlaps

Very interestingly, one investigated zipping site showed a contrary, inverted organization of lamellar overlaps (figure 17, embryo zeta). The angle measurements for the anterior compartment had a negative value, contrary to measurements within the anterior compartment of the other seven zipping sites.

Upon examination of a time lapse recording taken prior to cryo-fixation (figure 17 A), I noticed an irregular spacing of some opposing posterior stripes (labeled) and anterior ones (not labeled) at the dorsal opening, being different on the left and the right lateral side. I speculate that the misplacing of the stripes caused initial mismatching of opposing cell pairs, such that anterior cells contacted opposing posterior ones and vice versa. It seemed as though the zipping site had to re-organize the initial contacts of opposing LE cells, ensuring correct sealing of opposing compartments. This sorting occurred far

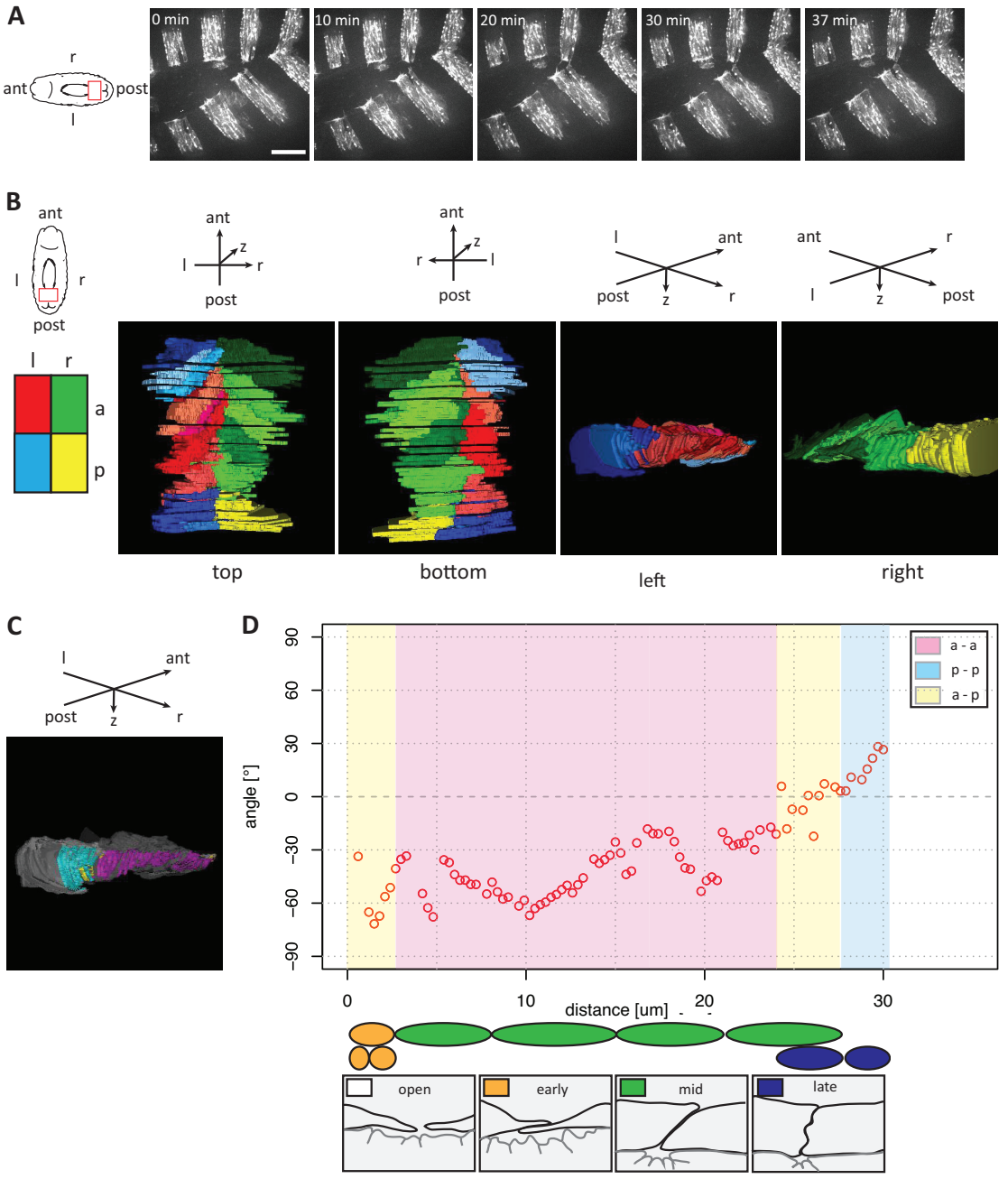

Figure 17: **Analysis of the lamellar organization of embryo zeta revealed an inverted arrangement of lamellar overlaps.**

(A) Selected movie frames of embryo zeta prior to high pressure freezing and sample preparation. Scale bar depicts 25 μm. **(B)** Various 3D representations of the reconstructed, segmented posterior zipping site. **(C)** 3D representation of the reconstructed left leading edge cells (grey), the interaction surface with the opposing right cells (not shown) either in magenta for interactions between anterior compartmental cells or in cyan, representing interactions between posterior compartmental cells. **(D)** Angle measurements along the posterior zipping site from start (0 μm) to end of zipping (30 μm). Interactions between

anterior or posterior cells are shaded in magenta or cyan, respectively. Interactions between anterior and posterior opposing cells are shaded in yellow. The zipping stage of interacting leading edge cells is shown in a simplified manner along the zipping axis.

behind the zipping front. The mismatching and the sorting step could alter the regular pattern observed with the other seven zipping sites, affecting the lamellar overlap organization of up to five cells within the next zipping, anterior compartment (17 D).

Whether the observed misplacing of opposing stripes is the cause or the consequence of the observed inverted, differing cell behavior could not be answered.

The inverted organization of the lamellar overlap is displayed via the 3D representation from different views (figure 17 B, C), and via the plotting of measured angles along the zipping site (figure 17 D). Thus, comparing the reconstructed zipping sites of embryo beta and zeta, embryo zeta seemed to present an exception from the cell behavior observed with the other seven samples. Therefore, analysis of anterior and posterior cell behavior within the next sections will discriminate between all 8 collected zipping sites, and those without embryo zeta.

3.3.4 Investigating the lamellar overlaps of the anterior and posterior zipping canthus within the same embryo

As already mentioned previously (subsection 3.2.1, figure 13 F), one out of eight analyzed zipping sites represented the anterior canthus. Two complete zipping sites were collected of the sample embryo delta. Usually, the first zipping site was missed since the assessment of when to start serial section collection was not trivial, as the late zipping stage did not differ in apparent landmarks from a long ago zipped stage. Highly interestingly, the two collected zipping sites within one sample might give insight into whether the organization of lamellar overlaps observed within the posterior zipping site also applies to the anterior one. If the cell behavior is exactly the same within the two zipping sites, I expect to find posterior cells of the left side to protrude over posterior cells of the right side, and anterior cells of the left side to dive underneath the anterior

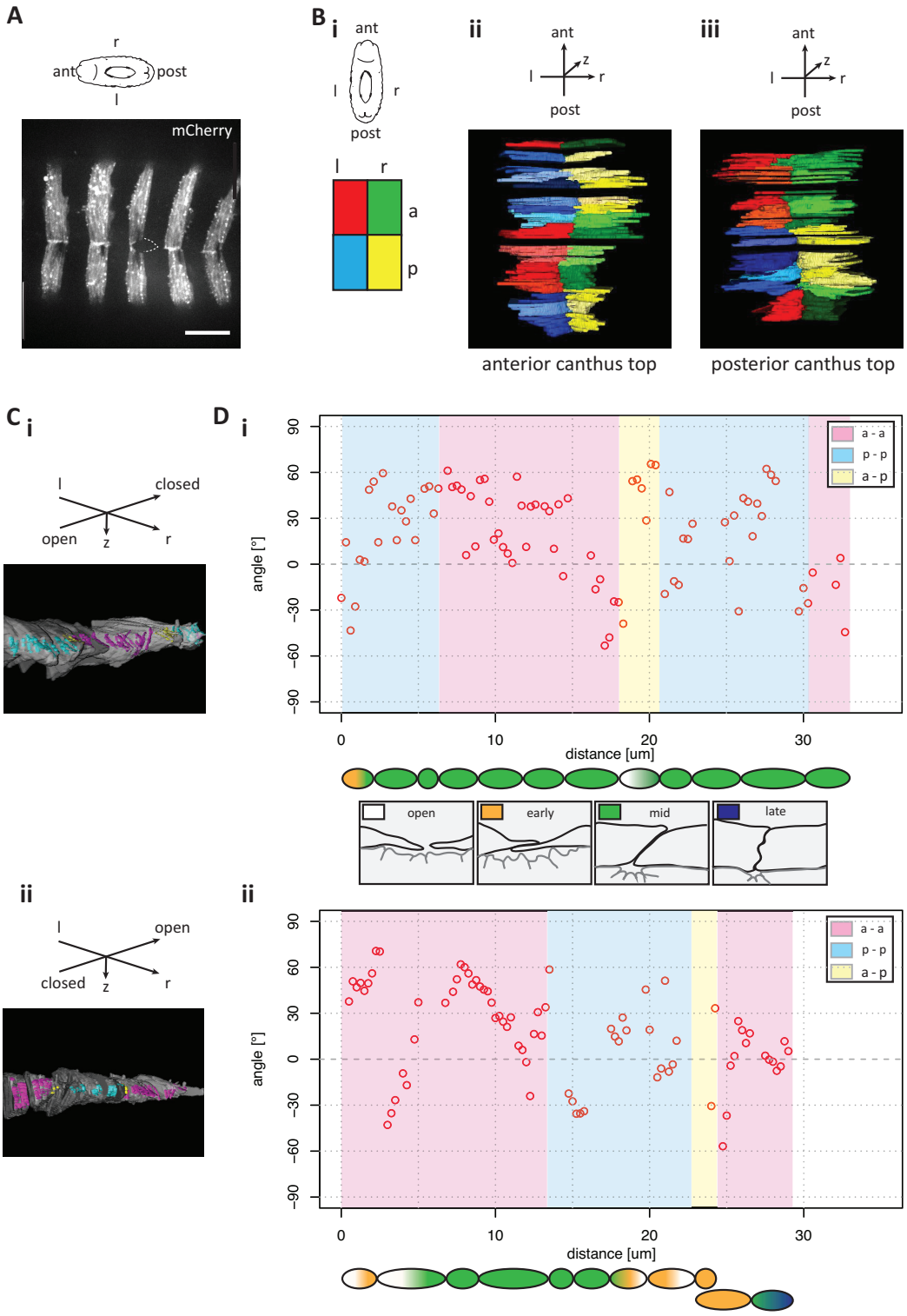

Figure 18: **The lamellar organization of the anterior and posterior zipping canthus in the same embryo, embryo delta.**

(A) Embryo delta prior to high pressure freezing and sample preparation. Scale bar depicts 25 μm. **(B)** 3D top view representations of the reconstructed, segmented anterior and posterior zipping site. **(C)** 3D representation of the reconstructed left leading edge cells (grey), the interaction surface with the opposing right cells (not shown) either in magenta for interactions between anterior compartmental cells or in cyan, representing interactions between posterior compartmental cells. Yellow depicts interactions between cells of anterior and posterior identity. **(i)** anterior canthus **(ii)** posterior canthus. **(D)** Angle measurements for the anterior canthus **(i)** and the posterior canthus **(ii)**. Interactions between anterior or posterior cells are shaded in magenta or cyan, respectively. Interactions between anterior and posterior opposing cells are shaded in yellow. The zipping stage of interacting leading edge cells is shown in a simplified manner along the zipping axis.

cells from the right side, independent of the anterior or posterior canthus identity of the zipping site.

Figure 18 A shows the embryo a few minutes prior to cryo-fixation. Obviously, the dorsal opening was almost closed, thus embryo delta represented the latest dorsal closure stage examined in this study. The interaction surface between opposing LE cells appeared smaller than in samples of earlier dorsal closure stage (compare figure 18 C with figures 16, 17 C). Further, several starts of zipping sites were present, i.e. two within the anterior and four within the collected posterior site (figure 18 D). The phenomenon of skipped cells, of zipping sites overtaking others was already observed previously with light microscopy (data not shown) and is common in late dorsal closure embryos, when the opposing lateral epidermal sheets are in close proximity to each other. The unconventional closing might be responsible for the less pronounced difference of angle measurements between the anterior and the posterior compartment (18 D). Thus, a definite conclusion of whether the anterior zipping site exhibits a similar overlap organization as observed in the posterior sites, could only be drawn with caution. Also, analysis of anterior and posterior cell behavior within the next sections will discriminate between all 8 collected zipping sites, and those without embryo delta.

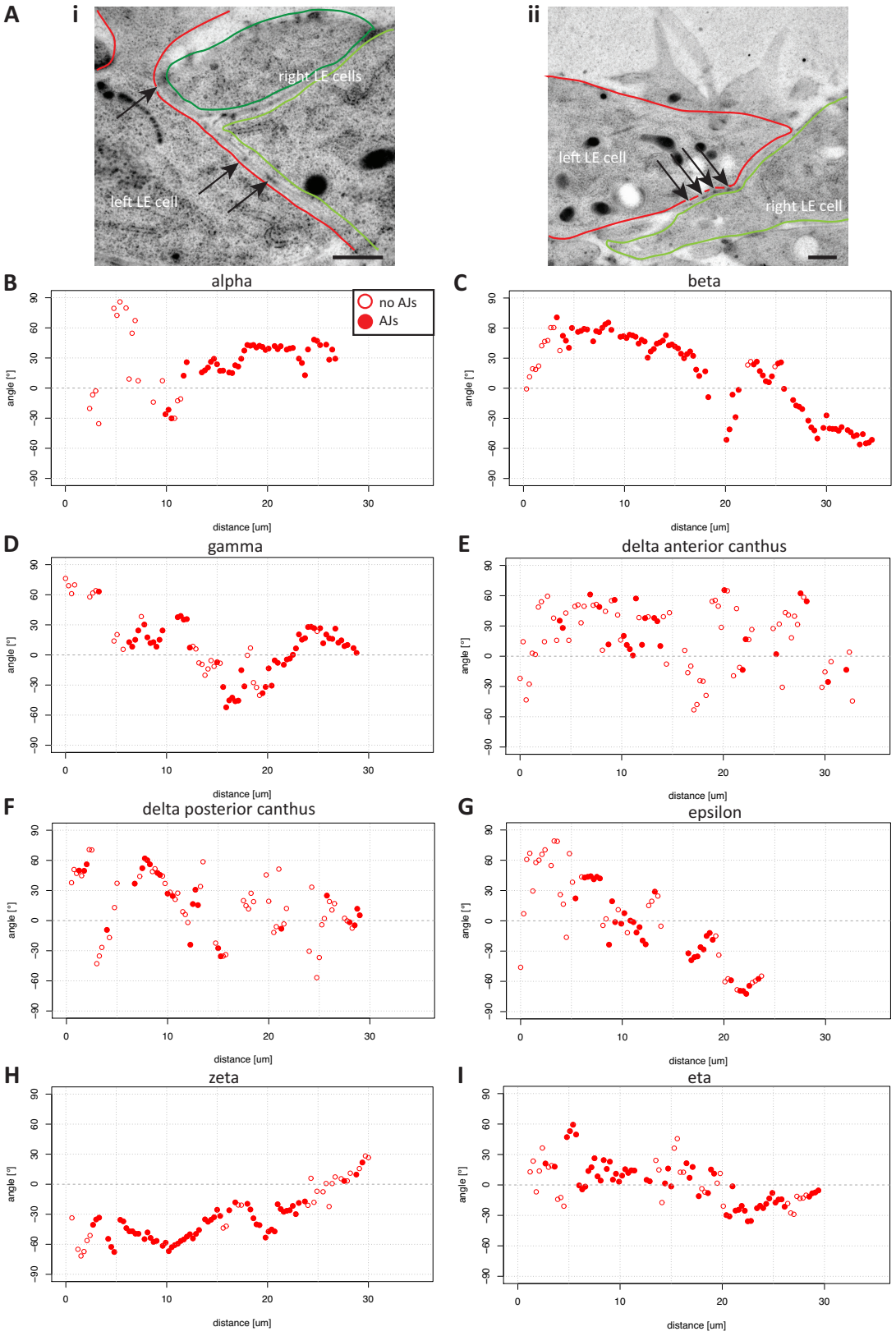

Figure 19: **Selection and representation of stabilized interactions between opposing LE cells within the eight analyzed zipping sites.**

(A) (i - ii) Two example EM micrographs of interacting anterior left (red) and right (green) leading edge cells. The arrows point out prospective adherens junctions with characteristic intercellular electron densities and membrane spacing of approximately 30 nm. Scale bar depicts 1 μm. **(B) - (I)** Angle measurements along the indicated zipping sites of the eight collected samples from start (0 μm) to end of zipping (30 μm). Filled circles represent an angle measurement of a putative stabilized overlap, since AJs appeared to be present. Note the different frequency of stabilized overlaps between the eight samples: for example, the zipping sites of embryo delta featured less adhesion sites between interacting cells compared to embryo beta and zeta.

3.3.5 Analysis of the contacts between cells that show adherens junctions - stable interactions - in comparison to all contacts

A further exploration of acquired image data was performed. Interactions between opposing LE cells were assessed based on the presence (see figure 19 A i, ii) or absence of AJs. The motivation was to pool those angle measurements of interacting cells, where a "correct" match has already occurred; the idea being that cells with a mismatch, meaning an incorrect partner (compartment-specific or cell number-specific), still need to adjust and sort their interactions (Millard and Martin [2008]). Thus, AJs are less likely to be present in those. AJs might represent a potentially good indicator to disentangle the dynamic cell-cell interactions occurring at the zipping site. Since I cryo-fixed the samples, only a snapshot can be analyzed. Although the zipping site equals a time line, where cells are present in different zipping stages, the dynamics of one cell could not be followed through time.

Zipping force is applied during mid zipping, sealing the opposing lateral epidermal sheets. Therefore, preliminary AJs between opposing LE cells are also formed to resist applied forces. Those AJs may mature later. The acquired data only allowed for the identification of prospective AJs, but not of their maturation state. Therefore, premature junctions were not distinguished from mature ones in the analysis. Also, the potential dynamics of the identified putative AJs could not be assessed.

Scatter plots displaying the measured angles along the zipping site from early to late zipping are shown in figure 19 B - I for the indicated zipping sites. Filled circles represent interactions with putative adhesion sites between interacting opposing cells. Since

the angle measurement was performed for a simplified interaction surface, representing sometimes the interaction surface of more than two interacting cells, also the identified stabilized overlaps represent a simplification. The label “AJs” was assigned whenever a putative adhesion structure between interacting cells was identifiable, not distinguishing whether an adhesion site was present between more than two interacting cells.

The later the zipping, the more likely to find AJs. Also, the number of identified stabilized overlaps varied from sample to sample: Within embryo beta, 72 % of all interactions appeared to be stabilized by putative AJs, whereas within embryo delta, both the anterior and posterior zipping site only scored with 22 and 21 %, respectively. This finding might also represent the late nature of the dorsal closure process. As described in figure 18, the opposing cell sheets were in close proximity over the whole width of the opening and several zipping sites were present. Also, the interaction surface between opposing cells appeared smaller than for the embryos in early to mid dorsal closure stages. The other zipping sites (alpha, gamma, delta, epsilon, eta, and zeta) showed between 42 and 61 % of adhesion structures. Strikingly, when analyzing only interactions without embryos delta and zeta, and only considering mid zipping stage cells and inspecting only anterior with anterior and posterior with posterior interactions, the score for identified AJs was increased to 77 %. This number appeared reasonable, since forces are applied during zipping. Therefore, the presence of AJs between opposing interacting cells is crucial for the process.

Note that the differing sample preservation might impact the identification of adhesion sites. The better preserved the sample, the more readily an identification of putative stabilized overlaps was possible, whereas a diminished sample preparation that was still sufficient for analysis of the membrane overlap organization might render an assignment of AJs more unlikely.

3.3.6 Examining the behavior of ”mixer cells” within the posterior compartment

Millard and Martin (Millard and Martin [2008]) suggested the significance of anterior versus posterior compartmental identity during zipping. Also, the investigated embryos of this study indicated a different cell behavior within the anterior or the posterior compartment. To study the lamellar organization within the posterior compartment in more detail, we focussed on the so called ”mixer cells” (Millard and Martin [2008], Gettings et al. [2010]). Those cells transdifferentiate during dorsal closure and change their compartmental identity. The term mixer cells does not refer to the ”mixed” interactions between opposing anterior and posterior cells, as indicated for instance in figure 18 D. The interesting phenomenon of mixer cells, crossing the segment boundary, was described previously (Gettings et al. [2010]) (figure 20 A, B). An anterior cell, positioned at the segment boundary to the posterior compartment, starts the expression of the posterior selector gene engrailed via JNK activation (figure 20 B, mixer cell labeled ”M”). This cell-fate switching requires the presence of groove cells in the cellular context, to only specify a certain cell as mixer cell, rendering the process a robust and safe one, since an imprecisely regulated pattern change would otherwise cause defects in epidermal sealing. Further, an anterior and a posterior cell from the second row intercalate into the first row of LE cells while obeying the segment boundary. The purpose of this reprogramming of the mixer cell and intercalation of the second row cells is not fully understood. Gettings and colleagues speculated, that the tension generated by the supracellular actin cable in LE cells is redistributed between more cells, avoiding possible epidermal ripping (Gettings and Noselli [2011]). Since the number of intercalating cells from the second epidermal row can be different from segment to segment, the balancing of tension can be adjusted segment-wise. This system is attractive for the study of transdifferentiation and its putative causes, be it differential compartment affinities, extracellular-matrix fences or changes in cortical tension.

In my samples, mixer cells were readily identifiable within the collected zipping site

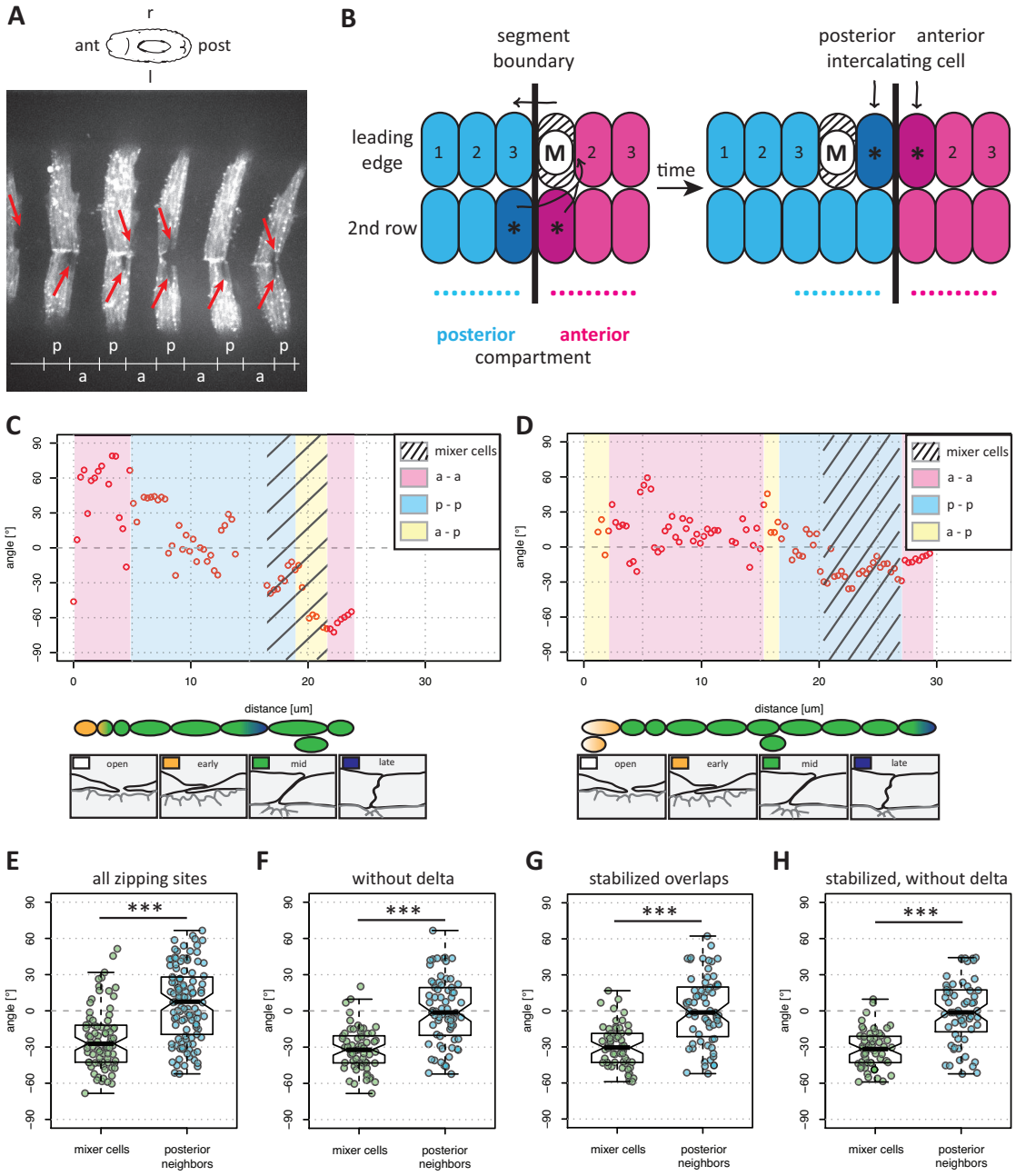

Figure 20: **Mixer cells show a different cell behavior compared to their posterior compartmental neighbors.**

(A) Cells of the posterior compartment are labeled via the engrailed-Gal4-UAS system. Within each posterior stripe, one cell was not labeled. Those cells are called mixer cells (red arrows). **(B)** Schematic displaying the movement of a formerly anterior cell ("M") into the posterior compartment, crossing the segment boundary. These cells start expressing the transcription factor engrailed later than their posterior neighbors, and thus commence the posterior transcriptome slightly delayed. From the second row of epidermal cells, an anterior and a posterior one intercalate into the first row while obeying the segment boundary.

Adapted from Gettings et al. [2010]. **(C) – (D)** Angle measurements of embryo epsilon (C) and embryo eta (D) along the zipping site, where identified mixer cells are shaded. **(E) - (H)** Comparison of angle measurements of interacting opposing LE cells for mixer cells and their posterior neighbors within the same compartment. The analyzed dataset comprised early and mid zipping stage measurements, and excluded mixed interactions between cells of two compartments. Boxplot **(E)** for all zipping sites (except alpha and zeta, which did not comprise cells fulfilling the aforementioned criteria), **(F)** without inconclusive, late dorsal closure stage embryo delta, **(G)** for all stabilized overlaps showing AJs, and **(H)** for stabilized overlaps excluding embryo delta. A Welsh Two Sample t-test revealed a significant difference of the angle measurements of the mixer cells and their posterior neighbors (p-value < 0.001 (***)).

via CLEM of serial sections: The label mixer cell was assigned to cells not showing the GFP-membrane signal yet, but being clearly flanked by posterior cells with GFP-label. Also, the light microscopic image prior to cryo fixation was consulted (such as in figure 20 A). Further, the posterior compartment usually comprised four to five cells. Of 142 segmented cells, comprising 60 posterior cells, 13 were identified as mixer cells (see also summarizing table 3 on cell-cell interactions in appendix A).

The angle measurements of two randomly chosen zipping sites, those of embryo epsilon and embryo eta, are displayed in figure 20 C and D, respectively. The shaded areas point out interactions of mixer cells. A summary panel pointing out the mixer cells within all the segmented zipping sites containing mixer cells can be found in appendix A, figure 41. Since the mixer cells within embryo eta (figure 20 D) are shifted towards each other, an interaction surface covering roughly two cell widths was designated as mixer cell.

We wanted to test, whether the mixer cells differed from their surrounding posterior, neighboring cells. It remains unclear, whether positional information is established within each cell, or within a specific region within a compartment or only within one cell to instruct neighboring cells to generate position-specific cell behavior.

I therefore analyzed the angle measurements for mixer cells and their posterior neighboring cells. The dataset comprised only early and mid zipping stages, since for late stages the angle measurement tended towards 0°. Also, mixed interactions between anterior and posterior cells were excluded, since they most likely represented overlaps that would need to be resolved and would not be permanent. The zipping site of embryo alpha

did not comprise the posterior compartment (see figure 37, appendix A). Embryo zeta did not contribute with mixer cell or posterior cell angle measurements, since they did not fulfill the aforementioned criteria (see figure 41, appendix A). Also, the mixer cell measurements for embryo gamma were excluded, since they represented a late zipping stage (see panel on embryo gamma in appendix A).

Strikingly, mixer cells showed a significant different cell behavior compared to their posterior neighbors (figure 20 E - H, Welsh Two Sample t-test). The median of the angles of mixer cells was around -30°, whereas the median of the angles for the posterior neighbors scored with 0°. This was true when comparing mixer cells with posterior neighbors for different datasets: when comparing measurements of all zipping sites (figure 20 E), when comparing measurements without the two zipping sites of embryo delta that had inconclusive measurements due to its late dorsal closure stage (figure 20 F), when comparing only stabilized overlaps with identified prospective AJs (see section 3.3.5, figure 20 G), and when comparing measurements for stabilized interactions without embryo delta (figure 20 H). The variability of the angle measurements was gradually reduced by the mentioned selection of certain conclusive, stabilized angle measurements. Interestingly, the interaction surface between opposing LE cells for mixer cells showed more often putative AJs compared to their posterior neighbors (68 % versus 55 %).

It appeared that mixer cells showed a more pronounced behavior, namely that the left side LE cells would protrude over the right ones. In contrast, the neighboring posterior cells within the same compartment showed a higher variability and no clear trend of lamellar overlap organization, as angles were recorded from +60 to -60°.

We conclude, that the mixer cells differed from posterior neighbors and therefore might be important for the establishment of differing cell behavior of anterior and posterior cells (see also next section 3.4). Since only 13 out of 60 posterior cells were designated as mixer cells, for comparisons of the anterior and the posterior compartmental cell behavior, the mixer cells and posterior cells were treated as one category, namely ”posterior”.

3.4 The recognition process during zipping appears to be compartment-specific and dependent on the left-right axis

3.4.1 The anterior and posterior compartmental cells show an alternating lamellar overlap organization within an embryo

The different lamellar overlap organization at the zipping site was already shown in figure 16 for embryo beta. The switch at compartment boundaries and the alternating behavior between the anterior and posterior compartment are displayed for all the embryos in figure 21. Angle measurements of cells in early and mid zipping were included, those of late zipping excluded. The hallmark of late zipping is the almost vertical, epithelia-like interface of former opposing leading edge cells. Since the seam would score with 0° in the established measurement process, those values were excluded for further plotting of anterior versus posterior compartment.

Except for embryos alpha and zeta, both the anterior and posterior compartment were covered in the serial section collection of the zipping site. A biostatistical comparison of the anterior versus the posterior compartment for an embryo revealed a significant difference for embryos beta, gamma, the posterior zipping site of embryo delta, and embryo eta.

This representation highlights the untypical cell behavior of anterior cells of embryo zeta (see also figure 17). Further analysis excluded the angle measurements of embryo zeta, when indicated, since it appeared to account for a distinct type of cell behavior.

The data suggested an importance of the left-right axis for assisting in the establishment of proper cell-cell recognition and matching at the zipping site. A role of the left-right axis during development is described only later during embryogenesis, during gut and testis rotation. Here, a different cell behavior is suggested, depending on the left-right axis and on the positional identity. Anterior right cells protruded over opposing left ones, whereas posterior cells showed an alternate behavior with left cells protruding over the right ones. The cell-cell recognition process appeared to be compartment-specific, and non-random. It pointed towards a putative significant impact of lamellar overlap

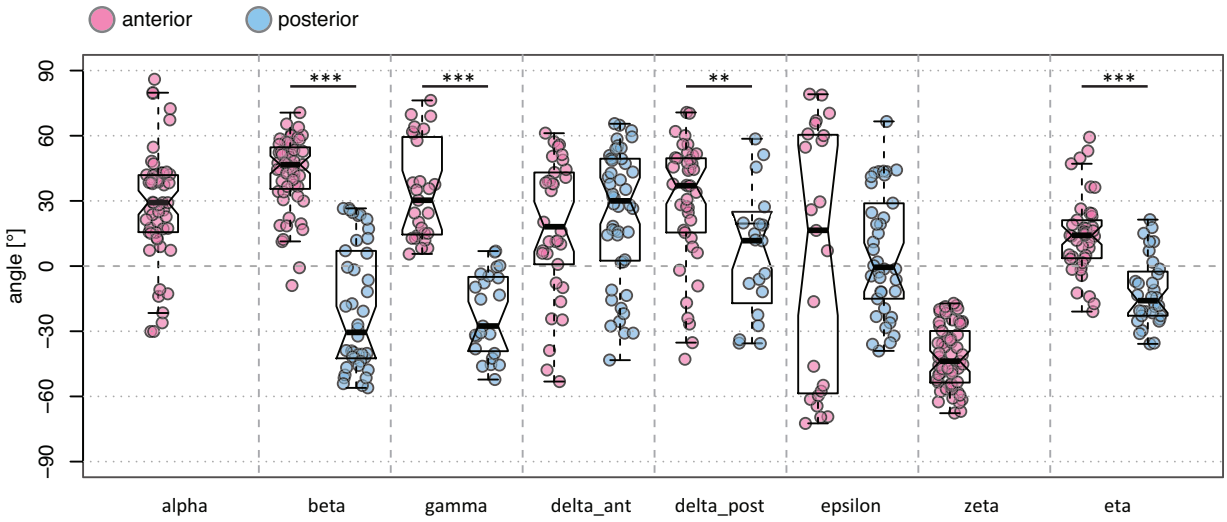

Figure 21: **Lamellar overlaps of opposing LE cells differ significantly within the anterior and posterior compartment.**
Angle measurements of the anterior (magenta) and posterior (cyan) compartment of the eight investigated embryos alpha to eta. Measurements of early and mid zipping stages were included, late zipping stage measurements were excluded. Also, mixed interactions between anterior and posterior opposing cells were excluded. Data was normally distributed according to the Shapiro-test, the Welsh Two Sample t-test revealed significant differences of the anterior and posterior compartment within embryo beta (***) and embryo gamma (***). Embryos delta_posterior_canthus and embryo eta were not normally distributed. The Mann-Whitney U-test revealed a significant difference in the measured angles of the anterior and the posterior compartment within the posterior canthus of embryo delta (**), and within embryo eta (***). p-value < 0.001 (***). p-value < 0.01 (**).

organization as a consequence of positional information and differential recognition.

To test whether the recorded angle measurements were influenced by the position within the embryo along the anterior-posterior axis, the angle measurements were plotted according to their segmental identity (figure 22). The fly embryo is regularly patterned, three thoracic segments are followed by eight abdominal ones. The eight investigated samples spanned a subset of those segments (figure 22 A). Angle measurements of early and mid zipping stages were pooled of seven samples, excluding embryo zeta that featured contrary cell behavior compared to the majority of zipping sites. In figure 22 B the contribution of a certain embryo to a distinct segmental compartment is listed. The

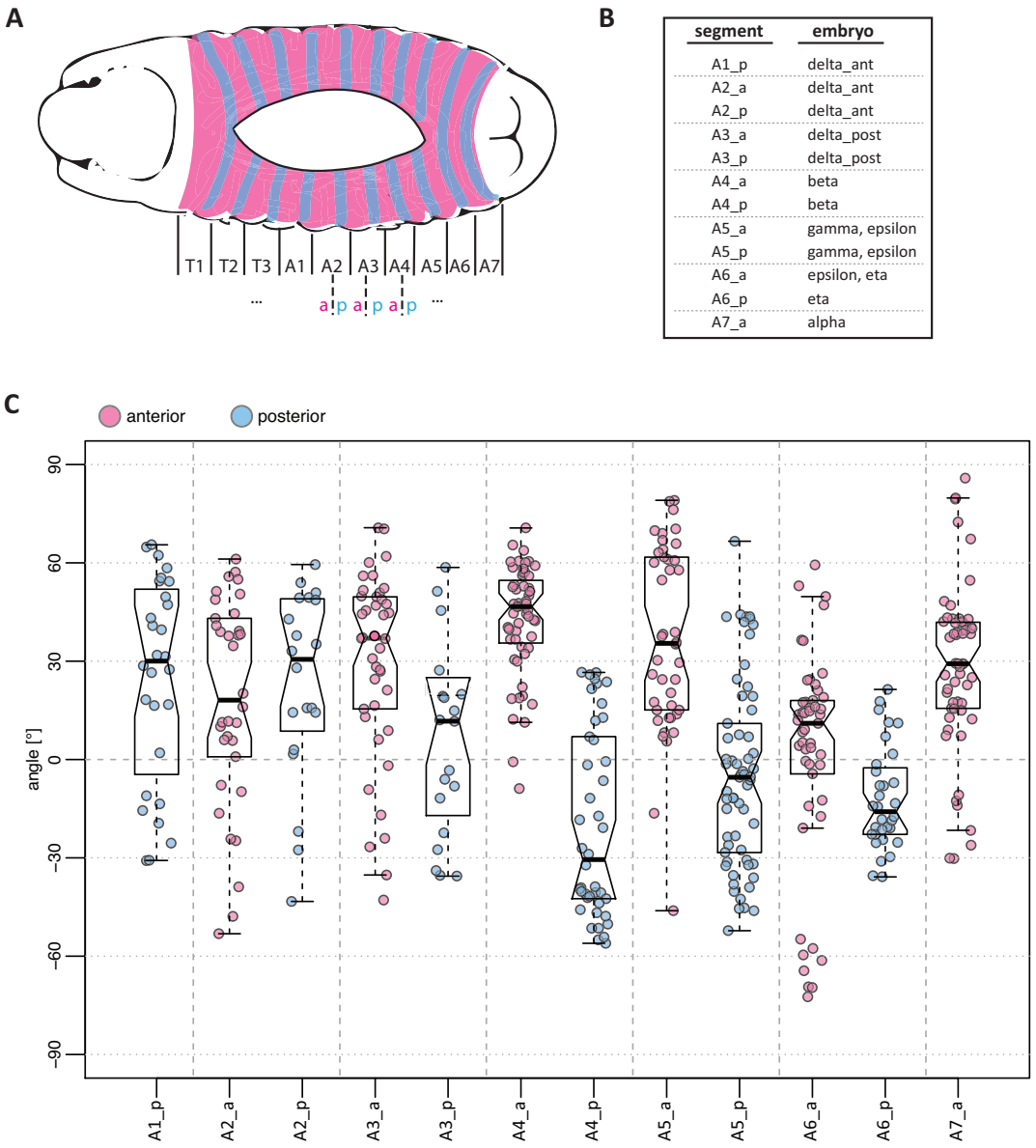

Figure 22: **Pooled angle measurements of lamellar overlaps from sampled zipping sites to a hypothetical embryo.**

(A) Schematic of an embryo, showing the respective thoracic segments T1-T3 and the abdominal segments A1-A7. The repetitive nature of anterior and posterior compartments is indicated. **(B)** Table summarizing which embryo contributed its angle measurements (from the previous figure) to which segment in the hypothetical embryo. **(C)** Angle measurements along the anterior-posterior axis of the hypothetical embryo, from abdominal segment A1 till A7.

alternating cell behavior, dependent on the anterior or posterior identity, became apparent from abdominal segment A3 onwards to segment A7 (figure 22 C). Independent of the position within the embryo, anterior cells showed a different cell behavior from posterior ones (compare for instance segment A4 with A5). The measurements of embryo delta (see figure 18) contributed to abdominal segments A1 and A2, rendering the resulting angle measurements of those segments inconclusive. Based on those results, we concluded that the angle measurements were independent of the segmental position within the embryo, at least for abdominal segments A3 to A7.

3.4.2 The majority of left anterior LE cells dives underneath right opposing ones, whereas the majority of left posterior LE cells protrudes over opposing right ones.

In order to achieve a better insight into the alternating cell behavior of anterior and posterior compartmental cells, various comparisons of different datasets for anterior and posterior cells were performed.

Figure 23 collocates various box plots for different data sets as indicated and described in the figure legend. The category of "mid compartment" was not introduced before. This category comprised 10 subsequent angle measurements per compartment for each collected zipping site. These 10 angle measurements were taken from the middle of one compartment. Whenever less than two cells were segmented for a compartment, angle measurements were omitted, since those did not correspond to a mid region within the compartment. Only mid zipping cells were taken into account and mixed interactions between cells of differing compartments were omitted. Seven zipping sites contributed to measurements of the anterior compartment, and five zipping sites contributed to the posterior one.

The observed different cell behavior, of anterior right cells protruding over left ones and that of posterior left cells protruding over right ones, was significant for all tested categories (p-value < 0.001 (***)). When excluding measurements of the inconclusive

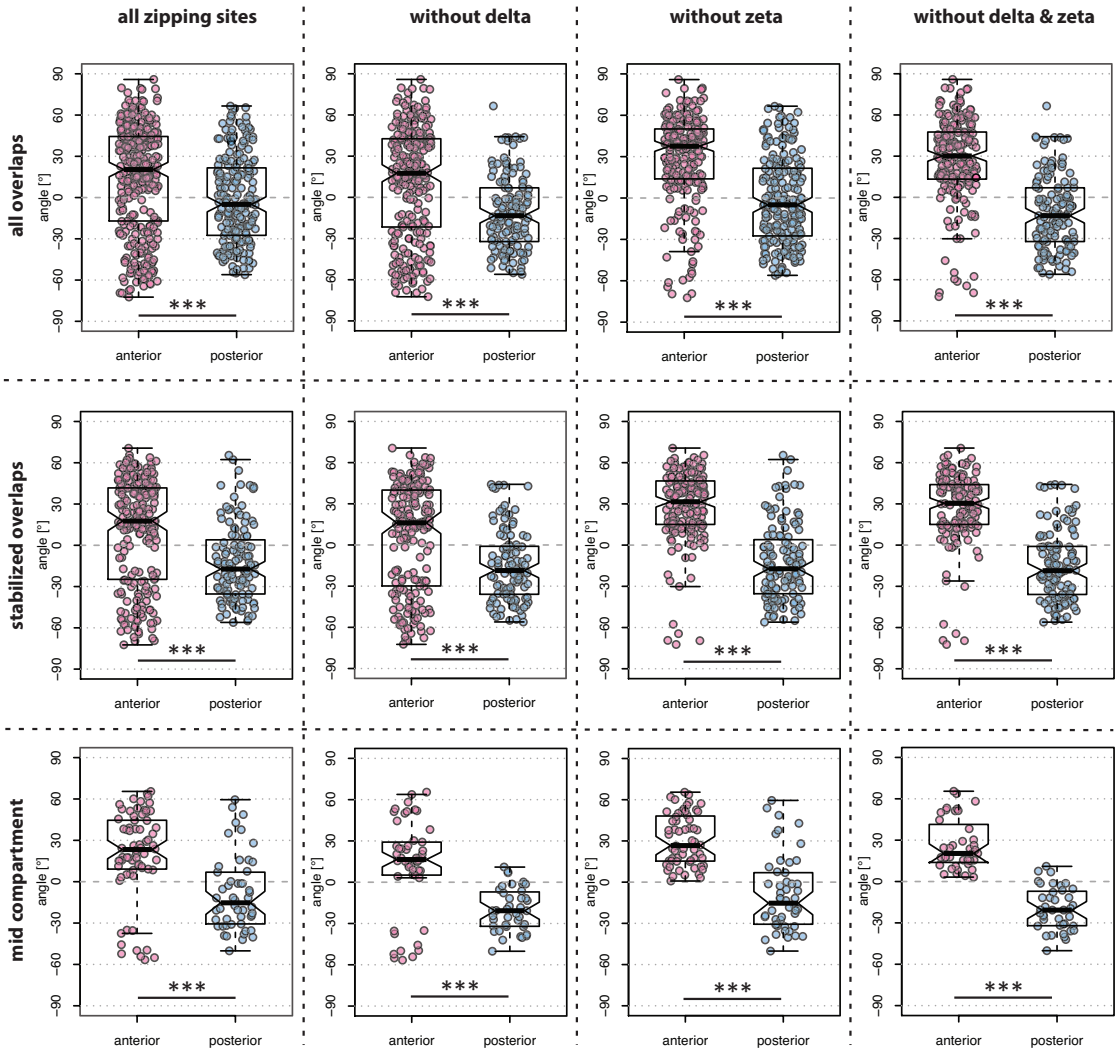

Figure 23: **Cells of the anterior and the posterior compartment show a significantly differing cell behavior.**

Angle measurements of opposing anterior and posterior cells show a significant difference. The panel displays various box plots comparing different datasets, as indicated, for the anterior and the posterior compartment. The horizontal lines distinguish three different categories: All overlaps comprised all angle measurements of early and mid zipping stage, non-mixed cell interactions. Stabilized overlaps refers to angle measurements of interaction sites with identified AJs. Mid compartment designates 10 angle measurements in the middle of a segmented anterior or posterior compartment. The vertical rows distinguish four different cases: All overlaps comprised all collected eight zipping sites. The remaining three cases comprised datasets where the measurements of one or more embryos were excluded (delta and / or zeta). The data was normally distributed (Shapiro-test), except for the measurements of "mid compartment, without delta" and "mid compartment, without delta and zeta". The Welsh Two Sample t-test was applied to normally distributed data and the Mann-Whitney U-test to not-normally distributed data. p-value < 0.001 (***).

embryo delta and embryo zeta with the inverted cell behavior, the median for the anterior and the posterior compartment became more pronounced. This difference was even more distinct when analyzing only stabilized overlaps. The median angle for anterior cells was approximately 30° for anterior cells and approximately -19° for posterior ones when excluding measurements of embryos delta and zeta. Overall, the variability of angle measurements was reduced when omitting embryos delta and zeta. The comparisons of angle measurements of the different compartments recorded in the middle of a compartment naturally comprised less data points. This might be a reason why the difference between anterior and posterior cells was not as pronounced, but still similar to the angle measurements covering a whole compartment. This might indicate, that the middle of the stripe is not the sole instructor of cell behavior.

In summary, the interacting anterior and posterior compartmental cells showed a significantly altering lamellar overlap structure. This is once more emphasized in figure 24, where rose plots display the frequency of a certain angle measurement for the anterior and the posterior compartment for all measurements and for stabilized interactions without embryos delta and zeta, respectively. The alternating trend of anterior and posterior cell behavior was apparent. The switch of cell behavior occurred close to the compartment boundary and seemed to involve the left-right axis in addition to cellular identity.

Strikingly, the median for the anterior or the posterior compartment was differently pronounced. For instance, the posterior median deviated less from 0° than the anterior one when comparing measurements of stabilized overlaps without embryos delta and zeta (figure 23). A possible explanation for the less pronounced dominance of posterior left cells protruding over opposing right ones may be found when plotting the distribution of measured angles along the zipping site (figure 25). Posterior angles were more often recorded towards late zipping stages (peaks from 20 - 30 μm), where the measured angle tended towards 0°. Thus, given a more even distribution of anterior and posterior angle

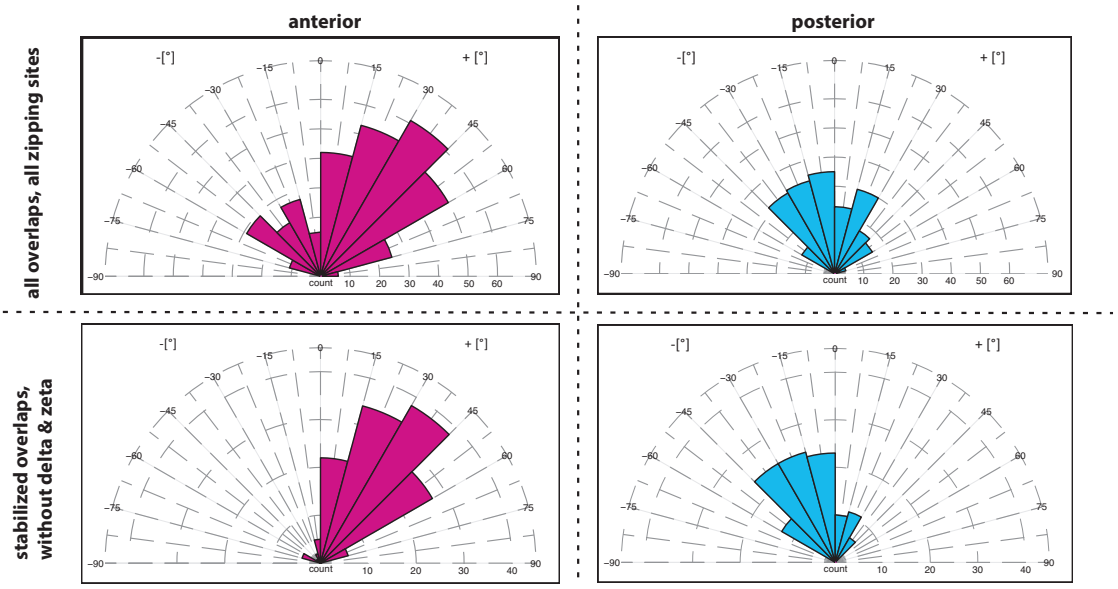

Figure 24: **Rose plots representing the inverted cell behavior of the compartments.** Rose plots displaying the frequency of a certain range of angle measurements from -90 to +90°. The inverted trend of angle measurements for anterior and posterior compartmental cells was obvious when comparing all overlaps and all zipping sites, as well as when comparing only stabilized overlaps excluding zipping sites of embryos delta and zeta.

measurements, one might find similar pronounced medians, deviating from 0° to the same extent. Alternatively, the less pronounced median for posterior cells might reflect the pooling of mixer cells with their posterior neighbors (see section 3.3.6). As shown in figure 20 E, mixer cells featured a median angle measurement of -30°, whereas the neighboring posterior cells scored with a median of 0°. This might reflect the exceptional role of mixer cells that cross segment boundaries via transdifferentiation. It remains a possibility, that the mixer cells held a special instructive role for the establishment of cell behavior and thus lamellar overlap organization.

The anterior and compartmental identity was able to explain the observed alternating cell behavior. Other variables could account in addition for the differing alternating lamellar overlaps. Although biologically highly unlikely, I wanted to test whether the distance from the zipping site, meaning the distance from the opening affected the angle values. As mentioned above, this analysis was complicated by the fact that the majority

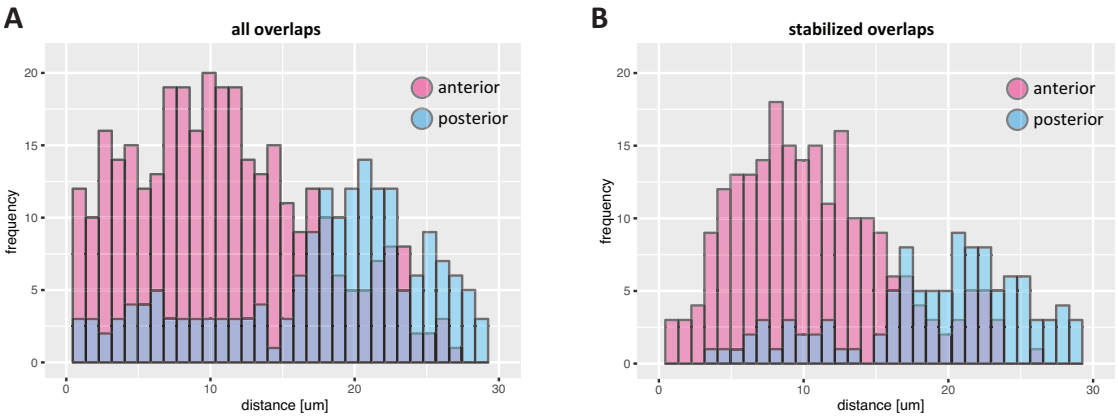

Figure 25: **Differing frequency of angle measurements along the zipping site.** **(A)** Comparison of the distribution of angle measurements for the anterior and posterior compartment along the zipping site. Angle measurements including early and mid interactions and measurements of all the eight collected zipping sites. **(B)** Same as in A; plotting only angle measurements of stabilized overlaps.

of anterior cells was present close to the opening and posterior ones were more distant from the opening, representing later zipping stages. A covariant analysis with ANOVA, a so called ANCOVA, was impossible to perform, since the assumptions for the test were not met by the acquired data set. The distance values were not independent of the anterior or posterior cell identity.

From a biological point of view, the hypothesis of distance from the zipping site accounting solely for the observed switch of lamellar overlaps at the compartment boundary, was rejected. The only influence the distance from the zipping site held was in form of the zipping stages, independent of anterior or posterior cell identity. The later the zipping and especially towards late zipping stages, the interface of the overlapping, opposing leading edge cells was raised horizontally, forming the characteristic interaction surface of cells within one epithelium.

In summary, the analysis of seven zipping sites via CLEM revealed a different lamellar overlap organization within the anterior and the posterior compartment. A switch of behavior correlated with the presence of the compartment boundary. One embryo

presented an exception to the found pattern, its inverted cell behavior might be due to mismatching and sorting steps complicating proper cell-cell recognition. Alternatively, the left-right axis might have been not established correctly.

4 Discussion: Cell-Cell Recognition During Zipping

4.1 The power and limitations of correlative light and electron microscopy

I established correlative light and electron microscopy to study the cell-cell recognition mechanism during zipping. Correlative microscopy was key, and information on both the anterior and posterior compartmental identity of cells, combined with knowledge on the structural organization of the lamellar overlaps was obtained (figure 11 A). The established protocol relies on two essential factors: First, I employed the protocol established by Kukulski et al. [2011], utilizing a gentle and slow freeze-substitution in the presence of low heavy metal concentration. Second, GFP signal was best preserved through the detrimental sample preparation steps of dehydration, heavy metal fixation, and ultraviolet irradiation when using a very strong expression (figure 11 G). Strong expression of GFP was achieved by utilizing a fly stock developed at Janelia Research Campus (Pfeiffer et al. [2012], figure 12 A) that was optimized for optimal translation via viral enhancers. The fly stocks employed in this correlative study were the basis for Nern and colleagues to study neuronal networks within the *Drosophila* medulla by light microscopy (Nern et al. [2015]). They modified the stocks further, such that each neuron could be stochastically labeled with a different fluorophore, tethered to the membrane. Thereby, single neurons could be distinguished within the densely packed brain in order to elucidate cell arrangements.

The fly stocks by Pfeiffer and colleagues (Pfeiffer et al. [2012]) proved very powerful in my hands: very remarkably, when I collected serial sections six weeks after completion of freeze-substitution, the sections still possessed a sufficient preservation of GFP fluorescence (figure 13 D). Nevertheless, light microscopy imaging needed to be performed best within two days after serial sectioning as after this step fluorescence decayed faster. The long retention of the GFP signal within the plastic samples proved fundamental for the simultaneous processing of several samples, allowing for the collection and analysis of eight different zipping sites in this study. These improvements were essential as this

is the first CLEM study involving such large volumes. Previous studies utilizing in-resin fluorescence retention investigated a smaller volume of interest; thus if light microscopy was performed on a few sections within a very short time, the fluorescence retention of commonly employed strains and stocks was sufficient (Kukulski et al. [2011], Fabrowski et al. [2013]).

I tested several fluorophores for their suitability for CLEM. Although neither the fluorescence of mCherry nor mNeonGreen were retained at all (figure 11 C, D), they might still hold the capacity to function in the established set-up if expressed at higher concentrations and if confined to sub-cellular structures such as the membrane for increased local concentration and thus signal detection. Alternatively, the SNAP-tag might still be a choice in other correlative studies, if problems concerning the specific chemical labeling post-sectioning could be addressed (figure 11 E). The SNAP-tag was already successfully used in correlative studies on the molecular arrangement of cadherins in adherens junctions of mouse epithelial cells (Perkovic et al. [2014]).

The correlative light and electron microscopy approach I implemented for studies of dorsal closure holds a great power to study other biological questions during fly development. By employing a specific Gal4-driver, one could readily label cells or tissues of interest during a certain developmental process with the strong GFP signal. Correlation of the LM and the EM of the very same section is now feasible, yielding optimal correlative analysis. For instance, as already started at the Janelia Research campus, mapping specific neurons within the fly brain could give structural and functional insight (Nern et al. [2015]). Relating this to dorsal closure, stochastic labeling of individual cells within the epidermis and subsequent analysis might reveal individual cell behavior.

Correlative microscopy has become a very powerful tool to study a plethora of biological questions in model organisms. The combined power of the two imaging modalities gives insights into processes that otherwise would be difficult to approach (de Boer et al. [2015]). Correlative microscopy is always adjusted to the biological system of

interest. Lately, the correlation even becomes multimodal: Karreman and colleagues combined intravital microscopy of metastatic mouse cells with X-ray microscopic computer tomography. Thereby, they relocate the imaged cancer cell for subsequent targeted ultrastructural analysis via focused-ion beam / scanning electron microscopy (Karreman et al. [2016]). A few groups performed CLEM analysis via array tomography, combining super-resolution microscopy with scanning electron microscopy to study mouse nervous systems (Micheva and Smith [2007]) and gap junctions in *C. elegans* (Markert et al. [2016]). Reduced photobleaching was achieved by performing light microscopy under cryogenic conditions. The challenge was to maintain the sample in a vitrified state during FLM and EM by the help of dedicated cryo-holders (Sartori et al. [2007], Schwartz et al. [2007], Schorb et al. [2016]). Also, the development of integrated microscopes at cryogenic conditions could simplify the working process. With integrated cryo-microscopes, one could reduce ice-contamination since transfer of the sample could be omitted and one could circumvent the need to transfer the coordinate system from one microscope to another.

For this study, sample preparation and data acquisition equaled the time needed for data analysis. For the study of even larger volumes, this picture changes. Recent developments in sample preparation and data acquisition shifted the bottleneck towards the data analysis part. A lately introduced automatic tape-collecting ultramicrotome (ATUM) was shown to be capable of collecting thousands of serial sections of the mouse cortex with highest accuracy within a minuscule amount of time (Schalek et al. [2011], Hayworth et al. [2014]). By recording scanning electron micrographs of these very thin sections, one omits the time-consuming acquisition and reconstruction of electron tomograms while achieving a sufficient resolution. Zeiss lately introduced a scanning electron microscope, where 61 beams acquire in parallel data of serial sections that were placed on a wafer support. Per second, 1.22 Gigapixel are generated, at a resolution of 1 to 4 nm per pixel (Eberle et al. [2015]). Also, structural neurobiology is employing serial block-face scanning electron microscopy or focused-ion beam scanning electron micro-

scopy to study neuronal arrangements and synaptic connections, acquiring terabytes of datasets where information of the connectome needs to be extracted (Takemura et al. [2013], Maco et al. [2014]).

The analysis of these substantial datasets either relies on manual segmentation of features of interest or employs automatic segmentation algorithms. An alternative is based on "citizen science". Citizen science describes the effort to involve the general public in scientific projects. On the one hand, people can gain a better understanding on how science is conducted. On the other hand, the researchers benefit from people assisting in the time-consuming analysis process. Successful citizen science projects include the www.eyewire.org project, where the connectome of the mouse retina was segmented (Kim et al. [2013]), or the project www.fold.it, where people performed better than computers in finding the entropically most favorable and stable folding state of several proteins of interest (Cooper et al. [2010], Khatib et al. [2011]). Also, several attempts to train computers to segment features of interest (pixel and object classification algorithms, Ilastik) have proven to assist in the segmentation process in numerous neurobiological structural projects (Kreshuk et al. [2011], Maco et al. [2014], Kreshuk et al. [2014]). Nonetheless, accurate tracing of sub-cellular features of interest within dense environments with a low signal-to-noise ratio (as is the case for my dataset) remains a challenge and currently available automated segmentation algorithms fail. Moreover, an algorithm is always optimized for the analysis of a specific problem and dataset. Therefore, without modifying the algorithm to the needs and specific characteristics of the own dataset, a successful application from one system to the other remains a challenge.

4.2 The lamellar overlap organization of zipping cells is dependent on the anterior-posterior compartmental identity and the left-right axis

With the established CLEM protocol, I was able to analyze eight complete zipping sites and gain knowledge on the lamellar overlap structure in relation to the compartmental

identity of the cells involved. I extracted both descriptive data on the cell-cell interactions (i.e. panel on embryo beta, figure 16 B, C), as well as quantitative data on the lamellar overlap angle (figure 14) or the number of cell-cell interactions (figure 15) for comparative analysis.

The analysis of individual zipping sites revealed similarities and differences in the organization of the overlaps of opposing LE cells (figure 21). Five out of eight analyzed zipping sites showed a common organization of lamellar overlaps. These cell-cell interactions suggested a dependence not only on the anterior-posterior cell identity as previously shown but also on the left-right axis (section 3.4). Thereby, the protrusions of anterior compartmental cells from the left side preferentially dived underneath the anterior compartmental cells from the opposing, right side. In turn, the posterior compartmental cells from the left side preferentially protruded over the posterior compartmental cells from the opposing, right side. This switch of cell-cell interaction behavior correlated well with the compartmental boundaries (figure 23). In many instances, this switch was not accurate. In particular for overlaps of posterior cells, a transition zone was observed (e.g. embryo epsilon, appendix A, figure 39). At the zipping site of embryo epsilon, the zipping canthus progressed from the posterior compartment to the anterior one, and it appeared as though the anterior cells might have influenced the overlapping angles of the posterior cells closest to them. As the anterior compartment generally comprises one to two more cells than the posterior, more matching cells within the anterior compartment are free to follow the preferred interaction rule of the left side diving under the right side, without disturbance from neighboring posterior cells that prefer the opposite way of matching. This may be the reason why the rule is more evident for matching anterior compartmental cells and accordingly, due to the fewer possible opposing interaction partners, the posterior cells might show less pronounced overlap rules. Interestingly, cells situated at a compartment boundary appeared to be slightly more often in contact with other cells from the opposing side. A maximum of four interactions between one cell from one side with four cells from the other side was observed, and those cells were often situated at compartment boundaries and within a ”mixed” overlap of anterior and posterior op-

posing cells (appendix A, table 3). By contacting many cells on the opposing side, the compartment boundary might be read out by different adhesion properties of anterior and posterior cells. Thus, an initial mismatch between anterior and posterior opposing cells could be corrected to ensure proper alignment of the compartments. Studying the behavior of the majority of cells in the analyzed zipping sites, I conclude that the switch in cell behavior correlated strongly with the observed compartment boundary (significant difference, see figures 23 and 24).

For one sample, that of embryo delta, an inconclusive cell behavior was observed (see embryo delta, figure 18). However, live imaging showed that the more dorsal closure progresses, the more chaotic it becomes. In particular, with high frequency the zipping front can jump several cells that will interact only later. In this way the initially clear zipping front becomes less well defined. Since the dorsal hole of embryo delta was almost completely closed (see figure 18 A) and the contact surface between opposing cells appeared not as large (figure 18 C), the trend seen for the other five zipping sites might be masked. Most likely therefore, the inconclusive lamellar overlap arrangements of embryo delta were due to the presence of poorly defined zipping sites.

Within the eight analyzed zipping sites, only one was situated at the anterior end of the dorsal opening (embryo delta_anterior). The experimental set-up did not allow for choosing between the anterior or the posterior zipping site for section collection. Only after section collection, a thorough analysis of anatomical landmarks revealed the anterior or posterior canthus identity (figure 13 F). The lamellar overlap organization appeared rather consistent along the anterior-posterior body axis for the different segments, although the measured angles of embryo delta proved hard to interpret (figure 22). It appears that the lamellar overlap organization is regulated in the same fashion for all the segments, from the most anterior segments to the most posterior ones.

Contrary to the other analyzed zipping sites, one out of eight sites (embryo zeta, figure 17) featured a clearly left/right biased lamellar overlap organization, but with reversed orientation. Anterior cells from the left side protruded over the opposing partner cells from the right. Unfortunately, I could not analyze any neighboring posterior cells and

therefore no conclusion about an alternating behavior between the anterior and posterior compartment can be drawn. There are four possible interpretations for the observed contradicting behavior of the anterior cells of sample zeta: 1) Live imaging before sample preparation revealed a shift along the anterior-posterior body axis of matching compartments (figure 17 A). It is possible, that this prevented matching cells from connecting to their correct opposing partners, as their filopodia normally cannot extend to connect with cells more than two to three cell diameters away. This small mismatch might result in the contradicting lamellar overlap and would be sorted out later. Whether the observed misplacing of opposing compartments is the cause or the consequence of the inverted, differing cell behavior could not be answered. 2) The establishment of the left-right axis might have failed (see also upcoming sections 4.5 and 4.6). 3) Since the method is not high-throughput, the eight analyzed zipping sites might not account for the real frequency of cell behavior. Embryo zeta might represent 50 % of the observed lamellar overlap structure in nature. If this was the case, the establishment of the asymmetry, the rise of the left-right axis, might be controlled via a stochastic trigger. Thereby, half of the embryos would establish a left-right and the other half a right-left asymmetry, that would be later relayed and maintained. Also, a ratio of 10 % to 90 % is possible. To get a better insight about the distributions of the observed contrary phenotypes, more data would be necessary. The establishment of left-right asymmetry later during fly development is discussed in more detail in section 4.5. Very interestingly, the rotation of the testis possesses a 100 % prevalence of a dextral turn in wildtype flies (Spéder et al. [2006]). If similar mechanisms would regulate the establishment of a left-right asymmetry during dorsal closure, one would expect an equivalent robustness. 4) The observed bias for a specific lamellar overlap organization of the majority of analyzed cells might be coincidental and the observed left-right asymmetry during zipping might not exist.

The observed correlation of the regular lamellar overlap pattern with anterior-posterior identity and the left-right axis dismisses the possibility of a solely tension-based zip-

ping process. Hypothetically, the tension created by the supra-cellular actomyosin cable within the LE cells could mechanically constrain certain cell-cell interactions. Thereby, cells of a specific compartment would be mechanically constrained from fusing with cells of the same compartment, within another segment.The tension could ensure that a mismatch between wrong opposing segments was mechanically unfavored and could not be stabilized. The observed regular pattern does not exclude a contribution of the actomyosin cable to matching. Embryos mutant for the cell adhesion molecule Echinoid and thus devoid of the actomyosin cable within the LE cells showed mismatching defects during zipping (Laplante and Nilson [2006], Lin et al. [2007]). Pairing of cells from one compartment with cells from two opposing compartments, as well as pairing of adjacent, but not opposing compartmental cells was observed when contacts were established perpendicularly to the dorsal midline (Lin et al. [2007]). Recent data from the Brunner lab points towards an importance of the actomyosin cable during zipping and matching (Pasakarnis et al. [2016]). Embryos selectively and acutely depleted for MyosinII in the epidermis lacked the supra-cellular actomyosin cable. Dorsal closure was slightly delayed but successfully closed the dorsal hole. The effect of epidermis-specific MyoII depletion was more pronounced during zipping. The LE cells had more protrusions and these were longer, enabling cells of the same compartment but from different segments to contact and interact, causing a significant delay in zipping and a puckering phenotype (Pasakarnis et al. [2016]).

If the matching process during zipping was regulated via the supra-cellular actomyosin cable in the epidermis cell bodies alone, the flexible parts of the cells, namely the filopodia and lamellar overlaps, would show a random, non-conclusive pattern. Since I observed a regular lamellar overlap pattern, I speculate that this organization is achieved via cell-cell recognition. The actomyosin cable might aid the matching process by generating a tension-based threshold, rendering mismatches of compartments of different segments harder.

In the following sections, I introduce and discuss the concepts of positional inform-

ation and of left-right asymmetry. Next, I try to combine those concepts into a bigger picture, proposing a putative mechanism on how cell-cell recognition during zipping could be achieved.

4.3 How to establish positional information within a tissue

The correlative analysis of the lamellar overlap pattern and the compartmental identity at the zipping site revealed for the majority of analyzed zipping sites a regular, significantly alternating cell behavior. Both the anterior and posterior compartmental identity and the position along the left or the right side of the embryo, respectively, appeared to influence the organization of opposing LE cells.

How could this differential lamellar organization be achieved? As already outlined in section 1.3, epidermal cells acquire positional information along the anterior-posterior body axis via a genetically tightly regulated hierarchical cascade of the segmentation control genes. Positional information refers to the process when cells acquire their position in relation to their neighbors or an axis. The positional value is interpreted resulting in differential cell fate and cell behavior (as reviewed in Wolpert et al. [2015]). The establishment of positional information follows a common theme: In *Drosophila*, gradients of morphogens are established from organizer structures, and their concentration at a specific location is translated, e.g. via the number of ligand-receptor complexes formed. A certain morphogen concentration would activate a specific intracellular response, such as e.g. transcription factors activating a specific set of genes.

Often, cells need to maintain their obtained positional information throughout embryogenesis, in morphostasis, during regeneration, and as a mechanism for cancer suppression (Levin [2012]). Several mechanisms contribute to pattern formation and maintenance - genetic programs imposing a specific fate on cells, directed growth and cell division, and mechanisms ensuring boundary formation and maintenance (Meinhardt [2015]). Cells of established compartments with lineage restriction need to resist cell proliferation and tissue deformation without mingling (Dahmann et al. [2011]). Two possible mechanisms

of boundary formation and maintenance are 1) differential cell adhesion (reviewed in Steinberg [2007], McNeill [2000]), and 2) differential cortical tension (reviewed in Dahmann et al. [2011], Aliee et al. [2012]). 1) It was shown that cells expressing different kinds of cadherins or different levels of the same type of cadherin sort out into separate populations (Friedlander et al. [1989]). 2) Similarly, cells can actively generate mechanical tension, resulting in contraction of their surfaces that are in contact with neighbors, thereby becoming sorted. Monier and colleagues described an actomyosin cable at the parasegment boundary within the *Drosophila* epidermis (Monier et al. [2010]). During developmental stages 8 to 11, mitosis occurs within the epidermis. Thereby, the boundary between the anterior and posterior compartment is challenged. In order to prevent cells from invading neighboring compartments, the tension created by the actomyosin cable at the parasegment boundary is sufficient to push cells back in their place. The authors concluded that regulation of actomyosin contractility at the boundary was key for boundary maintenance. From stage 12 onwards, marking the onset of DC, cell division within the epidermis stops and the cable regresses. Thus, the maintenance of the boundary at this stage must rely on an alternative mechanism - possibly that of differential cell adhesion. Interestingly, Monier and colleagues speculate that differential adhesion between anterior and posterior cells was established in the first place, being later interpreted into differential tensile properties of the two differing compartments via regulation of Echinoid and Bazooka/Par3 (Monier et al. [2010], Monier et al. [2011]). Thus, differential adhesion and differential cortical tension would not act exclusively, but could rather act during different time points of development and / or within different tissues during different morphogenetic events (Monier et al. [2011]).

Based on my correlative dataset, it appears that cells of the anterior versus the posterior compartment within the *Drosophila* epidermis behave differently. This could be accounted for by a difference of adhesion properties within the two compartments. Also, a separation of these cells based on differential tensile properties seems possible. Recognition during zipping appears on two levels: First, cells form contacts based on

their anterior-posterior compartmental identity (Millard and Martin [2008], this study). Second, the cells within a compartment sort out and find their correct opposing partner, such that the most posterior cell on one side contacts the most posterior cell of the other side (Millard and Martin [2008]).

I speculate that the recognition of opposing LE cells of one compartment could be achieved via a specific set, a specific amount / activity, a specific localization of receptor-ligand pairs. The sorting within a compartment could be achieved via gradients of adhesion molecules along the anterior-posterior body axis, or alternatively via differential tension.

4.4 Cell-cell recognition

Several pathways have been described mediating cell-cell recognition, regulating the attraction or repulsion of interacting cells (Halloran and Wolman [2006], Bashaw and Klein [2010], Honda and Mochizuki [2002]). During zipping, filopodia of the LE cells sweep their surrounding and establish contacts with neighboring and opposing cells (Jacinto et al. [2000]). Those filopodia are replaced / remodeled into lamellipodia, and the huge lamellar overlaps characteristic for the mid zipping stage.

The sensory function of those protrusions could be constituted via the prominent axon- and cell-guidance cues: netrins, semaphorins, ephrins, slits and their receptors (reviewed in Bashaw and Klein [2010]). Axon guidance plays a major role during neuronal developmental processes, such as the retinotectal mapping and crossing of the midline, and underlying principles are also applied during tissue boundary formation in somitogenesis and hindbrain development (Halloran and Wolman [2006], Umetsu et al. [2014]). Signaling during axon guidance regulates changes in actin and microtubule dynamics, as well as changes of adhesive properties. Common themes of signaling include endocytosis, proteolytic processing of receptors for activation, second messengers and Ca^{2+} to modulate activity of actin and microtubule effectors (Bashaw and Klein [2010]). Very interestingly, both Semaphorin and Eph receptor signaling were implied in closure events.

During ventral enclosure in *C. elegans*, a process that is reminiscent of dorsal closure, both semaphorins and ephrins mediate cell-cell recognition for proper matching of opposing cells (Ikegami et al. [2012]).

The sensory function of filopodia during zipping could also be mediated via cell adhesion molecules of the cadherin and immunoglobulin IG superfamilies, similar to neuronal development (Zipursky and Grueber [2013], McNeill [2000]). Thousands of different isoforms of the *Drosophila Dscam1* locus are produced via alternative splicing (Zipursky and Grueber [2013]), equipping each neuron with a unique combination of expressed isoforms. Thereby, protrusions (dendrites, axons, postsynaptic elements) from the same cell selectively do not interfere. This process is termed self-avoidance.

Further, cell-cell recognition and pattern formation can be achieved via lateral inhibition. The signaling of the extracellular ligand Delta to neighboring cells expressing the receptor Notch is well described in the establishment of bristles in the *Drosophila* notum. The cell expressing Delta first establishes the mechanosensory organ precursor cell. This cell laterally inhibits neighboring cells presenting the Notch receptor from adopting the same cell fate (Cohen et al. [2010]). The authors speculate that dynamic filopodia signaling, creating structured noise allowing for pattern refinement, would be an ideal alternative to morphogen diffusion as a mediator of developmental signaling at a distance. Based on computational modeling, stripes and spots of different cell types were simulated by modulation of the signal strength and the length of the described dynamic filopodia (Cohen et al. [2010]).

Combining the mentioned cell-cell recognition molecules on a qualitative and / or a quantitative level holds a great potential. Positional information along the anterior-posterior body axis might result in cells expressing an exclusive code of cell-cell recognition molecules. Based on my acquired correlative data, I conclude that at least cells from the anterior and the posterior compartment differ (figure 23). It is possible that one cell at the compartment boundary or within the compartment is sufficient to mediate the alternating cell behavior, being instructive on the neighboring cells within the

same compartment. In this respect, a closer look on the cellular behavior of mixer cells appeared advisable (section 3.3.6). Mixer cells were described as transdifferentiating cells, changing from anterior to posterior compartmental identity (Gettings et al. [2010], Gettings and Noselli [2011]). When comparing the lamellar overlaps of mixer cells with their neighboring posterior cells, the mixer cells showed a more pronounced tendency with a median of -30° compared to 0° (figure 20 E - H). Therefore, the mixer cells might possess a specialized positional information along the anterior-posterior body axis and hold a special function during matching. Millard and Martin speculated on mixer cell function for precise alignment within the compartment and attributed a keystone function to those cells (Millard and Martin [2008]).

Due to the rather low number of analyzed mixer cells, they were pooled with their posterior neighbors for comparative analysis of anterior versus posterior cell behavior. More data on mixer cells of more zipping sites would be necessary to study their function properly. Gettings and colleagues modified the number of occurring mixer cells by either overexpressing activated or dominant-negative JNK pathway components (Gettings et al. [2010]). Within the embryos without JNK activity, no mixer cells were specified, resulting in mismatching defects. However, the embryos also lacked the proper actomyosin cable within the LE cells. Thus, a direct effect of mixer cell presence on matching could not be distinguished from the missing tension at the leading edge assisting in proper matching. Studying the mentioned embryos with modified JNK activity with my established correlative analysis might spread further light on the importance of mixer cells during matching.

Mismatches between cells of the same compartment but of different segments were observed, creating X- and Y-shaped patterns (Millard and Martin [2008]). Therefore, the recognition appears not segment-specific. Each segment within the *Drosophila* epidermis possesses a unique identity imposed by the expression of homeotic selector genes. However, independent of the segment identity, all cells from a compartment appear to feature the same set of recognition entities (being it a specific set of cell adhesion mo-

lecules or specific tensile properties). This would argue for Engrailed and Wingless being in control for the establishment of specific recognition properties.

To identify underlying mechanisms and molecules regulating the matching of opposing LE cells during zipping, a Ph.D. student from the Brunner lab, Magdalene Adamczyk, performed a forward ethyl methanesulfonate mutagenesis screen (Adamczyk [2016]). Further, she analyzed mutants of factors involved in the recognition process during axon guidance such as semaphorins and ephrins. Unfortunately, no robust phenotype could be identified, most likely due to the experimental set-up where maternal contribution likely masked the outcome. Nevertheless, the axon guidance molecules remain promising candidates for mediating cell-cell recognition during zipping.

4.5 Left-right asymmetry is a recurring motif during *Drosophila melanogaster* embryogenesis

I showed that the lamellar overlap pattern of zipping cells appeared to be dependent on a left-right axis (section 3.4.2). Evolution generated a diversity of left-right patterning from cells to organs (Coutelis et al. [2014]). The left-right axis is established in relation to the anterior-posterior and dorso-ventral body axes in a secondary step (Levin and Palmer [2007]). Similarities of symmetry breaking are found between phyla, as reviewed in Coutelis et al. [2014], Spéder and Noselli [2007], and Vandenberg and Levin [2013]. The most prominent identified mechanism of left-right establishment might represent not the initial symmetry breaking event, but rather the asymmetry relaying and maintaining event. An asymmetric Nodal flow is observed within the mouse node, establishing differential gene expression on the left and the right side (reviewed in Coutelis et al. [2014]). The flow is established via nodal cilia, that are asymmetrically positioned towards the posterior side of the node cell due to planar-cell polarity signaling. The microtubule assembly and the specific function of microtubule motors determines the orientation and beat of the cilia and thus the Nodal flow. Another mechanism of left-right establishment

is found during the first cleavages of a *Xenopus* embryo: due to planar cell polarity (PCP) signaling, the cytoskeleton asymmetrically positions ion pumps and ion channels. This causes a difference in pH and transmembrane voltage and thus in the concentration of small signaling molecules (reviewed in Spéder and Noselli [2007], and Vandenberg and Levin [2013]). Also within invertebrates such as *C. elegans* and snails, the actin cytoskeleton was shown to constitute an important role in left-right asymmetry (Coutelis et al. [2014], Naganathan2014). Several lines of evidence now point towards the importance of sub-cellular asymmetries in establishing left-right asymmetry on a large scale, such as a tissue or an organ (Li and Bowerman [2010]). The intrinsic polarity of actin filaments and microtubules, as well as motor-protein function along those oriented cytoskeletal tracks could constitute the symmetry-breaking event that is later relayed into differential gene expression for the maintenance of the established left-right axis (reviewed in Levin and Palmer [2007]).

In this light, studies in *Drosophila* indicated the importance of an unconventional myosin motor protein for the establishment of left-right asymmetry: Although the establishment of the anterior-posterior and dorso-ventral body axes is well understood in *Drosophila*, studies on the left-right axis only emerged a decade ago. Those reports focused on other morphogenetic events than dorsal closure, occurring later during embryogenesis and larval development. Several organs in *Drosophila* show a handedness, among these are the brain, the visceral organs and male genitalia. The unconventional myosin *myo31DF*, also termed *myoID*, was identified as a situs inversus gene. Without its function, the visceral organs (Spéder et al. [2006]) and male genitalia (Hozumi et al. [2006]) show a reversed looping. MyoID is symmetrically expressed in the anterior and posterior compartment of larval segment A8, that constitutes the male genital discs. A permissive role was established for MyoID in the anterior compartment, repressing sinistral looping. Whereas in the posterior compartment, MyoID has an instructive role for dextral looping (Spéder et al. [2006]).

It was proposed that MyoID in posterior cells transports dextral-specific information to the asymmetric junctions (at the boundary of anterior and posterior compartment)

(Spéder et al. [2006]). Thereby, MyoID would act as a trigger breaking symmetry. The left-right asymmetry would need to be relayed and maintained via dedicated signaling pathways (Petzoldt et al. [2012]). Adherens junctions were identified as recruiters of MyoID (Spéder et al. [2006], Petzoldt et al. [2012]). The scaffold of cadherins and catenins might represent a signaling platform for MyoID for the establishment and maintenance of left-right asymmetries. Computational modeling proved that the anterior-posterior asymmetry established via asymmetric AJs and MyoID function could be translated into a left-right asymmetry through remodeling of cell contacts via intercalation or rotation (Hozumi et al. [2006], Taniguchi et al. [2011]).
Apart from AJs, other regulators of MyoID have been identified: The Hox gene *abdominal-B* was shown to act as an upstream regulator of *myoID* expression (Coutelis et al. [2013]). The function of MyoID was shown to be independent of microtubules, but dependent on the actin cytoskeleton (Taniguchi et al. [2007]). Myo61F, also termed MyoIC, was shown to posses antagonistic function to MyoID (Hozumi et al. [2006]). MyoIC is excluded from AJs, as it is repressed by DE-Cadherin (Petzoldt et al. [2012]).

MyoID is a promising candidate for the establishment of the left-right axis in the zipping epidermis. I suggest to study the effect of the established mutants (Hozumi et al. [2006], Spéder et al. [2006]) on matching during zipping. First, time-lapse recordings of MyoID-mutants might reveal a mismatching phenotype or a zipping delay. If that was the case, a thorough analysis with the established CLEM method might give further insights into the nature of the observed mismatches: By removing MyoID function only in one compartment by using a specific driver for the posterior or the anterior compartment, one might learn about effects of MyoID on the lamellar overlap pattern. Further, if a mismatching phenotype was present, it would be interesting to know whether the EGFP-tagged MyoID-construct was able to rescue the phenotype. If this was the case, it would be worth to replace the endogenous *myoID* locus with an EGFP-tagged MyoID via the recently described Crispr/Cas9-technique (Jinek et al. [2012]). Then, time lapse recordings of the endogenous MyoID might give further insights into its putative role

for matching. If no mismatching phenotype was obvious by the initial time-lapse experiments of the mutant embryos, a maternal effect possibly masked and rescued the phenotype. The deGradFP-system is a powerful tool to acutely deplete protein function (Caussinus et al. [2013], Pasakarnis et al. [2016]). It might be worthwhile employing the Crispr/Cas9-technique and the deGradFP-system for tissue-specific knock-down of MyoID with temporal control and further analysis of a possible mismatching phenotype.

4.6 Towards a mechanism for cell-cell recognition during zipping?

This CLEM study emphasized again the importance of the anterior-posterior compartmental identity in proper cell-cell matching during zipping and presented new evidence for the additional importance of a left-right asymmetry.

The left-right axis is always generated in relation to the two prevailing body axes: anterior-posterior and dorso-ventral (Coutelis et al. [2014], figure 26 A, B). The dorso-ventral axis in this case refers to the polarization of the epithelium within the plane by planar cell polarity signaling (Kaltschmidt et al. [2002]). An epidermal cell can read out its position in relation to its neighbors of the same side, as they share common junctions where signaling occurs. Along the anterior-posterior axis, the segmentation cascade introduced in section 1.3, namely Engrailed, Wingless, and Hox genes enable epidermal cells to establish their position along the anterior-posterior axis. In addition, the dorso-ventral axis could be read out by the presence of different interfaces: the LE cells are surrounded by epithelial neighbors on three sides. The fourth side points towards the dorsal opening and senses the presence of amnioserosa cells (Eltsov et al. [2015]).

A summary on putative mechanisms, signaling pathways and molecular candidates for the regulation of proper cell-cell matching during zipping is shown in figure 26 C. A lot of questions remain, especially concerning the establishment and the maintenance of the left-right asymmetry. Also, the molecular basis for cell-cell recognition remains elusive. The diagram in figure 26 C revisits the introduced, starting hypothesis for the analysis of the lamellar overlap organization at the zipping site, namely the putative differential

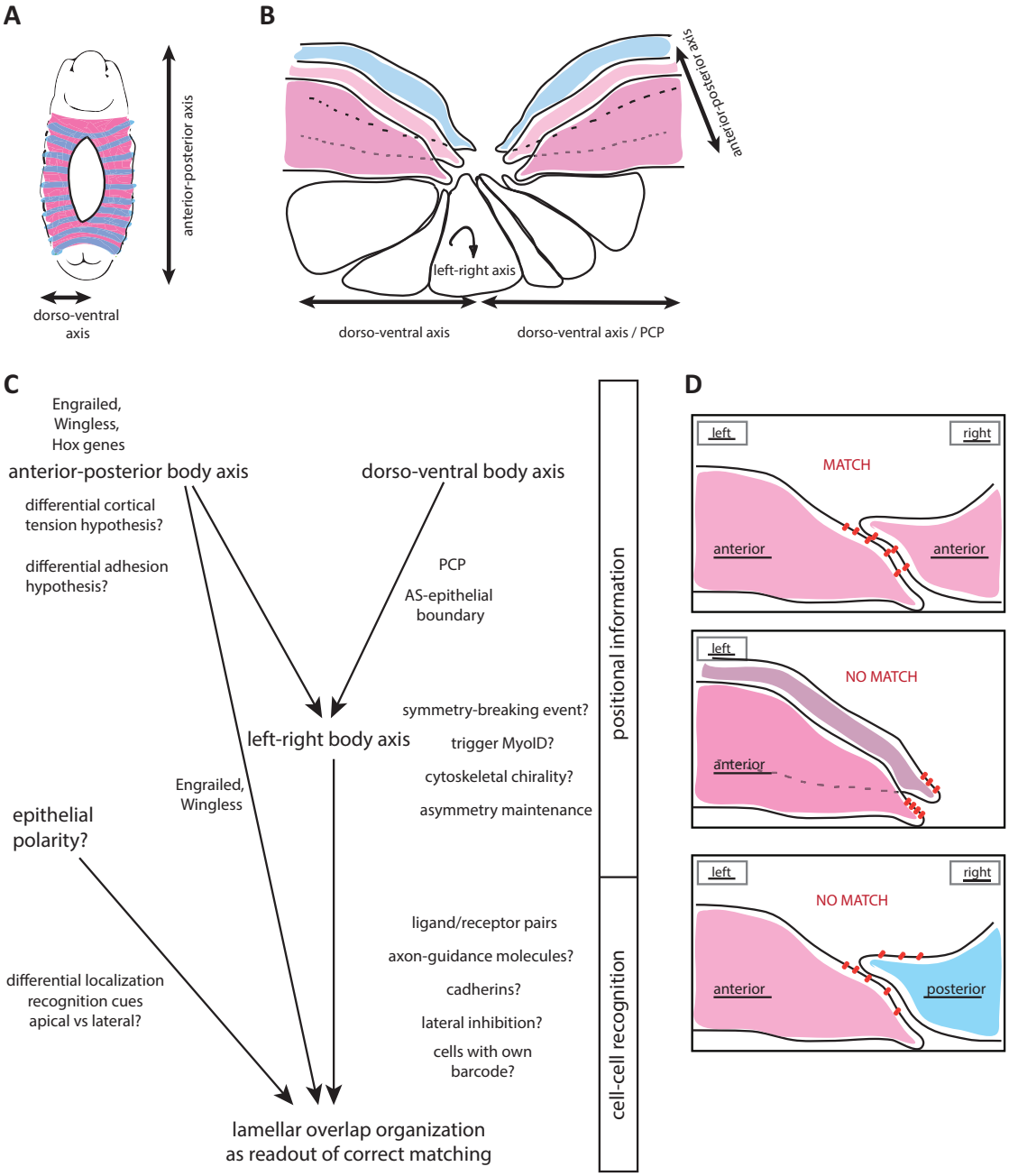

Figure 26: **Towards a mechanism for correct cell-cell recognition during zipping.** **(A)** Schematic of the anterior-posterior and dorso-ventral axis of an embryo undergoing dorsal closure. **(B)** In relation to the anterior-posterior and the dorso-ventral axis (polarity of the epidermis in the plane, PCP), the left-right axis could be established perpendicular to the two prevailing axes. **(C)** Diagram proposing possible mechanisms to establish proper matching during zipping. The numerous question marks indicate putative mechanisms, signaling pathways and molecular candidates. Positional information establishes the left-right body axis. How this is achieved on a molecular level, remains elusive. One possible candidate is MyoID, as it was shown to establish left-right asymmetry in the *Drosophila* visceral organs

and male genitalia. MyoID might trigger the establishment of the left-right axis within the epidermis. The observed lamellar overlap pattern pointed towards an importance of the anterior-posterior compartmental identity and the left-right axis for ensuring proper zipping. I speculate that the involved cell-cell recognition mechanism might involve axon guidance molecules. **(D)** Also, the introduced hypothesis of a differential localization of recognition cues on the apical or the lateral side via epithelial polarity could explain the observed lamellar overlap pattern. If both the left-right axis and the anterior-posterior identity would influence the localization of specific ligand/receptor pairs, matching of cells between the same compartment would be supported, while interactions of cells from the wrong compartment would not be stabilized. The differential localization could further account for the fact, that cells from the same side and the same compartment cannot fuse.

localization of recognition cues on the apical versus the lateral side of the protrusions. As schematically shown in figure 26 D, the differential localization of recognition entities could account for proper matching and is in concordance with the observed lamellar overlap organization in this study.

This raises of course another question: If the differential localization of recognition molecules would be proved to be true in the future, which mechanism could ensure differential ligand/receptor localization? Epithelial polarity, also termed apico-basal polarity within epidermal cells, would constitute a candidate signaling pathway. The importance of the apico-basal polarity, also during dorsal closure, is reviewed in Tepass [2012] and Flores-Benites and Knust [2016]. One could speculate that dependent on players of the apical-basal polarity, e.g. Bazooka at the AJs, ligand and receptors would be transported via cytoskeletal tracks either to the apical or the basolateral membrane, dependent on the left-right axis (MyoID as a transporter?) and the anterior-posterior identity.

In order to gain a better understanding on the observed left-right asymmetry during zipping, I suggest the analysis of certain mutants. I have discussed mechanisms for establishing positional information within a tissue and introduced a few cell-cell recognition molecules. Focussing on those candidates for subsequent experiments might shed light on a mechanism on how the left-right axis is established in relation to both the anterior-posterior and the dorso-ventral axis. This left-right axis would then act in concert with the anterior/posterior compartmental identity to instruct proper cell-cell

recognition during zipping. Another promising candidate, as discussed above, is MyoID (figure 26 C).

For the analysis of candidates, I suggest not to use the time-consuming established CLEM analysis, as it is by no means a high-throughput one. One can also not circumvent the rather low sample number by only analyzing a sub-volume of the zipping site with correlative microscopy. Although the majority of the analyzed lamellar overlaps followed a clear trend for the anterior versus the posterior compartment, a thorough analysis on the zipping stage and the neighboring cells is crucial for correct interpretation of the data.

Therefore, screening of mutants might ask for the development of yet another, faster method for analyzing more samples at a time. Super-resolution microscopy breaks the diffraction limit and might be capable of resolving the lamellar overlaps with a thickness of 200 nm to 2 μm. Several transgenic fly stocks were developed for performing super-resolution microscopy; e.g. microtubules were recorded in larva (Schnorrenberg et al. [2016]). Further, employment of the Flybow-system (Brunner lab) might circumvent axial resolution limits by labeling opposing cells with different fluorophores. An alternative method might be the establishment of expansion microscopy for the fly embryo: After chemical fixation the sample is infiltrated by an isotropically swellable polymer, resulting in expansion of the sample that could be imaged with a two- to four-fold increased resolution (Chozinski et al. [2016]).

4.7 Concluding Remarks

Evidence for the importance of the left-right axis in addition to that of the anterior-posterior compartmental identity for proper cell-cell recognition during zipping is documented here for the first time. It appeared as if a dedicated, sophisticated recognition mechanism ensured proper cell matching. A mechanism relying solely on physical constraints enacted via the actomyosin cable within LE cells could not explain the regular pattern observed within lamellar overlaps of zipping cells.

It is of major importance that zipping occurs correctly: On the one hand, a hole in the epidermis is likely to cause infections and decrease fitness. On the other hand, zipping needs to occur precisely for the sealed epidermis to maintain its proper segmentation into anterior and posterior compartments. Mutations causing mismatching defects during dorsal closure do so likewise during related tissue sealing processes that occur later during development, e.g. during thorax closure and abdominal epidermis closure (Ninov et al. [2007]). Those mismatches would also affect underlying structures, such as muscles, nerves and trachea (Furlong [2004], Krzemien et al. [2012]).

5 Results: Microtubule Organization and Morphology during Zipping

The sealing of the dorsal hole during mid embryogenesis relies on the concerted action of several forces. On the one hand, pulsed apical constrictions of AS cells bring the lateral epidermal sheets closer to the midline. On the other hand, the supracellular acto-myosin cable within LE cells provides tension to assist dorsal closure. The final force for dorsal closure, the zipping force, was only recently suggested to be a consequence of depolymerizing microtubules (Eltsov et al. [2015]), and not, as previously thought mediated by actin dynamics (Jacinto et al. [2000]). Based on large-volume electron tomography data, Eltsov and colleagues speculated that the minus-end directed microtubule motor protein Dynein, anchored to the cell cortex, produces the zipping force. They propose that cortical-tethered dynein captures MTs, initiates their depolymerization and pulls on them by its motor activity. Thus, forward movement of cellular content would be started, as the MTs could not depolymerize freely (Eltsov et al. [2015]).

In this part of the thesis, I optimize and apply the established protocol for electron tomography of plastic cross-sections of the fly embryo (see Eltsov et al. [2015]) to the distal, rear part of a LE cell. Until now, only the proximal, front of a LE cell was investigated (Eltsov et al. [2015]). I want to address how a force generated at the leading edge cell front could be transmitted to the opposite distal cell cortex to result in a shortening of the interacting leading edge cell fronts producing the zipping force. I will assess this by structural analysis of the microtubule organization, spatial distribution, and dynamics (figure 5 B).

To that means, I document the identification of optimal tomogram acquisition parameters and explain the utilization of dual-axis tomography. In order to ease segmentation, I explored the possibility of automated tracing of MTs. Using the available methods for automated segmentation did not trace MTs correctly within my acquired dataset. Consequently, I present manually segmented models, describing the MTs in the distal volume of one LE cell. I finally discuss how the observed different MT polarity integrates

into a putative model of force transmission within the mid-zipping LE cell.

5.1 Identification of optimal electron tomography acquisition parameters to study sub cellular structures in zipping leading edge cells

Electron tomography gives great insight into the sub cellular organization (McEwen and Marko [2001]). Reconstructing larger volumes by recording tomograms of serial sections holds an even greater potential of elucidating ultrastructure in a larger context (Eltsov et al. [2015]). Employment of cryo-fixation, a sophisticated freeze-substitution protocol utilizing the non-polar resin HM20, and a dedicated microscope for the acquisition of tomograms was proved to be superior for the study of ultrastructure (Vanhecke et al. [2008], Nixon et al. [2009]) compared to conventional sample preparations including chemical fixation and acquisition of 2D electron micrographs.

Details on the sample preparation, the image acquisition, the reconstruction process via the IMOD software package, and the achieved pixel size are specified in section 2.3, Material and Methods. The cryo-fixation of the fly embryo proved a difficult, critical step. In first attempts, I used the available high-pressure freezing machine Leica HPM100 (Center of Microscopy and Image Analysis, ZMB, University of Zurich) for vitrification and preservation of the sample. 2D electron micrographs revealed the presence of many fragmented MTs (data not shown). Note that the preservation achieved with the Leica HPM100 (ZMB, University of Zurich) gave satisfying results for the study of the lamellar cell overlaps during CLEM analysis (section 3.1). For the cell-cell recognition analysis during zipping, I employed a five times lower amount of heavy metals for staining to retain fluorescence in resin, and performed no additional staining of the semi-thick sections with uranyl acetate and lead citrate. Consequently, the achieved contrast and the recording of 2D electron micrographs instead of tomograms did not allow for the identification of non-ideal sample preparation. Nevertheless, for the study aimed at describing the membrane organization of the lamellar overlaps and not at resolving finest details of the ultrastructure, the achieved quality was sufficient.

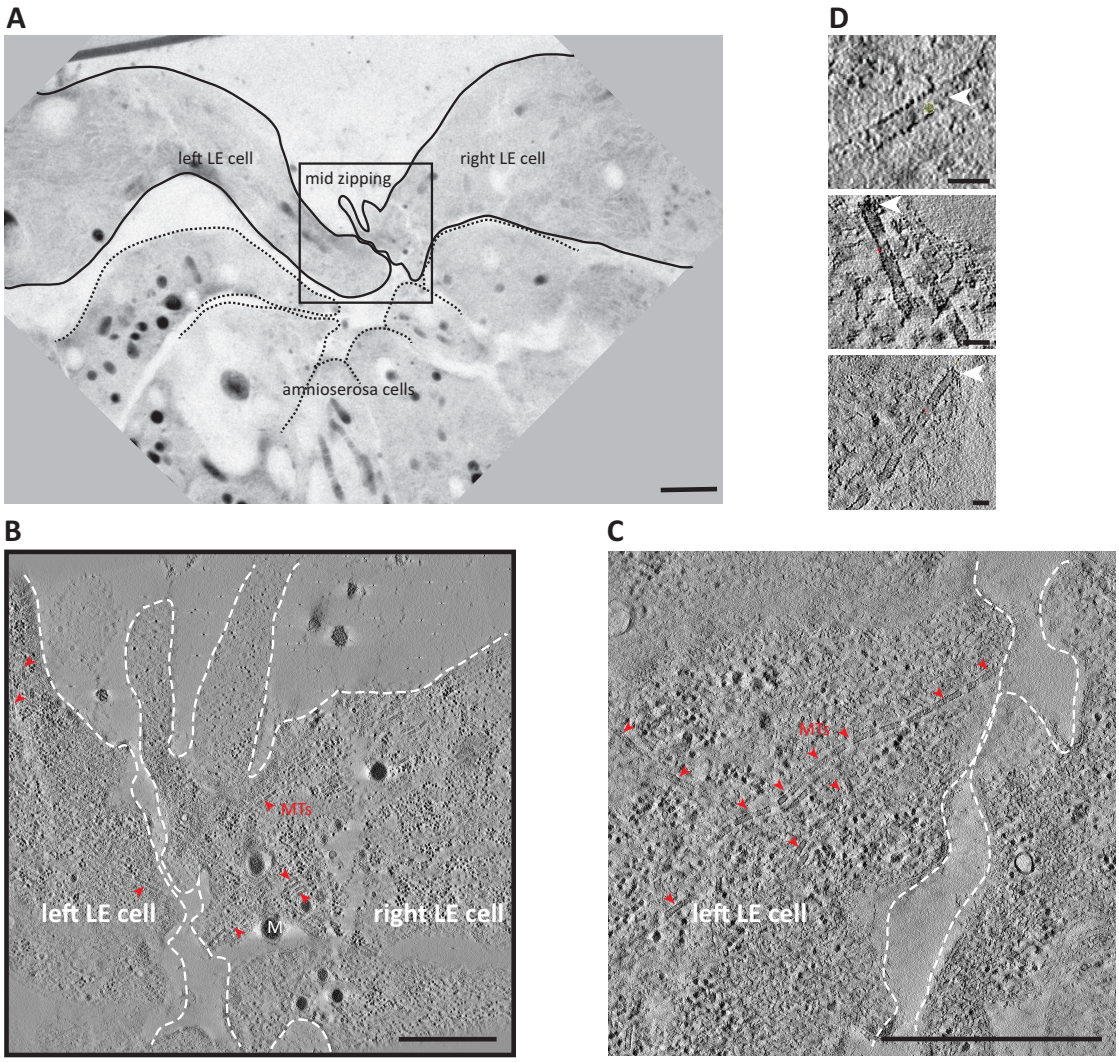

Figure 27: **Single-axis tomography of opposing LE cells during mid-zipping.** **(A)** Low-magnification electron micrograph showing the region of single-axis tomogram acquisition (black box). **(B)** Tomographic slice of the boxed region in A, exemplifying the achieved data quality in regard to sample preparation and data acquisition. Microtubules are labeled with red arrowheads. **(C)** Detail from B, showing more clearly the organization of the preserved microtubules at the zipping front. Microtubules appeared to be fragmented. **(D)** Three examples of microtubule end morphology (slicer window, IMOD). Data quality hindered exact determination of plus and minus ends, albeit the examples shown might represent a plus end (top) and minus ends (beneath) (white arrowheads). Scale bar depicts 2 μm (A), 1 μm (B, C), and 50 nm (D), respectively.

As the cryo-fixation was insufficient for the ultrastructural analysis of microtubules and their end structures, I utilized another high-pressure freezing machine: a Baltec HPM010 from the Imaging Center at the ETH Zurich. The same model machine was used by Eltsov et al. [2015] for excellent ultrastructural preservation. To familiarize with the protocol by Eltsov et al. [2015] and to find optimal imaging conditions, I recorded single-axis electron tomograms with a FEI 30 of the front, proximal part of mid-zipping LE cells.

Figure 27 documents the achieved sample preservation and image quality. I recorded seven tomograms of interacting, opposing LE cells during mid zipping (figure 27 A). A tomogram slice of the reconstructed volume of the boxed region in A is presented in figure 27 B. The close-up view in figure 27 C shows the identification of microtubules within the reconstructed volume (red arrow heads). The microtubules appeared fragmented again. Most likely, this was due to an imperfect cryo fixation, caused by the huge volume of a fly embryo (500 μm x 200 μm), outbidding the capacity of high-pressure freezing. The imperfect sample preservation is further presented in figure 27 D, where the challenging, difficult identification of MT end structures is exemplified. We concluded that the achieved sample preservation and employed imaging parameters were not sufficient for an objective investigation of the ultrastructure within this dataset.

To improve the sample preservation for the study of MTs, I tested another Baltec HPM010 machine for high-pressure freezing (see also section 2.3.1, Material and Methods, for details on the whole sample preparation and data acquisition process). Samples that I high-pressure froze with the Baltec HPM010 at the University of Frankfurt possessed satisfactory ultrastructural preservation (figure 28). I processed those cryo-fixed samples and collected serial sections of mid zipping cells. Before tomogram acquisition, the sections were first "flattened" by applying a huge electron dose (2000 - 3000 electron counts per Å^2) within the microscope, in order to heat and thus plane the sections, removing folds that would otherwise deteriorate imaging quality. A limited specimen tilting range results in missing spatial information. This missing information has the

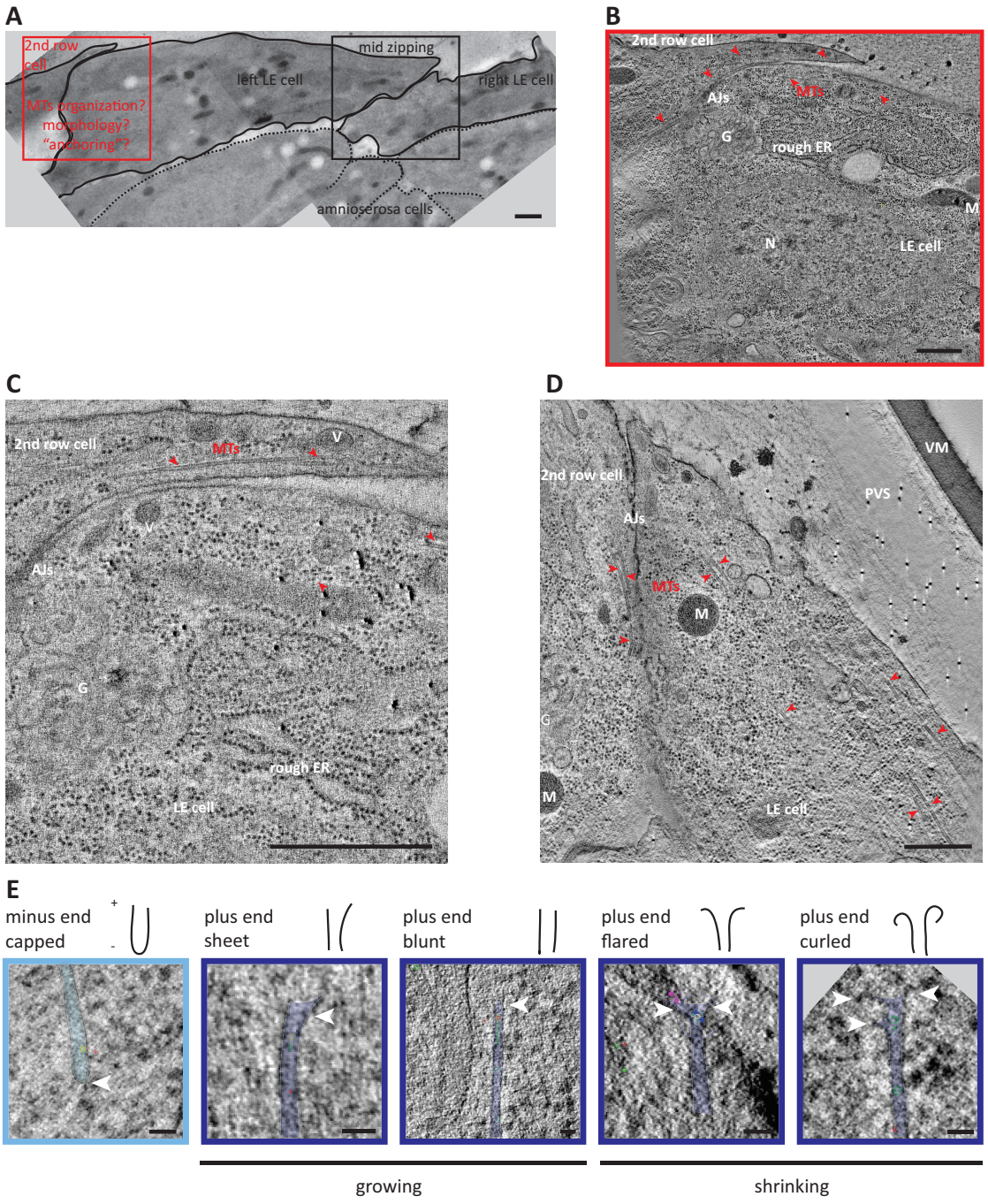

Figure 28: **Dual-axis tomography of the distal, rear part of a LE cell.**
(A) Low-magnification electron micrograph showing the two regions of interest for this study: the mid zipping interactions of opposing leading edge cells (black box), and the distal part of LE cells (red box). **(B)** Higher magnification tomographic slice of the red boxed region in A, displaying the sample quality, the sample preservation and richness in features. **(C), (D)** Detailed, tomographic slices of the 2nd row epidermal cells contacting the leading

edge cell. **(E)** Utilizing the slicer function within IMOD for determination of the microtubule end morphology and categorization into minus ends (light blue), and plus ends (dark blue). Contrary to single-axis tomography (figure 27), assessing the end structure was more straightforward, since the signal-to-noise ratio was improved. In the figure, several structures are labeled: microtubules (MTs, red arrow heads), Adherens junctions (AJs), Golgi (G), nucleus (N), rough endoplasmic reticulum (ER), mitochondrium (M), vesicle (V), vitelline membrane (VM), and perivitelline space (PVS). Scale bar depicts 1 μm (A – D), and 50 nm (E), respectively.

shape of a missing wedge in the Fourier space of reconstructions (Kováčik et al. [2014]). Therefore, I recorded dual-axis tomograms of the distal part of a LE cell (figure 28 A, red box). The recording of a tilt series from + to - 60°, turning of the sample by 90°, and the additional recording of another tilt series, reduces the missing wedge in the frequency domain of the image (Mastronarde [1997]). Thus, far greater representation of sub cellular features is achieved by missing only spatial information of the ultrastructure due to a missing pyramid, and not a missing wedge (Mastronarde [1997]). As seen in tomographic slices of reconstructed volumes of the rear LE cell (figure 28 B, C, and D), the wealth of detail was far enhanced compared to single-axis tomography (figure 27). Even more importantly, the method improved the reconstruction and assessment of microtubule end structures. Figure 28 E depicts identified minus and plus end structures, reconstructed from volumes of dual-axis tomography. Nevertheless, as discussed in the upcoming paragraphs (5.2), the achieved data quality was not comparable to the one performed by Eltsov and colleagues (compare the contrast and data quality of figure 28 E with figure 6 A in Eltsov et al. [2015]). The inferior data quality was most likely due to unachieved electron dose applied for electron tomography acquisition, rendering an optimal signal-to-noise ratio (cotrast) impossible. The long exposure time used, although not achieving the electron dose intended, likely caused image shifts and reduced resolution. Thus, I recommend using the free software "SerialEM" (Mastronarde [2005]) for upcoming studies, enabling control of the microscope in a way to achieve a high electron dose. This software was not yet installed on the used FEI F30 microscope when I recorded dual-axis electron tomography data.

5.2 Automated and manual segmentation of microtubule filaments

Studies aiming at high resolution of big volumes involve many time-consuming steps: testing parameters for optimal sample preservation; optimal conditions for image acquisition; and processing data by reconstruction and segmentation of structures of interest. In particular, this last step, if done manually, constitutes a bottle-neck on a research project.

To ease the time-consuming manual segmentation step with inherent human subjectivity, many research groups developed automated approaches for the tracing of filaments. For instance, automated tracing of a dense actin network within cryo-electron tomograms of filopodia of *Dictyostelium* was successfully achieved (Rigort et al. [2012b]). Weber and colleagues modified that automated tracing algorithm further to segment microtubules within plastic embedded *C. elegans* embryos (Weber et al. [2012]).

I tested the algorithm developed by Weber et al. [2012] for tracing microtubules within my single-tilt axis electron tomography dataset. The procedure combines automated template matching with automated tracing. During 3D template matching, the normalized cross-correlation of a template (of a certain geometry resembling that of a MT) with the tomogram is computed. Second, the centerlines of the identified tubes are traced. Several parameters need to be specified to achieve optimal segmentation results:

- *mask radius and length:* The template needs to be specified to describe the hollow MT tubes best. Weber and colleagues specified the mask radius and length from test tomograms of *C. elegans*. The longer the mask length, the more it is robust to noise. This comes at the prize of reducing the sensitivity to curved structures and MT ends. I used values for radius and length of the template that were recommended by Weber et al. [2012], see also figure 29 A.

- *Min seed correlation C_{min} and Min continuation quality S_{min}:* The template matching step assigned each voxel with a correlation and orientation value. In a second step, a line search is iteratively performed. Starting from a seed point with a correlation value higher than that of C_{min}, the algorithm tries to find a centerline representing

a MT. The line search is stopped when no candidate point within the search cone of the template scores higher than the threshold determined by S_{min}. Weber and colleagues recommended to set these parameters to a value of 0.3 for C_{min}, and 0.18 - 0.2 for S_{min} for single-axis electron tomograms (Weber et al. [2012]).

- *Search cone length and angle:* The size of the search cone and its opening angle determine which neighboring voxels are tested for being a candidate for the next point on the MT centerline. The larger the angle, the more curved structures are identified.

I tested a possible application of the automated tracing algorithm for the segmentation of microtubules on single-axis tomography data (figure 29 B - F). For this, I employed the visualization and data analysis software Amira. A test run on a graphics card usually lasted between 2-4 hours for a small sub volume of one tomogram. Binning of the data set, and preprocessing by a noise reduction median filter for enhancement of contrast was performed in some of the test runs (see figure legend 29). The parameter space was explored in its tight margins, as suggested by the authors, thus testing different values for S_{min} and the orientation of the search cone (figure 29 C - F). I also tested a tomogram from Eltsov et al. [2015] (figure 29 B).

The algorithm scored very poorly in identifying microtubules (purple arrow heads, figure 29 B - F) and highly overestimated the number of microtubules, identifying sub cellular structures obviously not representing microtubules at all. A possible explanation may come from the differing data quality and characteristics within the tomograms of the fly embryo and test tomograms of *C. elegans*. The parameters for automated tracing were initially specified for tomograms of *C. elegans* (Weber et al. [2012]). When Weber and colleagues tested their algorithm on tomograms of *Drosophila melanogaster* epithelial wing cells, the algorithm output unsatisfying results due to a high number of false positives. They claim that membranes present in the fly sample and not in the worm sample would influence the performance of the algorithm. Weber and colleagues clearly state

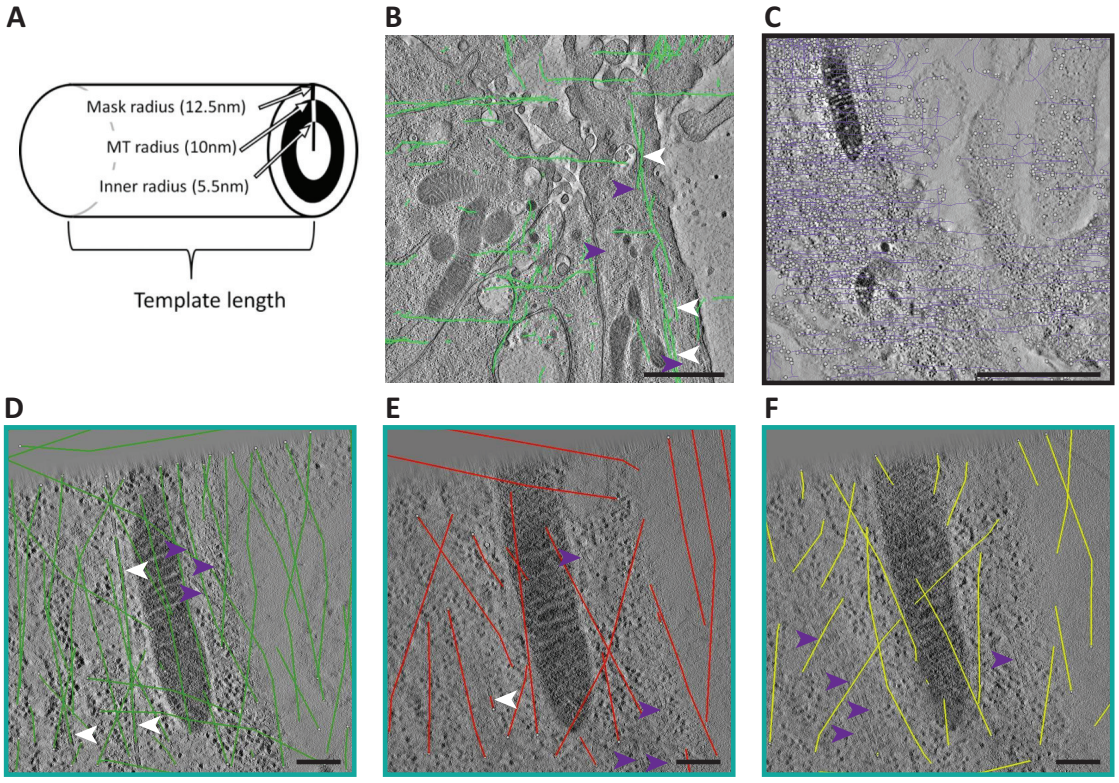

Figure 29: **Automated tracing of MTs with the visualization and data analysis software Amira.**
(A) Structure of the idealized template and its parameters (from Weber et al. [2012]). The template, imitating the microtubule's geometry, was cross-correlated with the tomogram. Identified seed points of the microtubules were further utilized to iteratively perform a line search, identifying neighboring voxels representing the microtubule. **(B) – (F)** Five different results of automated microtubule tracing of single-tilt axis tomograms, using different parameter settings (Cmin, Smin, orientation, cone size). White arrowheads indicate microtubules that were faithfully identified, purple ones point out unnoticed microtubules. **(B)** Tomogram of a leading edge cell during early zipping, from Eltsov et al. [2015]. The dataset was preprocessed with binning 1 and a noise-reducing median filter, to preserve edges and to remove noise. Cmin = 0.3, Smin = 0.19. **(C)** Tomogram from figure 27 C; the chosen parameter settings rendered identification of microtubules impossible. Only false-positives were detected by the algorithm (lilac lines). Binning 3, Cmin = 0.3, Smin = 0.2. **(D) – (F)** Automated tracing of a subvolume of the tomogram shown in C using different parameter settings. **(D)** Data unbinned, Cmin = 0.3, Smin = 0.18. **(E)** Same parameters as in D, orientation was 0.3 instead of 0.2. **(F)** Unbinned data, noise reduction median filter applied, Cmin = 0.3, Smin = 0.18. Scale bar depicts 1 μm (B, C), and 250 nm (D – F), respectively.

that the automated tracing was more susceptible to low quality data than the human eye. Also, the algorithm performed better on dual-axis tomography data (Weber et al.

[2012]). Exploring the parameter space was far beyond the scope of this work. The unsatisfying results stopped the further employment of the automated tracing algorithm for segmentation of MTs within tomograms of the fly.

Thus, although I recorded dual-axis tomograms of the fly embryo meanwhile, we decided to use the tedious manual segmentation of tomogram data and not to spend time on the cumbersome adjustment of parameters necessary for optimal performance of the automated tracing algorithm.

I segmented the dual-axis tomography dataset (quality being shown in figure 28) manually, using the IMOD software and the 3dmod segmentation toolkit (Kremer et al. [1996]). It has already proved to be a meaningful tool for segmentation of microtubules and determination of their end morphologies in fission yeast and fly embryos (Höög et al. [2007], Eltsov et al. [2015]).

Figure 30 displays such a model segmentation, the used symbols for sub cellular features are listed in A. The microtubules were manually traced within the tomogram, employing the modeling technique of open contours placing points along the length of a microtubule (figure 30 B). Either the zap window displaying a tomogram plane or the slicer window adjusting the orientation in x, y and / or z were used. This allowed for the following of a microtubule not running within the plane of the section. Also, prospective adhesion sites within the zonula adherens were segmented (white arrow heads figure 30 C) (Tepass and Hartenstein [1994]): AJs show a typical spacing of adjacent membranes of approximately 30 nm and electron-densities between the interacting membranes, most likely representing adhesion molecules.

Sequence 30 D shows the sequential addition of manually segmented features onto the tomographic data: cell membranes (i), microtubules (ii, iii), microtubule minus and plus ends (iv), indeterminable ends (v), and microtubules leaving the section (vi).

Many MTs extended over more than one tomogram (300 nm thickness), as they ran slightly out of the xy-plane. However, due to shearing and deformation of sections in

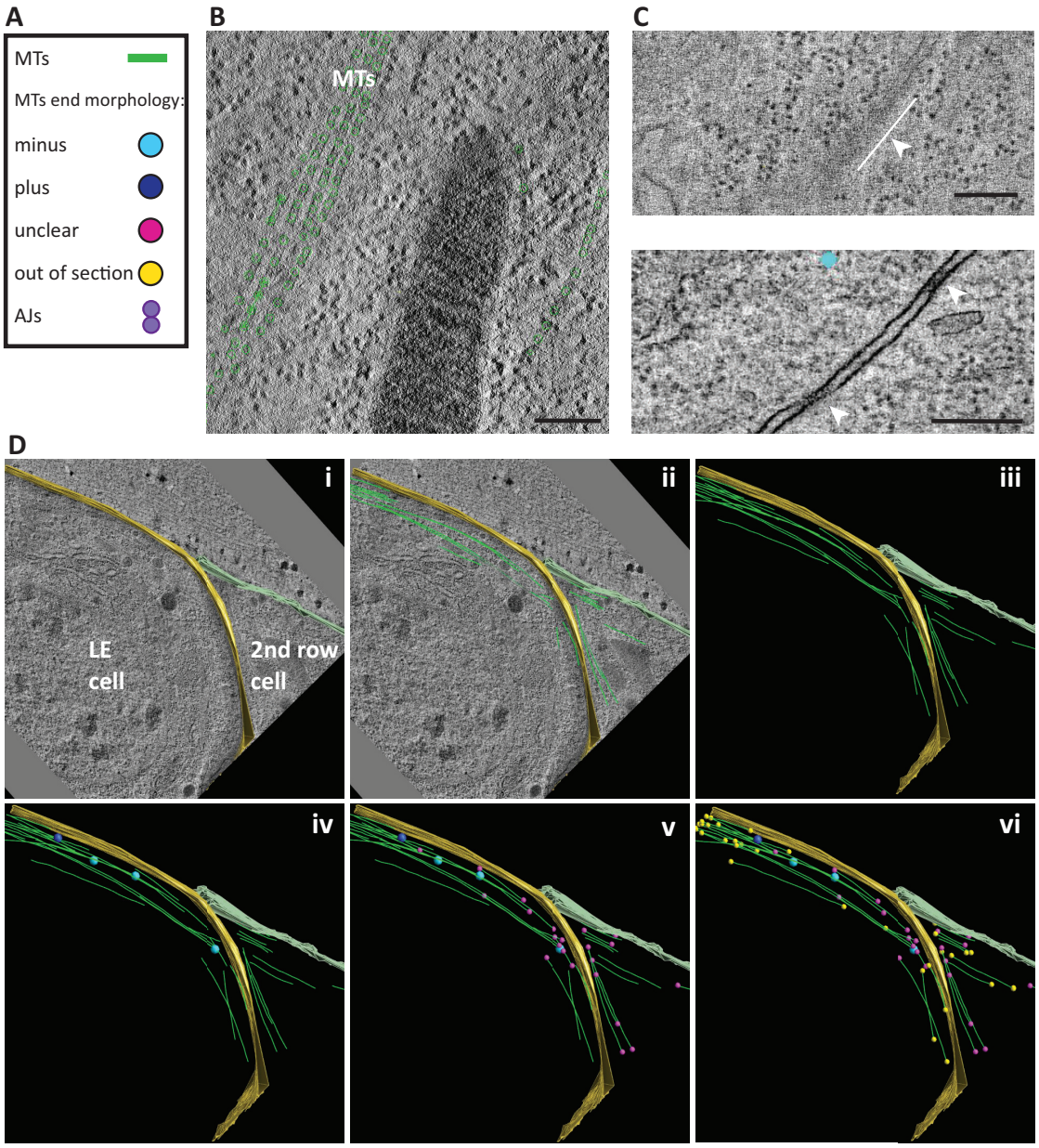

Figure 30: **Manual tracing of MTs using the IMOD software.**
(A) Overview of symbols representing segmented features. **(B)** Tomographic slice with manually traced microtubules (green points). **(C)** Tomographic slices of junctions (white arrowheads). Apical junctions with inter membrane electron densities (most likely adhesion molecules), representing prospective adherens junctions, forming the zonula adherens (Tepass and Hartenstein [1994]). **(D)** Sequence of manual segmentation of plasma membrane **(i)**, microtubules **(ii), (iii)**, microtubule plus and minus ends **(iv)**, microtubules with unclear end morphology **(v)**, and microtubules leaving the tomogram section **(vi)**. Scale bar depicts 250 nm (B, C).

sectioning and data acquisition, I could not join microtubules across tomograms. I assessed the end morphology of this subpopulation of microtubules then in an adjacent, consecutive section. More severe were the rather low contrast and image quality, impairing an identification of a majority of microtubule ends. This complicated a statistical meaningful analysis and conclusion.

5.3 The microtubule organization, dynamics and anchoring appears different in the distal part of a leading edge cell during mid zipping

I imaged 9 serial sections in total, covering approximately 3 x 3 μm of the rear part of a left and a right leading edge cell. Those 18 tomograms were manually segmented, identifying microtubule organization and end morphologies.

Representative models of the investigated volume of the rear part of a leading edge cell are displayed in figure 31. They depict the presence of apically bundled microtubules. The occasional identification of microtubule end morphology revealed both minus and plus ends next to each other within those bundles, pointing towards an antiparallel arrangement.

Very interestingly, both plus and minus ends were found in a similar number close to the distal cell cortex, facing the 2nd row epidermal cell. The data quality allowed in some cases for the assignment of shrinking or growing classes (see also figure 28 E), but most of the time an unambiguous identification was impossible. However, the minus ends were clearly distinguishable from plus ends by their capped morpholgy (Höög et al. [2007]).

A second population of microtubules was especially apparent in figure 28 A and B, running along the apico-basal cell axis close the the distal cortex.

A quantification, summarizing the findings of those 18 tomograms, is depicted in table 2. 183 microtubule ends within those sections were scrutinized, revealing in total 31 minus and 21 plus ends in close proximity to the distal cell cortex. More than two thirds of the end structures could not be determined.

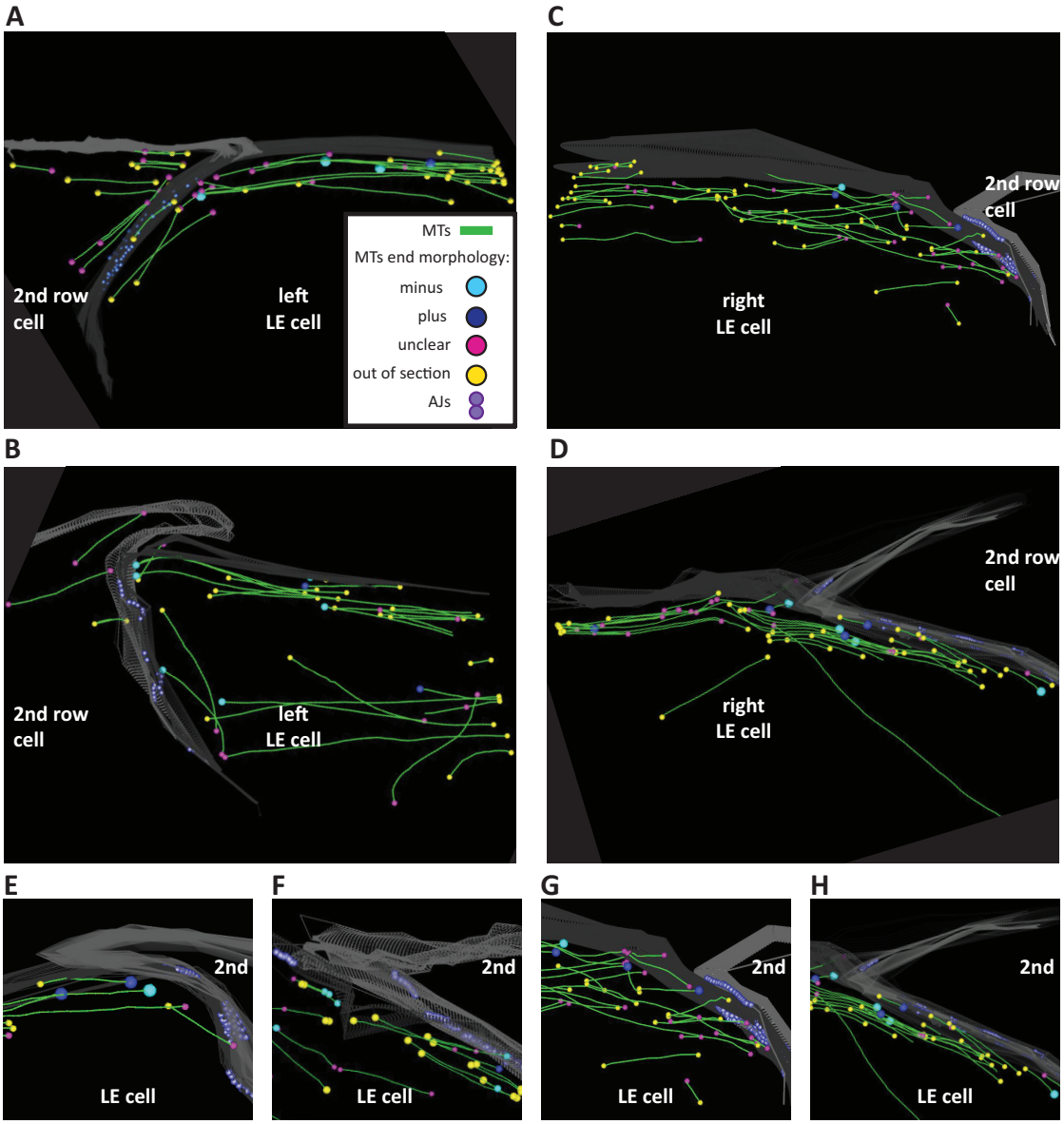

Figure 31: **Several manually segmented models of MT organization, morphology, and proximity to the cell cortex in the distal part of LE cells.**

(A) – (D) Four chosen example models, displaying the bundled, apical organization of microtubules within the leading edge cells. The bundles are antiparallely organized. A few microtubules ran perpendicular to those apical bundles along the very rear part of the leading edge cells, close to the cell cortex (A, B). Both plus (dark blue) and minus ends (light blue) of microtubules were found close to the cell distal cortex. Most microtubules left the section (yellow) and a high number of microtubules was not to be categorized faithfully (pink). **(E) – (H)** Details of more models, revealing the presence of both plus and minus ends at the distal cell cortex at roughly equal numbers.

section	minus end		plus end		indeterminable		leaving	
	left	right						
1	3	0	1	1	10	2	13	8
2	1	0	2	0	4	4	8	4
3	6	0	1	0	5	9	11	13
4	1	6	0	2	8	5	10	13
5	1	1	1	3	6	14	6	14
6	0	0	1	0	8	11	6	14
7	4	1	2	0	6	9	13	10
8	1	1	0	0	7	8	12	5
9	1	4	3	4	5	10	18	15
TOTAL	**31**		**21**		**131**		**193**	

Table 2: **Listing the occurrence of a certain microtubule end structure in the investigated volume of the distal, rear part of a LE cell.**

6 Discussion: Microtubule Organization and Morphology during Zipping

6.1 Electron tomography for the structural analysis of microtubule organization and dynamics during mid zipping

Electron tomography has proved a powerful tool to elucidate the MT organization and dynamics at great resolution (Höög et al. [2007], Eltsov et al. [2015]). Insights into the ultrastructure reveal details that cannot be visualized with light microscopic resolution, that assist in forming our understanding of biological processes at the sub cellular, molecular level.

In this part of the thesis, I employed electron tomography to study microtubules in LE cells during mid zipping. The acquisition of dual-axis electron tomograms revealed more ultrastructural details as single-axis electron tomography (see figures 27 and 28). As expected, the reduced missing wedge (Mastronarde [1997]) resulted in improved assessment of sub cellular details, such as the microtubule end morphology (28 E). Nevertheless, upcoming tomogram acquisitions should be performed under more optimal conditions. By using SerialEM for controlling the electron microscope, the electron dose and thus the achieved signal-to-noise ratio can be far enhanced. This would augment identification of plus and minus end MT structures and further categorization into growing or shrinking microtubules. Within this study, only one third of the microtubule end structures were assessed (table 2).

In this work, I tested an automated segmentation algorithm to assist in the segmentation of MTs (Weber et al. [2012]). I did not explore the parameter space to its full extent. Those automated algorithms are a robust and helpful method when optimized to a specific dataset. The adjustment of the parameters might prove difficult and time-consuming, though. For my dataset of single-axis electron tomography data, the algorithm performed unsatisfactorily (figure 29 C - F). Hardly any microtubules were identified correctly, whereas numerous false-positive microtubules were segmented by the algorithm. The same insufficient result was recapitulated for the dataset by Eltsov

et al. [2015], that comprised excellent ultrastructural preservation (figure 29 B). This was a strong indication that a major effort was needed to implement the automated segmentation algorithm to assist in segmenting MTs in my dataset. Therefore, I chose to perform the segmentation manually instead (figure 30). The general application and success of automated tracing algorithms, including template matching or pixel and object classification approaches, has been shown in numerous publications (Rigort et al. [2012c], Kreshuk et al. [2011], Maco et al. [2014], Kreshuk et al. [2014]). As is discussed in greater detail in section 4.1, automated segmentation algorithms are key to tackle the new arising bottle-neck in ultrastructural analysis of large volumes of interest, such as structural analysis and inferred functional understanding of the fly brain (Takemura et al. [2013]).

6.2 Both plus and minus ended MTs are present at the distal apical cortex of mid zipping LE cells

Microtubules exhibit various functions; e.g. the transport of cargo, directing growth and migration, and constituting the mitotic and meiotic spindle. The asymmetric microtubule network within the fertilized *Drosophila* egg serves as tracks for the biased transport of *oskar* mRNA to the posterior pole of the cell by kinesin motor proteins (Zimyanin et al. [2008]). Microtubules are fundamental in axonal growth cones for the exploration of the environment for guidance cues. Most importantly, the kinetochore microtubules ensure the correct segregation of chromosomes during mitosis. Microtubules have been also implied to act during zipping. Drug-injections affecting MT stability, as well as depletion of MTs by a severing protein, resulted in zipping defects (Jankovics and Brunner [2006], Adamczyk [2016]). Large-volume electron tomography data revealed the presence of more shrinking than growing MTs in the vicinity of adhesion structures in the proximal part of mid zipping LE cells (Eltsov et al. [2015]). The special spatial organization and dynamics of microtubules was reminiscent of spindle positioning in *C. elegans* (Nguyen-Ngoc et al. [2007]) and human cells (Kotak et al. [2012], Yi et al.

[2013]). The mitotic spindle is positioned by dynein-microtubule interactions. Dynein is anchored via a ternary complex to the cell cortex (Kotak et al. [2012]) and captures incoming plus-end microtubules. By the dynein minus-end directed motor activity and initiation of depolymerization of MTs, a pulling force is generated. Eltsov and colleagues speculated on dynein functioning during zipping to pull the opposing epithelial sheets together (Eltsov et al. [2015]). They proposed that the force produced by dynein could not solely be used to move sub cellular components, but also to shape cells and tissues during morphogenesis. *In vitro* studies estimated the pulling force generation capacity of dynein to several pN (Laan et al. [2012]). Having indications for the contributors to the zipping force, another question remained. It concerns possible force transmission mechanisms from the front, proximal part of a LE cell to the back, distal part of a LE cell. How can a force applied in the front result in the overall forward-movement of the whole LE cell and the whole epidermal tissue?

Here, I documented the microtubule organization, polarity and end morphology in the distal part of a leading edge cell (figure 32 III). In contrast to the proximal part of the leading edge cell (figure 32 I), where more plus end microtubules undergoing depolymerization are present (Eltsov et al. [2015]), I found both plus and minus ends to a similar extent in the distal part (table 2). I identified two populations of microtubules: apical bundles of antiparallel microtubules (in agreement with light microscopy data from Jankovics and Brunner [2006]) and several microtubules running along the apico-basal (epithelial polarity) axis (figure 31).

The close proximity of depolymerizing microtubules to the proximal cortex led to the hypothesis of a dynein anchor generating a zipping force (Eltsov et al. [2015]). Based on my tomogram data of the distal part of the leading edge cell, I could not recognize the same organization. As both plus and minus end microtubules were apically present, dynein might not anchor MTs at the distal cortex, or alternatively might only anchor a subset, the plus ended ones.

Before dorsal closure progression, MTs transiently reorganize from the characteristic epithelial apico-basal distribution to a proximo-distal one at the apical side of epithelial

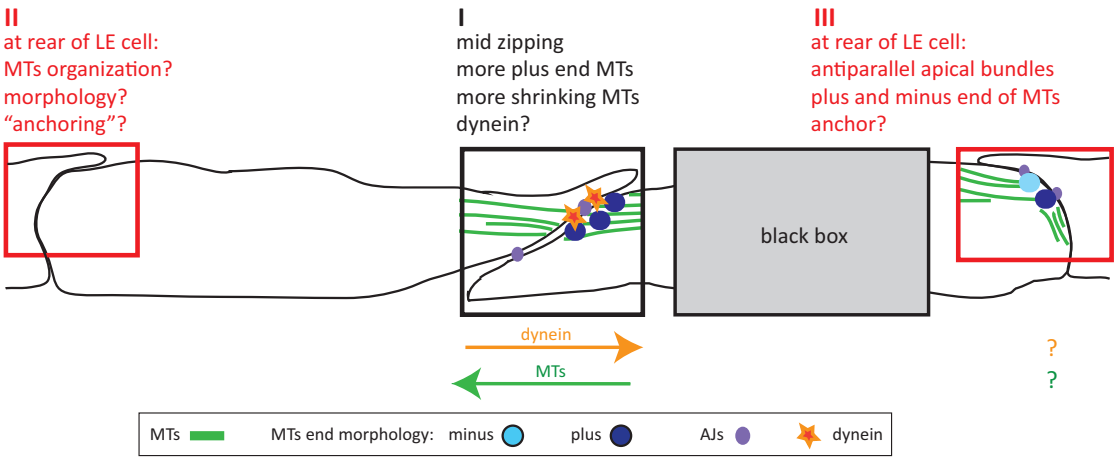

Figure 32: **Schematic representation of the microtubule organization within leading edge cells during mid-zipping.**
The study by Eltsov and colleagues (Eltsov et al. [2015]) proposed a force-generating mechanism by shrinking microtubules anchored (via dynein?) to the cell cortex, the zipping force **(I)**. It remained unclear, how a zipping force at the front of opposing leading edge cells is transmitted throughout the cell, resulting in net forward movement **(II)**. Investigation of the distal part of a leading edge cell revealed apical antiparallel microtubule bundles as seen in I, but observed an equal amount of both plus and minus ends close to the cell cortex **(III)**. This suggests a different mechanism of anchoring of microtubules to the cortex compared to I. The force transmission mechanism remains uncertain.

cells (Jankovics and Brunner [2006]). Within my tomographic dataset of the distal part of LE cells, I identified a second subset of MTs that ran along the apico-basal axis close to the distal lateral cortex. Those MTs might represent a remnant. They might fulfill alternative functions than force generation, such as cargo transport or mechanical stabilization of the cell.

6.3 Towards a zipping force generation and transmission model

The low number of scrutinized microtubules and identified microtubule ends impaired the drawing of conclusions on a possible mechanism for force transmission. Since several mechanisms are conceivable, a more thorough analysis of more cells during zipping is highly recommendable.

The association of MTs to the cortex would be a plausible mechanism for force transmis-

sion throughout the cell. A pulling force that is applied in the front could be transmitted through the MT bundles to the distal part of the cell. The attachment of MTs to the distal cell cortex could in theory promote the forward movement of the distal cell cortex and thus the whole cell. LE cells are connected via AJs to their neighboring cells. The forward movement of one cell might influence and promote the forward movement of the neighbors in a collective manner. So far, electron tomography data on the central apical part of LE cells is missing due to the small field of view during image acquisition. Studying the cellular region within that black box (figure 32) might give further indications for a force transmission mechanism. The microtubules might be anchored to the apical cortex throughout the cell to assist in the forward pulling of the distal part.

Alternatively or in parallel to anchoring of MTs for force transmission, MT sliding might be important. Microtubule motors can cross-link and slide antiparallel MTs in respect to each other (Sharp et al. [2000], Tanenbaum et al. [2013], Bachmann and Straube [2015]). It is conceivable that those motors would be regulated in a way to shift the antiparallel microtubules such, that an overall shrinkage of the bundle occurred.

In principle, another zipping force generation mechanism is conceivable. Cytoplasmic pulling on MTs by dynein. Contrary to the first discussed mechanism, dynein would not be tethered to the membrane. Dynein exerts force on membranous organelles by moving them along microtubule tracks. This viscous drag would also generate an opposing force towards the plus end of a MT (reviewed in McNally [2013]). In the zipping system, this might produce additional forces contributing to the forward movement of the LE cell to seal the dorsal gap. Kimura and colleagues described cytoplasmic pulling during pronuclear centration in *C. elegans* prior to the first mitotic division (Kimura and Kimura [2011]). They claim that both cortical and cytoplasmic pulling of dynein would contribute equally to centrosome positioning. This observation emphasizes the force generation capacity of cytoplasmic dynein pulling.

In order to further revisit the MT organization and dynamics throughout a whole mid zipping LE cell, more electron tomography data is needed. Additionally, it might be interesting to address further questions, such as how a force produced in the proximal

part of a LE cell exerts a contrary force on the cell cortex and how it is balanced. Or, how does substrate adhesion of a LE cell to underlying extracellular-matrix influence this process?

Super-resolution microscopy and bleaching experiments probing for the dynamics of MTs might also prove vital for the study of the force generation and transmission process. Light microscopic methods lack the superior ultrastructural resolution electron tomography can provide. Nevertheless, light microscopy facilitates live imaging of a high number of samples, adding key understanding to the biological process.

6.4 Concluding Remarks

Further studies should not only focus on the microtubules, but also on the suggested other contributor to force generation - dynein. A lab colleague, Magdalene Adamczyk, studied the importance of dynein during zipping. By specifically inhibiting dynein with drug-injections of ciliobrevinD, she observed a zipping arrest or delay (Adamczyk [2016]). Genetic depletion of dynein to study its function during zipping proved problematic as dynein is maternally distributed. The maternally deposited dynein mRNA and protein could rescue possible effects caused by dynein depletion (Adamczyk [2016]). Only later during development, mutant larva died. Therefore, Magdalene Adamczyk generated transgenic flies where dynein can be knocked-down acutely using the deGradFP-system (Caussinus et al. [2013], Adamczyk [2016]). The study of these transgenic flies will give meaningful insight into the role of dynein during force generation. If those mutants show a phenotype during zipping, the detailed analysis of MT organization might give further insight into the force generation and transmission mechanism. Further questions to address in dynein mutants are, whether MTs display an altered organization or whether they would still be present in close proximity to the cortex and adhesion structures? Are there still more depolymerizing MTs in the proximal part of LE cells? And how are MTs organized in the distal part of LE cells?

Answers to these questions will assist in establishing the action of microtubules and

possibly dynein in the process of force generation during zipping. Although dorsal closure and forces contributing to dorsal closure have been studied for a few decades, new studies and technologies will give further insight into the complex cell biological processes underlying this fusion event.

7 Results: Establishing Sample Preparation for Cryo-ET of Fly Embryos

The superiority of cryogenic structural analysis is introduced in section (1.7.3). Preserving the sample in a frozen, hydrated environment and in a near-native state, opens a window for studying macromolecular assemblies and the reconstruction of three-dimensional ultrastructures, down to the nano-scale conformation of proteins.

Naturally, the sample preparation differs for the structural analysis of purified proteins and the analysis of more complex, multicellular organisms. Thin structures as the mentioned purified protein complexes or also cells grown on EM grids can readily be vitrified by plunge-freezing. Flat regions at the periphery of attached cells where the thickness does not exceed 1000 nm are amenable to imaging with the electron beam without more ado (Lučič et al. [2013]; Mader et al. [2010]). Within multicellular organisms the side of interest is often covered by other cellular layers and hidden. These organisms exceed the maximum thickness for imaging with electrons by far, impeding structural studies of complex organisms. Thus, analysis of specific sites within the organism need an extra level of sample preparation. The bulk specimen is vitrified by means of high-pressure freezing. Further, thinning methods were developed, allowing for the generation of samples being amenable to EM analysis (Lučič et al. [2013]; Mader et al. [2010]).

In this part of the thesis, I summarize my attempts to establish methods for the generation of thin specimens of the *Drosophila melanogaster* embryo for cryo-electron tomographic analysis. I present the application of cryo-electron tomography to re-vitrified frozen sections of fly embryos. Further, I describe the steps developed toward the application of cryo-focused-ion beam milling as an alternative thinning method. I discuss why this method requires further development for the application in fly embryos, whereas it has proved to work in *C. elegans*.

7.1 Cryo-ET of re-vitrified frozen sections as a tool for better structural understanding of morphogenetic processes in *Drosophila melanogaster*

Cryo-electron microscopy of vitrified sections (CEMOVIS) was reintroduced for the study of macromolecular assemblies of various tissues (Hsieh et al. [2002], Al-Amoudi et al. [2004]). The whole work procedure is performed at cryogenic temperates, starting with cryo fixation via high-pressure freezing and finishing with cryo electron microscopy. The sectioning remains a skillful, demanding process, nevertheless the thin sections give great structural insight. The cryosections suffer from several artifacts, though: The cause of knife marks, chatter, crevasses, compression, and breaks are described by Al-Amoudi et al. [2005], and Bouchet-Marquis and Hoenger [2011]. They further discuss how to alleviate such artifacts, mainly by using very thin sections of 50 nm and a rather fast sectioning speed.

Since those sections represent only a small volume due to their thinness, another approach was established: that of cryo-electron tomography of vitrified frozen sections (cryo-ET of VFSs, Sabanay et al. [1991]). The method is based on the procedure developed by Tokuyasu (Tokuyasu [1973]), involving the chemical fixation of a tissue, sucrose infiltration, freezing, ultrasectioning, rehydration, revitrification of sections and cryo-electron microscopy. Bokstad and colleagues applied the cryo-ET of re-VFSs approach to the study of adhesion structures within gizzard smooth muscles and mouse epithelia (Bokstad et al. [2012]). They found less sectioning artifacts within their cryo sections of 300 – 400 nm thickness. This most likely was accounted for by the rehydration of the sections. Further, they claimed that chemical fixation and sucrose infiltration protected ultrastructure optimally. Since the sections were rehydrated at room temperature, one could include the addition of fiducial gold markers, enabling the tomogram reconstruction of a rather thick volume of up to 400 nm. Addition of fiducials at cryogenic temperatures was described a few years ago (Gruska et al. [2008] and modified by Harapin et al. [2015]), abrogating the limit on investigated thickness for CEMOVIS-

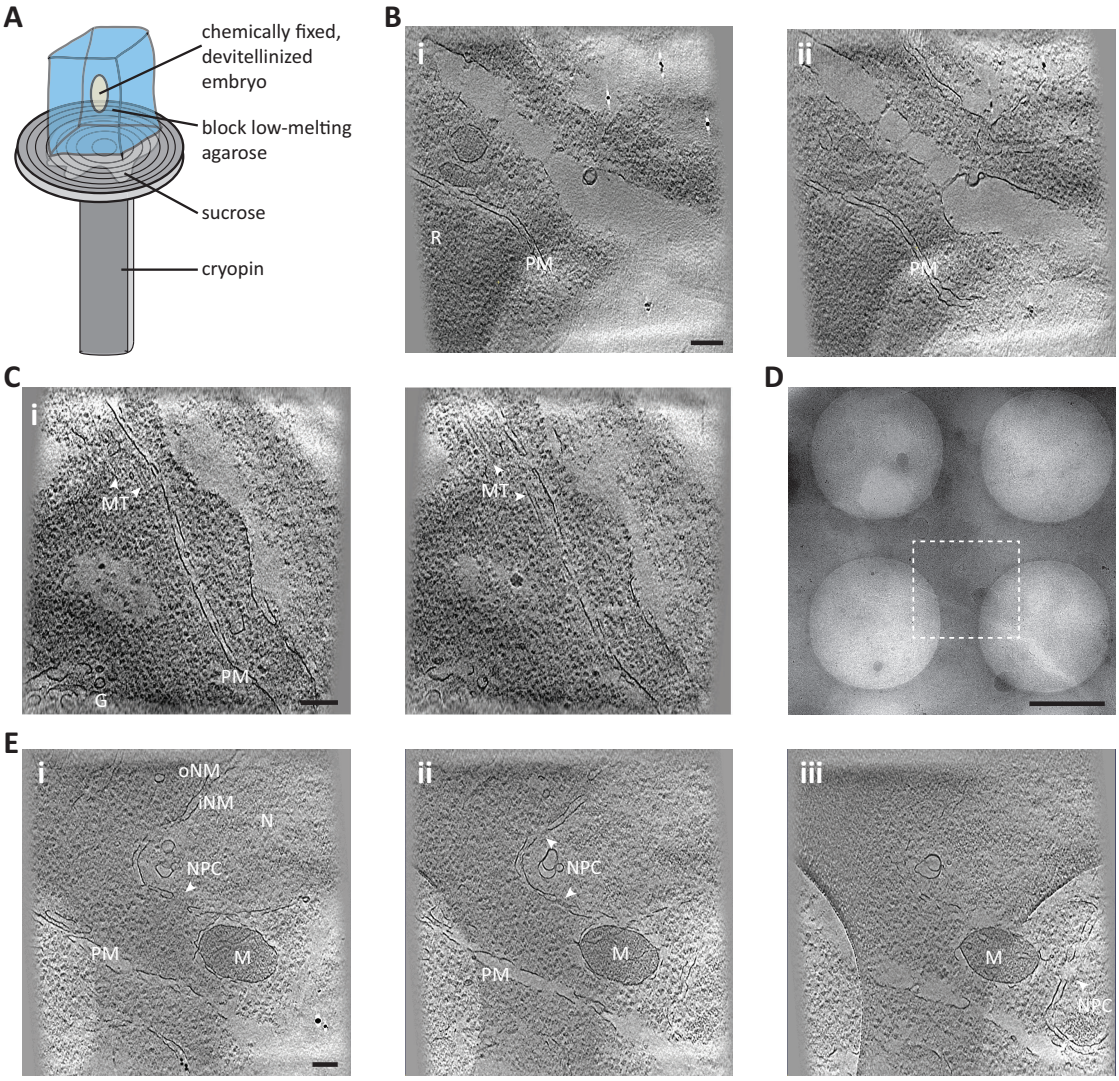

Figure 33: **Cryo-electron tomography of re-vitrified frozen sections of *Drosophila melanogaster* embryos.**

(A) Schematic overview of the attachment of a chemically fixed, devitellinized embryo (embedded in low-melting agarose) with sucrose onto a cryopin. The assembly was quickly frozen at –120 °C in a cryochamber. **(B) – (E)** Re-vitrified sections from fly embryos analyzed by cryo-ET at –17 μm defocus. **(B)** Tomographic slices of 4 nm thickness showing features of the cytoplasm (R for ribosomes) and the plasma membrane (PM). Scale bar depicts 100 nm. **(C)** Tomographic slices, 4 nm thickness, through a reconstructed volume of cytoplasm featuring microtubules (MT) and Golgi (G). Scale bar depicts 200 nm. **(D)** A lower magnification cryo-EM image of a hydrated section, 300 nm in thickness, showing a typical region used for data acquisition. Scale bar depicts 1 μm. **(E)** Successive tomographic slices (4 nm in thickness) of the boxed region shown in D, of a reconstructed volume revealing the nucleus (N), the inner and outer nuclear membrane (iNM, oNM), nuclear pore complexes (NPC), and mitochondria (M). Scale bar depicts 200 nm.

sections above 100 nm without loss of high-resolution information.

I applied cryo-ET of re-VFSs to study the fly embryo. Perturbing the ultrastructure less by circumventing detrimental steps such as heavy metal staining and dehydration most likely will yield in a better representation of the ultrastructure. This comes at a price, namely the reduced contrast and the limited field of view. Also, serial sectioning is most often unsuccessful.

The results are presented in figure 33. Panel A illustrates the embedding of the dechorionated, chemically fixed, devitellinized embryo into a block of low-melting agarose. By orienting that block and glueing it with sucrose onto a cryopin, the collection of cross-sections was enabled. The quality of sample preservation and the identification of sub cellular features such as membranes, microtubules, and nuclear pore complexes are depicted in panels C – E. Although the sections suffer from artifacts such as breaks and folds, the method is applicable to the study of the ultrastructure of the fly embryo.

Another drawback of the cryo-ET of re-VFSs approach is the challenge to identify a specific site of interest within the embryo. The intention in the beginning of this project was to study the cytoskeleton at the zipping site. The demanding sectioning process, the cumbersome section handling, the impossibility of serial section collection and the very complicated finding of the region of interest rendered this impossible, though.

We intended to circumvent the mentioned problems by applying another promising method that was being established in the lab - namely the application of cryo-focussed ion beam milling as an alternative thinning method prior to cryo-electron tomography.

7.2 Establishing cryo-focused ion beam milling as a sample preparation tool for cryo-ET

Cryo-FIB/SEM was already employed for the structural analysis of bacteria, and eukaryotic cells (Marko et al. [2007], Rigort et al. [2010], Rigort et al. [2012a], Wang et al. [2012]). A novel version was further developed in the Medalia lab for the study of *C.*

elegans embryos and adult worms. Thus, the focused-ion beam approach is no longer limited to the ablation of biological material within single cell organisms, but is applicable to multicellular organisms (Harapin et al. [2015]).

By sublimating biological material with a focused Gallium-ion beam, one prepares a thin specimen, a so called lamella, usable for the acquisition of cryo-electron tomograms. This alternative thinning approach is performed under constant cryogenic conditions, thus avoiding detrimental sample preparation steps such as chemical fixation, dehydration and heavy metal staining. One "opens a window" into the interior of a cell, thus the study of macromolecular structures and even supramolecular assemblies *in situ* becomes possible, retaining the cellular context. Further, the cryo-FIB approach allows to circumvent artifacts associated with cryo-ultramicrotomy, mainly compression (Marko et al. [2007], Harapin et al. [2015]).

Several milestones were accomplished by Harapin and colleagues: 2-Methylpentane was introduced as freezing media. Being liquid at –150 °C, it enabled retrieval of the vitrified sample after high-pressure freezing without physically disturbing it. 2-Methylpentane was further completely sublimed at –150 °C under high vacuum conditions, making each part of the sample accessible for cryo-thinning. Also, an adjusted, custom-built cryo-holder was built, enabling the accessibility of the sample all over the grid, the milling of the sample in plane with the focused-ion beam, and the transfer of the grid into a standard holder for cryo-ET. Further, they developed a procedure to apply fiducial gold markers under cryogenic conditions onto the lamella, prior to cryo-ET. Thus, the reconstruction of the nuclear lamina in adult worms within rather thick lamellae became available (Harapin et al. [2015]).

We intended to use this method, employing a dual beam of cryo-FIB milling and additional supervision and targeting of the process via scanning electron microscopy, for the study of dorsal closure in fly embryos (35 A).

The established conditions for cryo fixation of the fly embryos is depicted in figure 34 B. Several different "glues" for the attachment of embryos to the EM grid were

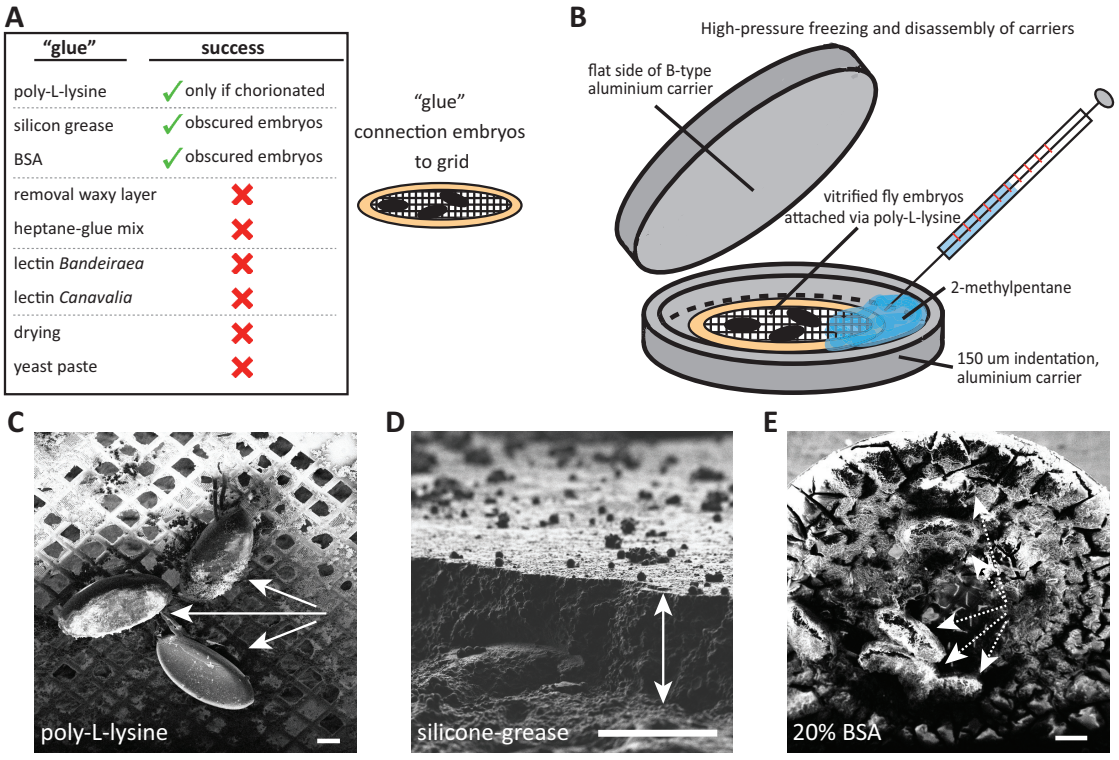

Figure 34: **Establishing high-pressure freezing of *Drosophila melanogaster* embryos prior to cryo-FIB/SEM milling procedures.**
(A) Several different "glues" were tested to attach the fly embryos to an EM-grid. **(B)** Schematic of the high-pressure freezing setup: Attached embryos on an EM-grid were transferred into the well of a 150 μm deep aluminium-platelet carrier and covered with 2-methylpentane. The flat side of a B-type aluminium carrier closed the assembly. **(C)** SEM overview image. 2-methylpentane was successfully sublimated at -150 °C under vacuum conditions prior to cryo-FIB/SEM processing. Only poly-L-lysine resulted in satisfying attachment of chorionated embryos, without obscuring biology. Scale bar depicts 100 μm. **(D)** FIB side view. Silicone-grease (scale bar depicts 100 μm) and **(E)** BSA masked the embryos (SEM overview image, scale bar 200 μm); determination of the area for milling was rendered impossible.

tested, as listed in panel A and described in 2.5. Neither the lectins from *Bandeiraea* or *Canavalia*, nor alteration of the vitelline membrane with permeabilization solvents, with a heptane-glue mix, with drying of the embryos, nor glueing with a paste of suspended yeast cells accomplished permanent attachment of the embryos onto the EM-grid. Only poly-L-lysine, 20 % BSA or impregnation with silicone grease attached the embryos permanently, withstanding disassembly of the sandwich after high-pressure freezing and

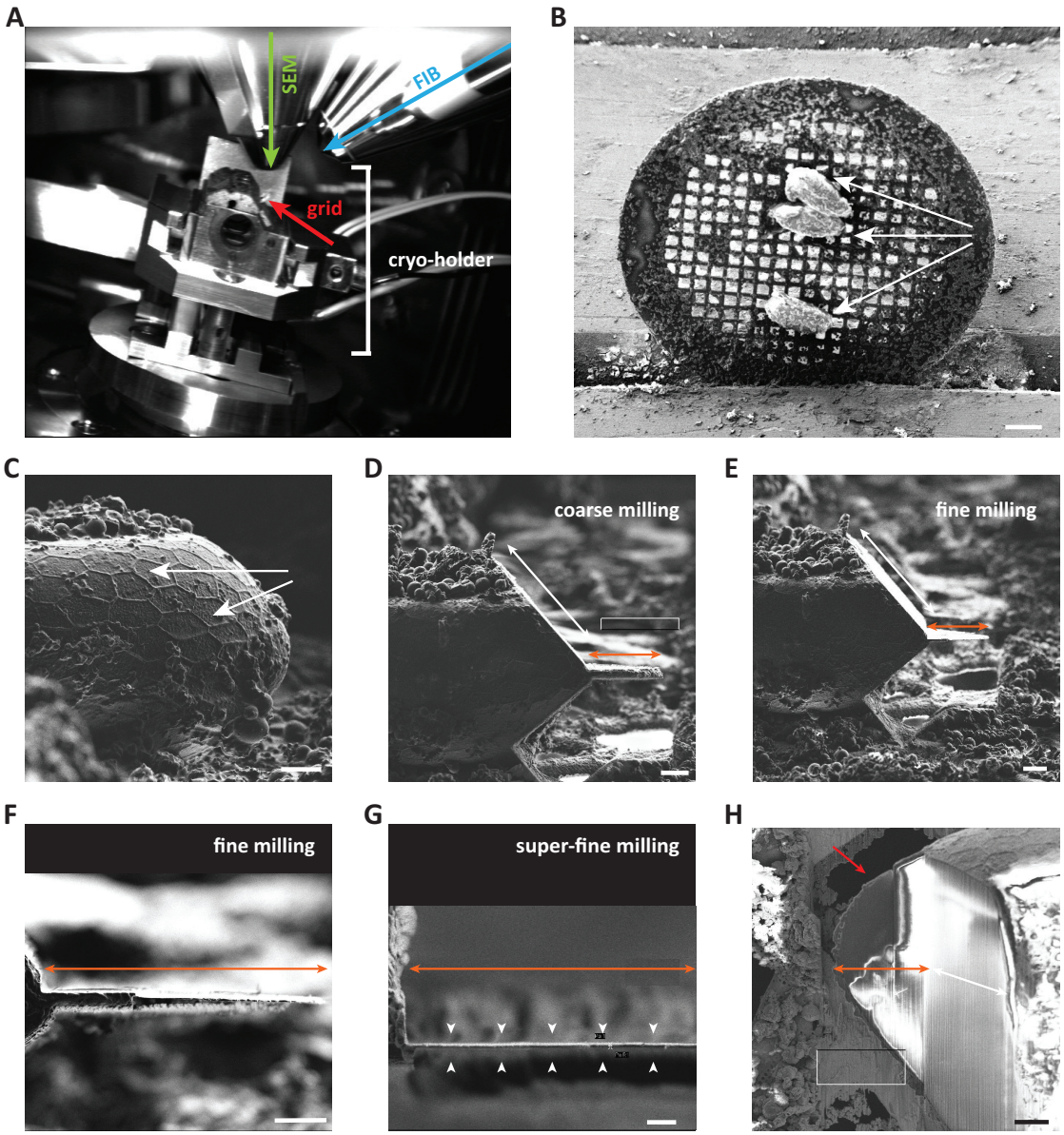

Figure 35: **Fabrication of a 200 – 300 nm thick lamellae using cryo-focussed ion beam milling as a thinning method prior to cryo-electron tomography.**
(A) The cryo-holder inside the cryo-FIB/SEM machine. Galium-ions from the FIB-column ablate biological material, imaging is performed using the SEM or the FIB column. **(B)** SEM overview image of the processed sample grid clamped into the cryo-holder and three attached embryos (white arrows). **(C)** FIB side view of an intact, chorionated fly embryo. The arrows point out the imprint of the hexagonal follicle cells, produced during oogenesis. **(D)** FIB side view of the embryo in A after several rounds of coarse milling with high currents, creating a lamella of several micrometer thickness (orange double arrow, < 10 μm thickness) and a flat slope on the body of the embryo (white double arrow). Thus, later tilting of the sample with the cryostage during high-tilt projection acquisition was enabled without blocking of

the electron beam. **(E), (F)** FIB side views of the lamella after multiple additional rounds of fine milling at lower currents, creating a 3 μm thick lamella. **(G)** FIB side view of further thinning of the lamella down to 200 – 500 nm by very low currents to avoid heat damage. The white arrowheads show a 200 nm thin lamella. **(H)** SEM top view of the lamella (orange double arrow) and the created slope (white double arrow) after milling. The dimensions of the lamella are 200 nm thickness , 20 μm width and 80 μm length. A grid hole (red arrow) was evident underneath the lamella, allowing in principle for cryo-ET of a huge area of interest. Scale bar depicts 300 μm (B), 20 μm (C, D, E, H), 10 μm (F), and 2 μm (G), respectively.

transfer from liquid nitrogen to several machines and finally to the cryo-electron microscope (see 2.5). As presented in panel 34 C and 35 B, the embryos were not obscured by the poly-L-lysine after sublimation of the freezing media 2-methylpentane, whereas both silicone grease (figure 34 D) and BSA (34 E) masked the vitrified embryos completely. Unfortunately, poly-L-lysine only facilitated attachment of embryos still having a chorion. Thus, we had to resign from the idea of creating lamella of embryos undergoing dorsal closure, since without the removal of the chorion the area of interest was not to be located with SEM (figure 35 C). Nevertheless, possible structural insights into other developmental processes within the fly, i.e. a putative diffusion barrier between peripheral nuclei within the fly syncytium (Frescas et al. [2006], Mavrakis et al. [2009]), gave motivation to continue.

Several lamellae were produced via cryo-focused ion beam milling, the process being shown for two representative lamellas in figures 35 and 36. Within successive rounds of material ablation, I removed material below and above the region of interest. First, high milling currents of 16 nA were applied, coarsely ablating material down to a $<$ 10 μm thick lamella (figure 35 D). To avoid biological material from the unmilled part of the fly embryo to come into the electron beam during high-tilt image acquisition, a slope was generated. Several rounds of coarse milling removed material adjacent to the lamella (figure 35 D, white double arrow). Since rough milling of the lamella introduced a substantial amount of heat to the sample, the lamella was further thinned with a 240 pA probe yielding a 3 μm lamella (figure 35 E, F). Finally, fine milling with a 50 pA probe reduced the lamella thickness to approximately 200 – 300 nm (figure 35 G).

Reducing the sample thickness to a few hundreds of nanometer was rapidly performed

within *C. elegans* embryos but lasted already 30 hours in adult worms (Harapin et al. [2015]). The fly embryo simply possesses larger dimensions compared to the worm, with a diameter being three times that of the adult worm. Thus, cryo-milling took routinely 3 – 4 days, with ablation time windows of 0.5 – 3 hours, producing a lamella of ˜300 nm x 20 μm x 80 μm. Running the cryo-FIB for this long was only accomplished by using a self-refillable dewar, customized by Andres Kaech from the Centre of Microscopy and Image Analysis (ZMB) from the University of Zurich.

Several attempts of creating a thin lamella via FIB-ablation and subsequent cryo-ET were undertaken. The created lamellae appeared thin enough after fibbing by scanning electron microscopy assessment (figures 35 G and 36 E). The embryo and the generated lamella were successfully transferred into the cryo-electron microscope, as both were still recognizable (data not shown). Nevertheless, it was not possible to record tomograms or 2D electron micrographs of the lamella. One possible explanation was the presence of a gridbar right underneath the lamella, blocking the electron beam. Therefore, the grid bar underneath one generated lamella was removed in successive rounds of coarse milling within 6 hours (figure 36 B, C). Although the lamella appeared thin enough for electron tomography and although the electron beam should not have been obscured, a tomogram of the lamella could not be recorded (figure 36 F). Most likely, the very long milling procedures over several days, and / or the transfer of the grid caused severe ice contamination and stability problems. The lamella represents a very thin structure that was surrounded mainly by vacuum, but was not directly cooled by attachment to the metal grid or bulk biological structures such that a heat / cold transfer would regulate the temperature optimally.
12 lamellae within 12 independent samples were generated in total. Unfortunately, none gave any structural insight.

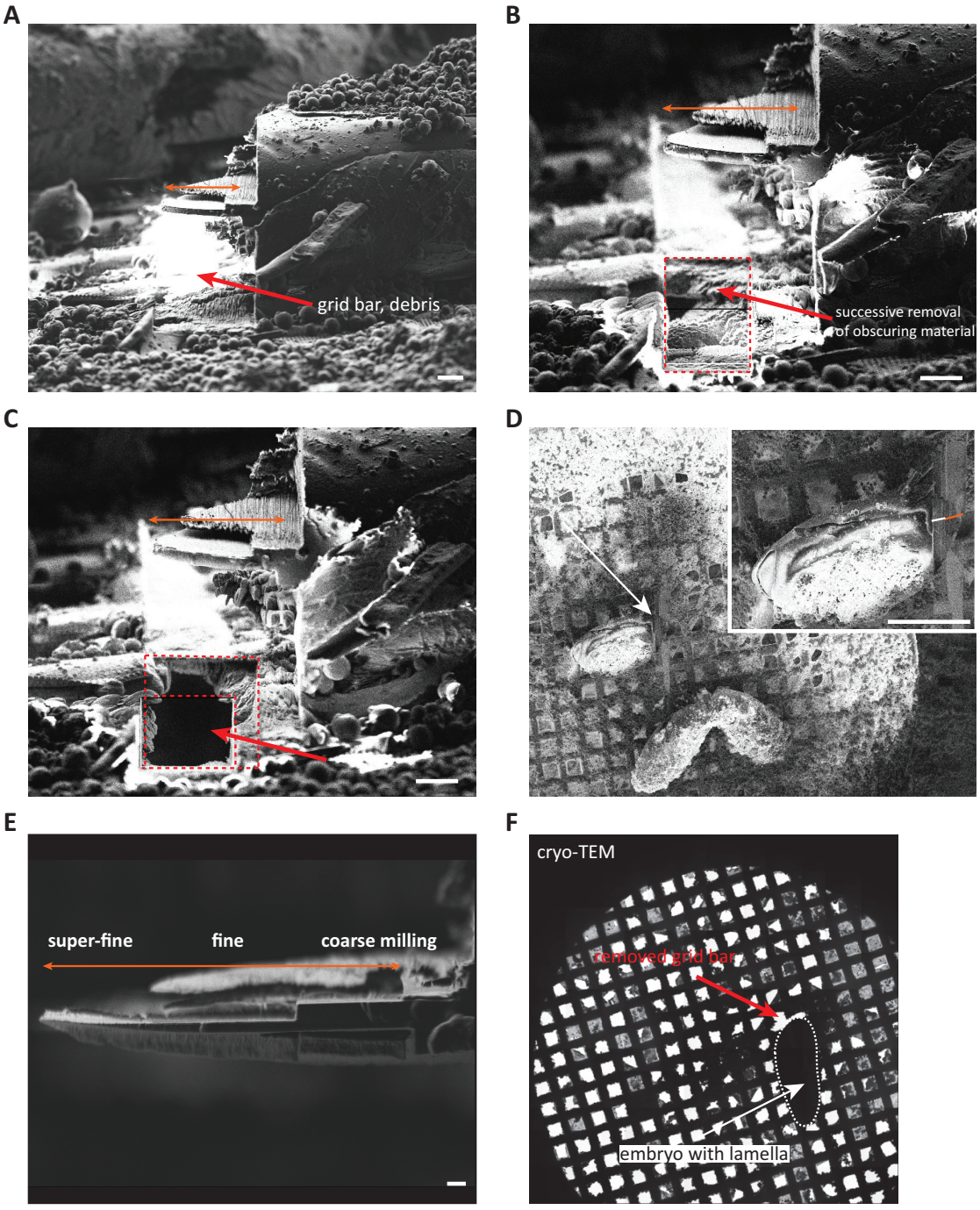

Figure 36: **Clearing of the area underneath the milled lamella to facilitate optimal cryo-electron tomography.**
(A) FIB side view of an embryo after several rounds of coarse milling with high currents, creating a thick lamella (orange arrow). The red arrow indicates ice, debris and the gridbar underneath the lamella. **(B), (C)** FIB side views of the successive removal of the grid bar

(red box, arrow). **(D)** SEM overview of the processed embryo (white arrow) and in the inset display of lamella (orange) and created slope (white). **(E)** After generating a slope on the body of the embryo, the lamella (orange double arrow, FIB side view) was further thinned with lower currents to a thickness of 200 – 500 nm. **(F)** Grid Atlas, overview image of the sample grid with the processed embryo (white double arrow) recorded with the TITAN Krios. The red arrow labels the removed grid bar. Scale bar depicts 20 μm (A, B, C), 200 μm (D) and 2 μm (E), respectively.

8 Discussion: Establishing Sample Preparation for Cryo-ET of Fly Embryos

8.1 The challenges of Cryo-microscopy

In this part of the thesis, I described the attempts to establish sample preparation for structural analysis of fly embryogenesis by cryo-electron tomography. Therefore, I tested two thinning methods in order to achieve a sample competent for cryo-microscopy. I successfully established cryo-ET of re-vitrified frozen sections by adapting an existing protocol for chicken smooth muscle (Bokstad et al. [2012], see section 7.1). Thereby, I employed cryo-sectioning to obtain thin sections. Alternatively, I tried to establish cryo-focused ion beam milling for ablation of biological material to obtain a thin, section-like structure that is called a lamella (see section 7.2).

I encountered drawbacks and technical problems for both sample preparation methods. Cryo-ET of re-vitrified frozen sections involved chemical fixation of fly embryos. Although the structural preservation appeared sufficient (figure 33 B - E), vitrification of biological samples was proved to be superior in terms of ultrastructural preservation (Vanhecke et al. [2011]). The ultrastructural integrity was further compromised by the cryo-sectioning process with inherent mechanical perturbations, such as compression, knife marks, and crevasses (Al-Amoudi et al. [2005], and Bouchet-Marquis and Hoenger [2011]). The mentioned drawbacks were the motivation to test the utilization of cryo-FIB/SEM milling for the generation of thin samples. I established the cryo-fixation of *Drosophila* embryos by high-pressure freezing (figure 34). Embryos with chorion were attached to EM-grids via poly-L-lysine interaction (figure 34 B, C). I was not successful in attaching embryos without a chorion permanently to the grid. Therefore, ultrastructural analysis of embryos during dorsal closure could not be addressed. Staging of embryos based on developmental time can be imprecise and blind generation of the lamella would be too inefficient. In total, 12 lamella of syncytial embryos were generated (figure 35). Despite several attempts, no lamella could be imaged with cryo-EM. The most likely explanation is accumulated ice contamination that obscured biological features. The fly

embryo represents a large structure for FIB-ablation. Usually, creation of one lamella took three to four days. Although the sample was continuously cooled to -156 °C, the long preparation time and the transfer of the lamella to the microscope might have caused the contamination and stability problems. The lamella represents a very thin structure of a few hundred nanometer that is only attached at one side to the bulk specimen (figure 36 E). The majority of the lamella is not directly cooled but surrounded by vacuum. Therefore, the heat / cold transfer might not optimally regulate the temperature and cause ice contamination. The longer the milling takes, the more ice could accumulate.

I recommend to pursue cryo-ET of fly embryos by performing the first established method, that of cryo-ET of re-vitrified frozen sections. Additional work might focus on the employment of high-pressure freezing instead of chemical fixation for augmented preservation (Ripper et al. [2008]). Cryo-FIB/SEM proved a very time-demanding, cost-intensive sample preparation for fly embryos. To overcome these technical problems would require a major effort that would have gone beyond the scope of my Ph.D. Nevertheless, cryo-FIB/SEM proved to be a very powerful, valid tool for sample preparation, creating a window into smaller model organisms, such as bacteria and *C. elegans* (Marko et al. [2007], Harapin et al. [2015]). By circumventing mechanical perturbations of the sample, an improved structural insight is gained.

Cryo-electron microscopy will prove an important tool to elucidate very specific questions during *Drosophila* embryogenesis. Given the small field of view that can be imaged, and the rather complicated location of the region of interest and the preparation of thin sections, the study of dorsal closure will prove challenging. The challenge is to locate the region of interest, for instance zipping, and collect sections. The benefit will be tremendous, as the cryo-approach preserves ultrastructure best. For instance, organization of cytoskeletal elements as the actin cable and motor proteins in leading edge cells during zipping are difficult to preserve with conventional sample preparation for room-temperature microscopy. Therefore, cryo-EM promises unprecedented details of cellular ultrastructure at physiological conditions.

8.2 Concluding Remarks

Structural analysis by cryo-electron tomography provides the highest resolution detail of cellular ultrastructure. New technical developments in the field have further increased resolution and improved molecular identification and will continue to do so (Villa et al. [2013]). Those are low-dose image recording, automatic image recording and processing, processing with larger computational power, direct electron detection devices, energy-filtering, and phase plates (reviewed in Villa et al. [2013], Schröder [2015]). The new generation of digital cameras detects electrons directly. Thereby, the correction of electron-beam induced sample motion becomes feasible and leads to increased resolution of 3 Å (Schröder [2015]). The low detector quantum efficiency of CCD detectors is overcome, yielding in a higher contrast. Also very exciting is the introduction of phase plates. So far, contrast was enhanced by recording images in defocus. Now, phase plates promise high-contrast imaging close to the focus, resulting in increased resolution (Danev and Baumeister [2016]).

9 References

Adamczyk, M. (2016). Analysis of force generation and cell-cell recognition during zipping in dorsal closure of Drosophila melanogaster. PhD thesis, University of Zurich.

Agronskaia, A. V., Valentijn, J. a., van Driel, L. F., Schneijdenberg, C. T. W. M., Humbel, B. M., van Bergen en Henegouwen, P. M. P., Verkleij, A. J., Koster, A. J. and Gerritsen, H. C. (2008). Integrated fluorescence and transmission electron microscopy. Journal of structural biology *164*, 183–9.

Al-Amoudi, A., Chang, J.-J., Leforestier, A., McDowall, A., Salamin, L. M., Norlén, L. P. O., Richter, K., Blanc, N. S., Studer, D. and Dubochet, J. (2004). Cryo-electron microscopy of vitreous sections. The EMBO journal *23*, 3583–8.

Al-Amoudi, A., Studer, D. and Dubochet, J. (2005). Cutting artefacts and cutting process in vitreous sections for cryo-electron microscopy. Journal of structural biology *150*, 109–21.

Aliee, M., Röper, J.-C., Landsberg, K. P., Pentzold, C., Widmann, T. J., Jülicher, F. and Dahmann, C. (2012). Physical mechanisms shaping the Drosophila dorsoventral compartment boundary. Current biology : CB *22*, 967–76.

Bachmann, A. and Straube, A. (2015). Kinesins in cell migration. Biochem Soc Trans *43*, 79–83.

Bashaw, G. J. and Klein, R. (2010). Signaling from axon guidance receptors. Cold Spring Harbor perspectives in biology *2*, a001941.

Betzig, E., Patterson, G. H., Sougrat, R., Lindwasser, O. W., Olenych, S., Bonifacino, J. S., Davidson, M. W., Lippincott-Schwartz, J. and Hess, H. F. (2006). Imaging intracellular fluorescent proteins at nanometer resolution. Science (New York, N.Y.) *313*, 1642–5.

Bokstad, M., Sabanay, H., Dahan, I., Geiger, B. and Medalia, O. (2012). Reconstructing adhesion structures in tissues by cryo-electron tomography of vitrified frozen sections. Journal of structural biology *178*, 76–83.

Bouchet-Marquis, C. and Hoenger, A. (2011). Cryo-electron tomography on vitrified sections: a critical analysis of benefits and limitations for structural cell biology. Micron (Oxford, England : 1993) *42*, 152–62.

Brand, A. and Perrimon, N. (1993). Targeted gene expression as a means of altering cell fates and generating dominant phenotypes. Development *118*, 401–415.

Campos-Ortega, J. and Hartenstein, V. (1985). The embryonic development of Drosophila melanogaster. Springer-Verlag.

Cardona, A., Saalfeld, S., Schindelin, J., Arganda-Carreras, I., Preibisch, S., Longair, M., Tomancak, P., Hartenstein, V. and Douglas, R. J. (2012). TrakEM2 Software for Neural Circuit Reconstruction. PLoS ONE *7*, e38011.

Caussinus, E., Kanca, O. and Affolter, M. (2013). Protein knockouts in living eukaryotes using deGradFP

and green fluorescent protein fusion. Curr Protoc Protein Sci *73*, 1–13.

Chozinski, T. J., Halpern, A. R., Okawa, H., Kim, H.-J., Tremel, G. J., Wong, R. O. L. and Vaughan, J. C. (2016). Expansion microscopy with conventional antibodies and fluorescent proteins. Nature methods *1*, 1–7.

Cohen, M., Georgiou, M., Stevenson, N. L., Miodownik, M. and Baum, B. (2010). Dynamic filopodia transmit intermittent Delta-Notch signaling to drive pattern refinement during lateral inhibition. Developmental cell *19*, 78–89.

Cooper, S., Khatib, F., Treuille, A., Barbero, J., Lee, J., Beenen, M., Leaver-Fay, A., Baker, D., Popovic, Z. and ¿57, . F. p. (2010). Predicting protein structures with a multiplayer online game. Nature *466*, 756–760.

Coutelis, J.-B., Géminard, C., Spéder, P., Suzanne, M., Petzoldt, A. G. and Noselli, S. (2013). Drosophila left/right asymmetry establishment is controlled by the Hox gene abdominal-B. Developmental cell *24*, 89–97.

Coutelis, J.-B., González-Morales, N., Géminard, C. and Noselli, S. (2014). Diversity and convergence in the mechanisms establishing L/R asymmetry in metazoa. EMBO reports *15*, 926–37.

Dahmann, C., Oates, A. C. and Brand, M. (2011). Boundary formation and maintenance in tissue development. Nature reviews. Genetics *12*, 43–55.

Danev, R. and Baumeister, W. (2016). Cryo-EM single particle analysis with the Volta phase plate. eLife *5*, 1–14.

de Boer, P., Hoogenboom, J. P. and Giepmans, B. N. G. (2015). Correlated light and electron microscopy: ultrastructure lights up! Nature methods *12*, 503–13.

Eberle, a. L., Mikula, S., Schalek, R., Lichtman, J., Knothe Tate, M. L. and Zeidler, D. (2015). High-resolution, high-throughput imaging with a multibeam scanning electron microscope. Journal of microscopy *259*, 114–20.

Eibauer, M., Pellanda, M., Turgay, Y., Dubrovsky, A., Wild, A. and Medalia, O. (2015). Structure and gating of the nuclear pore complex. Nature communications *6*, 7532.

Eltsov, M., Dubé, N., Yu, Z., Pasakarnis, L., Haselmann-Weiss, U., Brunner, D. and Frangakis, A. S. (2015). Quantitative analysis of cytoskeletal reorganization during epithelial tissue sealing by large-volume electron tomography. Nature cell biology *17*, 605–14.

Fabrowski, P., Necakov, A. S., Mumbauer, S., Loeser, E., Reversi, A., Streichan, S., Briggs, J. a. G. and De Renzis, S. (2013). Tubular endocytosis drives remodelling of the apical surface during epithelial morphogenesis in Drosophila. Nature communications *4*, 2244.

Flores-Benites, D. and Knust, E. (2016). Dynamics of epithelial cell polarity in Drosophila: how to regulate the regulators? Current Opinion in Cell Biology *42*, 13–21.

Franke, J. D., Montague, R. a. and Kiehart, D. P. (2005). Nonmuscle myosin II generates forces that transmit tension and drive contraction in multiple tissues during dorsal closure. Current biology : CB *15*, 2208–21.

Frescas, D., Mavrakis, M., Lorenz, H., Delotto, R. and Lippincott-Schwartz, J. (2006). The secretory membrane system in the Drosophila syncytial blastoderm embryo exists as functionally compartmentalized units around individual nuclei. The Journal of cell biology *173*, 219–30.

Friedlander, D. R., Mège, R. M., Cunningham, B. A. and Edelman, G. M. (1989). Cell sorting-out is modulated by both the specificity and amount of different cell adhesion molecules (CAMs) expressed on cell surfaces. Proceedings of the National Academy of Sciences of the United States of America *86*, 7043–7.

Furlong, E. E. (2004). Integrating transcriptional and signalling networks during muscle development. Current opinion in genetics & development *14*, 343–50.

Gettings, M. and Noselli, S. (2011). Mixer Cell formation during dorsal closure: a new developmental model of JNK-dependent natural cell reprogramming in Drosophila. Fly *5*, 327–32.

Gettings, M., Serman, F., Rousset, R., Bagnerini, P., Almeida, L. and Noselli, S. (2010). JNK signalling controls remodelling of the segment boundary through cell reprogramming during Drosophila morphogenesis. PLoS biology *8*, e1000390.

Gorfinkiel, N. and Arias, A. M. (2007). Requirements for adherens junction components in the interaction between epithelial tissues during dorsal closure in Drosophila. Journal of cell science *120*, 3289–98.

Grabenbauer, M., Geerts, W. J. C., Fernadez-Rodriguez, J., Hoenger, A., Koster, A. J. and Nilsson, T. (2005). Correlative microscopy and electron tomography of GFP through photooxidation. Nature methods *2*, 857–62.

Grossman, E., Dahan, I., Stick, R., Goldberg, M., Gruenbaum, Y. and Medalia, O. (2012). Filaments assembly of ectopically expressed Caenorhabditis elegans lamin within Xenopus oocytes. Journal of structural biology *177*, 113–118.

Grünewald, K., Medalia, O., Gross, A., Steven, A. and Baumeister, W. (2003). Prospects of electron cryotomography to visualize macromolecular complexes inside cellular compartments: implications of crowding. Biophysical Chemistry *100*, 577–591.

Gruska, M., Medalia, O., Baumeister, W. and Leis, A. (2008). Electron tomography of vitreous sections from cultured mammalian cells. Journal of structural biology *161*, 384–92.

Halloran, M. C. and Wolman, M. a. (2006). Repulsion or adhesion: receptors make the call. Current opinion in cell biology *18*, 533–40.

Harapin, J., Börmel, M., Sapra, K. T., Brunner, D., Kaech, A. and Medalia, O. (2015). Structural analysis of multicellular organisms with cryo-electron tomography. Nature methods *12*, 634–6.

Harapin, J., Eibauer, M. and Medalia, O. (2013). Structural Analysis of Supramolecular Assemblies by Cryo-Electron Tomography. Structure *21*, 1522–1530.

Harden, N. (2002). Signaling pathways directing the movement and fusion of epithelial sheets: lessons from dorsal closure in Drosophila. Differentiation; research in biological diversity *70*, 181–203.

Hayworth, K. J., Morgan, J. L., Schalek, R., Berger, D. R., Hildebrand, D. G. C. and Lichtman, J. W. (2014). Imaging ATUM ultrathin section libraries with WaferMapper: a multi-scale approach to EM reconstruction of neural circuits. Frontiers in neural circuits *8*, 68.

Honda, H. and Mochizuki, A. (2002). Formation and maintenance of distinctive cell patterns by co-expression of membrane-bound ligands and their receptors. Developmental dynamics : an official publication of the American Association of Anatomists *223*, 180–92.

Höög, J. L., Schwartz, C., Noon, A. T., O'Toole, E. T., Mastronarde, D. N., McIntosh, J. R. and Antony, C. (2007). Organization of interphase microtubules in fission yeast analyzed by electron tomography. Developmental cell *12*, 349–61.

Hozumi, S., Maeda, R., Taniguchi, K., Kanai, M., Shirakabe, S., Sasamura, T., Spéder, P., Noselli, S., Aigaki, T., Murakami, R. and Matsuno, K. (2006). An unconventional myosin in Drosophila reverses the default handedness in visceral organs. Nature *440*, 798–802.

Hsieh, C.-e., Marko, M., Frank, J. and Mannella, C. A. (2002). Electron tomographic analysis of frozen-hydrated tissue sections. Journal of structural biology *138*, 63–73.

Hutson, M. S., Tokutake, Y., Chang, M.-S., Bloor, J. W., Venakides, S., Kiehart, D. P. and Edwards, G. S. (2003). Forces for morphogenesis investigated with laser microsurgery and quantitative modeling. Science (New York, N.Y.) *300*, 145–9.

Ikegami, R., Simokat, K., Zheng, H., Brown, L., Garriga, G., Hardin, J. and Culotti, J. (2012). Semaphorin and eph receptor signaling guide a series of cell movements for ventral enclosure in C. elegans. Current Biology *22*, 1–11.

Jacinto, a., Wood, W., Balayo, T., Turmaine, M., Martinez-Arias, a. and Martin, P. (2000). Dynamic actin-based epithelial adhesion and cell matching during Drosophila dorsal closure. Current biology : CB *10*, 1420–6.

Jacinto, A., Wood, W., Woolner, S., Hiley, C., Turner, L., Wilson, C., Martinez-Arias, A. and Martin, P. (2002a). Dynamic analysis of actin cable function during Drosophila dorsal closure. Current biology : CB *12*, 1245–50.

Jacinto, A., Woolner, S. and Martin, P. (2002b). Dynamic analysis of dorsal closure in Drosophila: from genetics to cell biology. Developmental cell *3*, 9–19.

Jankovics, F. and Brunner, D. (2006). Transiently reorganized microtubules are essential for zippering during dorsal closure in Drosophila melanogaster. Developmental cell *11*, 375–85.

Jinek, M., Chylinski, K., Fonfara, I., Hauer, M., Doudna, J. and Charpentier, E. (2012). A porgrammable dual-RNA-guided DNA endonuclease in adaptive bacterial immunity. Science *337*, 816–21.

Kaltschmidt, J. a., Lawrence, N., Morel, V., Balayo, T., Fernández, B. G., Pelissier, A., Jacinto, A. and Martinez Arias, A. (2002). Planar polarity and actin dynamics in the epidermis of Drosophila. Nature cell biology *4*, 937–44.

Karreman, M. a., Agronskaia, A. V., Verkleij, A. J., Cremers, F. F. M., Gerritsen, H. C. and Humbel, B. M. (2009). Discovery of a new RNA-containing nuclear structure in UVC-induced apoptotic cells by integrated laser electron microscopy. Biology of the cell / under the auspices of the European Cell Biology Organization *101*, 287–99.

Karreman, M. a., Mercier, L., Schieber, N. L., Solecki, G., Allio, G., Winkler, F., Ruthensteiner, B., Goetz, J. G. and Schwab, Y. (2016). Fast and precise targeting of single tumor cells in vivo by multimodal correlative microscopy. Journal of cell science *129*, 444–56.

Keppler, A., Gendreizig, S., Gronemeyer, T., Pick, H., Vogel, H. and Johnsson, K. (2003). A general method for the covalent labeling of fusion proteins with small molecules in vivo. Nature biotechnology *21*, 86–9.

Khatib, F., DiMaio, F., Group, F. C., Group, F. V. C., Cooper, S., Kazmierczyk, M., Gilski, M., Krzywda, S., Zabranska, H., Pichova, I., Thompson, J., Popovic, Z., Jaskolski, M. and Baker, D. (2011). Crystal structure of a monomeric retroviral protease solved by protein folding game players. Nature structural and molecular biology *18*, 1175–1177.

Kiehart, D. and Galbraith, C. (2000). Multiple forces contribute to cell sheet morphogenesis for dorsal closure in Drosophila. The Journal of cell ... *149*, 471–490.

Kim, J., Greene, M., Zlateski, A., Lee, K., Richardson, M., Turaga, S., Purcaro, M., Balkam, M., Robinson, A., Behabadi, B., Campos, M., Denk, W. and Seung, H. (2013). Space-time wiring specificity supports direction selectivity in the retina. Nature *509*, 331–336.

Kimura, K. and Kimura, A. (2011). Intracellular organelles mediate cytoplasmic pulling force for centrosome centration in the Caenorhabditis elegans early embryo. Proceedings of the National Academy of Sciences of the United States of America *108*, 137–42.

Kirschner, M. and Mitchison, T. (1986). Beyond self-assembly: from microtubules to morphogenesis. Cell *45*, 329–342.

Kohl, J., Ng, J., Cachero, S., Ciabatti, E., Dolan, M.-J., Sutcliffe, B., Tozer, A., Ruehle, S., Krueger, D., Frechter, S., Branco, T., Tripodi, M. and Jefferis, G. S. X. E. (2014). Ultrafast tissue staining with chemical tags. Proceedings of the National Academy of Sciences of the United States of America *111*, E3805–14.

Kolotuev, I., Bumbarger, D. J., Labouesse, M. and Schwab, Y. (2012). Targeted ultramicrotomy: a

valuable tool for correlated light and electron microscopy of small model organisms., vol. 111,. Elsevier.

Kolotuev, I., Schwab, Y. and Labouesse, M. (2010). A precise and rapid mapping protocol for correlative light and electron microscopy of small invertebrate organisms. Biology of the cell / under the auspices of the European Cell Biology Organization *102*, 121–32.

Kornberg, T. (1981). Engrailed: a gene controlling compartment and segment formation in Drosophila. Proceedings of the National Academy of Sciences of the United States of America *78*, 1095–9.

Kotak, S., Busso, C. and Gönczy, P. (2012). Cortical dynein is critical for proper spindle positioning in human cells. The Journal of cell biology *199*, 97–110.

Kováčik, L., Kereïche, S., Höög, J., Jůda, P., Matula, P. and Raška, I. (2014). A simple fourier filter for suppression of the missing wedge ray artefacts in single-axis electron tomographic reconstructions. J Struct Biol *186*, 141–52.

Kremer, J. R., Mastronarde, D. N. and McIntosh, J. R. (1996). Computer visualization of three-dimensional image data using IMOD. Journal of structural biology *116*, 71–6.

Kreshuk, A., Koethe, U., Pax, E., Bock, D. and Hamprecht, F. (2014). Automated detection of synapses in serial section transmission electron microscopy image stacks. PLoS One *9*, e87351.

Kreshuk, A., Straehle, C., Sommer, C., Koethe, U., Cantoni, M., Knott, G. and Hamprecht, F. (2011). Automated detection and segmentation of synaptic contacts in nearly isotropic serial electron microscopy images. PLoS One *6*, e24899.

Krzemien, J., Fabre, C. C. G., Casal, J. and Lawrence, P. a. (2012). The muscle pattern of the Drosophila abdomen depends on a subdivision of the anterior compartment of each segment. Development (Cambridge, England) *139*, 75–83.

Kukulski, W., Schorb, M., Welsch, S., Picco, A., Kaksonen, M. and Briggs, J. a. G. (2011). Correlated fluorescence and 3D electron microscopy with high sensitivity and spatial precision. The Journal of cell biology *192*, 111–9.

Kukulski, W., Schorb, M., Welsch, S., Picco, A., Kaksonen, M. and Briggs, J. a. G. (2012). Precise, correlated fluorescence microscopy and electron tomography of lowicryl sections using fluorescent fiducial markers., vol. 111,. Elsevier.

Laan, L., Pavin, N., Husson, J., Romet-Lemonne, G., van Duijn, M., López, M. P., Vale, R. D., Jülicher, F., Reck-Peterson, S. L. and Dogterom, M. (2012). Cortical dynein controls microtubule dynamics to generate pulling forces that position microtubule asters. Cell *148*, 502–14.

Lam, S. S., Martell, J. D., Kamer, K. J., Deerinck, T. J., Ellisman, M. H., Mootha, V. K. and Ting, A. Y. (2015). Directed evolution of APEX2 for electron microscopy and proximity labeling. Nature methods *12*, 51–4.

Laplante, C. and Nilson, L. a. (2006). Differential expression of the adhesion molecule Echinoid drives

epithelial morphogenesis in Drosophila. Development (Cambridge, England) *133*, 3255–64.

Larsen, C. W., Hirst, E., Alexandre, C. and Vincent, J.-P. (2003). Segment boundary formation in Drosophila embryos. Development (Cambridge, England) *130*, 5625–35.

Lemaitre, B., Nicolas, E., Michaut, L., Reichhart, J. and Hoffman, J. (1996). The dorsoventral regulatory gene cassette spätzle/Toll/cactus controls the potent antifungal response in Drosophila adults. Cell *86*, 973–83.

Levin, M. (2012). Morphogenetic fields in embryogenesis, regeneration, and cancer: non-local control of complex patterning. Bio Systems *109*, 243–61.

Levin, M. and Palmer, R. (2007). Left-right patterning from the inside out: widespread evidence for intracellular control. BioEssays *29*, 271–287.

Li, R. and Bowerman, B. (2010). Symmetry breaking in biology. Cold Spring Harbor perspectives in biology *2*, a003475.

Lin, H.-P., Chen, H.-M., Wei, S.-Y., Chen, L.-Y., Chang, L.-H., Sun, Y.-J., Huang, S.-Y. and Hsu, J.-C. (2007). Cell adhesion molecule Echinoid associates with unconventional myosin VI/Jaguar motor to regulate cell morphology during dorsal closure in Drosophila. Developmental biology *311*, 423–33.

Lučič, V., Rigort, A. and Baumeister, W. (2013). Cryo-electron tomography: the challenge of doing structural biology in situ. The Journal of cell biology *202*, 407–19.

Maco, B., Holtmaat, A., Jorstad, A., Fua, P. and Knott, G. W. (2014). Correlative in vivo 2-photon imaging and focused ion beam scanning electron microscopy: 3D analysis of neuronal ultrastructure., vol. 124,. 1 edition, Elsevier Inc.

Mader, A., Elad, N. and Medalia, O. (2010). Cryoelectron tomography of eukaryotic cells. Methods in enzymology *483*, 245–65.

Markert, S. M., Britz, S., Proppert, S., Lang, M., Witvliet, D., Mulcahy, B., Sauer, M., Zhen, M., Bessereau, J.-L. and Stigloher, C. (2016). Filling the gap: adding super-resolution to array tomography for correlated ultrastructural and molecular identification of electrical synapses at the C. elegans connectome. Neurophotonics *3*, 041802.

Marko, M., Hsieh, C., Schalek, R., Frank, J. and Mannella, C. (2007). Focused-ion-beam thinning of frozen-hydrated biological specimens for cryo-electron microscopy. Nature methods *4*, 215–7.

Martell, J. D., Deerinck, T. J., Sancak, Y., Poulos, T. L., Mootha, V. K., Sosinsky, G. E., Ellisman, M. H. and Ting, A. Y. (2012). Engineered ascorbate peroxidase as a genetically encoded reporter for electron microscopy. Nature biotechnology *30*, 1143–8.

Martin, P. and Wood, W. (2002). Epithelial fusions in the embryo. Current opinion in cell biology *14*, 569–74.

Martinez-Arias, A. and Lawrence, P. A. (1985). Parasegments and compartments in the Drosophila

embryo. Nature *313*, 639–42.

Mastronarde, D. N. (1997). Dual-axis tomography: an approach with alignment methods that preserve resolution. Journal of structural biology *120*, 343–52.

Mastronarde, D. N. (2005). Automated electron microscope tomography using robust prediction of specimen movements. Journal of structural biology *152*, 36–51.

Mavrakis, M., Rikhy, R. and Lippincott-Schwartz, J. (2009). Plasma membrane polarity and compartmentalization are established before cellularization in the fly embryo. Developmental cell *16*, 93–104.

McDonald, K. (1999). High-pressure freezing for preservation of high resolution fine structure and antigenicity for immunolabeling. Methods in molecular biology (Clifton, N.J.) *117*, 77–97.

McEwen, B. F. and Marko, M. (2001). The emergence of electron tomography as an important tool for investigating cellular ultrastructure. The journal of histochemistry and cytochemistry : official journal of the Histochemistry Society *49*, 553–64.

McNally, F. J. (2013). Mechanisms of spindle positioning. The Journal of cell biology *200*, 131–40.

McNeill, H. (2000). Sticking together and sorting things out: adhesion as a force in development. Nature reviews. Genetics *1*, 100–8.

Medalia, O., Beck, M., Ecke, M., Weber, I., Neujahr, R., Baumeister, W. and Gerisch, G. (2007). Organization of actin networks in intact filopodia. Current biology : CB *17*, 79–84.

Medalia, O., Weber, I., Frangakis, A. S., Nicastro, D., Gerisch, G. and Baumeister, W. (2002). Macromolecular architecture in eukaryotic cells visualized by cryoelectron tomography. Science (New York, N.Y.) *298*, 1209–13.

Meinhardt, H. (2015). Models for patterning primary embryonic body axes: The role of space and time. Seminars in cell & developmental biology *42*, 103–117.

Micheva, K. D. and Smith, S. J. (2007). Array tomography: a new tool for imaging the molecular architecture and ultrastructure of neural circuits. Neuron *55*, 25–36.

Millard, T. H. and Martin, P. (2008). Dynamic analysis of filopodial interactions during the zippering phase of Drosophila dorsal closure. Development (Cambridge, England) *135*, 621–6.

Monier, B., Pélissier-Monier, A., Brand, A. H. and Sanson, B. (2010). An actomyosin-based barrier inhibits cell mixing at compartmental boundaries in Drosophila embryos. Nature cell biology *12*, 60–5; sup pp 1–9.

Monier, B., Pélissier-Monier, A. and Sanson, B. (2011). Establishment and maintenance of compartmental boundaries: role of contractile actomyosin barriers. Cellular and molecular life sciences : CMLS *68*, 1897–910.

Morata, G. and Lawrence, P. A. (1975). Control of compartment development by the engrailed gene in Drosophila. Nature *255*, 614–7.

Morgan, T. (1910). Sex limited inheritance in Drosophila. Science *32*, 120–2.

Muller, H. (1927). Artificial transmutation of the gene. Science *66*, 84–7.

Nern, A., Pfeiffer, B. D. and Rubin, G. M. (2015). Optimized tools for multicolor stochastic labeling reveal diverse stereotyped cell arrangements in the fly visual system. Proceedings of the National Academy of Sciences of the United States of America *112*, 2967–2976.

Nguyen-Ngoc, T., Afshar, K. and Gönczy, P. (2007). Coupling of cortical dynein and G alpha proteins mediates spindle positioning in Caenorhabditis elegans. Nature cell biology *9*, 1294–302.

Ninov, N., Chiarelli, D. and Martin-Blanco, E. (2007). Extrinsic and intrinsic mechanisms directing epithelial cell sheet replacement during drosophila metamorphosis. Wilhelm RouxÂťs archives of developmental biology *193*, 267–282.

Nisman, R., Dellaire, G., Ren, Y., Li, R. and Bazett-Jones, D. P. (2004). Application of quantum dots as probes for correlative fluorescence, conventional, and energy-filtered transmission electron microscopy. The journal of histochemistry and cytochemistry : official journal of the Histochemistry Society *52*, 13–8.

Nixon, S. J., Webb, R. I., Floetenmeyer, M., Schieber, N., Lo, H. P. and Parton, R. G. (2009). A single method for cryofixation and correlative light, electron microscopy and tomography of zebrafish embryos. Traffic (Copenhagen, Denmark) *10*, 131–6.

Nüsslein-Volhard, C. and Wieschaus, E. (1980). Mutations affecting segment number and polarity in Drosophila. Nature *287*, 795–801.

Nüsslein-Volhard, C. and Wieschaus, E. (1980). Mutations affecting segment number and polarity in Drosophila. Nature *287*, 795–801.

Pasakarnis, L., Frei, E., Caussinus, E., Affolter, M. and Brunner, D. (2016). Tissue-specific, acute MyosinII activity depletion dismisses current models of tissue force orchestration in dorsal closure. under revision .

Patla, I., Volberg, T., Elad, N., Hirschfeld-Warneken, V., Grashoff, C., Fässler, R., Spatz, J., Geiger, B. and Medalia, O. (2010). Dissecting the molecular architecture of integrin adhesion sites by cryo-electron tomography. Nat Cell Biol *12*, 909–15.

Peddie, C. J., Liv, N., Hoogenboom, J. P. and Collinson, L. M. (2014). Integrated light and scanning electron microscopy of GFP-expressing cells., vol. 124,. 1 edition, Elsevier Inc.

Perkovic, M., Kunz, M., Endesfelder, U., Bunse, S., Wigge, C., Yu, Z., Hodirnau, V.-V., Scheffer, M. P., Seybert, A., Malkusch, S., Schuman, E. M., Heilemann, M. and Frangakis, A. S. (2014). Correlative Light- and Electron Microscopy with chemical tags. Journal of structural biology *186*, 205–13.

Petzoldt, A. G., Coutelis, J.-B., Géminard, C., Spéder, P., Suzanne, M., Cerezo, D. and Noselli, S. (2012). DE-Cadherin regulates unconventional Myosin ID and Myosin IC in Drosophila left-right

asymmetry establishment. Development (Cambridge, England) *139*, 1874–84.

Pfeiffer, B. D., Ngo, T.-T. B., Hibbard, K. L., Murphy, C., Jenett, A., Truman, J. W. and Rubin, G. M. (2010). Refinement of tools for targeted gene expression in Drosophila. Genetics *186*, 735–55.

Pfeiffer, B. D., Truman, J. W. and Rubin, G. M. (2012). Using translational enhancers to increase transgene expression in Drosophila. Proceedings of the National Academy of Sciences of the United States of America *109*, 6626–31.

Phelps, C. B. and Brand, a. H. (1998). Ectopic gene expression in Drosophila using GAL4 system. Methods (San Diego, Calif.) *14*, 367–79.

Pierson, J., Vos, M., McIntosh, J. R. and Peters, P. J. (2011). Perspectives on electron cryo-tomography of vitreous cryo-sections. Journal of electron microscopy *60 Suppl 1*, S93–100.

Rand, M. D., Kearney, A. L., Dao, J. and Clason, T. (2010). Permeabilization of Drosophila embryos for introduction of small molecules. Insect biochemistry and molecular biology *40*, 792–804.

Rigort, A., Bäuerlein, F. J. B., Leis, A., Gruska, M., Hoffmann, C., Laugks, T., Böhm, U., Eibauer, M., Gnaegi, H., Baumeister, W. and Plitzko, J. M. (2010). Micromachining tools and correlative approaches for cellular cryo-electron tomography. Journal of structural biology *172*, 169–79.

Rigort, A., Bäuerlein, F. J. B., Villa, E., Eibauer, M., Laugks, T., Baumeister, W. and Plitzko, J. M. (2012a). Focused ion beam micromachining of eukaryotic cells for cryoelectron tomography. Proceedings of the National Academy of Sciences of the United States of America *109*, 4449–54.

Rigort, A., Günther, D., Hegerl, R., Baum, D., Weber, B., Prohaska, S., Medalia, O., Baumeister, W. and Hege, H.-C. (2012b). Automated segmentation of electron tomograms for a quantitative description of actin filament networks. Journal of structural biology *177*, 135–44.

Rigort, A., Villa, E., Bäuerlein, F. J. B., Engel, B. D. and Plitzko, J. M. (2012c). Integrative approaches for cellular cryo-electron tomography: correlative imaging and focused ion beam micromachining., vol. 111,. Elsevier.

Ripper, D., Schwarz, H. and Stierhof, Y.-D. (2008). Cryo-section immunolabelling of difficult to preserve specimens: advantages of cryofixation, freeze-substitution and rehydration. Biology of the cell / under the auspices of the European Cell Biology Organization *100*, 109–23.

Royston, P. (1995). Remark AS R94: A Remark on Algorithm AS 181: The W-test for Normality. Applied Statistics *44*, 547.

Sabanay, I., Arad, T., Weiner, S. and Geiger, B. (1991). Study of vitrified, unstained frozen tissue sections by cryoimmunoelectron microscopy. Journal of cell science *100 (Pt 1*, 227–36.

Saias, L., Swoger, J., D'Angelo, A., Hayes, P., Colombelli, J., Sharpe, J., Salbreux, G. and Solon, J. (2015). Decrease in Cell Volume Generates Contractile Forces Driving Dorsal Closure. Developmental Cell *d*, 1–11.

Sanson, B. (2001). Generating patterns from fields of cells Examples from Drosophila segmentation. EMBO reports *2*, 1083–1088.

Sartori, A., Gatz, R., Beck, F., Rigort, A., Baumeister, W. and Plitzko, J. M. (2007). Correlative microscopy: bridging the gap between fluorescence light microscopy and cryo-electron tomography. Journal of structural biology *160*, 135–45.

Schalek, R., Kasthuri, N., Hayworth, K., Berger, D., Tapia, J., Morgan, J., Turaga, S., Fagerholm, E., Seung, H. and Lichtman, J. (2011). Development of high-throughput, high-resolution 3D reconstruction of large-volume biological tissue using automated tape collection ultramicrotomy and scanning electron microscopy. Microsc. Microanal. *17*.

Schnorrenberg, S., Grotjohann, T., Vorbrüggen, G., Herzig, A., Hell, S. and Jakobs, S. (2016). In vivo super-resolution RESOLFT microscopy of Drosophila melanogaster. eLife *5*, e155567.

Schorb, M., Gaechter, L., Avinoam, O., Sieckmann, F., Clarke, M., Bebeacua, C., Bykov, Y., Sonnen, A., Lihl, R. and Briggs, J. (2016). New hardware and workflows for semi-automated correlative cryo-fluorescence and cryo-electron microscopy/tomography. Journal of structural biology *In press*.

Schröder, R. R. (2015). Advances in electron microscopy: A qualitative view of instrumentation development for macromolecular imaging and tomography. Archives of biochemistry and biophysics *581*, 25–38.

Schwartz, C. L., Sarbash, V. I., Ataullakhanov, F. I., McIntosh, J. R. and Nicastro, D. (2007). Cryo-fluorescence microscopy facilitates correlations between light and cryo-electron microscopy and reduces the rate of photobleaching. Journal of microscopy *227*, 98–109.

Shaner, N. C., Lambert, G. G., Chammas, A., Ni, Y., Cranfill, P. J., Baird, M. a., Sell, B. R., Allen, J. R., Day, R. N., Israelsson, M., Davidson, M. W. and Wang, J. (2013). A bright monomeric green fluorescent protein derived from Branchiostoma lanceolatum. Nature methods *10*, 407–9.

Sharp, D., Rogers, G. and Scholey, J. (2000). Roles of motor proteins in building microtubule-based structures: a basic principle of cellular design. Biochimica et Biophysica Acta *1496*, 128–141.

Shu, X., Lev-Ram, V., Deerinck, T. J., Qi, Y., Ramko, E. B., Davidson, M. W., Jin, Y., Ellisman, M. H. and Tsien, R. Y. (2011). A genetically encoded tag for correlated light and electron microscopy of intact cells, tissues, and organisms. PLoS biology *9*, e1001041.

Sjollema, K. a., Schnell, U., Kuipers, J., Kalicharan, R. and Giepmans, B. N. G. (2012). Correlated light microscopy and electron microscopy., vol. 111,. Elsevier.

Solon, J., Kaya-Copur, A., Colombelli, J. and Brunner, D. (2009). Pulsed forces timed by a ratchet-like mechanism drive directed tissue movement during dorsal closure. Cell *137*, 1331–42.

Sorrentino, S., Studt, J., Bokstad Horev, M., Medalia, O. and Sapra, K. (2016). Toward correlating structure and mechanics of platelets. Cell Adhesion and Migration *0*, 1–8.

Spéder, P., Adám, G. and Noselli, S. (2006). Type ID unconventional myosin controls left-right asymmetry in Drosophila. Nature *440*, 803–7.

Spéder, P. and Noselli, S. (2007). Left-right asymmetry: class I myosins show the direction. Current opinion in cell biology *19*, 82–7.

Spiegelhalter, C., Laporte, J. F. and Schwab, Y. (2014). Correlative Light and Electron Microscopy: From Live Cell Dynamic to 3D Ultrastructure. Methods in Molecular Biology *1117*, 485–501.

Steinberg, M. S. (2007). Differential adhesion in morphogenesis: a modern view. Current opinion in genetics & development *17*, 281–6.

Takemura, S., Bharioke, A., Lu, Z., Nern, A., Vitaladevuni, S., Rivlin, P., Katz, W., Olbris, D., Plaza, S., Winston, P., Zhao, T., Horne, J., Fetter, R., Takemura, S., Blazek, K., Chang, L., Ogundeyi, O., Saunders, M., Shapiro, V., Sigmund, C., Rubin, G., Scheffer, L., Meinertzhagen, I. and Chklovskii, D. (2013). A visual motion detection circuit suggested by Drosophila connectomics. Nature *500*, 175–183.

Tanenbaum, M., Vale, R. and McKenney, R. (2013). Cytoplasmic dynein crosslinks and slides anti-parallel microtubules using its two motor domains. eLIFE *2*, e00943.

Taniguchi, K., Hozumi, S., Maeda, R., Okumura, T. and Matsuno, K. (2007). Roles of Type I Myosins in Drosophila Handedness. Fly *1*, 1–4.

Taniguchi, K., Maeda, R., Ando, T., Okumura, T., Nakazawa, N., Hatori, R., Nakamura, M., Hozumi, S., Fujiwara, H. and Matsuno, K. (2011). Chirality in planar cell shape contributes to left-right asymmetric epithelial morphogenesis. Science (New York, N.Y.) *333*, 339–41.

Tepass, U. (2012). The apical polarity protein network in Drosophila epithelial cells: regulation of polarity, junctions, morphogenesis, cell growth, and survival. Annual review of cell and developmental biology *28*, 655–85.

Tepass, U. and Hartenstein, V. (1994). The development of cellular junctions in the Drosophila embryo. Developmental biology *161*, 563–96.

Tokuyasu, K. T. (1973). A technique for ultracryotomy of cell suspensions and tissues. The Journal of cell biology *57*, 551–65.

Toyama, Y., Peralta, X. G., Wells, A. R., Kiehart, D. P. and Edwards, G. S. (2008). Apoptotic force and tissue dynamics during Drosophila embryogenesis. Science (New York, N.Y.) *321*, 1683–6.

Turner, F. and Mahowald, A. (1976). Scanning electron microscopy of Drosophila embryogenesis. Developmental Biology *50*, 95–108.

Umetsu, D., Dunst, S. and Dahmann, C. (2014). An RNA interference screen for genes required to shape the anteroposterior compartment boundary in Drosophila identifies the Eph receptor. PloS one *9*, e114340.

Vandenberg, L. N. and Levin, M. (2013). A unified model for left-right asymmetry? Comparison and synthesis of molecular models of embryonic laterality. Developmental biology *379*, 1–15.

Vanhecke, D., Asano, S., Kochovski, Z., Fernandez-Busnadiego, R., Schrod, N., Baumeister, W. and Lučić, V. (2011). Cryo-electron tomography: methodology, developments and biological applications. Journal of microscopy *242*, 221–7.

Vanhecke, D., Graber, W. and Studer, D. (2008). Close-to-native ultrastructural preservation by high pressure freezing. Methods in cell biology *88*, 151–64.

Verkade, P. (2008). Moving EM: the Rapid Transfer System as a new tool for correlative light and electron microscopy and high throughput for high-pressure freezing. Journal of microscopy *230*, 317–28.

Villa, E., Schaffer, M., Plitzko, J. M. and Baumeister, W. (2013). Opening windows into the cell: focused-ion-beam milling for cryo-electron tomography. Current opinion in structural biology *23*, 771–7.

Wang, K., Strunk, K., Zhao, G., Gray, J. L. and Zhang, P. (2012). 3D structure determination of native mammalian cells using cryo-FIB and cryo-electron tomography. Journal of structural biology *180*, 318–26.

Watanabe, S. and Jorgensen, E. M. (2012). Visualizing proteins in electron micrographs at nanometer resolution., vol. 111,. Elsevier.

Watanabe, S., Punge, A., Hollopeter, G., Willig, K. I., Hobson, R. J., Davis, M. W., Hell, S. W. and Jorgensen, E. M. (2011). Protein localization in electron micrographs using fluorescence nanoscopy. Nature methods *8*, 80–4.

Weber, B., Greenan, G., Prohaska, S., Baum, D., Hege, H.-C., Müller-Reichert, T., Hyman, A. a. and Verbavatz, J.-M. (2012). Automated tracing of microtubules in electron tomograms of plastic embedded samples of Caenorhabditis elegans embryos. Journal of structural biology *178*, 129–38.

Willig, K. I., Harke, B., Medda, R. and Hell, S. W. (2007). STED microscopy with continuous wave beams. Nature methods *4*, 915–8.

Wolpert, L., Tickle, C. and Martinez-Arias, A. (2015). Principles of Development. 5th edition, Oxford.

Yahav, T., Maimon, T., Grossman, E., Dahan, I. and Medalia, O. (2011). Cryo-electron tomography: gaining insight into cellular processes by structural approaches. Current opinion in structural biology *21*, 670–7.

Yi, J., Wu, X., Chung, a. H., Chen, J. K., Kapoor, T. M. and Hammer, J. a. (2013). Centrosome repositioning in T cells is biphasic and driven by microtubule end-on capture-shrinkage. The Journal of Cell Biology *202*, 779–792.

Young, P. E., Richman, A. M., Ketchum, A. S. and Kiehart, D. P. (1993). Morphogenesis in Drosophila

requires nonmuscle myosin heavy chain function. Genes & Development *7*, 29–41.

Zimyanin, V., Belaya, K., Pecreaux, J., Gilchrist, M., Clar, A., Davis, I. and St Johnston, D. (2008). In vivo imaging of oskar mRNA transport reveals the mechanism of posterior localization. Cell *134*, 843–853.

Zipursky, L. and Grueber, W. (2013). The molecular basis of self-avoidance. Annual review of neuroscience *36*, 547–68.

Abbreviations

AJs adherens junctions

ANCs actin-nucleating centers

AS amnioserosa

C. elegans Caenorhabditis elegans

CEMOVIS cryo-electron microscopy of vitrified frozen sections

CLEM correlative light and electron microscopy

cryo-FIB cryo-focused ion beam

DAB diaminobenzidine

DCdorsal closure

ddH_2O double-distilled water

EM electron microscopy

ET electron tomography

FLM fluorescent light microscopy

Gal4-UAS Gal4 - upstream activating sequence

GFP green fluorescent protein

HPF high-pressure freezing

IVS intervening sequence

LE leading edge

LM light microscopy

LN_2 liquid nitrogen

MT microtubule

MyoID unconventional Myosin ID

o/n over night

PCP planar cell polarity

re-VFSs re-vitrified frozen sections

RT room-temperature

ssTEM serial-section transmission electron microscopy

TEM transmission electron microscopy

Appendix A - Supplementary Figures

Table 3: **Summarizing table on cell-cell interactions**
Sample refers to the analyzed zipping site. Cell number indicates the position of the cell within the zipping site, where cell 1 is closest to the dorsal opening. Left side indicated by l, right one by r. Anterior compartmental identity encoded with a, posterior one with p. Number of interactions specifies the number of interactions with opposing LE cells. AJs specifies the percentage of inspected sections with AJs, where the cell of interest contributed to the simplified interaction surface. The interaction width points out the width (in μm) of the cell of interest with opposing leading edge cells. It does not necessarily represent the actual width of the cell. The zipping stage distinguishes the following categories: o for open, e for early, m for mid, and l for late zipping. Cells were also categorized as intermediate, i.e. oe represents a cell being both in open and early zipping stage. Segment specifies the abdominal segment identity. The row on mixer cells informs about the mixer cell identity with y for yes and n for no. The a-p interaction column informs, whether the investigated cell formed also mixed interactions with cells of other compartmental identity (y for yes and n for no).

sample	**cell number**	**left/ right identity**	**a/p identity**	**number of interactions**	**Ajs [%]**	**interact width [μm]**	**zipping stage**	**segment**	**mixer cell**	**a-p interaction**
alpha	1	l	a	1	0	4.5	oe	A7	n	n
alpha	2	l	a	2	0	4.8	e	A7	n	n
alpha	3	l	a	2	62.5	3.6	m	A7	n	n
alpha	4	l	a	2	95	6	m	A7	n	n
alpha	5	l	a	3	80	11.4	m	A7	n	n
alpha	1	r	p	1	0	4.5	oe	A6	n	n
alpha	2	r	a	1	0	2.4	e	A7	n	n
alpha	3	r	a	1	0	2.7	e	A7	n	n
alpha	4	r	a	3	68	6.3	m	A7	n	n
alpha	5	r	a	2	84	7.5	m	A7	n	n
alpha	6	r	a	1	86	2.1	m	A7	n	n
beta	1	l	a	3	27	4.5	em	A4	n	n
beta	2	l	a	2	80	3	m	A4	n	n
beta	3	l	a	2	100	5.7	m	A4	n	n
beta	4	l	a	3	100	9.3	m	A4	n	n
beta	5	l	a	1	100	6	m	A4	n	n
beta	6	l	p	2	86	2.4	m	A4	n	n
beta	7	l	p	2	83	4.2	ml	A4	n	n
beta	8	l	p	1	100	4.5	m	A4	y	n
beta	9	l	p	2	100	4.2	m	A4	n	n
beta	1	r	a	1	0	3	em	A4	n	n
beta	2	r	a	1	37.5	2.4	m	A4	n	n
beta	3	r	a	1	100	2.4	m	A4	n	n
beta	4	r	a	4	100	11.1	m	A4	n	n
beta	5	r	a	2	100	6	m	A4	n	n
beta	6	r	p	1	100	2.1	m	A4	n	n
beta	7	r	p	2	77	4.2	ml	A4	n	n
beta	8	r	p	3	93	5.7	m	A4	y	n

sample	cell number	left/ right identity	a/p identity	number of interactions	Ajs [%]	interaction width [μm]	zipping stage	segment	mixer cell	a-p interaction
beta	9	r	p	2	100	4.2	m	A4	n	n
gamma	1	l	a	2	11	4.8	em	A5	n	n
gamma	2	l	a	2	42	5.4	m	A5	n	n
gamma	3	l	a	1	71	2.4	m	A5	n	n
gamma	4	l	a	3	63	6.9	m	A5	n	y
gamma	5	l	p	2	60	4.5	m	A5	n	y
gamma	6	l	p	2	71	7.2	ml	A5	n	n
gamma	7	l	p	2	93	5.8	l	A5	y	n
gamma	1	r	a	2	0	2.4	e	A5	n	n
gamma	2	r	a	2	46	5.4	m	A5	n	n
gamma	3	r	a	1	71	2.4	m	A5	n	n
gamma	4	r	a	2	85	5.4	m	A5	n	n
gamma	5	r	a	2	44	4.8	m	A5	n	y
gamma	6	r	p	2	50	6.6	m	A5	n	n
gamma	7	r	p	1	77	6.9	ml	A5	n	n
gamma	8	r	p	2	94	6	l	A5	y	n
delta_a	1	l	p	1	0	2.7	em	A2	n	n
delta_a	2	l	p	1	33	2.1	m	A2	n	n
delta_a	3	l	p	1	0	1.5	m	A2	n	n
delta_a	4	l	a	2	43	2.4	m	A2	n	y
delta_a	5	l	a	2	60	3	m	A2	n	n
delta_a	6	l	a	1	62.5	2.7	m	A2	n	n
delta_a	7	l	a	2	0	3.9	m	A2	n	n
delta_a	8	l	p	1	17	2.4	om	A1	n	y
delta_a	9	l	p	1	29	2.1	m	A1	n	n
delta_a	10	l	p	2	25	3	m	A1	n	n
delta_a	11	l	p	2	27	4.5	m	A1	n	y
delta_a	12	l	a	1	25	2.4	ml	A1	n	n
delta_a	1	r	p	1	0	2.7	em	A2	n	n
delta_a	2	r	p	1	33	2.1	m	A2	n	n
delta_a	3	r	p	2	17	2.4	m	A2	n	y
delta_a	4	r	a	2	54	3.6	m	A2	n	n
delta_a	5	r	a	2	60	3.3	m	A2	n	n
delta_a	6	r	a	1	0	3	m	A2	n	n
delta_a	7	r	a	2	11	3.3	om	A2	n	y
delta_a	8	r	p	1	33	2.1	m	A1	n	n
delta_a	9	r	p	2	40	1.5	m	A1	n	n
delta_a	10	r	p	1	25	3	m	A1	y	n
delta_a	11	r	p	2	27	4.5	m	A1	n	n
delta_a	12	r	a	2	25	2.4	ml	A1	n	y
delta_p	1	l	a	1	43	2	oe	A3	n	n
delta_p	2	l	a	2	11	2.5	em	A3	n	n
delta_p	3	l	a	2	62.5	2.25	m	A3	n	n
delta_p	4	l	a	2	47	4.25	m	A3	n	n
delta_p	5	l	p	2	0	1.75	m	A3	n	y
delta_p	6	l	p	1	50	2.5	m	A3	n	n
delta_p	7	l	p	1	0	2.25	oem	A3	n	n
delta_p	8	l	p	2	12.5	3.25	oe	A3	y	n
delta_p	9	l	p	1	0	1.5	e	A3	n	y
delta_p	10	l	a	2	33	4.75	ml	A4	n	n
delta_p	1	r	a	2	33	2.75	oe	A3	n	n
delta_p	2	r	a	1	14	3	em	A3	n	n

sample	cell number	left/ right identity	a/p identity	number of interactions	Ajs [%]	interaction width [μm]	zipping stage	segment	mixer cell	a-p interaction
delta_p	3	r	a	1	83	1.75	m	A3	n	n
delta_p	4	r	a	2	37.5	2	m	A3	n	n
delta_p	5	r	a	2	45.5	3	m	A3	n	y
delta_p	6	r	p	2	33	4	m	A3	n	n
delta_p	7	r	p	1	0	2.25	oem	A3	n	n
delta_p	8	r	p	1	12.5	3	oe	A3	y	n
delta_p	9	r	p	0	0	1	o	A3	n	n
delta_p	10	r	a	2	11	3.5	e	A4	n	y
delta_p	11	r	a	1	50	2.75	ml	A4	n	n
epsilon	1	l	a	1	0	1.8	e	A5	n	n
epsilon	2	l	a	2	0	1.8	em	A5	n	n
epsilon	3	l	a	3	0	1.8	m	A5	n	y
epsilon	4	l	p	2	64	4.5	m	A5	n	n
epsilon	5	l	p	1	82	3.3	m	A5	n	n
epsilon	6	l	p	1	50	4.8	ml	A5	n	n
epsilon	7	l	p	2	69	5.1	m	A5	y	y
epsilon	8	l	a	2	46	3.9	m	A6	n	n
epsilon	1	r	a	1	0	1.8	e	A5	n	n
epsilon	2	r	a	2	0	1.8	em	A5	n	n
epsilon	3	r	a	1	0	1.5	m	A5	n	n
epsilon	4	r	p	2	64	3.6	m	A5	n	y
epsilon	5	r	p	2	73	4.5	m	A5	n	n
epsilon	6	r	p	2	20	3.9	ml	A5	n	n
epsilon	7	r	p	1	100	2.4	m	A5	y	n
epsilon	8	r	a	2	25	2.7	m	A6	n	y
epsilon	9	r	a	2	50	3.9	m	A6	n	y
zeta	1	l	p	1	0	1.2	e	A5	n	y
zeta	2	l	p	1	0	1.5	e	A5	y	y
zeta	3	l	a	1	72	6.6	m	A6	n	n
zeta	4	l	a	2	100	9	m	A6	n	n
zeta	5	l	a	4	91	15	m	A6	n	n
zeta	6	l	a	3	61	11.1	m	A6	n	y
zeta	7	l	p	1	17	6.3	l	A6	n	n
zeta	8	l	p	1	33	3	l	A6	n	n
zeta	1	r	a	3	33	5.2	e	A6	n	y
zeta	2	r	a	2	100	4.8	m	A6	n	n
zeta	3	r	a	2	100	5.1	m	A6	n	n
zeta	4	r	a	3	92	3.6	m	A6	n	n
zeta	5	r	a	2	86	7.2	m	A6	n	n
zeta	6	r	p	3	18	6	l	A6	n	y
eta	1	l	p	1	0	1.8	oe	A5	n	y
eta	2	l	a	2	25	1.2	oe	A6	n	n
eta	3	l	a	2	43	2.1	m	A6	n	n
eta	4	l	a	2	100	2.4	m	A6	n	n
eta	5	l	a	2	100	3.6	m	A6	n	n
eta	6	l	a	2	86	3.3	m	A6	n	n
eta	7	l	a	2	60	1.5	m	A6	n	n
eta	8	l	p	4	50	2.7	m	A6	n	y
eta	9	l	p	2	50	3	m	A6	n	n
eta	10	l	p	2	100	3.9	m	A6	y	n
eta	11	l	p	1	91	3.6	m	A6	y	n
eta	12	l	a	1	40	3	ml	A7	n	n

sample	cell number	left/ right identity	a/p identity	number of interactions	Ajs [%]	interaction width [μm]	zipping stage	segment	mixer cell	a-p interaction
eta	1	r	a	2	14	3.3	oe	A6	n	y
eta	2	r	a	2	30	3	m	A6	n	n
eta	3	r	a	2	100	4.8	m	A6	n	n
eta	4	r	a	3	73	4.5	m	A6	n	n
eta	5	r	a	3	33	3.6	m	A6	n	y
eta	6	r	p	2	50	1.2	m	A6	n	n
eta	7	r	p	2	58	3.9	m	A6	n	n
eta	8	r	p	1	85	4.2	m	A6	n	n
eta	9	r	p	2	94	5.7	m	A6	y	n
eta	10	r	a	1	40	3	ml	A7	n	n

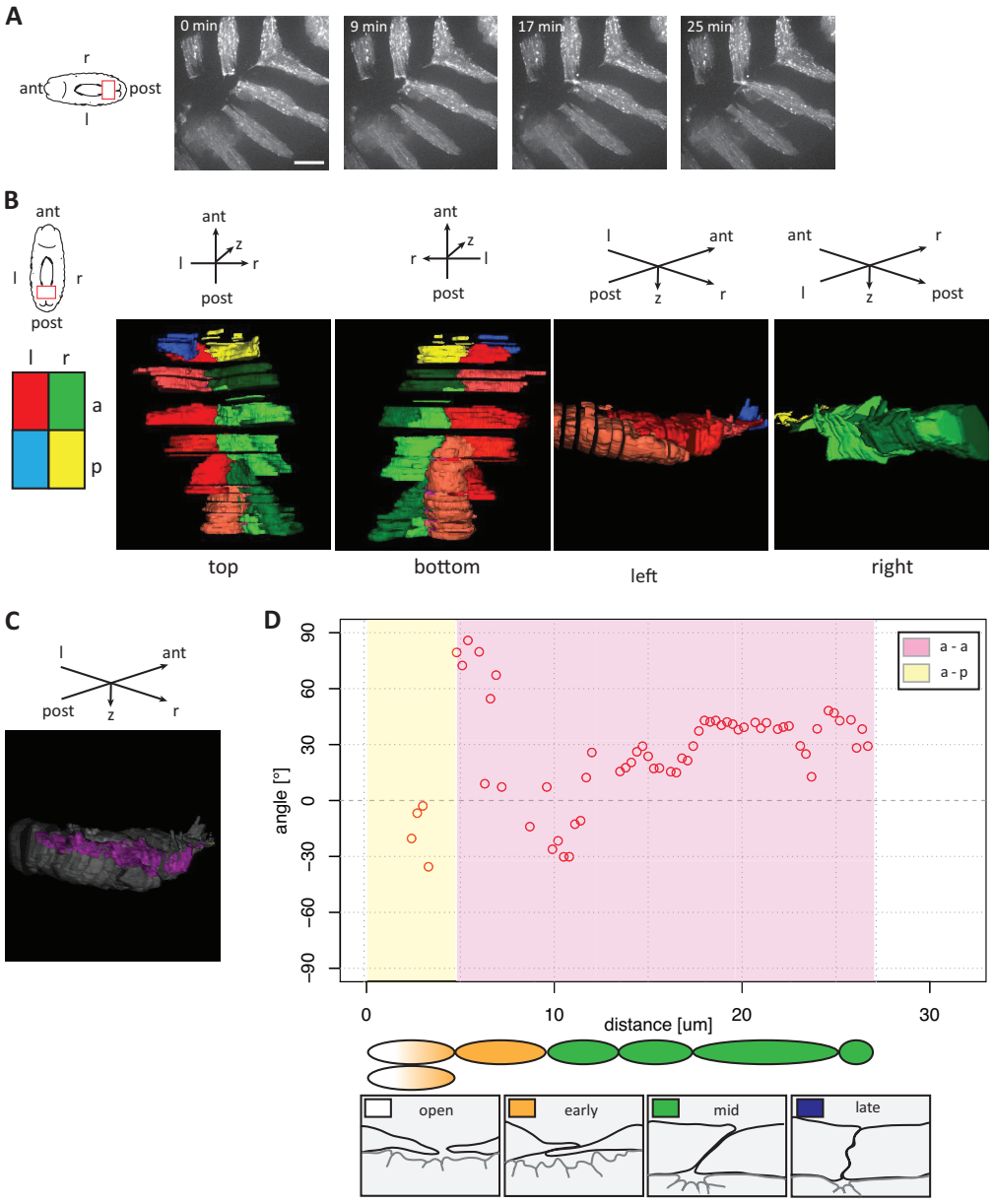

Figure 37: **Supplementary information embryo alpha.** Supplementary information on the behavior of anterior LE cells at the zipping site of embryo alpha. All panels summarizing the cellular behavior of a certain sample are constructed in the same way. Therefore, consult the figure legend of figure 16 for details. The right-side anterior LE cells protrude over the opposing left ones. Scale bar depicts 25 μm (A).

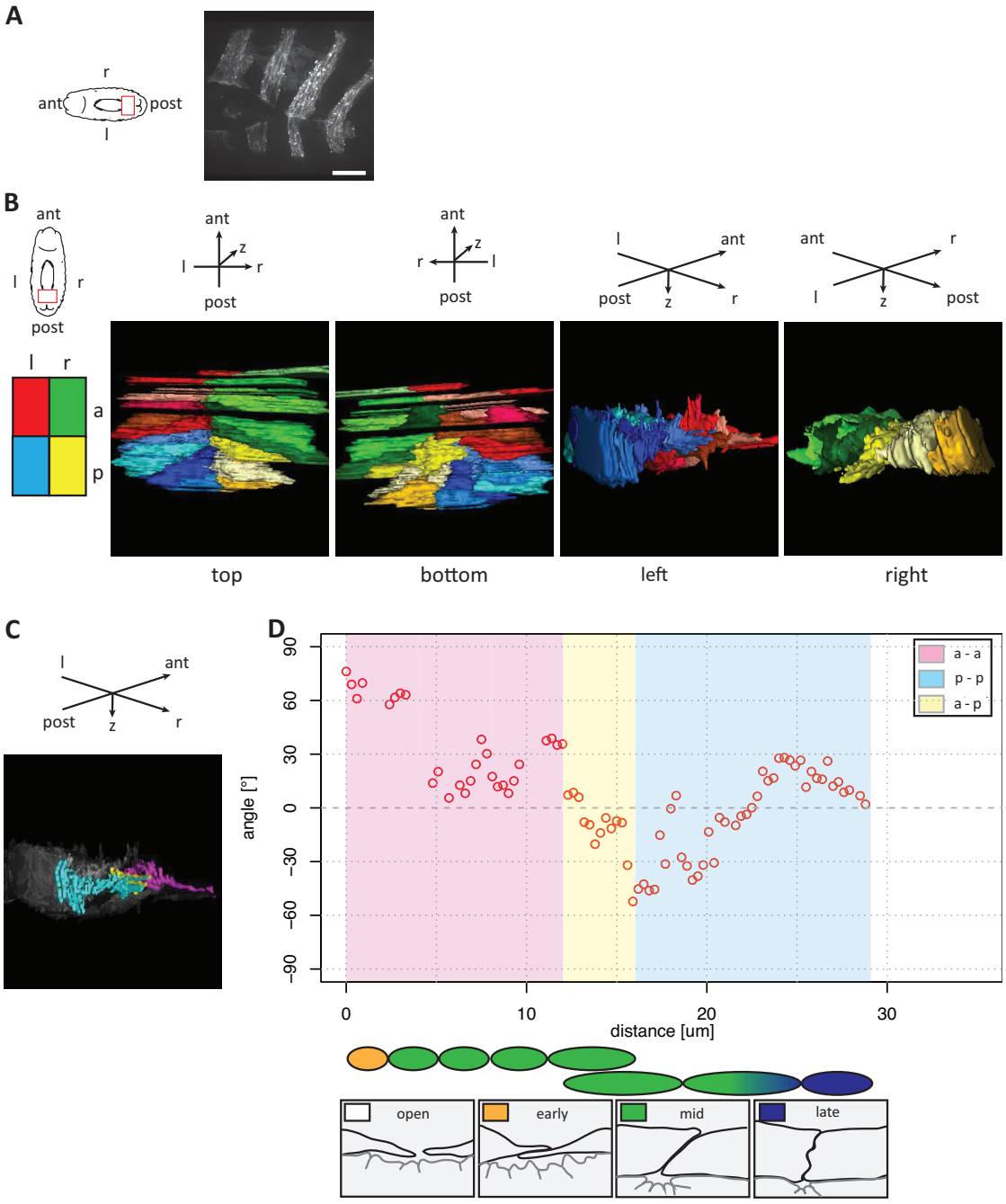

Figure 38: **Supplementary information embryo gamma.** Summary panel on the cellular behavior of anterior and posterior compartmental cells of embryo gamma. Scale bar depicts 25 μm (A).

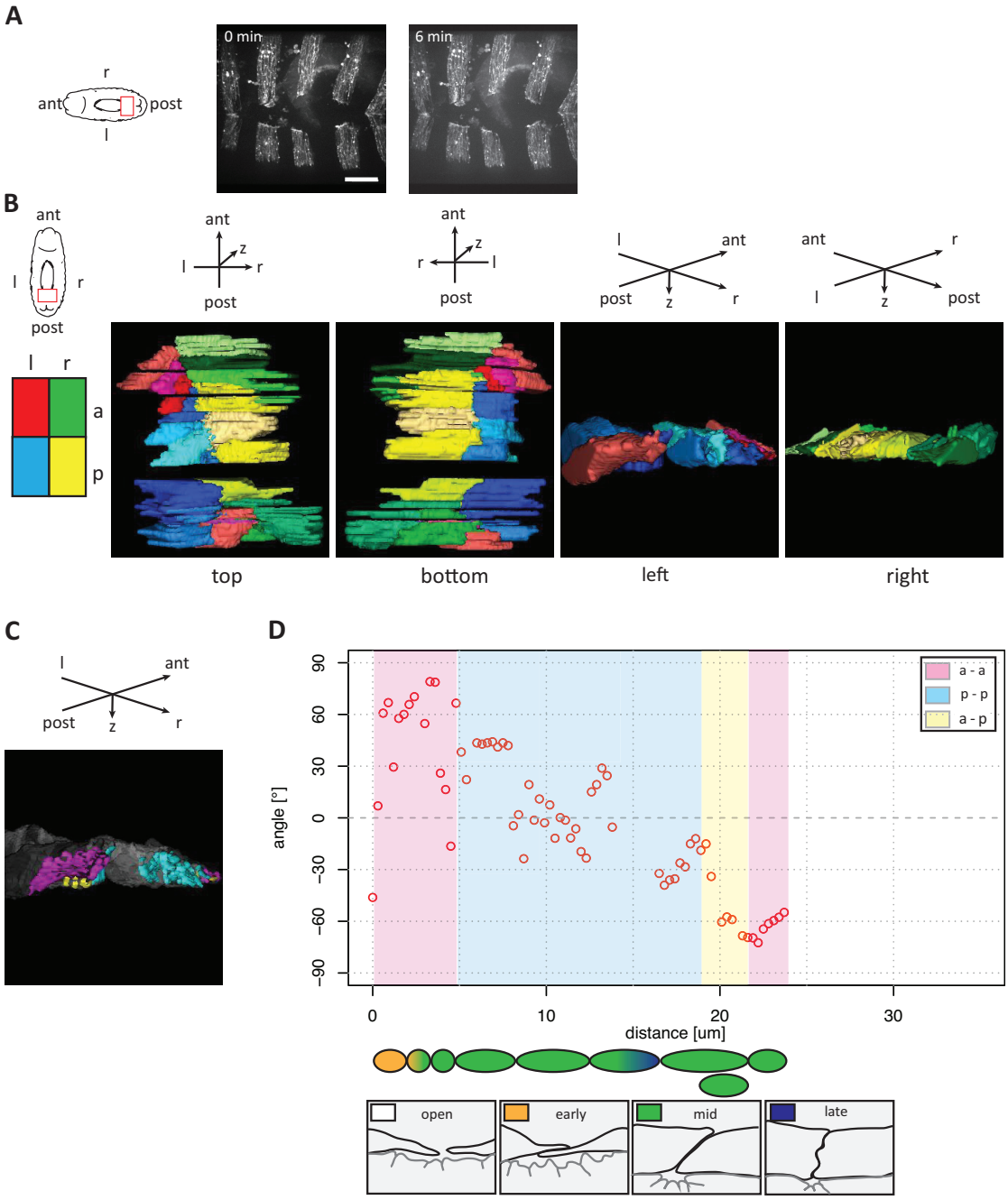

Figure 39: **Supplementary information embryo epsilon.** Summary panel on the cellular behavior of anterior and posterior compartmental cells of embryo epsilon. Scale bar depicts 25 μm (A).

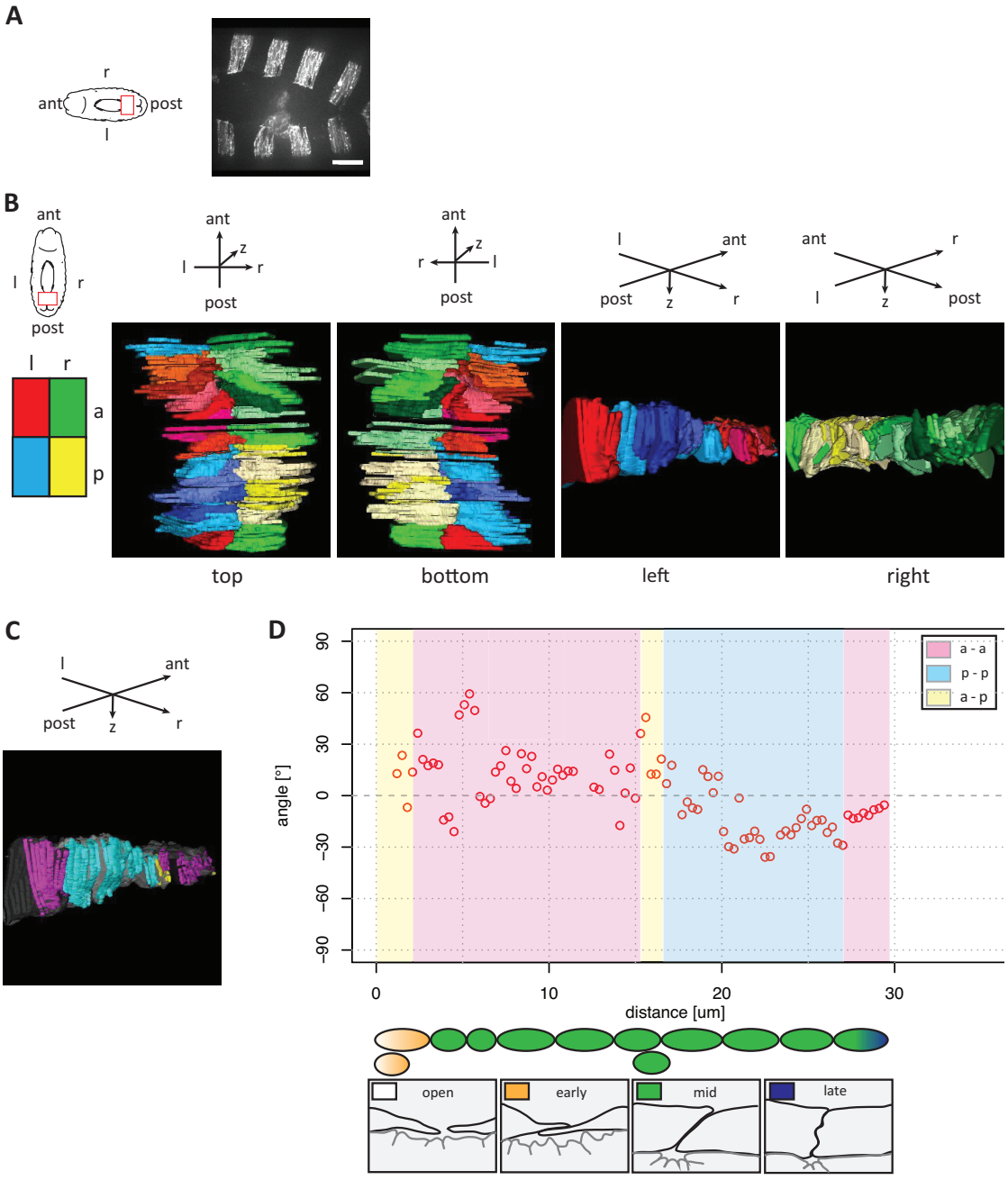

Figure 40: **Supplementary information embryo eta.** Summary panel on the cellular behavior of anterior and posterior compartmental cells of embryo eta. Scale bar depicts 25 μm (A).

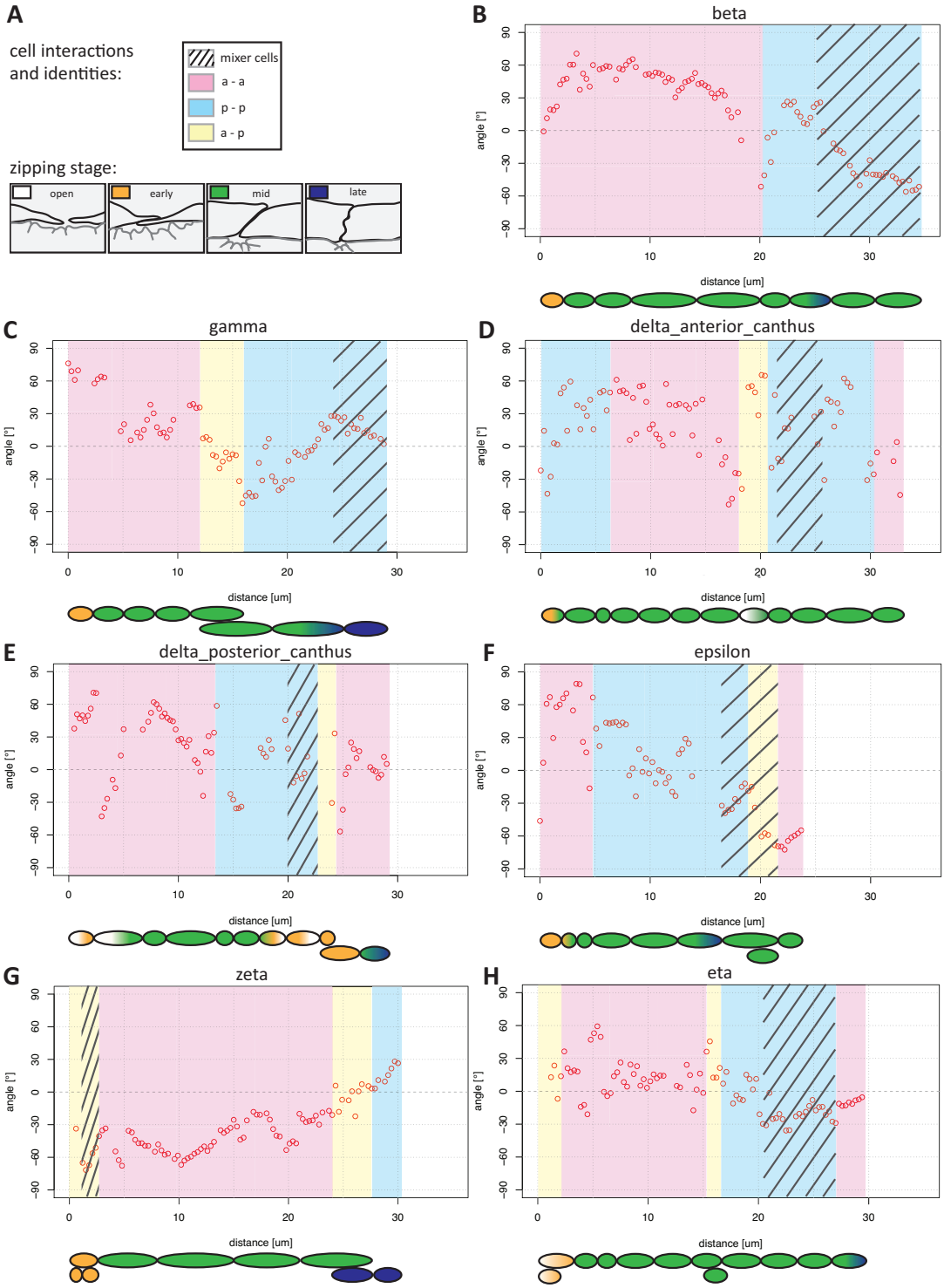

Figure 41: **The identification of mixer cells within the posterior compartment of the investigated CLEM samples.** Summary panel displaying the occurrence of mixer cells (absent for embryo alpha). **A** Legend displaying coding for cell-cell interactions, cell identity, and the zipping stage. **B - H** Angle measurements plotted against distance from the opening of the zipping site for the indicated embryo. Note the occurrence of one mixer cell towards the posterior of the posterior compartment.

Appendix B - Publication

BRIEF COMMUNICATIONS

Structural analysis of multicellular organisms with cryo-electron tomography

Jan Harapin[1], Mandy Börmel[1,2], K Tanuj Sapra[1], Damian Brunner[2], Andres Kaech[3] & Ohad Medalia[1,4,5]

We developed a method for visualizing tissues from multicellular organisms using cryo-electron tomography. Our protocol involves vitrifying samples with high-pressure freezing, thinning them with cryo-FIB-SEM (focused-ion-beam scanning electron microscopy) and applying fiducial gold markers under cryogenic conditions to the lamellae post-milling. We applied this protocol to acquire tomograms of vitrified *Caenorhabditis elegans* embryos and worms, which showed the intracellular organization of selected tissues at particular developmental stages in otherwise intact specimens.

Cryo-electron tomography (CET) has become the method of choice for structural studies of cells, organelles and macromolecular complexes[1–4]. Vitrification is used to instantaneously arrest all biological processes in order to preserve samples in a frozen, hydrated, near-native state[5,6], thereby circumventing the unwanted side effects of chemical fixation[7]. However, CET is limited by the thickness of the specimen of interest. Cryo-FIB-SEM is a relatively new technique that incorporates sample vitrification and is an alternative to conventional sample-thinning methods. This technique produces thin lamellae of the regions of interest[8–11], which can then be imaged by CET. However, these lamellae are devoid of surface fiducial markers, which makes tomographic imaging and reconstruction challenging because of the inherently lower signal-to-noise ratio of images of specimens thicker than ~300 nm (ref. 12). Here we describe a protocol for high-pressure freezing (HPF) and cryo-FIB-SEM milling of multicellular specimens, addition of surface fiducial markers under cryogenic conditions post-milling and CET imaging (**Fig. 1e**).

We vitrified adult worms with HPF using 2-methylpentane because it is a liquid at −150 °C and can facilitate the disassembly of aluminum carriers without fracturing the specimens or dislodging them from the electron microscopy (EM) grids. Furthermore, 2-methylpentane could be sublimed within minutes at −150 °C and high vacuum, ensuring full exposure of the sample during milling (**Fig. 1b** and **Supplementary Fig. 1h**). This offers a substantial improvement over traditional cryoprotectants (for example, 1-hexadecene)[13], which make the sample indistinguishable from these chemicals after freezing (**Fig. 1a**).

In order to facilitate easy control over the milling procedure, we modified a Leica prototype cryo-holder such that the EM grids are attached at their rims (**Supplementary Fig. 1a–c**). This enabled us to spread samples over the entire surface of the grid and orient the grid in-plane with the FIB column, thereby increasing the overall throughput of the technique. Additionally, this makes it possible to remove the grid from the cryo-holder, add fiducial markers and insert it into any cryo-transmission electron microscope (cryo-TEM).

The shape of the milling object used for thinning worms and their embryos was a parallelogram (**Fig. 1f**) that left a 150° internal angle between the lamella and the nonmilled material (**Supplementary Fig. 1j**). This prevented the nonmilled sides from getting into the path of the beam and occluding the imaging area at high tilts during tilt-series acquisition.

Plunge-frozen *C. elegans* embryos (**Fig. 1c**) were semifinely milled above and below the region of interest with a 240-pA probe. This step was followed by a fine-milling step using a 50-pA probe. This resulted in ~330-nm-thick lamellae that were on average very flat and stable for imaging in a cryo-TEM (**Fig. 1d** and **Supplementary Fig. 1e,g**). Adult worms were rough milled with a 4-nA probe until the region of interest was reduced to ~5-µm-thick lamellae (**Supplementary Fig. 1h–j**).

High-current milling reduced the overall milling time; however, substantial amounts of heat were transferred to the sample. After the first round of milling, the quality of the vitrification could be assessed by checking for the presence of cracks in the sample (**Supplementary Fig. 1f**). Samples were then semifinely milled with a 240-pA probe to remove the heat-afflicted material. The amount of heat delivered by this probe was well tolerated by the sample, as there were no evident morphological distortions of the lamella such as changes in its shape from straight to bent (data not shown). The ~2-µm-thick lamellae from adult worms were finely milled using a 50-pA probe, and this resulted in ~660-nm-thick lamellae (**Supplementary Fig. 1i**). We thinned both embryos and worms to ~30-µm-wide lamellae (**Supplementary Fig. 1e,j**), covering the full diameter of the specimen. It took ~30 h to reduce an adult worm to a lamella, compared to the ~3 h it took per embryo. In our experience, 30-µm-wide lamellae are mechanically stable for further handling and processing.

[1]Department of Biochemistry, University of Zurich, Zurich, Switzerland. [2]Institute of Molecular Life Sciences, University of Zurich, Zurich, Switzerland. [3]Center for Microscopy and Image Analysis, University of Zurich, Zurich, Switzerland. [4]Department of Life Sciences in the Negev, Ben-Gurion University, Beer-Sheva, Israel. [5]National Institute for Biotechnology in the Negev, Ben-Gurion University, Beer-Sheva, Israel. Correspondence should be addressed to O.M. (omedalia@bioc.uzh.ch) or A.K. (andres.kaech@zmb.uzh.ch).

RECEIVED 10 SEPTEMBER 2014; ACCEPTED 16 MARCH 2015; PUBLISHED ONLINE 11 MAY 2015 ; DOI:10.1038/NMETH.3401

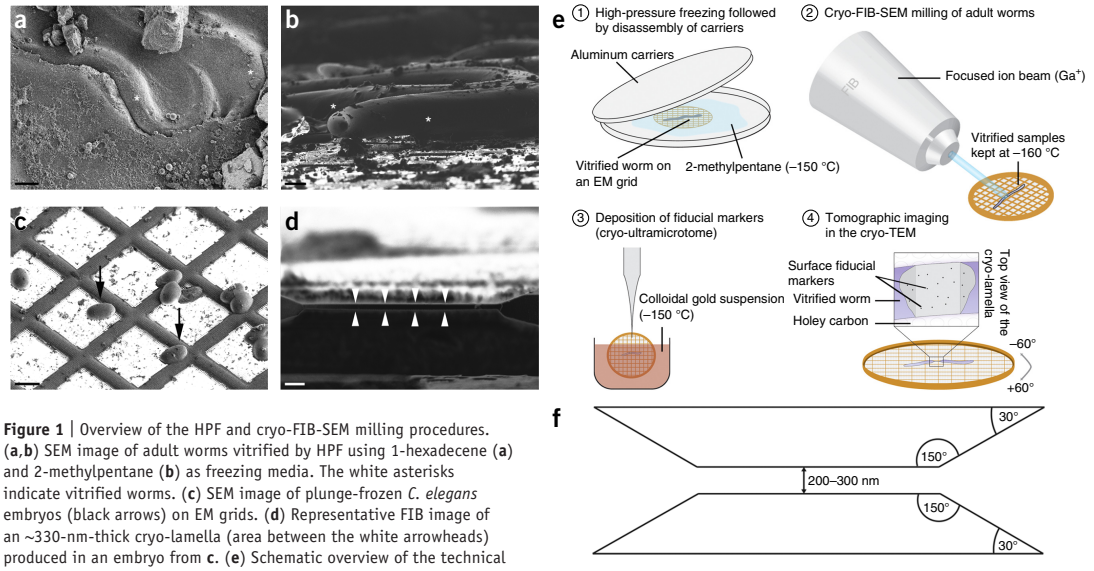

Figure 1 | Overview of the HPF and cryo-FIB-SEM milling procedures. (**a**,**b**) SEM image of adult worms vitrified by HPF using 1-hexadecene (**a**) and 2-methylpentane (**b**) as freezing media. The white asterisks indicate vitrified worms. (**c**) SEM image of plunge-frozen *C. elegans* embryos (black arrows) on EM grids. (**d**) Representative FIB image of an ~330-nm-thick cryo-lamella (area between the white arrowheads) produced in an embryo from **c**. (**e**) Schematic overview of the technical procedures for tomographic imaging of milled worms. (**f**) Drawing of the parallelogram shapes (i.e., milling objects) used for cryo-FIB-SEM thinning of embryos and worms above and below the region of interest. Scale bars, 40 µm (**a**–**c**) and 2 µm (**d**).

Owing to the nature of the cryo-FIB-SEM milling procedure, fiducial gold markers have to be added after milling to ensure spatial proximity between the sample and the markers. We synthesized 10-nm gold nanoparticles in 2-methylpentane and applied the nanoparticles to the surface of the lamellae (Online Methods). The distribution of gold markers along the surface of the grids and the lamella was even (**Fig. 2a**), enabling unhindered reconstructions of cellular interiors of both embryos and adult worms (**Fig. 2b**–**e** and **Supplementary Fig. 2c**–**e**, respectively). Furthermore, grids prepared using gold resuspended in 2-methylpentane were free of toluene and other surface contamination (**Supplementary Fig. 2b**); the gold particles that were resuspended in toluene were covered in ice contamination clusters and appeared clumped (**Supplementary Fig. 2a**).

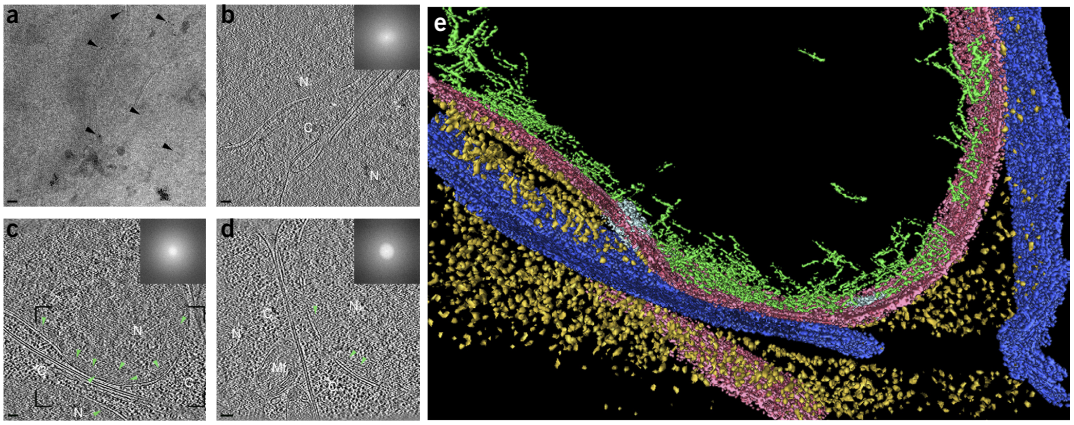

Figure 2 | CET of vitrified *C. elegans* embryos. (**a**) Cryo-TEM image of a 0°-tilt projection showing individual fiducial gold markers (arrowheads) on the lamellar surface. (**b**) 4-nm tomographic slice recorded on an embryo overexpressing the native ce-lamin, at a defocus value of –6 µm. The final resolution was determined from the first zero of the contrast transfer function (CTF) and calculated to be 3.4 nm. (**c**,**d**) Tomographic slices (4 nm and 3.4 nm, respectively) acquired on embryos overexpressing the native ce-lamin (green arrowheads), with a defocus value of –16 µm. The final resolution was determined from the first zero of the CTF and calculated to be 5.6 nm for both tomograms. The power spectra for tomograms **b**–**d** were generated using the 0°-tilt projection images and are shown as insets. N, nucleus; C, cytoplasm; Mt, mitochondrion; asterisks indicate nuclear pore complexes. (**e**) Surface rendered view, generated using Amira 5.4.2, corresponding to the black-framed area in **c**. Dark blue, plasma membrane; pink, nuclear membrane; gold, ribosomes; light blue, nuclear pore complexes; green, filamentous structures adjacent to the inner nuclear membrane. Scale bars, 200 nm.

We acquired tomograms with a moderate to high defocus (−6 µm to −16 µm) and detected structures and macromolecular complexes typically found in a eukaryotic cell, including free and membrane-bound cytoplasmic ribosome assemblies, mitochondria and vesicles (**Fig. 2c–e**, **Supplementary Fig. 2c–e** and **Supplementary Videos 1** and **2**). We were particularly interested in visualizing the nuclear lamina, a filamentous protein layer underlying the nuclear envelope[14,15]. Purified and ectopically expressed *C. elegans* lamins (ce-lamins) had previously been visualized by cryo-electron microscopy[16,17]. However, the low resolution limited the structural analysis of the nuclei. Therefore, we applied our procedure to wild-type embryos that overexpressed GFP-labeled ce-lamin (**Supplementary Fig. 3**). As expected, ~6- to 8-nm-thick filamentous structures were detected at the nuclear periphery (**Fig. 2c** and **Supplementary Fig. 2c**). However, specific labeling approaches will be required to unambiguously identify these structures within the crowded nuclear environment. The cryo-FIB–milled adult worms were imaged on ~660-nm-thick lamellae at −16-µm defocus (**Supplementary Fig. 2c**,**e**). Despite the low signal-to-noise ratio, these data could be aligned using fiducial markers, revealing many of the same features as the tomograms acquired on thinner embryo lamellae (**Fig. 2b–d**).

Our method enables the visualization of >200-nm-thick, vitrified multicellular specimens by cryo-FIB-SEM milling and deposition of fiducial markers onto the sample before CET. We were able to align and reconstruct three-dimensional volumes of ~660-nm-thick lamellae, which would have been impossible without the use of high-contrast fiducials. The cryo-FIB-SEM approach has already offered glimpses into the organization macromolecular complexes within cells[9,11], and together with the improvements described here, it opens up the possibility of acquiring high-resolution information from the cellular interiors of intact tissues. We were able to show the retention of the fluorescent signal post-thinning in *C. elegans* embryos. This will eventually enable the identification and localization of proteins of interest with high precision and accuracy on the surface of the thin cryo-lamellae using various forms of the correlative light and electron microscopy approach. Structural approaches using three-dimensional imaging techniques have so far not been used to study *C. elegans* in a near-native state in detail despite it being a well-established model system[18]. We also demonstrate the possibility of carrying out cryo-FIB-SEM milling on embryos of *Drosophila melanogaster*, another extensively studied model organism (**Supplementary Fig. 4**). Cryo-FIB-SEM in conjunction with CET and averaging procedures can be used to describe the structure of macromolecular complexes *in situ* and at specific stages of development, which will provide more detailed insights into the cellular and macromolecular remodeling taking place within complex organisms.

METHODS

Methods and any associated references are available in the online version of the paper.

Note: Any Supplementary Information and Source Data files are available in the online version of the paper.

ACKNOWLEDGMENTS

We thank Y. Gruenbaum (The Hebrew University of Jerusalem) for providing us with the strains of *C. elegans* used in this study. This work was supported by a European Research Council (ERC) Starting Grant (243047 INCEL) and the Swiss National Science Foundation (SNSF 31003A_141083/1).

AUTHOR CONTRIBUTIONS

J.H., A.K., K.T.S., D.B. and O.M. designed the experiments and wrote the manuscript. J.H. and M.B. carried out the experiments.

COMPETING FINANCIAL INTERESTS

The authors declare no competing financial interests.

1. Fridman, K., Mader, A., Zwerger, M., Elia, N. & Medalia, O. *Nat. Rev. Mol. Cell Biol.* **13**, 736–742 (2012).
2. Yahav, T., Maimon, T., Grossman, E., Dahan, I. & Medalia, O. *Curr. Opin. Struct. Biol.* **21**, 670–677 (2011).
3. Gan, L. & Jensen, G.J. *Q. Rev. Biophys.* **45**, 27–56 (2012).
4. Lučič, V., Rigort, A. & Baumeister, W. *J. Cell Biol.* **202**, 407–419 (2013).
5. Dobro, M.J., Melanson, L.A., Jensen, G.J. & McDowall, A.W. *Methods Enzymol.* **481**, 63–82 (2010).
6. Dubochet, J. & Sartori Blanc, N. *Micron* **32**, 91–99 (2001).
7. Dubochet, J. *et al. Q. Rev. Biophys.* **21**, 129–228 (1988).
8. Marko, M., Hsieh, C., Schalek, R., Frank, J. & Mannella, C. *Nat. Methods* **4**, 215–217 (2007).
9. Rigort, A. *et al. Proc. Natl. Acad. Sci. USA* **109**, 4449–4454 (2012).
10. Wang, K., Strunk, K., Zhao, G., Gray, J.L. & Zhang, P. *J. Struct. Biol.* **180**, 318–326 (2012).
11. Hsieh, C., Schmelzer, T., Kishchenko, G., Wagenknecht, T. & Marko, M. *J. Struct. Biol.* **185**, 32–41 (2014).
12. Grimm, R., Typke, D., Barmann, M. & Baumeister, W. *Ultramicroscopy* **63**, 169–179 (1996).
13. Dahl, R. & Staehelin, L.A. *J. Electron Microsc. Tech.* **13**, 165–174 (1989).
14. Burke, B. & Stewart, C.L. *Nat. Rev. Mol. Cell Biol.* **14**, 13–24 (2013).
15. Ho, C.Y. & Lammerding, J. *J. Cell Sci.* **125**, 2087–2093 (2012).
16. Ben-Harush, K. *et al. J. Mol. Biol.* **386**, 1392–1402 (2009).
17. Grossman, E. *et al. J. Struct. Biol.* **177**, 113–118 (2012).
18. Kipreos, E.T. *Nat. Rev. Mol. Cell Biol.* **6**, 766–776 (2005).

ONLINE METHODS

Cryo-holder and shutter design. The prototype cryo-holder (**Supplementary Fig. 1a**) of the VCT100 cryo-transfer system (Leica Microsystem) was modified in order to accommodate standard EM grids (Quantifoil Micro tools GmbH) at a 30° preset angle with respect to the horizontal base line, which translates into a 6° angle between the sample and the FIB column in the Auriga cross-beam system (Carl Zeiss Microscopy GmbH). The attachment slit for EM grids is composed of two aluminum pieces. Opening and closing is regulated via a screw located on the top part: clockwise rotation to open and counter clockwise to close; the base is freely movable (**Supplementary Fig. 1b**). The shutter was redesigned as an aluminum box that completely envelops the cryo-holder and facilitates contamination-free specimen transfer from liquid nitrogen to high-vacuum conditions and back (**Supplementary Fig. 1c**). The shutter is always attached to the tip of the manipulator of the VCT100 cryo-transfer-shuttle (Leica Microsystems) via a Teflon ring. This allowed us to rotate the tip of VCT100 in order to attach or detach the entire cryo-holder from the cryo-stages inside the various devices used throughout this procedure (**Supplementary Fig. 1d**).

Plunge freezing of *C. elegans* embryos. Mixed populations of adult worms were synchronized by bleaching, and embryos were isolated on a large scale and collected in 1.5-mL Eppendorf tubes in M9 buffer[19]. Approximately 40 embryos were applied onto plasma-cleaned, holey carbon, copper grids (Quantifoil) in a 3-µL droplet using siliconized pipette tips and inspected under a binocular. Grids were then blotted 3–6 s (**Fig. 1c**), plunged into liquid ethane and stored.

High-pressure freezing (HPF) of adult worms. Adult worms were washed off plates with M9 buffer (either at a particular stage of development or as a mixed population), and a desired dilution was pipetted onto plasma-cleaned C-coated copper grids using siliconized pipette tips. An approximately 2-µL droplet of worm suspension was applied directly onto the center of the EM grid to prevent the worms from spreading toward the edges. Grids were then blotted on filter paper to remove the bulk of the liquid and air-dried briefly (up to max. 5 s). Grids were then quickly transferred into the 100-µm-deep cavity of an acetone-cleaned 6-mm aluminum carrier (Wohlwend Engineering), which was premoisturized with a small droplet of 2-methylpentane (Sigma). After the grid stuck to the carrier, the compartment was filled with 2-methylpentane using a Hamilton syringe until the sample was completely covered. A flat 6-mm aluminum carrier was quickly placed on top, causing the excess solution to drain into the surrounding filter paper. The sandwiched assembly was then quickly transferred into the middle plate setup at the loading station of the HPM100 high-pressure freezing machine (Leica Microsystems). Samples were frozen without using ethanol as synchronization fluid in order to avoid surface contamination. Aluminum carriers were inspected for pressure-induced deformation after the freezing process, and bent carriers were discarded. Straight carriers were transferred into the FC6 cryo-ultramicrotome chamber (Leica Microsystems) at −150 °C, causing 2-methylpentane to thaw (melting point is −160 °C), and taken apart after ~10 min. Grids were inspected under a binocular, and only those containing physically intact worms were retrieved with tweezers and stored in grid boxes in liquid nitrogen.

Preparation for cryo-FIB-SEM. Grids containing vitrified worms were attached to the slit of the modified cryo-holder at the cryo-station (Leica Microsystems). They were transferred with the VCT100 shuttle to the cryo-stage of the BAF060 freeze-fracturing device (Leica Microsystems) cooled to −150 °C. After ~15 min, 2-methylpentane completely sublimed under high-vacuum (approximately 10^{-7} mbar), leaving the surface of the EM grid free of any embedding material and the sample fully exposed. We applied a layer of carbon ~20 nm thick to the surface of the grids by electron beam evaporation in order to facilitate subsequent SEM imaging and cryo-FIB-SEM milling. Grids were then transferred with the VCT100 onto the cryo-stage of the Auriga cross-beam system, which was actively kept at −156 °C. Grids containing vitrified embryos were coated with 10 nm of carbon coat and transferred to the Auriga without further processing.

Platinum deposition and correlative light and electron microscopy. We deposited platinum ~3 µm thick around the embryos from a distance of 3 mm using the built-in gas injection system (GIS) of the Auriga cross-beam platform according to a previously described protocol for cold deposition[20]. The GIS temperature was set to 25 °C and the deposition time was 4–6 s, resulting in platinum thicknesses of 1–3 µm. The deposition process was driven by the thermal gradient between the deposition gas and the cold specimen surface and no beams are used to assist it.

After milling was completed, the EM grid carrying the vitrified embryos was quickly thawed in 4% PFA at room temperature and left in the fixative for 10 min. Bright-field and fluorescence images were acquired on a Leica fluorescence microscope (DMI 4000B, Leica) and overlaid.

Cryo-FIB-SEM milling. The Zeiss Auriga cross-beam system used in this study was aligned once per week and remained stable throughout the duration of the entire milling procedure. After the sample was inserted, the stage was brought to the desired position and left to settle for about 15 min, which eliminated drift-related imaging issues. Features of interest were from that point onward centered using the beam shift dials in between rounds of milling. We chose the lamella-type milling approach, which entailed a gradual reduction of total sample volume above and below the horizontal midplane.

Intact worms are up to 1 mm in length and 60 µm in diameter. Rough milling was performed in several rounds, starting with a 4-nA probe and continuing with a 240-pA probe to reduce the thickness around the area of interest in the middle plane of the worm. Once the thickness was ~2 µm, fine milling was performed at 50 pA, leaving an ~660-nm-thick lamella. In this case the milling depth of the Ga^+ beam was set to 8 µm owing to the huge diameter of the worm, and the whole procedure took ~30 h (milling was carried out in multiple steps that individually took 1–3 h, depending on the beam current strength and milling depth set). After milling was completed, the cryo-holder was retrieved from the Auriga and the grids were stored in grid boxes.

Embryos of *C. elegans* are approximately 40 µm × 20 µm in size, so rough milling was performed using a 240-pA probe, reducing the middle of the sample to a 2-µm thick lamella. Fine milling was performed using a 50-pA probe, leaving an ~330-nm-thick lamella. The Ga^+ beam was set to a milling depth of 3 µm, and the whole procedure took ~3 h per embryo.

doi:10.1038/nmeth.3401

The surfaces of the lamellae initially exhibited typical FIB-related artifacts post-milling. These included curtaining, some gallium-ion deposition at the edges of the lamellae and a slight increase in thickness of the area on the lamella where the beam exits the sample (due to defocusing). We found that curtaining as well as big variations in thickness can be circumvented by setting the milling depth of the beam to approximately twice what was actually needed. The beam penetration depth on the Auriga can be calibrated to suit different kinds of materials. We routinely used the calibration for silicon as a reference and found the milling depth for frozen biological material to be approximately ten times less than that needed for silicon (setting the milling depth to 1 µm resulted in actual milling depth of approximately 10 µm for embryos and worms).

Fiducial markers for the cryo-lamellae. We modified a toluene-based synthesis of suspensions of colloidal gold particles similarly to a previously described procedure[21]. A solution containing 50 mg of tetrachloroauric acid (Sigma) in 1.0 g (1.2 mL) of oleylamine (Acros Organics) and 1.0 mL of toluene was quickly injected into a solution containing 1.7 g (2.9 mL) of oleylamine in 49 mL of toluene at 110 °C. The reaction was carried out for 2 h at this temperature, after which the products were precipitated by the addition of 100 mL of methanol. Particles ~10 nm in diameter were isolated by centrifugation at 500*g*, methanol was decanted and the tubes were left to air-dry in order to evaporate residual methanol. Finally, the gold particles were resuspended in 1 mL in 2-methylpentane. Where needed, the gold particles were further diluted to a desired concentration with 2-methylpentane. Gold was applied to the lamellae in the cryo-ultramicrotome chamber at −150 °C, inside 0.5 mL wells of an aluminum box (produced by our in-house workshop) similarly to in a previously described procedure[22]. Grids were briefly immersed in the gold suspension (2–3 s), rinsed twice by immersion into liquid ethane in adjacent wells, blotted extensively (>20 s) with filter papers until no residual liquid could be observed on the tweezers or the grids, and stored in grid boxes. The quality of the gold-particle synthesis, as well as the particle distribution, was assessed on empty plunge-frozen grids in the cryo-TEM (**Supplementary Fig. 2a**,**b**)

Cryo-electron tomography (CET) and annotations. Specimens were analyzed in a 300-kV FEG FEI Polara transmission electron microscope equipped with a Gatan post-column GIF 2002 energy filter. Tilt series were acquired—covering either an angular range of −54° to +60° (**Fig. 2c** and **Supplementary Fig. 2a**,**b**) or, in specific cases, −40° to +40° owing to spatial constraints (**Fig. 2b**,**d**)—with 2° tilt increments and defocus values ranging from −6 µm to −16 µm, for both the embryos and worms. Primary magnifications of 41,000× and 50,000× were used, and this resulted in a 4.08-nm and 3.36-nm pixel size, respectively. Projection images (2,048 × 2,048 pixels) were aligned using 10-nm fiducial gold markers and reconstructed by means of a weighted back-projection algorithm, as implemented by the TOM toolbox software package[23]. The width of the energy slit used for tomographic imaging was 20 eV. Images were collected on a Gatan Ultrascan 4000 CCD camera. Resolutions of tomograms were estimated from the first zero crossing over the CTF and are indicated in the figure panel. Power spectra demonstrating the absence of crystalline ice were generated using the 0°-tilt projections of each of the respective tomograms (**Fig. 2b–d** and **Supplementary Fig. 2c**,**e**). We acquired 18 tomograms from *C. elegans* embryos and 5 from adult worms. Slices from representative tomograms were displayed in the figure panels. Three-dimensional rendering and annotating was carried out using the Amira 5.4.2 software (FEI).

19. Strange, K., Christensen, M. & Morrison, R. *Nat. Protoc.* **2**, 1003–1012 (2007).
20. Hayles, M.F., Stokes, D.J., Phifer, D. & Findlay, K.C. *J. Microsc.* **226**, 263–269 (2007).
21. Hiramatsu, H. & Osterloh, F.E. *Chem. Mater.* **16**, 2509–2511 (2004).
22. Gruska, M., Medalia, O., Baumeister, W. & Leis, A. *J. Struct. Biol.* **161**, 384–392 (2008).
23. Nickell, S. *et al. J. Struct. Biol.* **149**, 227–234 (2005).

doi:10.1038/nmeth.3401

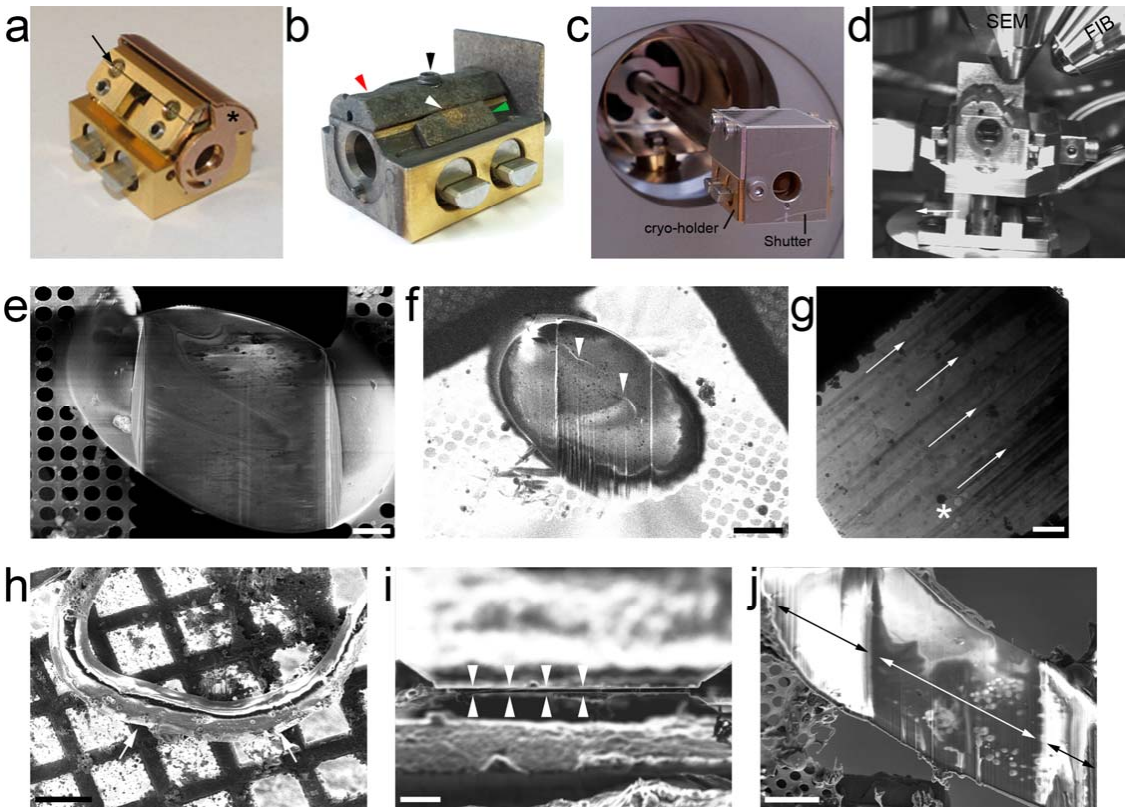

Supplementary Figure 1

Cryo-holder design and overview of the cryo-FIB-SEM procedure carried out on embryos and worms

(**a**) The prototype cryo-holder. The attachment slit (black arrow) and shutter (black asterisk) were redesigned to accommodate standard EM grids at a 6° angle with respect to the FIB column in the Auriga crossbeam system. (**b**) The two-piece attachment slit is regulated by a screw (black arrow head) on the upper component (red arrow head), while the base is freely movable (green arrow head). (**c**) The aluminum shutter envelops the cryo-holder while attached to the tip of the rod of the VCT100 shuttle via a Teflon ring. (**d**) The cryo-holder inside the Auriga. (**e**) SEM image of a well-vitrified embryo. The lamella is flat and no cracks are present. (**f**) SEM image of a cracked embryo. Cracks in the sample (white arrow heads) can be observed immediately upon the removal of the top of the sample with the cryo-FIB. (**g**) Cryo-TEM image of an embryo lamella showing the full dimensions of a lamella used for tomographic imaging. White asterisk indicates areas used for focusing and tracking and white arrows show the direction of the Ga+ beam milling. (**h**) SEM image of a vitrified worm (white arrows) after the sublimation of 2-methylpentane. (**i**) FIB image of the worm lamella (area in between white arrow heads) after milling. (**j**) SEM image of the worm lamella from top showing the full dimensions of the milled area (white double arrow) and the non-milled sides (black double arrows). Scale bars represent 2 µm (**g**), 5 µm (**e,i**), 10 µm (**f,j**), and 100 µm (**h**).

Nature Methods: doi:10.1038/nmeth.3401

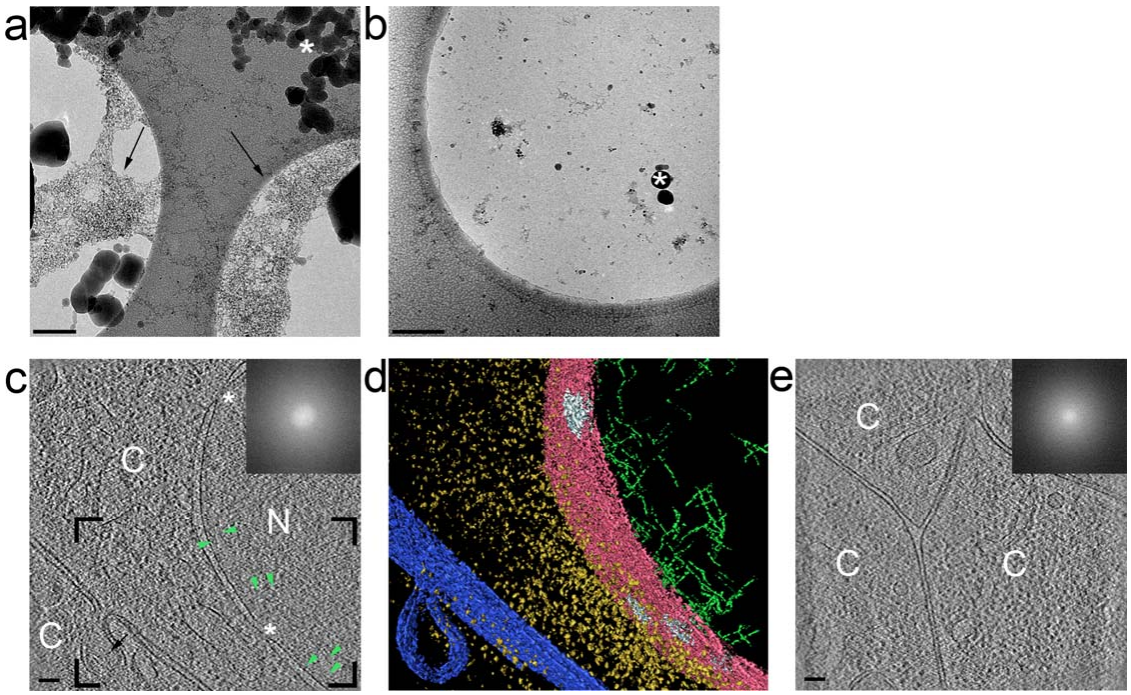

Supplementary Figure 2

Cryo-electron microscopy of gold nanoparticles and CET of vitrified *C. elegans* worms

(**a**) Cryo-TEM image of gold nanoparticles synthesized in toluene and spread on the surface of a plunge frozen EM grid. The grid is covered by ice contamination that varies both in thickness and size (white asterisk) and shows the markers clustering within this contamination (black arrows). (**b**) Cryo-TEM image of gold nanoparticles synthesized in 2-methylpentane and spread on the surface of a plunge-frozen EM grid. Individual markers are evenly distributed along the grid surface and contamination is barely detectable (compare the areas indicated by the white asterisks). (**c,e**) 3.4 nm thick tomographic slices acquired with a –16 µm defocus on a worm cryo-lamella. Green arrow heads point towards filamentous structures adjacent to the INM, the black arrow points to a plasma membrane protrusion and the white asterisks indicate the position of NPCs. (N – nucleus, C – Cytoplasm). (**d**) A surface rendered view corresponding to the black-framed area in panel a. Plasma membrane – dark blue, nuclear membrane – pink, ribosomes – gold, NPCs – light blue, and filamentous structures adjacent to the INM – green. Final resolution of both tomograms was estimated from the first zero of the CTF and calculated to be 5.4 nm. Scale bars represent 250 nm (**a,b**) and 200 nm **(c,e**).

Nature Methods: doi:10.1038/nmeth.3401

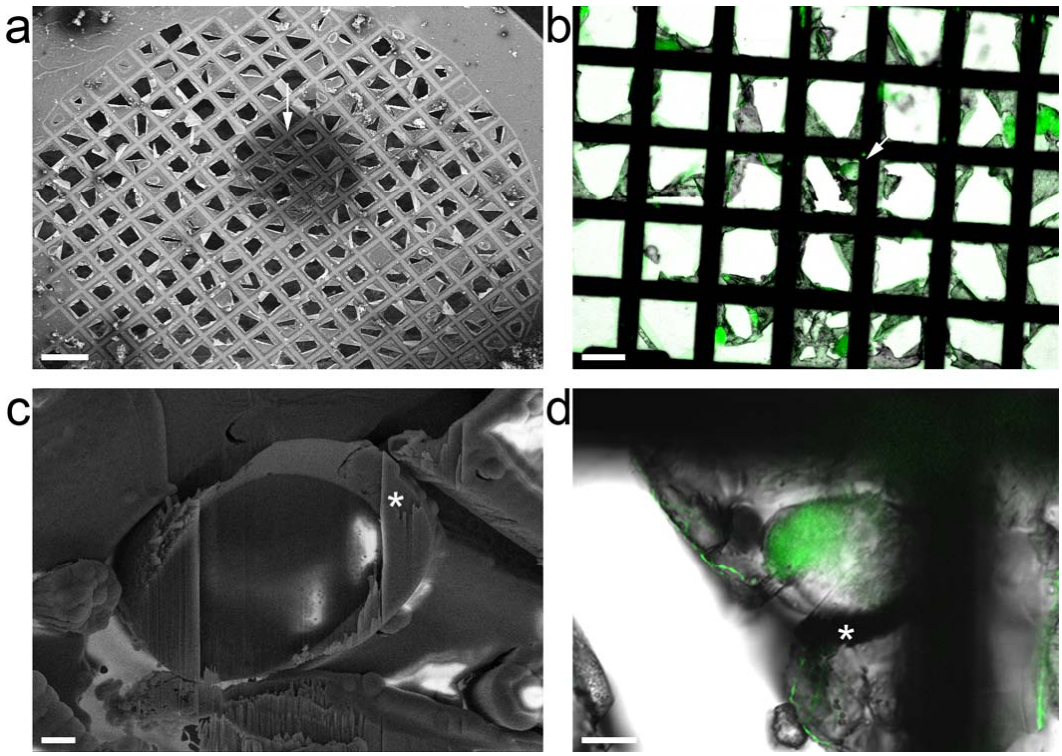

Supplementary Figure 3

Correlative light and electron microscopy of *C. elegans* embryos expressing lamin-GFP

(**a**) SEM overview of the grid before milling. The embryo that will be milled is indicated by the white arrow. (**b**) Bright-field-fluorescence channel overlay showing the same embryo post-milling, fixed in 4% PFA (white arrow). (**c**) SEM image of the embryo post-milling. White asterisk indicated the area where platinum was deposited inside the cryo-FIB-SEM device to facilitate milling. (**d**) Bright-field-fluorescence channel overlay showing bright lamin-GFP signal inside the thicker, non-milled sides of the embryo, and its distribution throughout the thin lamella. The white asterisk indicated the area where platinum was deposited (same as in panel c). The bright-field-fluorescence images (**b,d**) are rotated approximately 40° clock-wise compared to the SEM images (**a,c**). Scale bars indicate 200 µm (**a**), 50 µm (**b**), 5 µm (**c**), and 10 µm (**d**).

Nature Methods: doi:10.1038/nmeth.3401

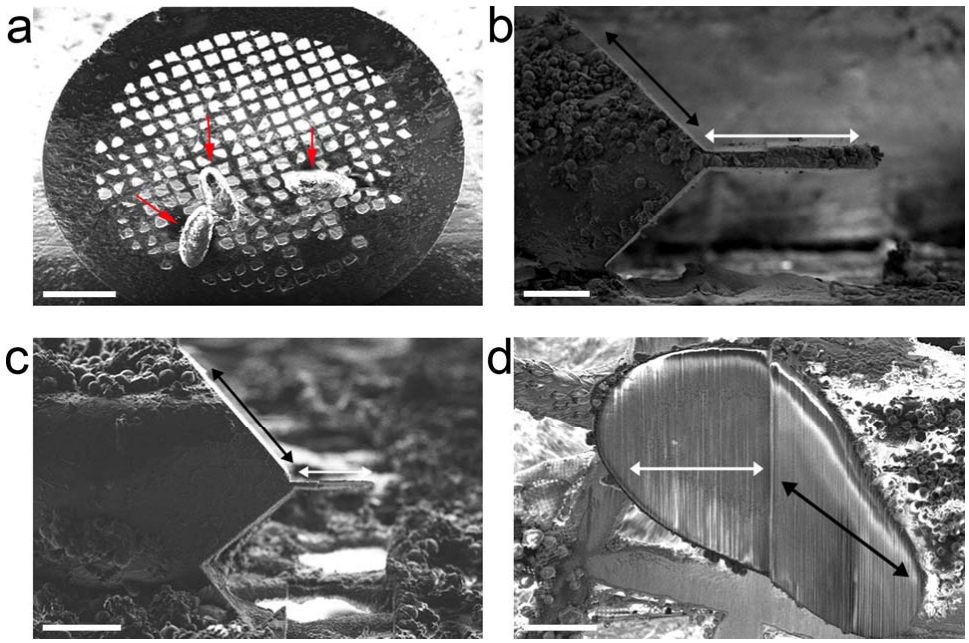

Supplementary Figure 4

Cryo-FIB milling of *Drosophila melanogaster* embryos

(**a**) SEM overview image of the EM grid bearing 3 *D. melanogaster* embryos (red arrows). (**b**) FIB side view of the edge of the embryo after several rounds of milling with high currents. (**c**) FIB side view of the thin lamella after successive rounds of course and fine milling. The area underneath the lamella is also cleared in order to facilitate tomographic imaging. (**d**) SEM top view of the lamella after milling. Black double arrows indicate the non-milled slopes surrounding the lamella and the white double arrows indicate the lamella itself. Scale bars indicate 500 µm (**a**) and 50 µm (**b–d**).

Nature Methods: doi:10.1038/nmeth.3401